UNIVERSIDADE FEDERAL DO CEARÁ

CENTRO DE TECNOLOGIA

DEPARTAMENTO DE ENGENHARIA DE TELEINFORMÁTICA

PROGRAMA DE PÓS-GRADUAÇÃO EM ENGENHARIA DE TELEINFORMÁTICA

DOUTORADO EM ENGENHARIA DE TELEINFORMÁTICA

GILDERLAN TAVARES DE ARAÚJO

TENSOR-BASED APPROACHES FOR CHANNEL ESTIMATION IN IRS-ASSISTED MIMO WIRELESS COMMUNICATIONS

FORTALEZA

2024

GILDERLAN TAVARES DE ARAÚJO

TENSOR-BASED APPROACHES FOR CHANNEL ESTIMATION IN IRS-ASSISTED MIMO WIRELESS COMMUNICATIONS

Thesis presented to the Graduate Program in Teleinformatics Engineering of the Federal University of Ceará as a partial requisite to obtain the Ph.D. degree in Teleinformatics Engineering

Advisor: Prof. Dr. André Lima Férrer de Almeida.

FORTALEZA

2024

Dados Internacionais de Catalogação na Publicação
Universidade Federal do Ceará
Sistema de Bibliotecas
Gerada automaticamente pelo módulo Catalog, mediante os dados fornecidos pelo(a) autor(a)

A689t Araújo, Gilderlan Tavares de.
Tensor-Based Approaches for Channel Estimation in IRS-Assisted MIMO Wireless Communications / Gilderlan Tavares de Araújo. – 2024.
170 f. : il. color.

Tese (doutorado) – Universidade Federal do Ceará, Centro de Tecnologia, Programa de Pós-Graduação em Engenharia de Teleinformática, Fortaleza, 2024.
Orientação: Prof. Dr. André Lima Férrer de Almeida.

1. Intelligent reflecting surface. 2. tensor decomposition. 3. channel estimation. 4. MIMO system. I. Título.

CDD 621.38

GILDERLAN TAVARES DE ARAÚJO

TENSOR-BASED APPROACHES FOR CHANNEL ESTIMATION IN IRS-ASSISTED MIMO WIRELESS COMMUNICATIONS

Thesis presented to the Graduate Program in Teleinformatics Engineering of the Federal University of Ceará as a partial requisite to obtain the Ph.D. degree in Teleinformatics Engineering

Aproved on: 23 de Fevereiro de 2024

EXAMINING COMMITTEE

Prof. Dr. André Lima Férrer de Almeida (Orientador)
Federal University of Ceará (UFC)

Prof. Dr. A. Lee Swindlehurst
University of California Irvine (UCI), Irvine, USA

Prof. Dr. Gérard Favier
I3S Laboratory, Sophia Antipolis, France

Prof. Dr. Felix Dieter Antreich
Aeronautics Institute of Technology (ITA), São José dos Campos, Brazil

Prof. Dr. Walter da Cruz Freitas Júnior
Federal University of Ceará (UFC)

Prof. Dr. Fazal-E-Asim
Federal University of Ceará (UFC)

To you

AGRADECIMENTOS

First of all, I would like to thank God for allowing me to wake up every day with the necessary courage to enjoy the journey of life.

To my advisor, I would like to express my deep gratitude for your invaluable support and guidance throughout my research journey. Your dedication and expertise were pivotal in the development and completion of my thesis. Your insightful guidance, patience, and constant encouragement have been truly inspiring. I am thankful for sharing your knowledge and experience, as well as challenging me to reach my highest potential. I am immensely grateful to have such a committed and dedicated advisor. All the learning I have gained under your guidance will be invaluable for my future academic and professional endeavors. Once again, thank you very much for everything.

To my family, I would like to express my heartfelt gratitude for the unwavering support you've provided throughout this journey. Without your love, understanding, and encouragement, reaching this milestone in my life wouldn't have been possible. In particular:

My mother Maria Alice, your wise counsel and constant support have been instrumental to me. Your unwavering strength and love are a daily inspiration.

My dear wife Mikaelle, your unwavering patience, steadfast support, and understanding during the most challenging times formed the foundation that allowed me to dedicate myself to my work with peace of mind. Your presence by my side is my greatest treasure.

Dear children Bernardo and Lis, you are my motivation and joy. Your understanding during the long hours of study and research means more than words can express. Seeing the world through your eyes is a constant reminder of what truly matters.

I would like to extend my gratitude to my colleagues at work, especially Bruno Sokal, Kenneth Benício, Yuri Sales and Lucas Pessoas. Each one of you has played a significant role in shaping this project. Your collaboration, insights, and support have been invaluable contributions to the completion of this work.

Finally, I acknowledge the technical support from Ericsson Research, Sweden, and Ericsson Innovation Center, Brazil, under UFC.48 and UFC.51 Technical Cooperation Contract Ericsson/UFC.

In loving memory of Zilmar Gomes Barboza: Although I had the privilege of knowing her for a shorter time, her warmth, wisdom, and kindness left a lasting mark on all who had the honor of crossing paths with her.

RESUMO

A quinta geração (5G) está em sua versão comercial, e os pesquisadores começaram a olhar para as tecnologias potenciais a serem empregadas na próxima geração. Neste contexto, a superfície refletora inteligente (IRS) é uma tecnologia promissora para a sexta geração (6G) de sistemas sem fio, introduzindo o conceito de ambiente de rádio inteligente. Os ganhos prometidos das comunicações assistidas por IRS dependem da precisão das informações de estado do canal. Usando um framework tensorial, particularmente a decomposição tensorial, propomos diferentes soluções para resolver o problema de estimação de canal para diferentes cenários. Primeiramente, abordamos o design do receptor para um sistema de comunicação MIMO (múltiplas entradas, múltiplas saídas) assistido por IRS através de uma abordagem de modelagem tensorial para resolver o problema de estimação de canal usando métodos supervisionados (assistidos por piloto). Considerando um padrão estruturado no domínio do tempo de pilotos e deslocamentos de fase do IRS, apresentamos dois métodos de estimação de canal que dependem de uma modelagem tensorial de fatores paralelos (PARAFAC) dos sinais recebidos. O primeiro método tem uma solução em forma fechada baseada em uma fatorização de Khatri-Rao do canal MIMO em cascata, resolvendo problemas de aproximação de matrizes de posto 1, enquanto o segundo é um esquema iterativo de estimação alternada. A característica comum de ambos os métodos é o desacoplamento das estimativas das matrizes do canal MIMO envolvidas (estação base (BS)-IRS e IRS-terminal do usuário (UT)), o que proporciona melhorias de desempenho em comparação com métodos concorrentes baseados em estimativas de quadrados mínimos (LS) não estruturadas do canal em cascata. Neste cenário, os resultados numéricos mostram a eficácia dos receptores propostos, destacam os compromissos envolvidos e corroboram seu desempenho superior em comparação com soluções concorrentes baseadas em LS. Em segundo lugar, desenvolvemos algoritmos para estimar conjuntamente as matrizes de canal envolvidas e os símbolos transmitidos de maneira semi-cega. Isso é alcançado introduzindo um esquema de codificação espaço-temporal simples no transmissor, de modo que o modelo de sinal recebido possa ser vantajosamente construído usando o modelo tensorial PARATUCK. Como resultado, um receptor semi-cego é derivado explorando a estrutura algébrica do modelo tensorial PARATUCK. Neste contexto, formulamos inicialmente um receptor semi-cego baseado em um método de mínimos quadrados alternados trilineares que estima iterativamente os dois canais de comunicação envolvidos – IRS-BS e UT-IRS – e a matriz de símbolos transmitidos. Em segundo lugar, formulamos um receptor semi-cego de duas etapas aprimorado que explora eficientemente o link direto para

refinar iterativamente as estimativas de canal e símbolo. Além disso, discutimos o impacto de uma absorção imperfeita do IRS (reflexão residual) no desempenho do receptor proposto. Finalmente, formulamos um receptor semi-cego baseado em tensor para um sistema MIMO multiusuário de uplink assistido por IRS, onde a abordagem proposta depende de um modelo tensorial PARATUCK generalizado dos sinais refletidos pelo IRS, baseado em um receptor semi-cego de duas etapas em forma fechada usando fatorizações de Khatri-Rao e Kronecker.
Palavras-chave: Superfície refletora inteligente, decomposição tensorial, estimação de canal, sistema MIMO.

ABSTRACT

The fifth-generation (5G) is in its business version, and researchers have started to look at the potential technologies to be employed in the next generation. In this context, intelligent reflecting surface (IRS) is a promising technology for the sixth-generation (6G) of wireless systems by introducing the smart radio environment concept. The promised gains of IRS-assisted communications depend on the accuracy of the channel state information. Using a tensor framework, particularly tensor decomposition, we propose different solutions to solve the channel estimation problem for different scenarios. We firstly address the receiver design for an IRS-assisted multiple-input multiple-output (MIMO) communication system *via* a tensor modeling approach to solve the channel estimation problem using supervised (pilot-assisted) methods. Considering a structured time-domain pattern of pilots and IRS phase shifts, we present two channel estimation methods that rely on a parallel factors (PARAFAC) tensor modeling of the received signals. The first method has a closed-form solution based on a Khatri-Rao factorization of the cascaded MIMO channel by solving rank-1 matrix approximation problems, while the second is an iterative alternating estimation scheme. The common feature of both methods is the decoupling of the estimates of the involved MIMO channel matrices (base station (BS)-IRS and IRS-user terminal (UT)), which provides performance enhancements in comparison to competing methods that are based on unstructured least squares (LS) estimates of the cascaded channel. In this scenario, the numerical results show the effectiveness of the proposed receivers, highlight the involved trade-offs, and corroborate their superior performance compared to competing LS-based solutions. Second, we develop algorithms to jointly estimate the involved channel matrices and the transmitted symbols in a semi-blind fashion. This is achieved by introducing a simple space-time coding scheme at the transmitter, such that the received signal model can be advantageously built using the PARATUCK tensor model. As a result, a semi-blind receiver is derived by exploiting the algebraic structure of the PARATUCK tensor model. In this context, we first formulate a semi-blind receiver based on a trilinear alternating least squares method that iteratively estimates the two involved communication channels – IRS-BS and UT-IRS – and the transmitted symbol matrix. Second, we formulate an enhanced two-stage semi-blind receiver that efficiently exploits the direct link to refine the channel and symbol estimates iteratively. In addition, we discuss the impact of an imperfect IRS absorption (residual reflection) on the performance of the proposed receiver. Finally, we formulate a tensor-based semi-blind receiver for an IRS-assisted uplink multi-user MIMO (MU-MIMO) system where the proposed approach relies on a generalized PARATUCK tensor model of the signals reflected by the IRS, based on a two-stage closed-form semi-blind receiver using Khatri-Rao and Kronecker factorizations.

Keywords: Intelligent reflecting surface, tensor decomposition, channel estimation, MIMO system.

LIST OF FIGURES

LISTA DE TABELAS

LIST OF ABBREVIATIONS AND ACRONYMS

5G	fifth-generation
6G	sixth-generation
ALS	alternating least square
BALS	bilinear alternating least squares
BS	base station
CE	channel estimation
CONFAC	constrained factor
CRB	Cramér-Rao lower bound
CSI	channel state information
DS-CDMA	direct-sequence code-division multiple access
E-TALS	*enhanced* TALS
EVD	eigenvalue decomposition
IRS	intelligent reflecting surface
KF	Kronecker factorization
KPI	key performance indicator
KRF	Khatri-Rao factorization
LS	least squares
MIMO	multiple-input multiple-output
MISO	multiple-input single-output
mmWave	millimetre-wave
MU	multi-user
MU-MIMO	multi-user MIMO
NMSE	normalized mean square error
PARAFAC	parallel factors
RF	radio frequency
RIS	reconfigurable intelligent surface
SER	symbol error rate
SISO	single-input single-output
SNR	signal-to-noise ratio
STBC	space time block code

SVD	singular value decomposition
TALS	trilinear alternating least squares
THz	Terahertz communication
UT	user terminal

LIST OF SYMBOLS

Ae	Área efetiva da antena
B	Largura de faixa em que o ruído é medido em Hertz
d	Distância em metros
E	Campo elétrico
FA	Fator da antena
Gr	Ganho de recepção
h	Altura efetiva ou comprimento efetivo de uma antena
I	Corrente elétrica
k	Constante de Boltzmann's
K	Eficiência de irradiação
M	Variação do patamar de ruído em função da RBW
N	Condutor de neutro
NF	Figura de ruído
Ni	Potência do ruído na entrada
No	Potência do ruído na saída
P	Potência
R	Resistência
Si	Potência do sinal na entrada
So	Potência do sinal na saída
t	Tempo
V	Tensão
ZL	Impedância da antena
Zo	Impedância de referência (50Ω)
λ	Comprimento de onda
Γ	Coeficiente de reflexão

SUMMARY

1 INTRODUCTION

1.1 Motivation

Wireless communications have become a crucial part of technological advancements and developments. It has enabled the creation of new services, devices, and applications in various fields like education, industry, communication, and entertainment. This constant evolution of wireless communication has led to new demands, which require the improvement of wireless systems and all associated networks. According to (Wang *et al.*, 2023), mobile wireless traffic has grown exponentially. The global mobile subscriptions are expected to reach around 17.1 billion by 2030 (M.2370-0, 2015).

According to the study conducted by (Wang *et al.*, 2023), it is expected that the upcoming 6G technology will address the limitations and challenges of the existing 5G technology, which is currently in its business phase. Several companies have already unveiled their plans for the next technological generation, e.g., (Semaan *et al.*, 2023; DOCOMO, 2022; Inc., 2022), with a common expectation to launch the 6G technology around 2030. According to (Wang *et al.*, 2023), 6G involves some key performance indicators that are not covered in the 5G standardization, as shown in Figure 1. According to recent research, the deployment of 6G

Figura 1 – List of expected KPIs for 6G technology

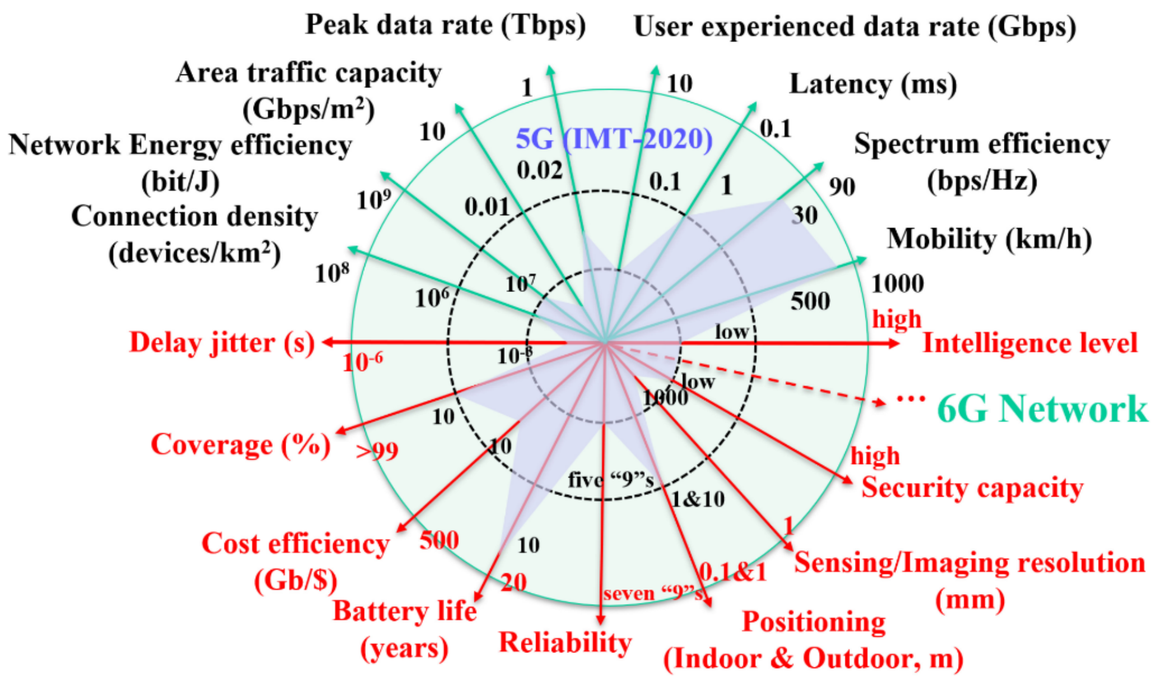

Fonte: Wang, Cheng-Xiang, et al. (Wang *et al.*, 2023) will potentially involve new technologies. The studies in (Banafaa *et al.*, 2023) and (Wang *et al.*, 2023) have listed several key technologies including Terahertz communication (THz) and IRS, among others. Although not mentioned in their lists, the work (Wong *et al.*, 2023) suggested the fluid antenna concept as another potential technology. It is worth noting that these technologies are not mutually exclusive, as they can work together. For example, the use of IRS has been investigated in THz communications (see (Zhao *et al.*, 2023) and references therein).

Among the different solutions, the interest of this thesis is on the IRS since it has been considered a disruptive technology due to its potential capability to change the current wireless communication system paradigm. In Figure 2, extracted from (Zheng *et al.*, 2022), the authors discuss a range of scenarios where the IRS can be employed. When a new technology is proposed,

Figura 2 – Illustration of candidate scenarios for IRS.

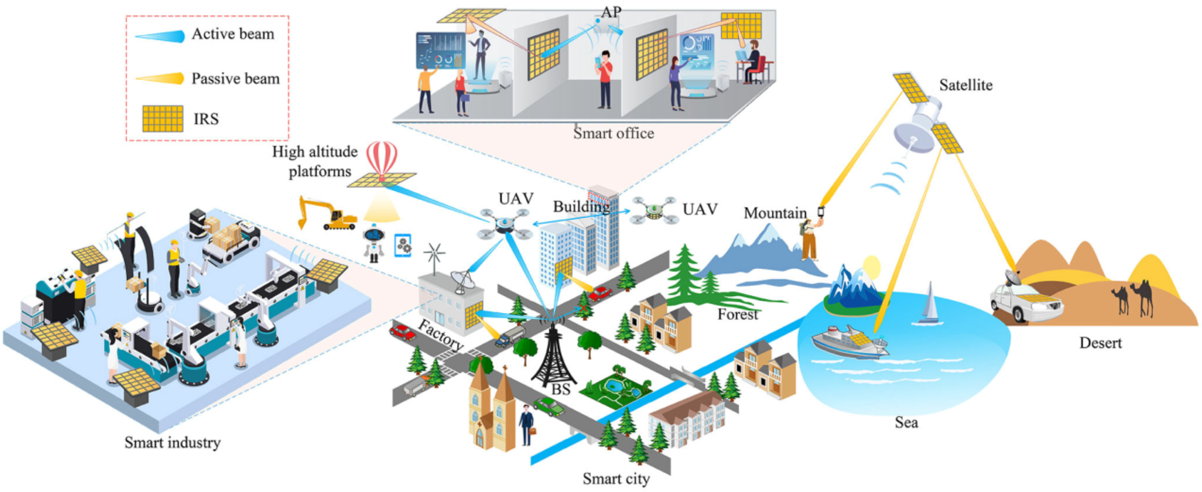

Fonte: B. Zheng, et al. (Zheng *et al.*, 2022)

several challenges are expected to arise. A significant challenge for IRS communications is channel estimation. Two main reasons can be highlighted in this regard. Firstly, a passive IRS cannot process pilot symbols, which means that channel estimation must be performed in the end nodes of the network (BS and/or UT), potentially overloading the chosen node. Secondly, large panel sizes usually imply a large number of channel coefficients to be estimated. This may require many pilot resources, which can affect the overall system spectral efficiency. The accuracy of the channel state information (CSI) acquisition is crucial because the gains provided by the IRS depend on a sufficiently accurate knowledge of the channel.

This thesis addresses the channel estimation problem in IRS-assisted wireless communication by resorting to tensor-based approaches. We propose signal models and algorithms that exploit the multilinear tensor structure of the involved channels and the received signals to solve the cascaded channel estimation as well as the joint channel and symbol estimation problem. Tensor decompositions are powerful mathematical tools to model and estimate the multidimensional structure of signals and data. As evidenced by the extensive signal processing literature, tensor modeling offers a concise and elegant way to solve a series of problems such as blind/semi-blind channel estimation and data detection in wireless CDMA and/or OFDM communications (Sidiropoulos *et al.*, 2000; Sidiropoulos; Dimic, 2001; Almeida *et al.*, 2007; Lathauwer; Castaing, 2007; Almeida *et al.*, 2008; Favier *et al.*, 2012a; Kofidis *et al.*, 2017), parameter estimation in array processing (Sidiropoulos; Bro, 2000; Salmi *et al.*, 2009; Roemer *et al.*, 2010; Nion; Sidiropoulos, 2010; Sørensen; Lathauwer, 2013; Han; Nehorai, 2014; Raimondi *et al.*, 2017; Li *et al.*, 2017; Gomes *et al.*, 2019a; Gomes *et al.*, 2019b; Podkurkov *et al.*, 2019; Zheng *et al.*, 2021b; Podkurkov *et al.*, 2021; Khamidullina *et al.*, 2021; Zheng *et al.*, 2023), design of space-time-frequency coding/decoding schemes with blind decoding capability (Sidiropoulos; Budampati, 2002; Almeida *et al.*, 2009; Favier *et al.*, 2012b; Almeida *et al.*, 2013; Liu *et al.*, 2013; Almeida; Favier, 2013; Favier; Almeida, 2014b; Araújo; Almeida, 2017), and, more recently, to design of multilinear beamforming filters (Ribeiro *et al.*, 2016; Zilli; Zhu, 2021), and multilinear modulation schemes (E-Asim *et al.*, 2020; Fazal-E-Asim *et al.*, 2020; Fazal-E-Asim *et al.*, 2022), to mention a few.

A major part of the aforementioned works utilizes the tensor decompositions at the receiver side for channel, symbol, or joint channel-symbol estimation usually under more relaxed conditions than matrix-based methods, such as in (Sidiropoulos *et al.*, 2000; Sidiropoulos; Dimic, 2001; Almeida *et al.*, 2007; Lathauwer; Castaing, 2007; Almeida *et al.*, 2008; Favier *et al.*, 2012a; Kofidis *et al.*, 2017), or to solve the parameter estimation problems in array processing, such as in (Sidiropoulos; Bro, 2000; Nion; Sidiropoulos, 2010; Salmi *et al.*, 2009; Sørensen; Lathauwer, 2013; Han; Nehorai, 2014; Gomes *et al.*, 2019a; Gomes *et al.*, 2019b; Li *et al.*, 2017; Podkurkov *et al.*, 2019; Zheng *et al.*, 2021b; Podkurkov *et al.*, 2021; Khamidullina *et al.*, 2021; Roemer *et al.*, 2010; Raimondi *et al.*, 2017; Zheng *et al.*, 2023). Another class of methods employs tensor decompositions as a multidimensional coding tool at the transmitter to design space-time or space-time-frequency schemes with built-in semi-blind decoding (Sidiropoulos; Budampati, 2002; Favier *et al.*, 2012b; Favier; Almeida, 2014b; Almeida *et al.*, 2009; Almeida *et al.*, 2013; Liu *et al.*, 2013; Araújo; Almeida, 2017; Almeida; Favier, 2013), or yet, to construct multilinear modulation schemes (E-Asim *et al.*, 2020; Fazal-E-Asim *et al.*, 2020; Fazal-E-Asim *et al.*, 2022). Tensors can also be used to directly model the wireless channel, and to derive parametric channel modeling/estimation algorithms (Weichselberger, 2004; Almeida *et al.*, 2006; Weis *et al.*, 2007; Costa; Haykin, 2008; Araújo *et al.*, 2019b). Figure 3 provides a high-level illustration of the use of tensor modeling in the wireless communication chain.

Figura 3 – Tensor model in the wireless communication MIMO system chain

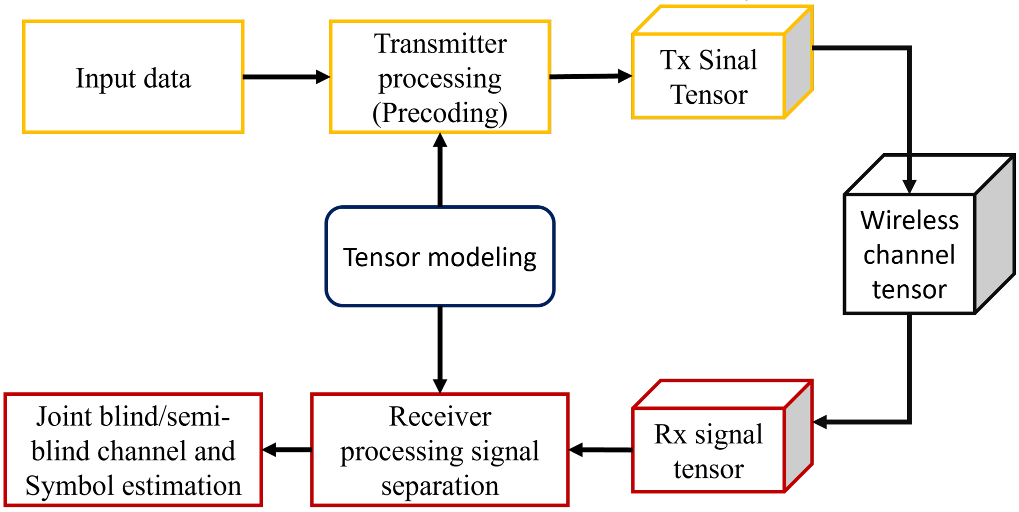

Fonte: Created by author based on de Almeida at al. (Almeida *et al.*, 2009)

Figura 4 – Summary of contributions from the perspective of tensor modeling and algorithms.

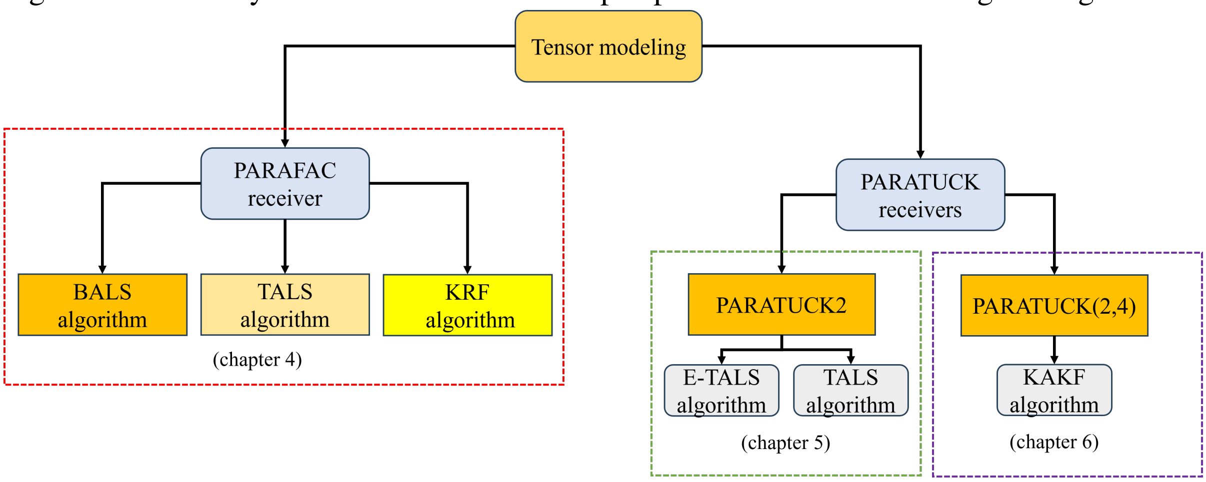

More recently, tensor modeling proved to be a powerful tool in IRS-assisted MIMO communication system to solve the channel estimation problem. Earlier works in channel estimation for IRS-assisted communications advocated the estimation of the cascaded channel only. However, as it will be shown later, it is possible to decouple the estimates of the involved channels. To this end, we exploit the multilinear algebraic structure of the received signal using a tensor decomposition approach to the channel estimation as well as the joint channel and symbol estimation. The benefits of estimating the individual channels include performance gains, less restrictive system parameter choices, semi-blind processing, and the ability to deal with channels varying at different time scales. The development of tensor methods for IRS-MIMO wireless communications is the focus of this thesis. Figure 4 summarizes our main scientific contributions. We propose various solutions to tackle the channel estimation problem in wireless communication systems assisted by Intelligent Reflecting Surfaces (IRS). In the pilot-assisted case, we show that the receiver signal fits as PARAFAC model, and three algorithms can derived to solve the cascaded channel estimation problem. Assuming the knowledge of the IRS phase shift matrix, (iterative) BALS and (closed-form) KRF algorithms are proposed to obtain decoupled estimates of the involved MIMO channels. Considering that the IRS elements may suffer from unknown impairments, the phase shift matrix is not perfectly known at the receiver and has to be estimated. To tackle this challenging scenario, we present a TALS algorithm that jointly estimates the involved channels and the IRS phase shift matrix during training. In this thesis, we also turn our attention to a semi-blind scenario, where training sequences are avoided. To solve the channel estimation problem in this case, we formulate a semi-blind receiver that can simultaneously estimate the two involved channel matrices while decoding the transmitted data, without requiring a prior pilot transmission phase. Considering the uplink single-user case, we show that the received signal follows a third-order PARATUCK model. Two algorithms to solve the joint channel and symbol estimation are formulated. Firstly, when the direct link between the BS and the UT is unavailable, we propose a TALS algorithm to deliver channel and symbol estimates. Secondly, assuming that the direct link is present, we formulate the so-called enhanced TALS (ETALS) to improve the performance by using the direct link as a warm start to estimate the channels and symbols in the IRS-assisted link, while refining the direct channel estimate.

Finally, we also considered a more challenging uplink multiuser scenario, where the channels linking the UTs and the IRS are subject to a block-time variation. Resorting to a generalized fourth-order PARATUCK-(2,4) tensor model, we propose efficient closed-form algorithms to estimate the common IRS-BS channel and the multiple UTs-IRS channels by exploiting the Kronecker and the Khatri-rao factorization schemes. The proposed tensor-based algorithms present interesting tradeoffs and offer degrees of freedom. Indeed, exploiting the uniqueness properties of tensor decompositions, we also derive conditions linking the number of transmitter and receiver antennas, the number of time slots, and the number of time-domain IRS phase shift patterns to ensure a unique channel and symbol recovery up to trivial scaling ambiguities. We also discuss the tradeoffs between the proposed closed-form and the iterative solutions in terms of performance and identifiability. Moreover, we show that decoupling the estimates of the individual channels from the cascaded channel using the proposed tensor approaches provides performance gains over traditional LS estimation methods, which are limited to estimating the cascaded channel.

1.2 Organization

This thesis comprises seven chapters, with an introduction and conclusion. The generic organization of the main content of the thesis is shown in Figure 5. Additionally, the appendices include further discussion about the main contributions presented in Chapters 4 and 5. A summary of each chapter is provided below.

Figura 5 – General Organization of the thesis

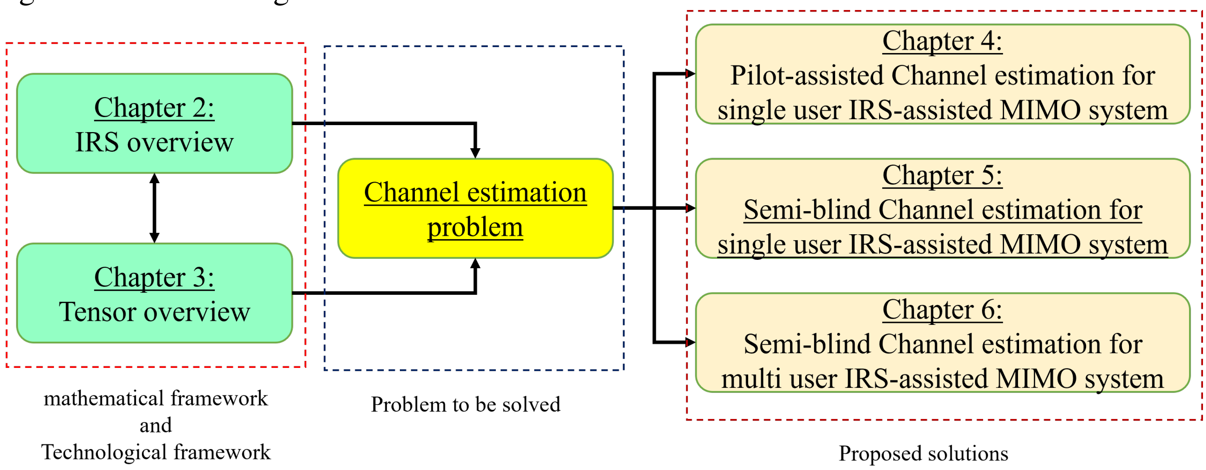

Chapter 2: The IRS is presented in this chapter. In particular, we define what is IRS, where we show how this technology works. The advantages and some disadvantages are presented, and where the studies of such technology are heading. In this sense, we light some IRS architects, for example, fully passive IRS and hybrid IRS, besides some trends for the IRS. To finalize this chapter, we present how the tensors are related to the IRS.

Chapter 3: Presents preliminaries about multi-linear algebra aiming to provide the basic necessary knowledge to a concise understanding of the scientific contribution of this thesis. We focus on the PARAFAC and generalized PARATUCK decomposition since it is used in the following chapters. Further, the main definition, operators, and concept are present. This chapter provides a short literature survey on different applications of tensor decompositions to wireless communication systems, including a discussion on the state-of-the-art tensor-based approaches for IRS-assisted communications.

Chapter 4: In this chapter, the pilot-assisted channel estimation problem for IRS-assisted MIMO wireless communication is addressed using a PARAFAC modeling based approach. We show how this tensor decomposition can be exploited to estimate the individual IRS-UT and IRS-BS channels. We present an iterative and closed-form solution to accomplish this task and discuss identifiability conditions and their implications in terms of system parameter settings. Generalizations of the proposed solution to multi-user cases are also discussed.

Chapter 5: We present a semi-blind joint channel and data symbol estimation approach that relies on a combination of PARAFAC and PARATUCK2 tensor models. Differently from the previous chapter, pilot symbols are avoided and data symbols are directly decoded during the channel estimation process. We show how the symbol estimates obtained at the first stage *via* the direct link can be used as a warm start to the second stage to enhance joint channel and symbol estimation using the IRS-assisted link. Trilinear TALS based algorithms are presented to solve the problem.

Chapter 6: Considering an uplink multiuser MIMO scenario, we adopt a more general modeling approach, where the IRS-UT channel is time-varying across multiple time blocks. Exploiting a fourth-order PARATUCK-(2,4) tensor model for the received signals, we formulate a closed-form semi-blind receiver for joint channel and symbol estimation. We show that channel and symbol estimates can be obtained efficiently by combining Kronecker factorization (KF) and Kronecker factorization problems.

Chapter 7: This chapter presents the conclusions and discusses some perspectives for future works.

1.3 Main publications

The main results presented in this document were published in the following journal and conference papers:

1.3.1 Journal Papers

[J1] **G. T. de Araújo**, A. L. F. de Almeida, R. Boyer and G. Fodor, "Semi-Blind Joint Channel and Symbol Estimation for IRS-Assisted MIMO Systems,"*IEEE Transactions on Signal Processing*, vol. 71, pp. 1184-1199, 2023.

[J2] **G. T. de Araújo**, P. R. B. Gomes, A. L. F. de Almeida, G. Fodor and B. Makki, "Semi-Blind Joint Channel and Symbol Estimation in IRS-Assisted Multiuser MIMO Networks,"*IEEE Wireless Communications Letters*, vol. 11, no. 7, pp. 1553-1557, July 2022.

[J3] **G. T. de Araújo**, A. L. F. de Almeida and R. Boyer, "Channel Estimation for Intelligent Reflecting Surface Assisted MIMO Systems: A Tensor Modeling Approach,"*IEEE Journal of Selected Topics in Signal Processing*, vol. 15, no. 3, pp. 789-802, April 2021.

1.3.2 Conference papers

[C1] **G. T. de Araújo** and A. L. F. de Almeida, "*PARAFAC-Based Channel Estimation for Intelligent Reflective Surface Assisted MIMO System,*"2020 IEEE 11th Sensor Array and Multichannel Signal Processing Workshop (SAM), Hangzhou, China, 2020, pp. 1-5

[C2] **G. T. de Araújo**, L. C. de Paula Pessoa and A. L. F. de Almeida, "*Channel Estimation for MIMO System Assisted by Intelligent Reflective Surface,*"XXXVIII Brazilian Symposium on Telecommunication and Signal Processing (SBrT), 2020.

[C3] **G. T. de Araújo** and A. L. F. de Almeida, L. Pessoa, "*Joint Pilot and Phase Shift Design for IRS-assisted MIMO Communications,*"XLI Brazilian Symposium on Telecommunication and Signal Processing (SBrT), 2023.

In addition to the papers cited previously, which consist of the core contributions of this thesis, the author has also participated in the following works:

1.4 Additional publications

1.4.1 Journal papers

[J4] P. R. B. Gomes, **G. T. d. Araújo**, B. Sokal, A. L. F. d. Almeida, B. Makki and G. Fodor, "Channel Estimation in RIS-Assisted MIMO Systems Operating Under Imperfections,"*IEEE Transactions on Vehicular Technology*, vol. 72, no. 11, pp. 14200-14213, Nov. 2023.

1.4.2 Conference papers

[C4] P. R. B. Gomes, **G. T. de Araújo**, B. Sokal, A. L. F. de Almeida, B. Makki and G. Fodor, "Tensor-Based Channel Estimation for RIS-Assisted Communications with Non-Ideal Phase Shift Responses,"2022 Workshop on Communication Networks and Power Systems (WCNPS), Fortaleza, Brazil, 2022.

[C5] L. C. de Paula Pessoa, **G. T. de Araújo**, P. R. B. Gomes and A. L. F. de Almeida, "IRS-Assisted Communications Under Practical Channel Estimation and Hardware Model,"XXXIX Brazilian Symposium on Telecommunication and Signal Processing (SBrT), 2021.

1.4.3 Best Paper Awards

It is worth mentioning that papers [C2], [C3], and [C4] received the best paper awards in the respective conferences.

2 INTELLIGENT REFLECTING SURFACE: AN OVERVIEW

This chapter presents an overview of the IRS technology by focusing on its definitions and fundamental principles. We also cover architectural and implementation aspects to some extent. We briefly highlight the main IRS architectures and address hardware-related issues. Additionally, we explore some applications and scenarios that can benefit from the use of IRS, and finally, we offer insights into the potential of IRS-assisted communications.

2.1 Introduction

Wireless communications have reached its 5G fifth generation. The propagation environment is an uncontrollable factor in the current wireless communication paradigm. The interaction of electromagnetic waves with elements between transmitters and receivers cannot be managed. Consequently, the communication link can only be adapted at the endpoints to enhance service quality (Renzo *et al.*, 2020; Wu *et al.*, 2021). Recent research in the wireless communication literature indicates that a new technology could potentially alter this existing paradigm. This innovation envisions optimizing the environment between the transmitter and receiver rather than solely adapting to it. We are referring to Intelligent Reflecting Surfaces, a technology capable of enhancing the propagation environment of wireless communication to make it more controllable, in contrast to its current random characteristics (Renzo *et al.*, 2020).

The paradigm shift mentioned earlier is illustrated in Figure 6. In this figure, we observe a shadowing zone (left-side scenario) where the reflected signal fails to reach the user, leaving them without service. However, the dead zone is eliminated by introducing the IRS to assist communication between the BS and the users (right-side scenario). This occurs because the IRS intentionally redirects the reflected signal falling onto it to a desired region.

Figure 7 illustrates the difference between traditional wireless communication and the smart wireless environment in a simplified manner. As previously mentioned, electromagnetic waves can interact with the objects in the transmission path, making the propagation environment more favorable. This suggests that in IRS-assisted wireless communication, both the end nodes and the channel can be optimized. This concept is contrary to the current state-of-the-art wireless communication, where the effect of the environment on the signal is reduced by adopting or applying certain techniques at the endpoints.

Figura 6 – Conventional wireless communication environment *versus* IRS-assisted wireless communication environment.

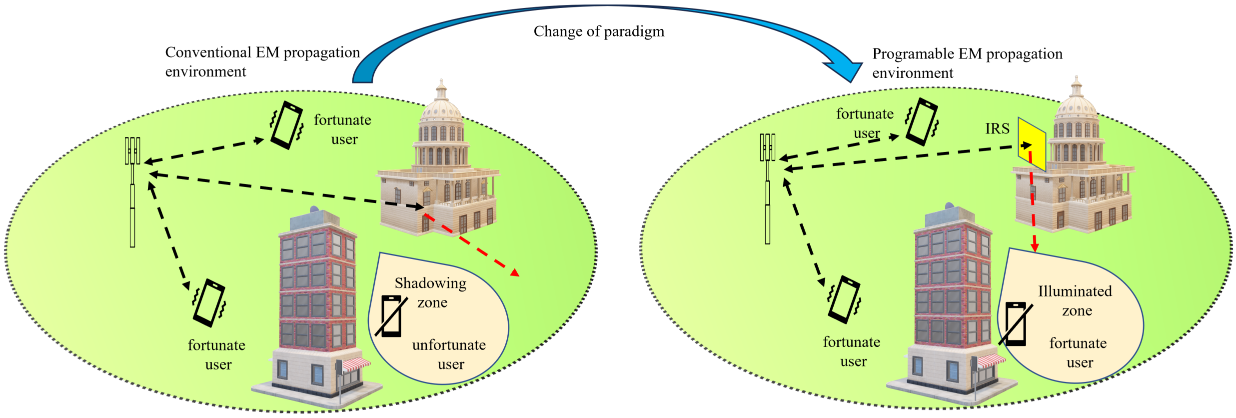

Figura 7 – Global point of view about the traditional wireless environment versus a programmable wireless environment.

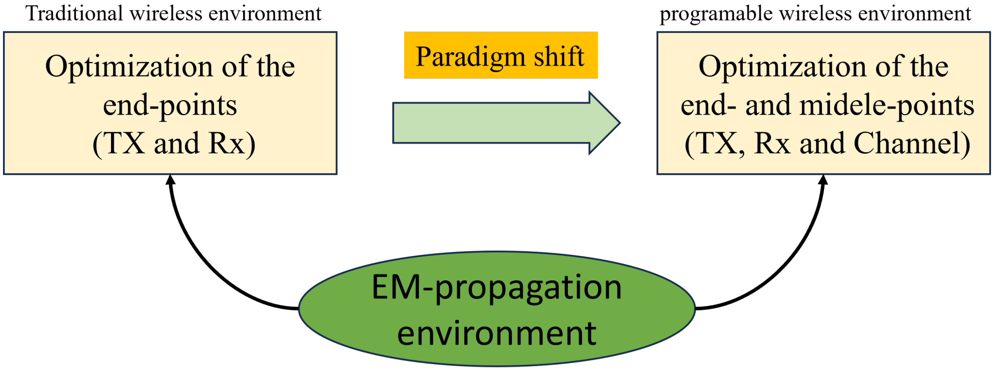

2.2 Definition

The IRS is a promising technology for beyond 5G or for the next generation of communication 6G (Long *et al.*, 2021; Jiang; Luo, 2023). However, what exactly is an IRS? Let us explore some questions related to the functionality of intelligent surfaces before defining them. Intelligent surfaces, also known as reconfigurable intelligent surface (RIS), are essentially the same thing, and these terms are often used synonymously. However, some authors highlight different functionalities that can be enabled by using intelligent surfaces. According to (Renzo *et al.*, 2020), who uses the term RIS, the functionality of RIS can be classified into two categories: electromagnetic-based design and communication-based design. It is important to note that IRS/RIS can be used for various purposes, from reflection to aiding the modulation schemes. Figure 8 illustrates these functions.

In recent works, the term RIS has been used frequently[1]. However, (Rasilainen *et*

[1] The RIS term has gained popularity in literature due to its ability to perform functions beyond reflections. This

al., 2023) pointed out that in most of these works, the RIS functions only as a reconfigurable *reflecting* surface, despite ongoing debates about its definition and working mode. Based on this, the IRS is defined as a flat structure composed of passive elements. Each element acts as an independent reflector that can manipulate the amplitude and/or phase shift response of incoming electromagnetic waves (Basar *et al.*, 2019; Zheng *et al.*, 2022)[2]. The IRS is an interesting technology for energy efficiency, as it does not require radio frequency (RF) chains. With its phase manipulation capability, the beamforming passive (phase shifts) and active (precoders and combines) can be leveraged to optimize system performance (Wu; Zhang, 2019).

Figura 8 – Classification of the IRS functionality from two different perspectives, electromagnetic and communication.

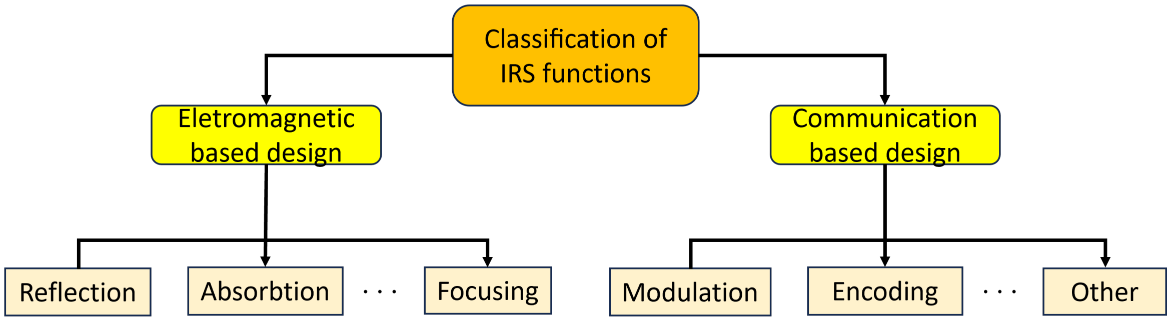

2.3 Basic principle

To understand how this technology works, it is important to first understand what IRS is. Essentially, IRS refers to the use of tunable elements embedded in a structure to manipulate the amplitude and/or phase of an incoming electromagnetic signal. This is illustrated in Figure 9 for the case of a single input, single output (single-input single-output (SISO)) scenario. The signal arrives at the IRS, where each element acts upon it before the signal is reflected towards a receiver. The tunable elements used to manipulate the characteristics of the electromagnetic wave could include PIN or varactor diodes, for example.

Mathematically, the receiver signal at the Rx is given as

$$y = \sum_{n=1}^{N} h_n g_n a_n e^{j\theta_n}, \tag{2.1}$$

broader vision of intelligent surfaces is supported by the recent state-of-the-art technology, where different architectures (e.g. STAR-RIS) require different operation modes.

2 This definition is in line with the basic idea of the IRS. However, over time, various IRS architectures have been proposed, which we explore in the next section.

Figura 9 – Basic principle of IRS operation.

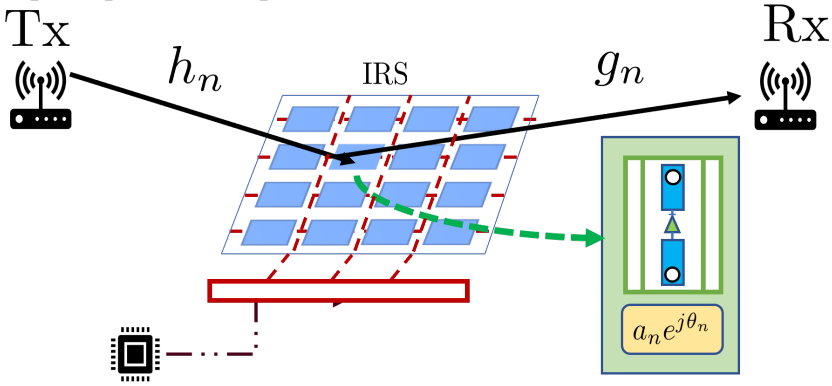

where $h_n g_n$ represents the complex channel gain and $a_n e^{j\theta_n}$ represents the complex reflection gains corresponding to the nth IRS element. Here, a_n is the amplitude response, and θ_n is the IRS phase shift response. In cases where the amplitude coefficient is equal to 1, this means that all energy of the signal is reflected. However, this idealized scenario is widely considered in the literature.

Considering the downlink case, we can rewrite Equation (2.1) in a matrix form as follows. Note that the same statements apply to the uplink side, with the roles reversed. This is illustrated in the main contributions, where we consider a downlink communication in one part and an uplink side in the other part.

$$y = \mathbf{g}^{\mathrm{T}}\mathbf{S}\mathbf{h}x + b\,, \tag{2.2}$$

where $\mathbf{g} = [g_1\ g_2\ \ldots\ g_n]^{\mathrm{T}}$ and $\mathbf{h} = [h_1\ h_2\ \ldots\ h_n]^{\mathrm{T}}$ are the Tx-IRS and IRS-Rx channels, respectively, with $h_n = \alpha_n e^{-j\phi_n}$ and $g_n = \rho_n e^{-j\psi_n}$. $\mathbf{S} = \mathrm{diag}\left(a_1 e^{\theta_1}\ a_2 e^{\theta_2}\ \ldots\ a_N e^{\theta_N}\right) \in \mathbb{C}^{N\times N}$ represent the phase shift matrix, which has a diagonal design constructed from the phase shift vector $\mathbf{s} = [a_1 e^{\theta_1}\ a_2 e^{\theta_2}\ \ldots\ a_N e^{\theta_N}]^{\mathrm{T}} \in \mathbb{C}^{N\times 1}$, that contains all phase shift contribution from all IRS element. Depending on the case investigated, x is the pilot or data symbol, and b is the additive noise.

2.3.1 Tunable circuits

The principle behind the IRS is its ability to reconfigure the incident wave by adjusting the reflection phases, as explained in the definition section. Tunable elements such as PIN diodes, varactor diodes, liquid crystals, and graphene are embedded into the structure of the IRS to achieve this reconfigurability (Basar *et al.*, 2019; Renzo *et al.*, 2020; Chen *et al.*, 2021b; Sejan *et al.*, 2022; Rana *et al.*, 2023; Rasilainen *et al.*, 2023; Hassouna *et al.*, 2023).

Choosing the appropriate tunable element for the hardware modeling is important since the IRS can operate at any frequency. However, it is worth noting that different tunable elements have varying frequency efficiency levels.

In the microwave frequency band, electronic components such as PIN and varactor diodes can be utilized as tunable circuits (Abeywickrama *et al.*, 2020). However, these electronic devices are not practical in the THz or sub-THz frequency band. In such cases, liquid crystal and graphene materials can enable IRS to operate in high-frequency ranges (Renzo *et al.*, 2020; Sejan *et al.*, 2022; Rasilainen *et al.*, 2023). To illustrate this point, let us consider the varactor-based model of IRS presented in (Abeywickrama *et al.*, 2020).

$$\text{phase shif} = \arg(v_n) \quad \text{and} \quad \text{amplitude} = |v_n|\,, \tag{2.3}$$

where

$$v_n = \frac{Z_n(C_n,R_n) - Z_0}{Z_n(C_n,R_n) + Z_0}\,, \tag{2.4}$$

in which

$$Z_n(C_n,R_n) = \frac{j\omega L_1\left(j\omega L_2 + \dfrac{1}{j\omega C_n} + R_n\right)}{j\omega L_1 + \left(j\omega L_2 + \dfrac{1}{j\omega C_n} + R_n\right)} \tag{2.5}$$

denotes the equivalent circuit for the nth reflecting element, and Z_0 is the free space impedance. Then, considering the same values for the capacitance and resistance parameters as in (Abeywickrama *et al.*, 2020), we reproduce some results as follows.

In Figure 10, we can observe that the amplitude reaches its minimum value when the phase shift is almost zero. For a frequency of 2.4GHz, the phase shift range varies approximately from $-pi$ to π. Moreover, it is noticeable that the amplitude decreases more significantly as the resistance increases. Figure 11 demonstrates how the varactor model operates in high frequencies when $R_n = 1$. Notably, the amplitude is nearly equal to 1, indicating that almost all of the incident signal energy is reflected. However, the phase shift graphic shows that the phase remains constant in high frequencies, while the range of the phases in the lower frequency range is close to $[-\pi,\pi]$, as previously mentioned. These results demonstrate that the varactor-based model of the IRS acts solely as a reflector without any reconfigurability at high frequencies. This observation is significant since the IRS principle relies on adjusting the phases.

Figura 10 – Amplitude and phase shift dependence.

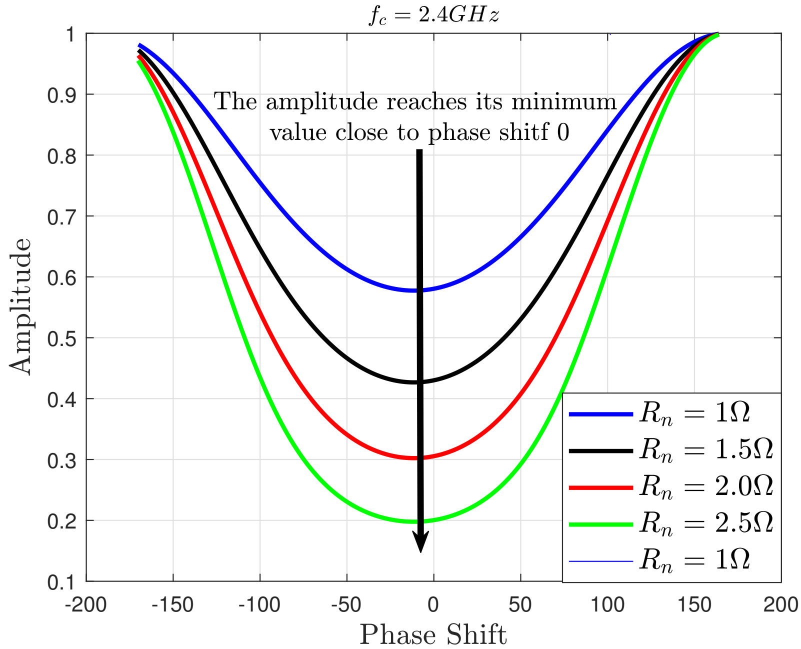

2.3.2 Optimal beamforming design

To fully leverage the potential of the IRS, it is crucial to optimize both the IRS phase shift and the precoders, which are commonly referred to as passive and active beamforming, respectively (Basar *et al.*, 2019; Wu; Zhang, 2019; Zappone *et al.*, 2021; Wang *et al.*, 2022; Zhang; Mao, 2023). In the existing literature, many proposed solutions have been proposed for optimizing passive and active beamforming design (Hua *et al.*, 2023; Abeywickrama *et al.*, 2020; Xing *et al.*, 2023). In this subsection, we first present some solutions for optimizing the IRS phase shifts in SISO and MIMO systems, where the aim is to determine the optimal phase shift vector that maximizes a global performance metric such as the signal-to-noise ratio (SNR). Then, we briefly discuss joint precoder and IRS optimization.

Single user SISO system

The maximum instantaneous SNR gains can be obtained when the incident and reflected signals are phase-aligned. This alignment requires canceling the channel phases (Basar *et al.*, 2019; Wang *et al.*, 2022). According to (Basar *et al.*, 2019), the SNR can be expressed as follows:

$$SNR = \frac{|\sum_{n=1}^{N} h_n g_n a_n e^{j\theta_n}|^2 E_s}{N_0}\,. \tag{2.6}$$

Figura 11 – Amplitude phase shift as a function of the capacitance and frequency effect.

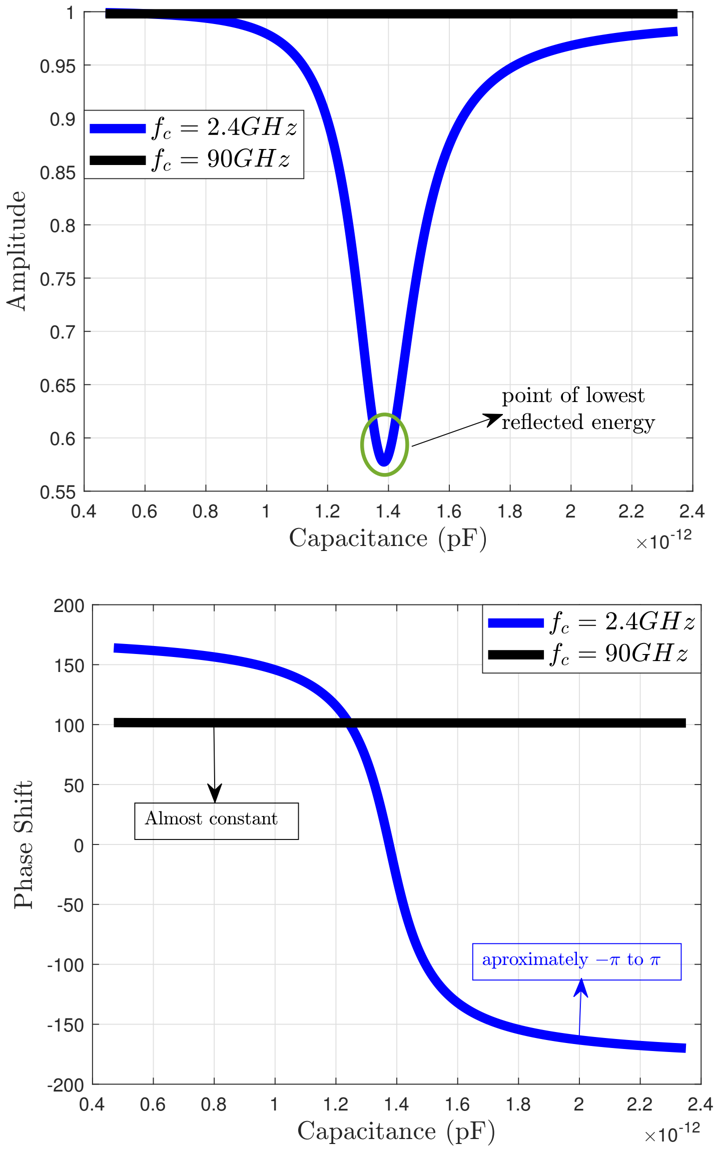

Assuming all N elements are equal to 1, and α_n and ρ_n follow independent Rayleigh distributions, the instantaneous SNR can be expressed as:

$$
\begin{aligned}
SNR &= \frac{|\sum_{n=1}^{N} \alpha_n e^{-j\phi_n} \rho_n e^{-j\psi_n} e^{j\theta_n}|^2 E_s}{N_0} \\
&= \frac{|\sum_{n=1}^{N} \alpha_n \rho_n e^{j(\theta_n - (\phi_n + \psi_n))}|^2 E_s}{N_0} \; .
\end{aligned}
\tag{2.7}
$$

It is important to note that the best design for the IRS phase shift vector in this particular case is given by:

$$
\theta_n^{\text{opt}} = \phi_n + \psi_n \text{ , for all } n \; . \tag{2.8}
$$

Remark 1 *Based on the assumption of a perfect condition, the authors in (Wu; Zhang, 2019; Basar et al., 2019) have shown that the SNR gain is proportional to* N^2*. To prove this, the authors* *have used the central limit theorem to demonstrate that the random variable* $\left(\sum_{n=1}^{N} \alpha_n \rho_n\right)^2$ *converges to a Gaussian distribution, which is true if* $N \gg 1$ *or* $N \to \infty$. *They have also concluded that the SNR follows a non-central chi-square random distribution.*

Single user MIMO system

Consider a Multiple Input Multiple Output MIMO downlink scenario[3], where the BS is equipped with M antennas, the UT is equipped with L antennas, and the IRS panel comprises N elements. The received signal can be expressed as

$$\mathbf{y} = \mathbf{GSHx} + \mathbf{b} \in \mathbb{C}^{L \times 1} , \tag{2.9}$$

where $\mathbf{G} \in \mathbb{C}^{L \times N}$, $\mathbf{H} \in \mathbb{C}^{N \times M}$ and $\mathbf{S}$ is as in the SISO case. In this scenario, the optimization process is more difficult since the objective function implies a non-convex optimization problem (Zhang; Zhang, 2020; Perović *et al.*, 2021; Wu *et al.*, 2021). For an IRS-assisted MIMO system, the achievable rate is defined as follows (Perović *et al.*, 2021):

$$R = \log_2 \det \left(\mathbf{I} + \frac{1}{N_0} \overline{\mathbf{H}} \mathbf{Q} \overline{\mathbf{H}}^{\mathrm{H}} \right) , \tag{2.10}$$

where $\overline{\mathbf{H}} = \mathbf{GSH}$ is the end-to-end channel, i.e. BS-IRS-UT (plus the BS-UT channel, if is consider that the direct BS-UT channel is available) and $\mathbf{Q}$ is the transmit covariance matrix. Assuming the knowledge of the channel and the covariance matrix, the optimization consists of solving the following problem:

$$\begin{aligned} &\max_{\mathbf{s}} \log_2 \det \left(\mathbf{I} + \frac{1}{N_0} \overline{\mathbf{H}} \mathbf{Q} \overline{\mathbf{H}}^{\mathrm{H}} \right) \\ &\text{s.t.} \quad |\mathbf{s}_n| = 1 , \quad n = 1, \ldots, N , \end{aligned} \tag{2.11}$$

where $\overline{\mathbf{H}}$ and $\mathbf{Q}$ are known such that $\mathbf{Q} \succeq \mathbf{0}$ and $\mathrm{tr}(\mathbf{Q}) = P$, and P denotes the average transmit power. In (Wu *et al.*, 2021) and (Sur; Bera, 2021), a discussion of several optimization problems and solutions for MISO and MIMO systems are provided.

Joint IRS phase shift and active beamformings

Future wireless communication networks will likely use a combination of passive devices, such as IRSs, and active network nodes such as BS and UTs. Therefore, optimal performance implies designing the active (BS and UT) and passive (IRS) beamformings (Wu;

[3] the same applies for the uplink by changing the roles of the transmitter and the receiver.

Zhang, 2020b). Several studies have addressed this problem, including (Wu; Zhang, 2019; Zappone *et al.*, 2021; Palmucci *et al.*, 2023; Hua *et al.*, 2023). Among these, we highlight the work (Zappone *et al.*, 2021) that optimizes the transmission precoder, phase shifts, and receive filter. In their analysis, the authors consider the overhead required for channel estimation and feedback of the optimum phase shifts to the IRS controller.

Remark 2 *It is important to note that many studies assume that the phase shift can assume any value between* 0 *and* 2π*. However, this assumption does not hold in practice due to hardware constraints. Specifically, assuming a more practical scenario with discrete IRS phase shifts, the optimization process is affected and the final performance may deviate from the optimum (continuous phase shift) one. In (Zheng et al., 2022), the authors provide a discussion of several works addressing beamforming optimization with a limited number of discrete phase shifts.*

2.4 IRS architectural designs

Until this point, we have discussed fully passive IRSs, for which only phase shifts are optimized, i.e., no (active) signal processing is possible at the IRS. Such a simplified setup implies some bottlenecks, including the channel estimation and the global path loss attenuation. Solving the channel estimation problem for the fully passive IRS is the main focus of this thesis.

In this section, for completeness, we present a brief overview of some IRS architectures such as the active and hybrid ones. Additionally, we discuss some recent advancements in IRS architectures beyond the reflection and diagonal designs.

2.4.1 Active IRS design

A passive IRS only has a reflector circuit in each element. Ideally, the amplitude response in the circuit should be unitary, meaning that the reflection is total (i.e. no absorption or imperfection losses). However, in some practical hardware models such as in the IRS varactor-based model, the amplitude response of each element may have a magnitude smaller than one. Due to challenges associated with a fully passive IRS, some authors have studied active IRS setups. This new architecture not only reflects the signal but also amplifies it. Some recent papers on this topic include (Khoshafa *et al.*, 2021; Liu *et al.*, 2022; Zhang *et al.*, 2023; Kang *et al.*, 2023). Figure 12 illustrates the difference between passive and active IRS (Zhang *et al.*, 2023). In the active structure, each IRS element consists of a phase shift circuit and an amplifier circuit.

Figura 12 – Active versus passive IRS

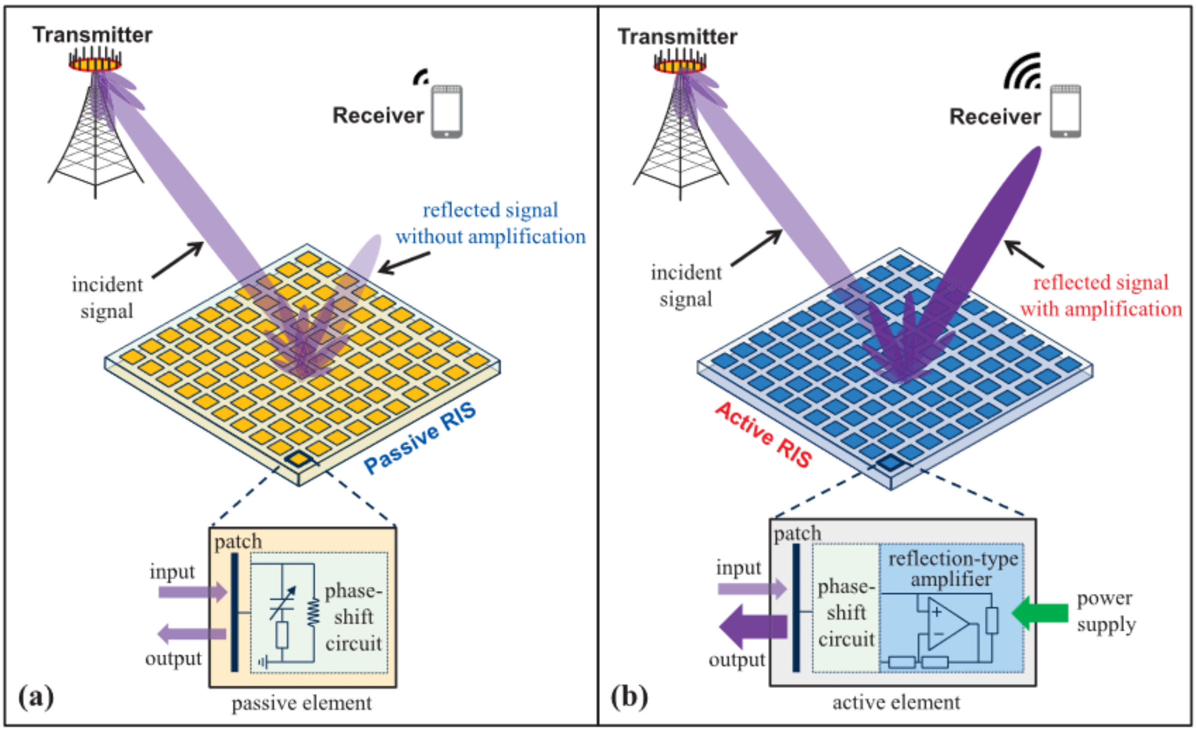

Fonte: Z. Zhang et al. (Zhang *et al.*, 2023)

However, one power amplifier per IRS element increases the power consumption. To address this issue, the work (Liu *et al.*, 2022) proposed a single amplifier circuit for each group of IRS elements to reduce power consumption.

2.4.2 Hybrid IRS design

Although an active IRS mitigates the multiplicative path loss problem, it introduces noise due to the integrated active power amplifier circuit on each IRS element (Sankar; Chepuri, 2022). An alternative solution to manage this problem is to adopt a hybrid architecture that includes both passive and active elements in the surface of IRS (Sankar; Chepuri, 2022). Different hybrid IRS designs have been proposed that use an amplifier circuit jointly with the IRS elements (Sankar; Chepuri, 2022; Liang *et al.*, 2022; Lyu *et al.*, 2023; Yigit *et al.*, 2023), or integrate sensors and/or RF chains to sense/receive the incident signal at the IRS (Lin *et al.*, 2021; Zhang; Zhang, 2023; Zhang *et al.*, 2023; Ghazalian *et al.*, 2023). To summarize the different architectural designs, the diagram in Figure 13 illustrates their main differences.

Figura 13 – Different architecture of the IRS presented in literature.

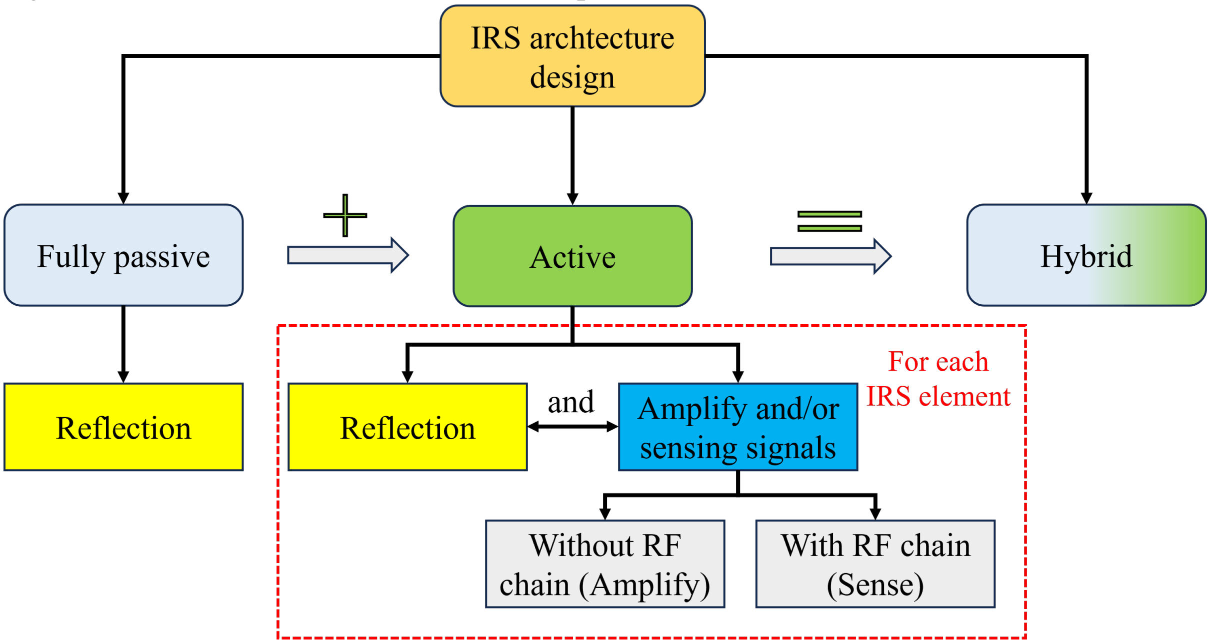

2.4.3 Non-diagonal IRS design

The works referenced earlier assumed that the phase shift matrix of the IRS has a diagonal structure. Physically, this implies that the IRS reflecting elements are independent of each other, i.e., no coupling exists between elements. However, as the investigation of hardware aspects of IRS has progressed, some authors proposed a non-diagonal structure for the phase shift matrix (Gradoni; Renzo, 2021; Qian; Renzo, 2021; Li *et al.*, 2022; Li *et al.*, 2023). This is evident in two cases. Firstly, non-diagonality occurs naturally due to electromagnetic effects that cause coupling between the elements (Gradoni; Renzo, 2021). Secondly, some researchers intentionally propose connecting some IRS elements, resulting in a non-diagonal phase shift matrix (Li *et al.*, 2022).

2.4.4 Simultaneous Transmitting and Reflection IRS (STAR-IRS)

In Section 2.2, we define the IRS as a reflection panel. However, we also mention that the IRS can be used for other purposes, such as refraction. To take advantage of this capability, some authors have proposed a new architecture where the incident signal is both reflected and transmitted simultaneously[4] (Liu *et al.*, 2021; Liu *et al.*, 2023; Zhang; Zhang, 2023; Mu *et al.*, 2022). This scenario is illustrated in Figure 14.

[4] The transmitted signal corresponds to the energy that is refracted toward the back side of the IRS.

Figura 14 – Simultaneous transmitting and reflection scenario.

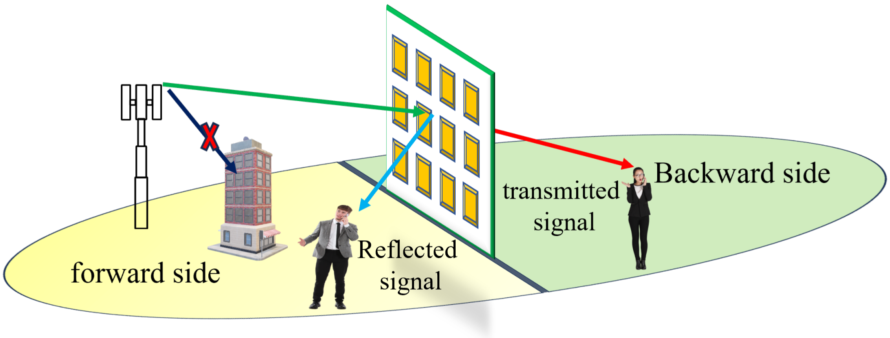

There are three modes to execute the STAR operation according to (Mu *et al.*, 2022)

- (I) **Energy splitting:** In this mode, each IRS element is divided into a reflector and a transmitter operating simultaneously, enabling 360-degree signal coverage.
- (II) **Mode switching:** Alternatively, the IRS panel can be split so that some elements only reflect while the remainder transmits simultaneously. This is similar to case (I).
- (III) **Time switching:** Different from (I) and (II) in time switching mode, the IRS operates on a time division protocol, meaning that it alternates between reflection and transmission.

2.5 Application and use cases

There are various use cases for the IRS in the literature, including coverage enhancement, spectral efficiency, beam management, physical layer security, localization accuracy, sensing capabilities, and energy efficiency, as mentioned in the (DGR/RIS-001,). These use cases require specific key performance indicator (KPI)s to be considered in the IRS-assisted system, such as rate/throughput, latency, reliability, and overhead, as stated in the (DGR/RIS-003,). Depending on these use cases and KPIs, the IRS can be utilized in different scenarios, such as cellular networks (Chen *et al.*, 2022; Chen *et al.*, 2022; Savkin *et al.*, 2023), vehicular communication (Zhu *et al.*, 2022), outdoor-to-indoor communication (Nemati *et al.*, 2021), and unmanned aerial vehicle (UAV) communication (Sur *et al.*, 2023).

Remark 3 *The literature offers various applications and scenarios for the technology in question. However, in this thesis, we have cited only a few examples to avoid making the document too lengthy while providing a clear understanding of its applicability.*

2.6 Summary

In this chapter, we provide a brief overview of IRS technology and discuss some of its main points. We define IRS and highlight how this technology can change the wireless communication paradigm. We also explain the different nomenclatures used in the literature, such as RIS and IRS. Additionally, we discuss the working principle of IRS and provide some hardware details, including the tunable elements. We present the phase shift optimization and the main architectures of IRS that have been explored in the literature. Finally, we conclude this chapter by showcasing some of the IRS applications.

3 MULTILINEAR ALGEBRA: AN OVERVIEW

This chapter provides an overview of the main definitions and properties used throughout this thesis. We focus on special matrix products such as Khatri-Rao, Kronecker, and Hadamard and their properties and relationships. We also discuss tensor decompositions, specifically the PARAFAC and PARATUCK2 tensor decompositions used extensively in the following chapters. Finally, we show how tensor modeling is related to IRS technology.

3.1 Definition and basic operations

Multilinear algebra can be seen as the algebra of the higher-order tensors (Lathauwer, 1997). Tensors, also named multidimensional (multi-index) arrays, or multi-way (N-way) arrays, can be seen as multi-dimensional generalizations of matrices (which are two-dimensional arrays) for higher orders. Tensors can be used to represent multidimensional data sets (Kolda; Bader, 2009; Cichocki *et al.*, 2015; Sidiropoulos *et al.*, 2017; Almeida, 2007). In this sense, we denote $\mathscr{X} \in \mathbb{C}^{I_1 \times I_2 \times \ldots \times I_N}$ as a tensor of order N where I_n, $n = 1, \ldots, N$, denotes the nth dimension, or the nth mode, of the tensor $\mathscr{X}$. In particular, scalars, vectors, and matrices are zero-order, first-order, and second-order tensors, respectively, since $N \leq 2$. Finally, for $N \geq 3$ we have the high-order tensors. Figure 15 illustrates a third order tensor $\mathscr{X} \in \mathbb{C}^{I_1 \times I_2 \times I_3}$.

Figura 15 – Third order tensor

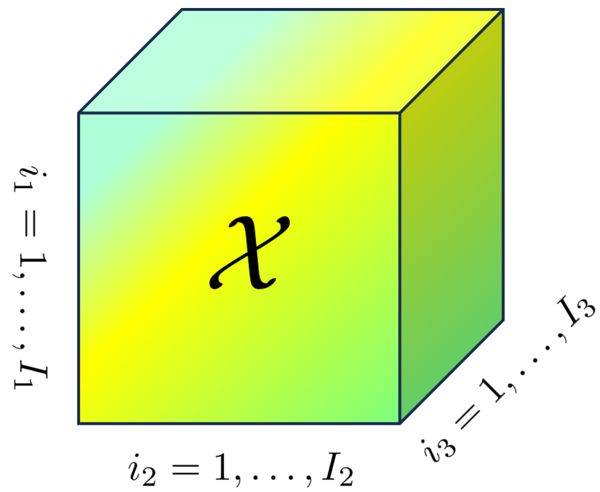

The use of tensor tools requires the understanding of certain basic definitions that are now presented.

Definition 1 *Scalar notation: Let consider a N-order tensor* $\mathscr{X} \in \mathbb{C}^{I_1 \times I_2 \times \ldots \times I_N}$*. Its scalar* *form is denoted as*

$$x_{i_1 i_2 \dots i_N} = [\mathscr{X}]_{i_1 i_2 \dots i_N} \,. \tag{3.1}$$

We can define the inner product between two tensors of the same dimension using the scalar notation.

Definition 2 *Inner production between tensor: Let us consider* $\mathscr{X} \in \mathbb{C}^{I_1 \times I_2 \times \dots \times I_N}$ *and* $\mathscr{Y} \in \mathbb{C}^{I_1 \times I_2 \times \dots \times I_N}$*. The inner product between* $\mathscr{X}$ *and* $\mathscr{Y}$ *is given by*

$$\langle \mathscr{X}, \mathscr{Y} \rangle = \sum_{i_1=1}^{I_1} \sum_{i_2=1}^{I_2} \cdots \sum_{i_N=1}^{I_N} x_{i_1 i_2 \dots i_N} y_{i_1 i_2 \dots i_N} \,. \tag{3.2}$$

Definition 3 *Outer product between two tensor: Given two tensors* $\mathscr{X} \in \mathbb{C}^{I_1 \times I_2 \times \dots \times I_N}$ *and* $\mathscr{Y} \in \mathbb{C}^{J_1 \times J_2 \times \dots \times J_M}$*, the outer product between them can be denoted as*

$$[\mathscr{X} \circ \mathscr{Y}]_{i_1 i_2 \dots i_N j_1 j_2 \dots j_M} = x_{i_1 i_2 \dots i_N} y_{j_1 j_2 \dots j_M} \,. \tag{3.3}$$

Definition 4 *Rank-*1 *tensor: A tensor* $\mathscr{X} \in \mathbb{C}^{I_1 \times I_2 \times \dots \times I_N}$ *is said to be a rank-*1 *tensor if it results from the outer product of N vectors as follows*

$$\mathscr{X} = \mathbf{a}_1 \circ \mathbf{a}_2 \circ \cdots \circ \mathbf{a}_N. \tag{3.4}$$

Definition 5 *Frobenius norm: Let us consider a N-order tensor* $\mathscr{X} \in \mathbb{C}^{I_1 \times I_2 \times \dots \times I_N}$*. Its Frobenius norm is denoted as*

$$\| \mathscr{X} \|_F = \sqrt{\langle \mathscr{X}, \mathscr{X} \rangle} = \left(\sum_{i_1=1}^{I_1} \sum_{i_2=1}^{I_2} \cdots \sum_{i_N=1}^{I_N} |x|^2_{i_1 i_2 \dots i_N} \right)^{\frac{1}{2}} . \tag{3.5}$$

Note that if $N = 2$, these definitions are the same as those for matrices, i.e. second-order tensors.

3.1.1 Tensor slices and unfolds

Tensors are generally used as a tool to handle multidimensional data structures. By resorting to tensor decompositions, multidimensional signals can be "observed" from different perspectives by resorting to slicing and unfolding concepts. These concepts are behind the computational procedures and routines used to compute tensor decompositions using matrix operations. We can slice a tensor $\mathscr{X}$ along its dimensions and organize/stack these slices properly to obtain the so-called unfolding, which are lower dimensional tensor/matrix representations of a higher order tensor that contain the same information but arranged in different forms. Let $\mathscr{X} \in \mathbb{C}^{I_1 \times I_2 \times I_3}$ be an arbitrary 3th order tensor, as shown in Figure 16.This tensor can be sliced in three different ways. In this example, the i_nth horizontal slice, $[\mathscr{X}]_{i_n..}$, is obtained by keeping the indices of the second and third dimensions fixed while varying the first dimension index. The same rules apply to determine the lateral and frontal slices. Continuing with this example, these slices can be reorganized to represent $\mathscr{X}$ *via* its nth (matrix) unfolding, which represents the nth matrix "visualization" of the tensor, $n = 1, \ldots, N$. Mathematically, each slice has the following dimension:

Figura 16 – Illustration of a third-order tensor sliced related to each of its modes.

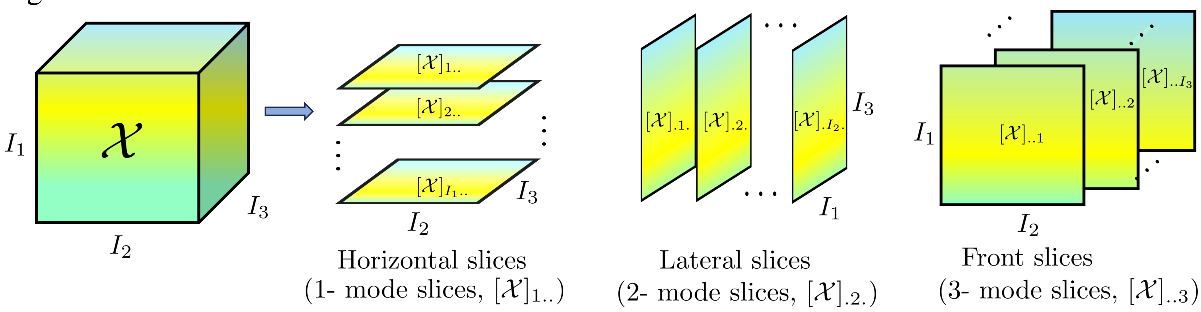

- Horizontal slices: $[\mathscr{X}]_{i_1..} \in \mathbb{C}^{I_2 \times I_3}$ for $i_1 = 1, 2, \ldots, I_1$
- Lateral slices: $[\mathscr{X}]_{.i_2.} \in \mathbb{C}^{I_1 \times I_3}$ for $i_2 = 1, 2, \ldots, I_2$
- Frontal slices: $[\mathscr{X}]_{..i_3} \in \mathbb{C}^{I_1 \times I_2}$ for $i_3 = 1, 2, \ldots, I_3$

3.1.2 Unfolding

The relationship between a tensor and its matrix notations can be established through the unfolding procedure. By rearranging the tensor in terms of its $n-$th mode slices, we can transform it into equivalent matrix forms, as shown in Figure 17. First, by rearranging the frontal slices, we obtain the 1-mode unfolding of $\mathscr{X}$, represented by $[\mathscr{X}]_{(1)} \in \mathbb{C}^{I_1 \times I_3 I_2}$. Similarly, by stacking the horizontal and lateral slices, we can obtain the 2-mode and 3-mode unfoldings, resulting in $[\mathscr{X}]_{(2)} \in \mathbb{C}^{I_2 \times I_1 I_3}$ and $[\mathscr{X}]_{(3)} \in \mathbb{C}^{I_3 \times I_1 I_2}$, respectively[1]. To put it simply, the process

Figura 17 – Illustration of the unfolding of a third order tensor.

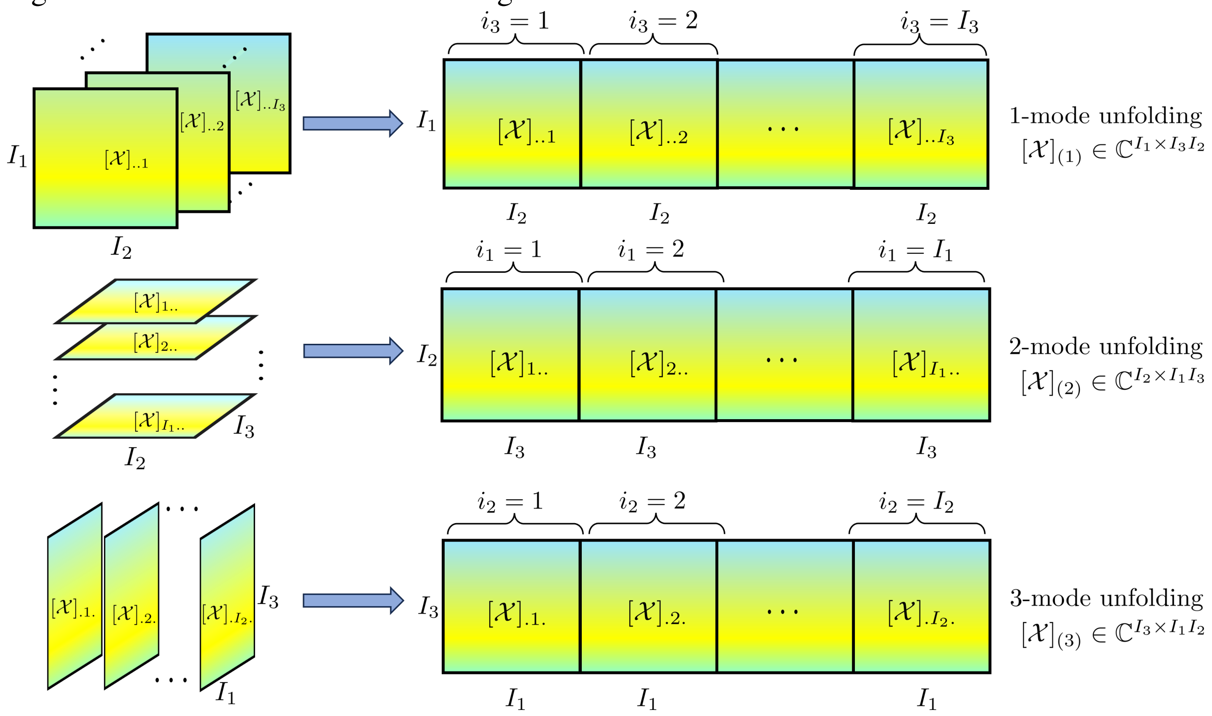

of converting a third-order tensor into a two-dimensional matrix can be expressed mathematically as follows:

$$
\begin{aligned}
&[\mathscr{X}]_{(1)} = [[\mathscr{X}]_{..1}\ [\mathscr{X}]_{..2}\ \dots\ [\mathscr{X}]_{..I_3}] \in \mathbb{C}^{I_1 \times I_3 I_2} \\
&[\mathscr{X}]_{(2)} = [[\mathscr{X}]_{1..}\ [\mathscr{X}]_{2..}\ \dots\ [\mathscr{X}]_{I_1..}] \in \mathbb{C}^{I_2 \times I_1 I_3} \\
&[\mathscr{X}]_{(3)} = [[\mathscr{X}]_{.1.}\ [\mathscr{X}]_{.2.}\ \dots\ [\mathscr{X}]_{.I_2.}] \in \mathbb{C}^{I_3 \times I_1 I_2}.
\end{aligned}
\tag{3.6}
$$

Alternatively

$$
\begin{aligned}
&[\mathscr{X}]_{(1)} = [[\mathscr{X}]_{..1}\ [\mathscr{X}]_{..2}\ \dots\ [\mathscr{X}]_{..I_3}] \in \mathbb{C}^{I_1 \times I_3 I_2} \\
&[\mathscr{X}]_{(2)} = \left[[\mathscr{X}]_{..1}^{\mathrm{T}}\ [\mathscr{X}]_{..2}^{\mathrm{T}}\ \dots\ [\mathscr{X}]_{..I_3}^{\mathrm{T}}\right] \in \mathbb{C}^{I_2 \times I_1 I_3} \\
&[\mathscr{X}]_{(3)} = [\mathrm{vec}([\mathscr{X}]_{..1})\ \mathrm{vec}([\mathscr{X}]_{..2})\ \dots\ \mathrm{vec}([\mathscr{X}]_{..I_3})] \in \mathbb{C}^{I_3 \times I_1 I_2}.
\end{aligned}
\tag{3.7}
$$

Note that alternatively, the three possible matrix unfoldings can be derived from the frontal slice. In a more general case, the n-mode unfolding of a tensor $\mathscr{X} \in \mathbb{C}^{I_1 \times I_2 \times \cdots \times I_N}$, is denoted as the matrix $[\mathscr{X}]_{(n)} \in \mathbb{C}^{I_n \times I_1 I_2 \dots I_{n-1} I_{n+1} I_N}$.

[1] The ordering of the columns of that define the matrix unfoldings can be done in different ways (Kolda; Bader, 2009).

3.2 Tensor n-mode product

When dealing with tensors of higher orders, i.e., with having more than three dimensions, it is common to represent them using the n-mode product notation. Let us define this notation.

Definition 6 *n-mode product: This special product consists of multiplying a tensor $\mathcal{X} \in \mathbb{C}^{I_1 \times I_2 \times \ldots \times I_n \times \ldots \times I_N}$ by a matrix $\mathbf{B} \in \mathbb{C}^{J \times I_n}$, resulting in a new tensor $\mathcal{Y} \in \mathbb{C}^{I_1 \times \ldots \times I_{n-1} \times J \times I_{n+1} \times \ldots \times I_N}$, where the nth dimension of $\mathcal{Y}$ is J, which corresponds to the dimension of the row space of $\mathbf{B}$.*

Defining the n-mode product between $\mathcal{X}$ and $\mathbf{B}$ as $\mathcal{Y} = \mathcal{X} \times_n \mathbf{B}$, its element-wise notation is given by [2]:

$$y_{I_1 \times \ldots \times I_{n-1} \times J \times I_{n+1} \times \ldots \times I_N} = (\mathcal{X} \times_n \mathbf{B})_{i_1 \times \ldots \times i_{n-1} \times j \times i_{n+1} \times \ldots \times i_N} = \sum_{i_n=1}^{I_n} x_{i_1 i_2 \ldots i_N} \, b_{j i_n} \, . \quad (3.8)$$

According to the definition (3.8), the n-mode product represents the multiplication of a tensor by a matrix. The following properties relate the n-mode product and tensor unfolding:

Property 1 *(Equivalence:)* $\mathcal{Y} = \mathcal{X} \times_n \mathbf{B} \Leftrightarrow [\mathcal{Y}]_{(n)} = \mathbf{B}\,[\mathcal{X}]_{(n)}$.

Property 2 *(Commutativity:)* $\mathcal{X} \times_m \mathbf{A} \times_n \mathbf{B} = \mathcal{X} \times_n \mathbf{B} \times_m \mathbf{A}$, $(m \neq n)$. *As a consequence, if $m = n$ we have*

$$\mathcal{X} \times_n \mathbf{A} \times_n \mathbf{B} = \mathcal{X} \times_n \mathbf{BA}.$$

3.3 Matrix operators and vectorization

In the following, we define some important matrix operators that are useful to represent tensor decompositions in matrix/vector formats. These operators and their related properties are commonly exploited in tensor decomposition algorithms.

3.3.1 Kronecker product

The Kronecker product is a frequently used tool in tensor modeling. According to (Loan, 2000), it has a rich algebra that enables practical, elegant, and fast algorithms.

[2] For more information about n-mode product, we refer the reader to (Lathauwer; Moor, 1996).

Definition 7 *Let us consider the matrices* $\mathbf{A} \in \mathbb{C}^{I \times J}$ *and* $\mathbf{B} \in \mathbb{C}^{P \times Q}$*. The Kronecker product between* $\mathbf{A}$ *and* $\mathbf{B}$ *is*

$$\mathbf{A} \otimes \mathbf{B} = \begin{bmatrix} a_{11}\mathbf{B} & a_{12}\mathbf{B} & \dots & a_{1J}\mathbf{B} \\ a_{21}\mathbf{B} & a_{22}\mathbf{B} & \dots & a_{2J}\mathbf{B} \\ \vdots & \vdots & \ddots & \vdots \\ a_{I1}\mathbf{B} & a_{I2}\mathbf{B} & \dots & a_{IJ}\mathbf{B} \end{bmatrix} \in \mathbb{C}^{IP \times JQ}.$$

NOTE: The Kronecker product is a non-commutative operation, which means that $\mathbf{A} \otimes \mathbf{B}$ is not equal to $\mathbf{B} \otimes \mathbf{A}$.

3.3.2 Khatri-Rao product

The Khatri Rao product is a mathematical operation that can be considered as the column-wise Kronecker product.

Definition 8 *Let us consider the matrices* $\mathbf{A} \in \mathbb{C}^{I \times R}$ *and* $\mathbf{B} \in \mathbb{C}^{J \times R}$*. The Katri-Rao product between* $\mathbf{A}$ *and* $\mathbf{B}$ *is*

$$\mathbf{A} \diamond \mathbf{B} = \left[\begin{array}{c} \mathbf{A}_{.1} \otimes \mathbf{B}_{.1} \quad \mathbf{A}_{.2} \otimes \mathbf{B}_{.2} \dots \mathbf{A}_{.K} \otimes \mathbf{B}_{.K} \end{array} \right] \in \mathbb{C}^{IJ \times R} \quad .$$

As an alternative, the Khatri Rao product can be expressed as a function of the Kronecker product:

$$\mathbf{A} \diamond \mathbf{B} = (\mathbf{A} \otimes \mathbf{B})\mathbf{Q}, \tag{3.9}$$

where $\mathbf{Q} \in \mathbb{R}^{R^2 \times R}$ is a selection matrix.

NOTE: In the Khatri-Rao product, the involved matrices must have the same number of columns.

3.3.3 Hadamard product

The Hadamard product involves an element-wise multiplication of corresponding matrix elements.

Definition 9 *Let us consider the matrices* $\mathbf{A} \in \mathbb{C}^{I \times J}$ *and* $\mathbf{B} \in \mathbb{C}^{I \times J}$*. The Hadamard product* *between* $\mathbf{A}$ *and* $\mathbf{B}$ *is*

$$\mathbf{A} \odot \mathbf{B} = \begin{bmatrix} a_{11}b_{11} & a_{12}b_{12} & \dots & a_{1J}b_{jj} \\ a_{21}b_{21} & a_{22}b_{22} & \dots & a_{2J}b_{2j} \\ \vdots & \vdots & \ddots & \vdots \\ a_{I1}b_{I1} & a_{I2}b_{I2} & \dots & a_{IJ}b_{IJ} \end{bmatrix} \in \mathscr{C}^{I \times J}.$$

In this case, the matrices have the same dimension.

Definition 10 *Vectorization: Let* $\mathbf{A} = [\mathbf{a_1}\ \mathbf{a_2}\ \dots\ \mathbf{a_J}] \in \mathbb{C}^{I \times J}$ *be an arbitrary matrix. The operador* $vec(\cdot)$ *is defined as*

$$vec(\mathbf{A}) = \begin{bmatrix} \mathbf{a_1} \\ \mathbf{a_2} \\ \vdots \\ \mathbf{a_J} \end{bmatrix} \in \mathbb{C}^{IJ \times 1}.$$

In the next subsection, we highlight the properties that link such products and/or vec$(\cdot)$ operators.

3.4 Properties relating Kronecker, Khatri Rao, and Hadamard products, and the vec$(\cdot)$ operator

In this section, we discuss the primary properties of the vec$(\cdot)$ operator and the special matrix products used in this thesis document. Although there are other properties related to these operators, we focus only on those exploited in this thesis to solve our problems. Let us consider arbitrary matrices $\mathbf{A} \in \mathbb{C}^{I \times J}$, $\mathbf{B} \in \mathbb{C}^{P \times Q}$, $\mathbf{C} \in \mathbb{C}^{J \times R}$ and $\mathbf{D} \in \mathbb{C}^{Q \times S}$.

Property 3 $(\mathbf{A} \otimes \mathbf{B})(\mathbf{C} \otimes \mathbf{D}) = (\mathbf{AC} \otimes \mathbf{BD})$.

If $S = R$ such that $\mathbf{C} \in \mathbb{C}^{J \times R}$ and $\mathbf{D} \in \mathbb{C}^{Q \times R}$, we have the following property

Property 4 $(\mathbf{A} \otimes \mathbf{B})(\mathbf{C} \diamond \mathbf{D}) = (\mathbf{AC}) \diamond (\mathbf{BD})$.

The property (4) establishes a connection between the Kronecker and Khatri-Rao product. Assuming $\mathbf{A} \in \mathbb{C}^{I \times J}$, $\mathbf{B} \in \mathbb{C}^{P \times J}$, $\mathbf{C} \in \mathbb{C}^{I \times J}$ and $\mathbf{D} \in \mathbb{C}^{P \times J}$, we have

Property 5 $(\mathbf{A} \diamond \mathbf{B})^H(\mathbf{C} \diamond \mathbf{D}) = (\mathbf{A}^H\mathbf{C}) \odot (\mathbf{B}^H\mathbf{D})$.

In mathematical terms, the property (5) establishes a connection between two types of matrix products, the Khatri-Rao and the Hadamard products. For $\mathbf{A} \in \mathbb{C}^{I \times J}$, $\mathbf{B} \in \mathbb{C}^{J \times P}$ and $\mathbf{C} \in \mathbb{C}^{P \times Q}$, we have the following property

Property 6 *$vec(\mathbf{ABC}) = (\mathbf{C}^T \otimes \mathbf{A})vec(\mathbf{B})$.*

If $\mathbf{B}$ is a diagonal matrix, the property (6) is rewritten as

$$\mathrm{vec}(\mathbf{ABC}) = (\mathbf{C}^{\mathrm{T}} \diamond \mathbf{A})\mathbf{b},$$

where $\mathbf{b}$ is a vector extracted from the diagonal of $\mathbf{B}$. An important property of diag$(\cdot)$ is:

Property 7 *$diag(\mathbf{a})\mathbf{b} = diag(\mathbf{b})\mathbf{a}$, for arbitrary vectors $\mathbf{a}$ and $\mathbf{b}$.*

3.5 Multilinear operators

The concepts of tensor n-mode product and tensor unfolding can be used to present multilinear operators, as discussed in (Kolda, 2006). Properties (1) and (2) show a relationship between these two concepts. In addition to n-mode unfoldings, multilinear operators involve the Kronecker and Khatri-Rao products. These operators provide a more complete understanding of the relationship between these concepts.

3.5.1 Tucker operator

The Tucker operator offers an efficient method to represent the multi-mode product between an Nth order tensor and N factor matrices $\mathbf{A}^{(n)}$, $n = 1, \ldots, N$.

Definition 11 *Tucker operator: Let $\mathscr{Y} \in \mathbb{C}^{I_1 \times I_2 \times \ldots \times I_n \times \ldots \times I_N}$ be a tensor of order N and $\mathbf{A}^{(n)} \in \mathbb{C}^{J_n \times I_n}$ be the factor matrices, $n = 1, \ldots, N$. The Tucker operator is defined as*

$$[\![\mathscr{Y}; \mathbf{A}^{(1)}, \mathbf{A}^{(2)}, \ldots, \mathbf{A}^{(N)}]\!] \triangleq \mathscr{Y} \times_1 \mathbf{A}^{(1)} \times_2 \mathbf{A}^{(2)} \cdots \times_N \mathbf{A}^{(N)} . \tag{3.10}$$

Then,

$$\mathscr{X} = [\![\mathscr{Y}; \mathbf{A}^{(1)}, \mathbf{A}^{(2)}, \ldots, \mathbf{A}^{(N)}]\!] \Leftrightarrow \mathscr{X} = \mathscr{Y} \times_1 \mathbf{A}^{(1)} \times_2 \mathbf{A}^{(2)} \cdots \times_N \mathbf{A}^{(N)} . \tag{3.11}$$

The unfolding notation for the tensor $\mathscr{X}$ in (3.11) is given by

$$[\mathscr{X}]_{(n)} = \mathbf{A}^{(n)} [\mathscr{Y}]_{(n)} (\mathbf{A}^{(N)} \otimes \cdots \otimes \mathbf{A}^{(n+1)} \otimes \mathbf{A}^{(n-1)} \otimes \cdots \otimes \mathbf{A}^{(1)})^{\mathrm{T}} . \tag{3.12}$$

Note: The expression in (3.12) represents the Tucker decomposition, which we discuss later.

3.5.2 Kruskal operator

The Kruskal operator is a special case of the Tucker operator, where the tensor $\mathscr{Y}$ in (3.10) is an identity tensor. Therefore, we need to define the identity tensor before defining the Kruskal operator.

Definition 12 *Identity tensor: A identity tensor, $\mathscr{I}_{N,R}$, is a N-order tensor of size $R \times R \times \ldots \times R$ such that,*

$$[\mathscr{I}_{N,R}]_{i_1 i_2 \ldots i_N} = \begin{cases} 1, & se, i_1 = i_2 = \cdots = i_N \ , \\ 0, & caso\ contrário\ . \end{cases}$$

and

$$[\mathscr{I}]_{(1)} = [\mathscr{I}]_{(2)} = [\mathscr{I}]_{(N)} = \mathbf{Q} \in \mathbb{C}^{N^{(N-1)} \times N}$$

where $\mathbf{Q}$ *is a selection matrix as in (3.9).*

Definition 13 *Kruskal operator: Let us consider $\mathscr{Y} = \mathscr{I}_{R,N}$. In this case, the Kruskal operator is defined as a particular case of the Tucker operator such that (3.10) becomes*

$$[\![\mathscr{I}_{R,N}; \mathbf{A}^{(1)}, \mathbf{A}^{(2)}, \ldots, \mathbf{A}^{(N)}]\!] \triangleq \mathscr{I}_{R,N} \times_1 \mathbf{A}^{(1)} \times_2 \mathbf{A}^{(2)} \cdots \times_N \mathbf{A}^{(N)} \ . \tag{3.13}$$

Then,

$$\mathscr{X} = [\![\mathscr{I}_{R,N}; \mathbf{A}^{(1)}, \mathbf{A}^{(2)}, \ldots, \mathbf{A}^{(N)}]\!] \Leftrightarrow \mathscr{X} = \mathscr{I}_{R,N} \times_1 \mathbf{A}^{(1)} \times_2 \mathbf{A}^{(2)} \cdots \times_N \mathbf{A}^{(N)} \ . \tag{3.14}$$

The nth mode unfolding for any arbitrary tensor can be defined with the help of the Tucker operator and its consequences mentioned in (3.12), the Khatri-Rao product defined in (3.9), and the identity tensor definition in (12), as follows:

$$[\mathscr{X}]_{(n)} = \mathbf{A}^{(n)} (\mathbf{A}^{(N)} \diamond \cdots \diamond \mathbf{A}^{(n+1)} \diamond \mathbf{A}^{(n-1)} \diamond \cdots \diamond \mathbf{A}^{(1)})^{\mathrm{T}} \ . \tag{3.15}$$

Note: The expression in (3.14) can be seen as the n-mode product representation of a PARAFAC decomposition. Also, the matrices $\mathbf{A}^{(n)}$ have the same number of columns.

3.6 Tensor Decomposition

The concept of tensor decomposition can be traced back to Hitchcock in 1927 (Hitchcock, 1927), but it gained more attention through the works of Tucker (Tucker, 1964; Tucker, 1966), Carroll and Chang (Caroll; Chang, 1970), and Harshman (Harshman, 1970). While Tucker introduced the Tucker decomposition in (Tucker, 1964; Tucker, 1966), the Canonical Polyadic Decomposition was independently developed by Carroll and Chang in psychometrics field (Caroll; Chang, 1970) and by Harshman in linguistics (Harshman, 1970). Later, tensor decompositions have found numerous applications in signal processing and wireless communications (Sidiropoulos *et al.*, 2017; Chen *et al.*, 2021). In this thesis, we specifically focus on the PARAFAC and PARATUCK2 decompositions, which are the ones exploited in our contributions. In the following, we elaborate more on the PARAFAC and formulate the PARATUCK2 decomposition, which can be seen as a hybrid of the PARAFAC and Tucker2 decomposition.

3.6.1 PARAFAC

The PARAFAC decomposition, also known as the Canonical Polyadic Decomposition (CPD), is one of the more common tensor decomposition. As mentioned, it was originally developed in psychometrics and linguistics. However, it has also gained popularity in different signal processing applications. One of the main reasons for its widespread use is its intrinsic uniqueness properties, which are required for many applications involving parameter estimation based on signals enjoying multiple diversities. As mentioned in (Sidiropoulos *et al.*, 2017), the built-in essential uniqueness under mild conditions is perhaps the main advantage of the low-rank tensor decomposition compared to matrix decomposition.

In linear algebra, a matrix can be decomposed in terms of its singular value and left and right singular vectors, using the well-known singular value decomposition (SVD). In this sense, recall that a matrix $\mathbf{A}$ of rank R can be written as a sum of rank-one matrices such that

$$\mathbf{A} = \sum_{r=1}^{R} \sigma_r \mathbf{u}_r \mathbf{v}_r^{\mathrm{T}} = \sum_{r=1}^{R} \sigma_r \mathbf{u}_r \circ \mathbf{v}_r \,. \tag{3.16}$$

The variables σ_r, $\mathbf{u}_r$, and $\mathbf{v}_r$ are the rth singular value, and the corresponding left and right singular vectors, respectively. The PARAFAC decomposition can be seen as one possible generalization of the matrix-rank decomposition to higher orders ($N > 2$). The PARAFAC decomposition expresses a tensor $\mathscr{X} \in \mathbb{C}^{I_1 \times I_2 \times \cdots \times I_N}$ as a linear combination of rank-1 tensors, where each one is given by the outer product of N vectors.

$$\mathscr{X} = \sum_{r=1}^{R} \mathscr{X}_r = \sum_{r=1}^{R} \lambda_r \mathbf{a}_r^{(1)} \circ \mathbf{a}_r^{(2)} \circ \cdots \circ \mathbf{a}_r^{(N)} \,. \tag{3.17}$$

The number of terms in such a linear combination corresponds to the tensor rank R defined as follows.

Definition 14 *Rank of a tensor: Let us consider the tensor $\mathscr{X} \in \mathbb{C}^{I_1 \times I_2 \times \dots \times I_N}$. The rank, R of the tensor $\mathscr{X}$ is defined as the minimum number of the rank-1 tensors used in a linear combination to produce $\mathscr{X}$.*

For simplicity of exposition, in this section, we discuss the PARAFAC decomposition by focusing on the third-order case. Without loss of generality, we also assume that $\lambda_r = 1$, $r = 1, \dots, R$.

An alternative and insightful representation of the PARAFAC decomposition can be seen in Figure 18 as a multilinear combination of three different factor matrices *via* an identity core tensor. Each factor matrix spans a different tensor dimension. This approach helps us gain a more comprehensive understanding of the PARAFAC decomposition as well as its comparison with more general decompositions such as the Tucker decomposition.

Figura 18 – Third-order tensor as a sum of rank-1 tensors

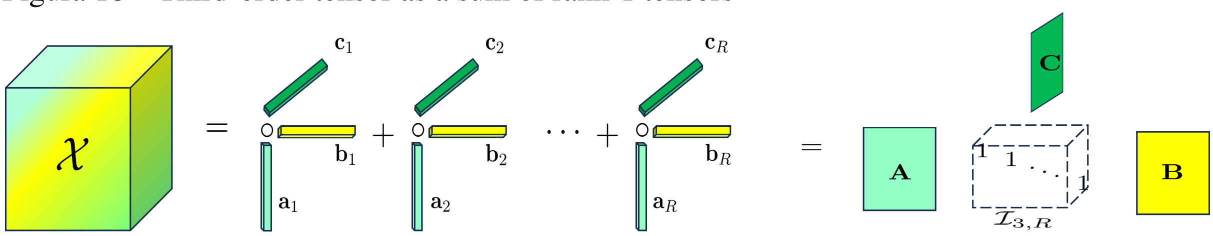

Considering $\mathscr{X} \in \mathbb{C}^{I_1 \times I_2 \times I_3}$, its scalar notation is given as

$$x_{i_1 i_2 i_3} = \sum_{r=1}^{R} a_{i_1 r} b_{i_2 r} c_{i_3 r}, \tag{3.18}$$

where $a_{i_1 r}$, $b_{i_2 r}$ and $c_{i_3 r}$ are the elements of the factor matrices $\mathbf{A} \in \mathbb{C}^{I_1 \times R}$, $\mathbf{B} \in \mathbb{C}^{I_2 \times R}$ and $\mathbf{C} \in \mathbb{C}^{I_3 \times R}$, respectively. It is also common to represent a PARAFAC decomposition in terms of its frontal slices as

$$[\mathscr{X}]_{..i_3} = \mathbf{A} D_{i_3}(\mathbf{C}) \mathbf{B}^{\mathrm{T}}, \, i_3 = 1, \dots, I_3 \, . \tag{3.19}$$

By following the procedure described in equations (3.7), we can represent the three matrix unfoldings of the tensor $\mathscr{X}$ in terms of its factor matrices as follows

$$\begin{aligned} [\mathscr{X}]_{(1)} &= \mathbf{A} \left(\mathbf{C} \diamond \mathbf{B} \right)^{\mathrm{T}}, \\ [\mathscr{X}]_{(2)} &= \mathbf{B} \left(\mathbf{C} \diamond \mathbf{A} \right)^{\mathrm{T}}, \\ [\mathscr{X}]_{(3)} &= \mathbf{C} \left(\mathbf{B} \diamond \mathbf{A} \right)^{\mathrm{T}} \, . \end{aligned} \tag{3.20}$$

For a tensor with an order higher than 3, a more suitable and compact representation resorts to the Kruskal operator defined in (3.14) and relies on the correspondence

$$\mathscr{X} = [\![\mathscr{I}_{R,N}; \mathbf{A}^{(1)}, \mathbf{A}^{(2)}, \dots, \mathbf{A}^{(N)}]\!] \Leftrightarrow \mathscr{X} = \mathscr{I}_{R,N} \times_1 \mathbf{A}^{(1)} \times_2 \mathbf{A}^{(2)} \cdots \times_N \mathbf{A}^{(N)} \, , \tag{3.21}$$

such that

$$[\mathscr{X}]_{(n)} = \mathbf{A}^{(n)}(\mathbf{A}^{(N)} \diamond \cdots \diamond \mathbf{A}^{(n+1)} \diamond \mathbf{A}^{(n-1)} \diamond \cdots \diamond \mathbf{A}^{(1)})^{\mathrm{T}} . \tag{3.22}$$

Uniqueness

Unlike general matrix decompositions, the PARAFAC decomposition has an intrinsic uniqueness property (up to trivial ambiguities). For the third-order case, in the seminal work (Kruskal, 1977), Kruskal originally provided a uniqueness condition for PARAFAC, which has become well-known as the "Kruskal condition". Later in (Sidiropoulos; Bro, 2000), Sidiropoulos extended this condition to arbitrary N-order tensors. Considering the general case of (Sidiropoulos; Bro, 2000), the PARAFAC decomposition is unique up to scaling and permutation ambiguities if

$$\sum_{n=1}^{N} k_{\mathbf{A}^{(n)}} \geq 2R + N - 1. \tag{3.23}$$

where $k_{\mathbf{A}}$ is the Kruskal rank which is defined as

Definition 15 *Kruskal rank: Let $\mathbf{A} \in \mathbb{C}^{I_1 \times R}$ be a matrix. The Kruskal rank $k_{\mathbf{A}}$ is the smallest k for which every set of k columns of $\mathbf{A}$ is linearly independent, i.e.,*

$$k_{\mathbf{A}} \leq r_{\mathbf{A}} \leq \min(I_1, R). \tag{3.24}$$

In particular, if $N = 3$, we obtain the Kruskal condition in (Kruskal, 1977) for the third-order PARAFAC decomposition

$$k_{\mathbf{A}} + k_{\mathbf{B}} + k_{\mathbf{C}} \geq 2R + 2, \tag{3.25}$$

If this condition is satisfied, then the factor matrices $\mathbf{A}$, $\mathbf{B}$, and $\mathbf{C}$ can be reconstructed from the third-order tensor $\mathscr{X}$ up to scaling and a common permutation of their columns. More specifically, any alternative set of matrices $\overline{\mathbf{A}}$, $\overline{\mathbf{B}}$, and $\overline{\mathbf{C}}$ leading to the same tensor $\mathscr{X}$ are linked to the true matrices by the following relationships $\overline{\mathbf{A}} = \mathbf{A}\prod\Delta_1$, $\overline{\mathbf{B}} = \mathbf{B}\prod\Delta_2$ and $\overline{\mathbf{C}} = \mathbf{C}\prod\Delta_3$, where $\prod$ is a permutation matrix and Δ_i, $i = 1, 2, 3$, are scaling matrices that compensate each other such that $\Delta_1\Delta_2\Delta_3 = \mathbf{I}_R$.

3.7 Tucker3

The Tucker3 decomposition was introduced in (Tucker, 1966). This decomposition represents an output tensor as a multilinear combination of input tensor transformed by factor matrices along each mode. Given an arbitrary third-tensor $\mathcal{X} \in \mathbb{C}^{I_1 \times I_2 \times I_3}$, the scalar form of its Tucker3 decomposition can be expressed as

$$x_{i_1,i_2,i_3} = \sum_{p=1}^{P} \sum_{q=1}^{Q} \sum_{r=1}^{R} a_{i_1,p} b_{i_2,q} c_{i_3,r} g_{p,q,r} \;, \tag{3.26}$$

where $a_{i_1,p}$, $b_{i_2,q}$, $c_{i_3,r}$ and $g_{p,q,r}$ are the entries of the factor matrices $\mathbf{A} \in \mathbb{C}^{I_1 \times P}$, $\mathbf{B} \in \mathbb{C}^{I_2 \times Q}$, $\mathbf{C} \in \mathbb{C}^{I_3 \times R}$ and the core tensor $\mathcal{G} \in \mathbb{C}^{P \times Q \times R}$, respectively. Figure 19 depicts a block diagram that illustrates the Tucker3 decomposition. The n-mode unfoldings can be factorized as

$$\begin{aligned}
[\mathcal{X}]_{(1)} &= \mathbf{A}[\mathcal{G}]_{(1)} \left(\mathbf{C} \otimes \mathbf{B}\right)^{\mathrm{T}} \\
[\mathcal{X}]_{(2)} &= \mathbf{B}[\mathcal{G}]_{(2)} \left(\mathbf{C} \otimes \mathbf{A}\right)^{\mathrm{T}} \\
[\mathcal{X}]_{(3)} &= \mathbf{C}[\mathcal{G}]_{(3)} \left(\mathbf{B} \otimes \mathbf{A}\right)^{\mathrm{T}}.
\end{aligned} \tag{3.27}$$

Figura 19 – Tucker3 tensor decomposition

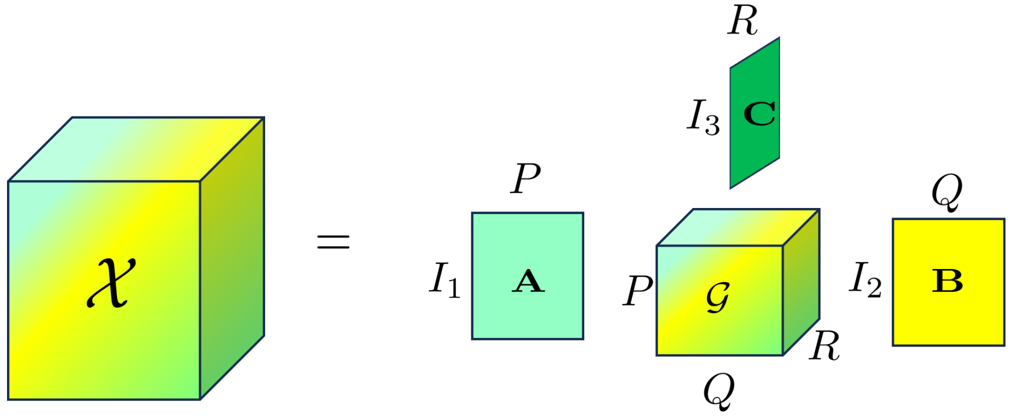

Tucker2: As a particular case, in which the factor matrix $\mathbf{C}$ is absorbed by the core tensor such that

$$h_{p,q,i_3} = [\mathcal{G} \times_3 \mathbf{C}]_{p,q,i_3}, \tag{3.28}$$

where h_{p,q,i_3} denotes the scalar element of the equivalent tensor $\mathcal{H} \in \mathbb{C}^{P \times Q \times I_3}$, we have a Tucker2 decomposition with the following scalar notation

$$x_{i_1,i_2,i_3} = \sum_{p=1}^{P} \sum_{q=1}^{Q} a_{i_1,p} b_{i_2,q} h_{p,q,i_3}. \tag{3.29}$$

Note that the Tucker2 decomposition boils down from the Tucker3 decomposition when $\mathbf{C} = \mathbf{I}_{I_3}$ and $\mathcal{G} = \mathcal{H}$.

3.7.1 PARATUCK2

Although the PARAFAC decomposition is the most popular tensor decomposition, its simplicity may not capture more complicated tensor structures, which arise in several real-world problems and signal models, including the ones addressed in this thesis. Another popular tensor decomposition sharing properties of the PARAFAC and Tucker decompositions is the so-called PARATUCK2 tensor decomposition. The PARATUCK2 was originally introduced by Harshman and Lundy in 1996 in the psychometrics field. Due to its flexible algebraic structure, it has been efficiently applied to solve problems in signal processing for wireless communication, as shown in (Ximenes *et al.*, 2014; Almeida *et al.*, 2009).

Considering a third-order tensor $\mathscr{X} \in \mathbb{C}^{I_1 \times I_2 \times I_1}$, the scalar notation for the PARATUCK2 case is:

$$x_{i_1 i_2 i_3} = \sum_{p=1}^{P} \sum_{q=1}^{Q} a_{i_1 p} b_{i_2 q} c^{\mathbf{A}}_{i_3 p} c^{\mathbf{B}}_{i_3 q} r_{pq}, \tag{3.30}$$

where, $a_{i_1 p}$, $b_{i_2 q}$, r_{pq}, $c^{\mathbf{A}}_{i_3 p}$, $c^{\mathbf{B}}_{i_3 q}$ are the entries of the matrices $\mathbf{A} \in \mathbb{C}^{I_1 \times P}, \mathbf{B} \in \mathbb{C}^{I_2 \times Q}, \mathbf{R} \in \mathbb{C}^{P \times Q}, \mathbf{C}^{\mathbf{A}} \in \mathbb{C}^{I_3 \times P}$ and $\mathbf{C}^{\mathbf{B}} \in \mathbb{C}^{I_3 \times Q}$, respectively. In practical applications, the PARATUCK2 decomposition is identified, in general, using frontal slice notation, which is given as:

$$[\mathscr{X}]_{..i_3} = \mathbf{A} D_{i_3}(\mathbf{C}^{\mathbf{A}}) \mathbf{R} D_{i_3}(\mathbf{C}^{\mathbf{B}}) \mathbf{B}^{\mathrm{T}} . \tag{3.31}$$

Let $D_{i_3}(\mathbf{C}^{\mathbf{A}}) \in \mathbb{C}^{P \times P}$ and $D_{i_3}(\mathbf{C}^{\mathbf{B}}) \in \mathbb{C}^{Q \times Q}$ be diagonal matrices, where the diagonal is formed by the i_3th row of the matrices $\mathbf{C}^{\mathbf{A}}$ and $\mathbf{C}^{\mathbf{B}}$, respectively. The core matrix, denoted as $\mathbf{R}$, determines the level of interaction between the components of the factor matrices $\mathbf{A}$ and $\mathbf{B}$. A block diagram of the PARATUCK2 model is shown in Figure 20.

Figura 20 – PARATUCK2 tensor model

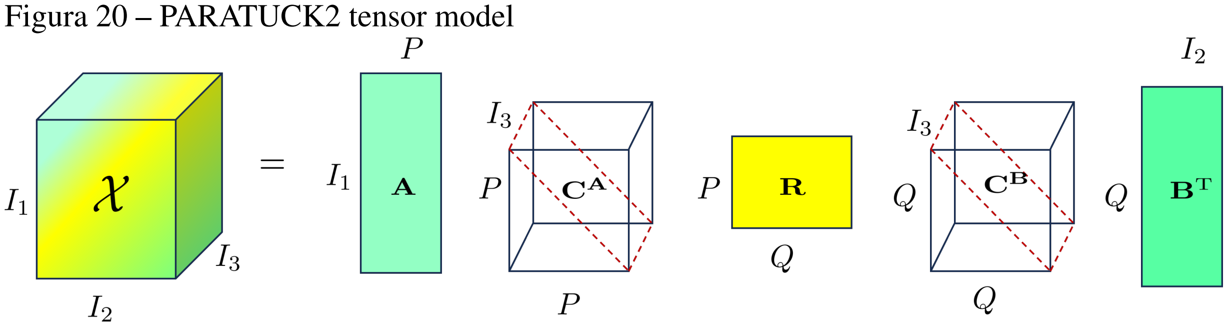

PARATUCK2 Uniqueness

While the PARAFAC and Tucker models have limitations, the PARATUCK2 is more suitable for complex scenarios where the powerful uniqueness properties of PARAFAC decomposition and the flexibility of the Tucker decomposition are required. Unlike the PARAFAC decomposition, the PARATUCK2 decomposition does not have a well-defined uniqueness condition. The work (Harshman; Lundy, 1996) provides some initial insights into this issue, exploring the scenario where $P = Q$. A more detailed study and conditions to ensure the uniqueness of the PARATUCK2 decomposition are provided in (Favier *et al.*, 2012b), (Almeida *et al.*, 2009) and (Favier; Almeida, 2014a).

3.7.2 PARATUCK(2-4)

A generalized PARATUCK2 approach for tensors has been proposed in (Almeida *et al.*, 2013), also called PARATUCK-(2,4) tensor decomposition. Its scalar form is given by:

$$x_{i_1 i_2 i_3 i_4} = \sum_{p=1}^{P} \sum_{q=1}^{Q} a_{i_1 p} b_{i_2 q} c^{\mathbf{A}}_{i_3 p} c^{\mathbf{B}}_{i_3 q} r_{pqi_4} \,, \tag{3.32}$$

and its frontal slice is obtained by staying fixed in the indices (i_1, i_4).

$$[\mathscr{X}]_{..i_3 i_4} = \mathbf{A} D_{i_3}(\mathbf{C}^{\mathbf{A}}) \mathbf{R}_{..i_4} D_{i_3}(\mathbf{C}^{\mathbf{B}}) \mathbf{B}^{\mathrm{T}} \,, \tag{3.33}$$

where $\mathbf{R}_{..\mathbf{i_4}}$ is the i_4th frontal slice of the tensor $\mathscr{R} \in \mathbb{C}^{P \times Q \times I_4}$. By comparing (3.32) with (3.30) the PARATUCK-(2,4) reduces to the PARATUCK-2 (also referred to as PARATUCK-(2,3) (Favier; Almeida, 2014b)) if $I_4 = 1$, i.e., when the core tensor $\mathscr{R} \in \mathbb{C}^{P \times Q \times I_4}$ simplifies to a core matrix $\mathbf{R} \in \mathbb{C}^{P \times Q}$.

3.7.3 Generalized PARATUCK-$(N1, N)$

Introduced by (Harshman; Lundy, 1996), the third-order PARATUCK2 decomposition was generalized by (Favier *et al.*, 2012b) to an N-order PARATUCK decomposition, which is referred to as PARATUCK-(N_1, N). The scalar form for an arbitrary tensor $\mathscr{X} \in \mathbb{C}^{I_1 \times I_2 \times \cdots \times I_N}$ that fits a N-order PARATUCK model is

$$x_{i_1,\ldots,i_{N_1},\ldots,i_N} = \sum_{r_1=1}^{R_1} \cdots \sum_{r_{N_1}=1}^{R_{N_1}} c_{r_1,\ldots,r_{N_1}, i_{N_1+2},\ldots,i_{N_1}} \prod_{n=1}^{N_1} a^{(n)}_{i_n, r_n} \phi_{r_n, i^{(n)}_{N_1+1}} \,, \tag{3.34}$$

where $a^{(n)}_{i_n, r_n}$ and $\phi_{r_n, i^{(n)}_{N_1+1}}$ are the entries of the factor and weighting matrices $\mathbf{A}^{(n)} \in \mathbb{C}^{I_n \times R_n}$ and $\Phi^{(n)} \in \mathbb{C}^{R_n \times I_{N_1+1}}$, respectively. Note that if $N_1 = 2$ and $N = 3$, equation (3.34) reduces to the well known third-order PARATUCK2 decomposition, which can also be called PARATUCK-(2,3), as in 3.7.1. On the other hand, when $N_1 = 2$ and $N = 4$, it reduces to the fourth-order PARATUCK-(2,4) tensor decomposition as in Section 3.7.2.

3.8 Algorithms

Typically, the factor matrices in the PARAFAC and PARATUCK decompositions are estimated using the ALS algorithm. However, in some cases, a closed-form solution may be possible. In this section, we focus on the presentation of the ALS algorithm for both tensor decompositions since it is the most popular and intuitive solution to compute their associated factors.

3.8.1 ALS-PARAFAC

The ALS algorithm is a well-known solution to estimate the factor matrices of a PARAFAC model. Considering the third-order case, this algorithm consists of finding estimates of the factor matrices **A**, **B** and **C** that minimize the following cost function

$$f(\mathbf{A},\mathbf{B},\mathbf{C}) = \left\| \mathscr{X} - \sum_{r=1}^{R} \mathbf{a}_r \circ \mathbf{b}_r \circ \mathbf{c}_r \right\|_F^2 . \tag{3.35}$$

To solve (3.35), we resort to the matrix unfoldings in (3.20) and formulate the following minimization problems as three conditional LS problems, as follows:

$$\begin{aligned} &\min_{\mathbf{A}} \left\| [\mathscr{X}]_{(1)} - \mathbf{A}\,(\mathbf{C} \diamond \mathbf{B})^{\mathrm{T}} \right\|_F^2 \\ &\min_{\mathbf{B}} \left\| [\mathscr{X}]_{(2)} - \mathbf{B}\,(\mathbf{C} \diamond \mathbf{A})^{\mathrm{T}} \right\|_F^2 \\ &\min_{\mathbf{C}} \left\| [\mathscr{X}]_{(3)} - \mathbf{C}\,(\mathbf{B} \diamond \mathbf{A})^{\mathrm{T}} \right\|_F^2, \end{aligned} \tag{3.36}$$

the solutions of which are respectively given by

$$\begin{aligned} \hat{\mathbf{A}} &= [\mathscr{X}]_{(1)} \left[(\mathbf{C} \diamond \mathbf{B})^{\mathrm{T}} \right]^{\dagger} \\ \hat{\mathbf{B}} &= [\mathscr{X}]_{(2)} \left[(\mathbf{C} \diamond \mathbf{A})^{\mathrm{T}} \right]^{\dagger} \\ \hat{\mathbf{C}} &= [\mathscr{X}]_{(3)} \left[(\mathbf{B} \diamond \mathbf{A})^{\mathrm{T}} \right]^{\dagger}. \end{aligned} \tag{3.37}$$

An ALS algorithm can be formulated to estimate the factor matrices from the LS solution present in (3.37). This estimation process is summarized in Algorithm 1. The convergence of the

ALS-PARAFAC algorithm is declared if $\|e(i)-e(i-1)\| \leq \delta$, where δ is a threshold and $e(i)$ denotes the error at the end of the ith iteration, which can be computed as

$$e(i) = \left\| [\mathscr{X}]_{(1)} - \hat{\mathbf{A}}_{(i)} \left(\hat{\mathbf{C}}_{(i)} \diamond \hat{\mathbf{B}}_{(i)} \right)^{\mathrm{T}} \right\|_F^2 . \tag{3.38}$$

Algoritmo 1: ALS-PARAFAC

Procedure
input : $i = 0$; *Initialize* $\hat{\mathbf{B}}_{(i-1)}$ and $\hat{\mathbf{C}}_{(i-1)}$
output : $\hat{\mathbf{A}}$, $\hat{\mathbf{B}}$ and $\hat{\mathbf{C}}$
begin
    $i = i + 1$;
    while $\|e(i) - e(i-1)\| \geq \delta$ **do**
        1: From $[\mathscr{X}]_{(1)}$, and using $\hat{\mathbf{B}}_{(i-1)}$ and $\hat{\mathbf{C}}_{(i-1)}$, estimate $\mathbf{A}$
        solving the following LS problem: $\min_{\mathbf{A}} \left\| [\mathscr{X}]_{(1)} - \mathbf{A} (\mathbf{C} \diamond \mathbf{B})^{\mathrm{T}} \right\|_F^2$
        the solution of which is given by

$$\hat{\mathbf{A}}_{(i)} = [\mathscr{X}]_{(1)} \left[\left(\hat{\mathbf{C}}_{(i-1)} \diamond \hat{\mathbf{B}}_{(i-1)} \right)^{\mathrm{T}} \right]^{\dagger}$$

        2: From $[\mathscr{X}]_{(2)}$, and using $\hat{\mathbf{A}}_{(i)}$ and $\hat{\mathbf{C}}_{(i-1)}$, estimate $\mathbf{B}$
        solving the following LS problem: $\min_{\mathbf{B}} \left\| [\mathscr{X}]_{(2)} - \mathbf{B} (\mathbf{C} \diamond \mathbf{A})^{\mathrm{T}} \right\|_F^2$
        the solution of which is given by

$$\hat{\mathbf{B}}_{(i)} = [\mathscr{X}]_{(2)} \left[\left(\hat{\mathbf{C}}_{(i-1)} \diamond \hat{\mathbf{A}}_{(i)} \right)^{\mathrm{T}} \right]^{\dagger}$$

        3: From $[\mathscr{X}]_{(3)}$, and using $\hat{\mathbf{A}}_{(i)}$ and $\hat{\mathbf{B}}_{(i)}$, estimate $\mathbf{C}$
        solving the following LS problem: $\min_{\mathbf{C}} \left\| [\mathscr{X}]_{(3)} - \mathbf{C} (\mathbf{B} \diamond \mathbf{A})^{\mathrm{T}} \right\|_F^2$
        the solution of which is given by

$$\hat{\mathbf{C}}_{(i)} = [\mathscr{X}]_{(3)} \left[\left(\hat{\mathbf{B}}_{(i)} \diamond \hat{\mathbf{A}}_{(i)} \right)^{\mathrm{T}} \right]^{\dagger}$$

        4: *Repeat steps* 1 to 3 *until convergence.*
        end
    end
    end
end

3.8.2 ALS-PARATUCK

As for the PARAFAC case, an iterative alternating estimation scheme can also be derived for the PARATUCK2 decomposition. In the following, we describe the ALS-PARATUCK algorithm that was originally presented in (Bro, 1998). Considering the frontal slice in (3.31), the cost function to be optimized is given by

$$
\begin{aligned}
& f(\mathbf{A}, D_{i_3}(\mathbf{C}^{\mathbf{A}}), \mathbf{R}, D_{i_3}(\mathbf{C}^{\mathbf{B}}), \mathbf{B}) \\
&= \min_{\mathbf{A}, D_{i_3}(\mathbf{C}^{\mathbf{A}}), \mathbf{R}, D_{i_3}(\mathbf{C}^{\mathbf{B}}), \mathbf{B}} \sum_{i_3}^{I_3} \left\| [\mathscr{X}]_{..i_3} - \mathbf{A} D_{i_3}(\mathbf{C}^{\mathbf{A}}) \mathbf{R} D_{i_3}(\mathbf{C}^{\mathbf{B}}) \mathbf{B}^{\mathrm{T}} \right\|_F^2 .
\end{aligned} \tag{3.39}
$$

To estimate $\mathbf{A}$ conditioned on the knowledge of the other factor matrices, we make use of the frontal slices in (3.31) by defining

$$
\mathbf{X} = \begin{bmatrix} [\mathscr{X}]_{..1}^{\mathrm{T}} \\ \vdots \\ [\mathscr{X}]_{..I_3}^{\mathrm{T}} \end{bmatrix} = \begin{bmatrix} \mathbf{B} D_1(\mathbf{C}^{\mathbf{B}}) \mathbf{R}^{\mathrm{T}} D_1(\mathbf{C}^{\mathbf{A}}) \\ \vdots \\ \mathbf{B} D_{I_3}(\mathbf{C}^{\mathbf{B}}) \mathbf{R}^{\mathrm{T}} D_{I_3}(\mathbf{C}^{\mathbf{A}}) \end{bmatrix} \mathbf{A}^{\mathrm{T}} \in \mathbb{C}^{I_2 I_3 \times I_1} . \tag{3.40}
$$

The solution for $\mathbf{A}$ in the LS sense is then given by

$$
\hat{\mathbf{A}}^{\mathrm{T}} = \begin{bmatrix} \mathbf{B} D_1(\mathbf{C}^{\mathbf{B}}) \mathbf{R}^{\mathrm{T}} D_1(\mathbf{C}^{\mathbf{A}}) \\ \vdots \\ \mathbf{B} D_{I_3}(\mathbf{C}^{\mathbf{B}}) \mathbf{R}^{\mathrm{T}} D_{I_3}(\mathbf{C}^{\mathbf{A}}) \end{bmatrix}^{\dagger} \mathbf{X} \tag{3.41}
$$

The estimation of $\mathbf{B}$ follows a similar procedure. Defining

$$
\overline{\mathbf{X}} = \begin{bmatrix} [\mathscr{X}]_{..1} \\ \vdots \\ [\mathscr{X}]_{..I_3} \end{bmatrix} = \begin{bmatrix} \mathbf{A} D_1(\mathbf{C}^{\mathbf{A}}) \mathbf{R} D_1(\mathbf{C}^{\mathbf{B}}) \\ \vdots \\ \mathbf{A} D_{I_3}(\mathbf{C}^{\mathbf{A}}) \mathbf{R} D_{I_3}(\mathbf{C}^{\mathbf{B}}) \end{bmatrix} \mathbf{B}^{\mathrm{T}} \in \mathbb{C}^{I_1 I_3 \times I_2} , \tag{3.42}
$$

an estimate of $\mathbf{B}$ in the LS sense can be obtained as

$$
\hat{\mathbf{B}}^{\mathrm{T}} = \begin{bmatrix} \mathbf{A} D_1(\mathbf{C}^{\mathbf{A}}) \mathbf{R} D_1(\mathbf{C}^{\mathbf{B}}) \\ \vdots \\ \mathbf{A} D_{I_3}(\mathbf{C}^{\mathbf{A}}) \mathbf{R} D_{I_3}(\mathbf{C}^{\mathbf{B}}) \end{bmatrix}^{\dagger} \overline{\mathbf{X}} . \tag{3.43}
$$

By applying the $\mathrm{vec}(\cdot)$ operator to (3.31), we obtain

$$
\begin{aligned}
\mathrm{vec}([\mathscr{X}]_{..i_3}) &= \mathrm{vec}(\mathbf{A} D_{i_3}(\mathbf{C}^{\mathbf{A}}) \mathbf{R} D_{i_3}(\mathbf{C}^{\mathbf{B}}) \mathbf{B}^{\mathrm{T}}) \\
&= \Big(\mathbf{B} D_{i_3}(\mathbf{C}^{\mathbf{B}}) \otimes \mathbf{A} D_{i_3}(\mathbf{C}^{\mathbf{A}}) \Big) vec(\mathbf{R}) \, , i_3 = 1, \ldots, I_3 .
\end{aligned} \tag{3.44}
$$

Stacking (3.44) we have

$$
\underbrace{\begin{bmatrix} \mathrm{vec}([\mathscr{X}]_{..1}) \\ \vdots \\ \mathrm{vec}([\mathscr{X}]_{..I_3}) \end{bmatrix}}_{\mathbf{x}} = \underbrace{\begin{bmatrix} (\mathbf{B} D_1(\mathbf{C}^{\mathbf{B}}) \otimes \mathbf{A} D_1(\mathbf{C}^{\mathbf{A}})) \\ \vdots \\ (\mathbf{B} D_{I_3}(\mathbf{C}^{\mathbf{B}}) \otimes \mathbf{A} D_{I_3}(\mathbf{C}^{\mathbf{A}})) \end{bmatrix}}_{\mathbf{Z} \in \mathbb{C}^{I_1 I_2 I_3 \times PQ}} vec(\mathbf{R}) \in \mathbb{C}^{I_1 I_2 I_3 \times 1} , \tag{3.45}
$$

or, equivalently,

$$\mathrm{vec}(\hat{\mathbf{R}}) = \mathbf{Z}^{\dagger}\mathbf{x}\,. \tag{3.46}$$

From this equation, the estimated matrix $\hat{\mathbf{R}}$ is obtained from a simple reshaping operation.

The estimation process for $\mathbf{C}^{\mathbf{A}}$ and $\mathbf{C}^{\mathbf{B}}$ is done row by row. To estimate the i_3th row of $\mathbf{C}^{\mathbf{A}}$, we first define

$$[\mathscr{X}]_{..i_3} = \mathbf{A}D_{i_3}(\mathbf{C}^{\mathbf{A}})\mathbf{F}_{i_3}^{\mathrm{T}}\,, \tag{3.47}$$

where $\mathbf{F}_{i_3} = \mathbf{B}D_{i_3}(\mathbf{C}^{\mathbf{B}})\mathbf{R}^{\mathrm{T}}$. Using the vec$(\cdot)$ operator and applying the property (6) to (3.47) we obtain

$$\begin{aligned} &\mathrm{vec}([\mathscr{X}]_{..i_3}) = (\mathbf{F}_{i_3} \diamond \mathbf{A})(\mathbf{C}^{\mathbf{A}}_{i_3.})^{\mathrm{T}} \\ &\quad \rightarrow (\hat{\mathbf{C}}^{\mathbf{A}}_{i_3.})^{\mathrm{T}} = (\mathbf{F}_{i_3} \diamond \mathbf{A})^{\dagger}\mathrm{vec}([\mathscr{X}]_{..i_3})\,, i_3 = 1, \ldots, I_3. \end{aligned} \tag{3.48}$$

To estimate the i_3th row of $\mathbf{C}^{\mathbf{B}}$, we define

$$[\mathscr{X}]_{..i_3} = \overline{\mathbf{F}}_{i_3}D_{i_3}(\mathbf{C}^{\mathbf{B}})\mathbf{B}^{\mathrm{T}}\,. \tag{3.49}$$

where $\overline{\mathbf{F}}_{i_3} = \mathbf{A}D_{i_3}(\mathbf{C}^{\mathbf{A}})\mathbf{R}$. Likewise, vectorizing (3.49) yields

$$\begin{aligned} &\mathrm{vec}([\mathscr{X}]_{..i_3}) = (\mathbf{B} \diamond \overline{\mathbf{F}}_{i_3})(\mathbf{C}^{\mathbf{B}}_{i_3.})^{\mathrm{T}} \\ &\quad \rightarrow (\hat{\mathbf{C}}^{\mathbf{B}}_{i_3.})^{\mathrm{T}} = (\mathbf{B} \diamond \overline{\mathbf{F}}_{i_3})^{\dagger}\mathrm{vec}([\mathscr{X}]_{..i_3})\,, i_3 = 1, \ldots, I_3. \end{aligned} \tag{3.50}$$

For a better understanding of the alternating least square (ALS)-PARATUCK2 we summarize the steps of the algorithm. The convergence criterion is the same as that of the ALS-PARAFAC algorithm. The error at ith iteration can be calculated as:

$$e(i) = \sum_{i_3=1}^{I_3} \left\| [\mathscr{X}]_{..i_3} - \hat{\mathbf{A}}_{(i)}D_{i_3}(\hat{\mathbf{C}}^{\mathbf{A}}_{(i)})\hat{\mathbf{R}}_{(i)}D_{i_3}(\hat{\mathbf{C}}^{\mathbf{B}}_{(i)})\hat{\mathbf{B}}^{\mathrm{T}}_{(i)} \right\|_F^2\,. \tag{3.51}$$

3.9 Tensor decompositions in wireless communications

As mentioned earlier in this chapter, tensor decompositions have first encountered applications in the chemometrics and psychometrics fields. Over the past two decades, it has been successfully applied in different knowledge areas. This section presents a discussion of the tensor decompositions applied to wireless communications[3].

[3] Our discussion and referencing focus on the journal papers since they bring more details and, in general, cover shorter conference versions.

Algoritmo 2: ALS-PARATUCK2

Procedure

input : $i = 0$; *Initialize* $\hat{\mathbf{B}}_{(i=0)}$, $\hat{\mathbf{R}}_{(i=0)}$, $\hat{\mathbf{C}}^{\mathbf{A}}_{(i=0)}$ and $\hat{\mathbf{C}}^{\mathbf{B}}_{(i=0)}$

output : $\hat{\mathbf{A}}$, $\hat{\mathbf{B}}_{(i=0)}$, $\hat{\mathbf{R}}_{(i=0)}$, $\hat{\mathbf{C}}^{\mathbf{A}}_{(i=0)}$ and $\hat{\mathbf{C}}^{\mathbf{B}}_{(i=0)}$

begin

$i = i + 1$;

while $\|e(i) - e(i-1)\| \geq \delta$ **do**

1. Using $\mathbf{C}^{\mathbf{A}}_{(i-1)}$, $\hat{\mathbf{R}}_{(i-1)}$, $\mathbf{C}^{\mathbf{B}}_{(i-1)}$ and $\hat{\mathbf{B}}_{(i-1)}$, find an LS estimate of $\mathbf{A}$ from equation (3.41)
2. Using $\mathbf{C}^{\mathbf{A}}_{(i-1)}$, $\hat{\mathbf{R}}_{(i-1)}$, $\mathbf{C}^{\mathbf{B}}_{(i-1)}$ and $\hat{\mathbf{A}}_{(i)}$, find an LS estimate of $\mathbf{B}$ from equation (3.43)
3. Using $\hat{\mathbf{B}}_{(i)}$, $\hat{\mathbf{A}}_{(i)}$, $\hat{\mathbf{C}}^{\mathbf{A}}_{(i-1)}$ and $\hat{\mathbf{C}}^{\mathbf{B}}_{(i-1)}$, find an LS estimate of $\mathbf{R}$ from equation (3.46);
4. From $\hat{\mathbf{B}}_{(i)}$, $\hat{\mathbf{R}}_{(i)}$, $\hat{\mathbf{A}}_{(i)}$, and $\hat{\mathbf{C}}^{\mathbf{B}}_{(i-1)}$, find an LS estimate of $\mathbf{C}^{\mathbf{A}}$ from equation (3.48);
5. From $\hat{\mathbf{B}}_{(i)}$, $\hat{\mathbf{R}}_{(i)}$, $\hat{\mathbf{A}}_{(i)}$, and $\hat{\mathbf{C}}^{\mathbf{A}}_{(i)}$, find an LS estimate of $\mathbf{C}^{\mathbf{B}}$ from equation (3.50);
6. Repeat steps 1 to 5 until the convergence.

end

end

end

end

3.9.1 SIMO and MIMO CDMA-based systems

The history of tensor decomposition for wireless communication started in Sidiropoulos in (Sidiropoulos *et al.*, 2000). In a seminal paper, Sidiropoulos established a link between blind direct-sequence code-division multiple access (DS-CDMA) multiuser detection and PARAFAC. The authors consider a CDMA system in a multiuser scenario such that the receiver signal is $\mathbf{A}D_P(\mathbf{H})\mathbf{S}$, (see eq. (2) in (Sidiropoulos *et al.*, 2000)) where $\mathbf{A} \in \mathbb{C}^{K\times M}$ is the compound flat fading/array response pattern, $\mathbf{H} \in \mathbb{C}^{P\times M}$ is the spreading code matrix, and $\mathbf{S} \in \mathbb{C}^{M\times N}$ is the information signal matrix. The dimensions P, M, and N denote the spreading gain, the number of antennas, and the number of symbols, respectively. From this, it was possible to note that the receiver signal can be seen as a third-order tensor that fits a PARAFAC model, whose dimensions are $K \times M \times N$ that represent three different kinds of diversity, which are spatial diversity (M), temporal diversity (N) and spreading diversity (P). This concept is illustrated in Figure 21. Later, some generalizations were proposed in (Sidiropoulos; Dimic, 2001; Lathauwer; Castaing, 2007; Almeida *et al.*, 2007) still considering a single antenna transmission but assuming more general channel models including multipath and frequency selectivity. In particular, (Almeida *et al.*,

2007) showed how the wireless channel structure impacts the tensor model structure, demonstrating unified modeling of three different multi-antenna wireless communications systems using a constrained block-PARAFAC modeling approach. The work also designed blind receivers for oversampling, direct-sequence, and multicarrier modulation scenarios. Generalization to multi-antenna transmission systems were proposed in a sequence of later papers (Sidiropoulos; Budampati, 2002; Almeida *et al.*, 2008; Almeida *et al.*, 2008b; Almeida *et al.*, 2008a). The works (Almeida *et al.*, 2008; Almeida *et al.*, 2008b; Almeida *et al.*, 2008a) provided generalizations of pure CDMA-based transmissions to the multiple-antenna case, by including space-time spreading based on constrained PARAFAC models by incorporating more space-time transmission schemes. In particular, (Almeida *et al.*, 2008a) formulated a new tensor decomposition called constrained factor (CONFAC), showing that building constraints into the structure of the tensor is instrumental in deriving flexible MIMO signaling schemes with different levels of spatial multiplexing and spreading. The paper demonstrated insightful practical examples and transmit signal designs to ensure channel and data identifiability.

Figura 21 – Illustration of the relationship communication problems with the multidimensional array structure.

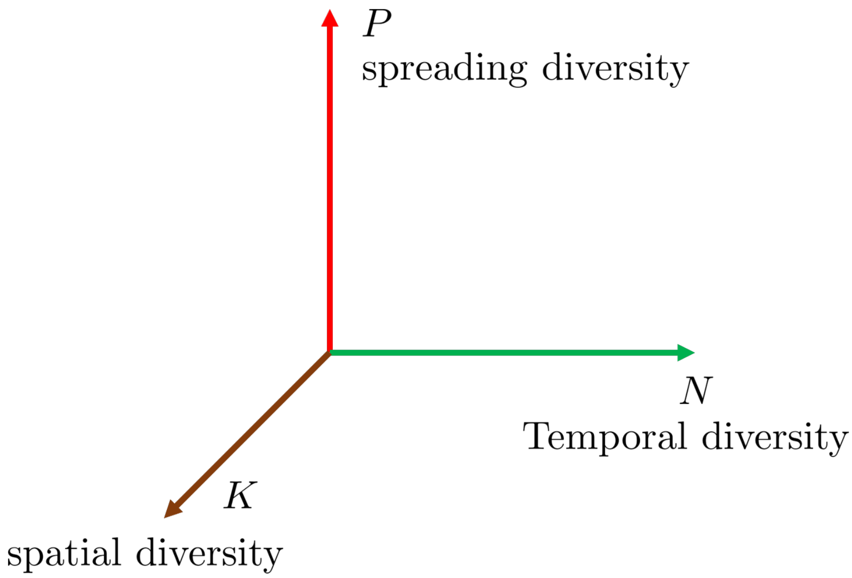

Fonte: Created by author inspired in Sidiropoulos at al. (Sidiropoulos *et al.*, 2000)

3.9.2 Space-time and space-time-frequency MIMO transceivers

As research efforts on wireless communication systems intensified towards the fourth generation, another category of tensor decomposition-based works exploits the tensor structures to explicitly synthesize space-time-frequency coding schemes with built-in blind/semi-blind decoding properties. Several studies evidenced various forms of efficiently exploiting space-time-frequency diversities and proposed efficient receivers based on tensor modeling. Some notable works in this field include (Sidiropoulos; Budampati, 2002; Favier *et al.*, 2012b; Favier; Almeida, 2014b; Almeida *et al.*, 2009; Almeida *et al.*, 2013; Araújo; Almeida, 2017; Almeida; Favier, 2013). In (Sidiropoulos; Budampati, 2002), a new class of space-time codes is proposed, which are linear block codes based on the Khatri-Rao product. The PARAFAC model is utilized in this work to provide built-in blind channel and symbol estimation at the receiver. The work (Almeida *et al.*, 2009) proposed a transceiver model based on a PARATUCK2 decomposition used to model space-time multiplexing-spreading architecture that enables blind channel and symbol estimation at the receiver. In (Araújo; Almeida, 2017), the authors proposed a semi-blind tensor-based receiver relying on the PARATUCK-(2,4) model, which exploits orthogonal space-time coding using a structured PARAFAC model that captures the space time block code (STBC) structure. This study designed the received signal as a fourth-order PARATUCK-(2,4) tensor model and recast it as a PARAFAC model. The channel is then estimated using a simple Kronecker factorization problem, and the resulting estimation is used to decode the symbols linearly.

Later in (Favier *et al.*, 2012b), the authors generalized the well-known PARATUCK2 model towards higher orders. Therein referred to as the PARATUCK-(N_1, N) decomposition. In that work, a special case of this decomposition, called PARATUCK-(2,4), was proposed to allow the spreading and multiplexing of the transmitted symbols in both space (transmit antennas) and time (chips and blocks) domains. By assuming more general MIMO-OFDM-CDMA systems, the works (Almeida; Favier, 2013; Almeida *et al.*, 2013; Favier; Almeida, 2014b) derived new constrained tensor models for the design of MIMO wireless communication systems combining space- and frequency-domain spreadings and/or followed by a space–frequency multiplexing. In (Favier; Almeida, 2014b), a tensor space-time-frequency (STF) coding model based on a fifth-order tensor PARATUCK-(2,5) model was proposed for MIMO-OFDM-CDMA systems. The authors showed how this tensor STF coding model generalizes schemes previously reported in the literature. A semi-blind receiver was also derived. The works (Almeida *et al.*, 2013) and (Almeida; Favier, 2013) resort to a fourth-order PARATUCK model that captures space-time-frequency spreading-multiplexing domains. More recently, (Sokal *et al.*, 2021) tackled a more challenging MIMO-OFDM setup that includes phase noise perturbations at both the transmitter and the receiver, and derived a PARAFAC-based solution for joint channel, symbol, and phase noise estimation. The receiver is divided into two stages where the first uses an iterative and closed-formed algorithm to estimate the channel and phase noise. In the second stage, the selective Kronecker product operator is used to leverage a PARATUCK2 model for the receiver signal at the subcarrier, and a zero-forcing (ZF) method is applied to estimate the data symbols.

3.9.3 Relaying and cooperative MIMO systems

The relay-assisted MIMO system introduced new challenges for wireless communication systems particularly related the channel estimation and symbol detection. Assuming that the communication between two network nodes (for example, a BS and a UT) is assisted by relays, the end-to-end communication can be divided into multiple wireless links, as illustrated in Figure 22. This figure considers a dual-hop single-relay case. In this simple relaying scenario, one can note the different wireless communication links, involving BS-UT, BS-RE, and RE-UT. Even in this simple MIMO relaying setup, channel estimation involves estimating three channel matrices at the receiver and/or at the relay. Starting from this setup and its generalizations (multiple relays, three-hop, and multi-hop cases), tensor decompositions where largely applied to solve the channel estimation and the joint channel-symbol estimation problems (Fernandes *et al.*, 2012; Ximenes *et al.*, 2014; Ximenes *et al.*, 2015; Cavalcante *et al.*, 2015; Favier *et al.*, 2016; Freitas *et al.*, 2018; Du *et al.*, 2020a; Sokal *et al.*, 2020; Han *et al.*, 2021b; Han *et al.*, 2021a; Du *et al.*, 2022; Pinho *et al.*, 2023). Most of these works relies on PARAFAC, PARATUCK, or a combination of both tensor decompositions as in (Ximenes *et al.*, 2014; Sokal *et al.*, 2020).

The work (Ximenes *et al.*, 2015) proposed a semi-blind receiver for MIMO relay-assisted communications capitalizing on a nested PARAFAC model. Different from (Ximenes *et al.*, 2014), the direct link is not available. Two-hop MIMO relaying communications exploiting tensor modeling with Khatri-Rao space-time coding schemes was also addressed in (Han *et al.*, 2021b; Sokal *et al.*, 2020; Pinho *et al.*, 2023). The authors of (Sokal *et al.*, 2020) derive a PARAFAC receiver, while the method of (Han *et al.*, 2021b) formulated a PARATUCK2-based receiver. Still exploiting the space-time diversity in MIMO relaying systems, (Favier *et al.*, 2016) proposed a transmission scheme in two stages where, in the first stage, a coded tensor of information is sent to relay. The relay encodes the receiver signal again and sends it to the destination. As a result, the receiver signal at the destination fits a nested Tucker model, which can be viewed as a generalization of the nested PARAFAC model that shows to be useful when the transmitter and/or relay applies tensor coding.

Figura 22 – Illustration of a two-hop relay assisted MIMO system

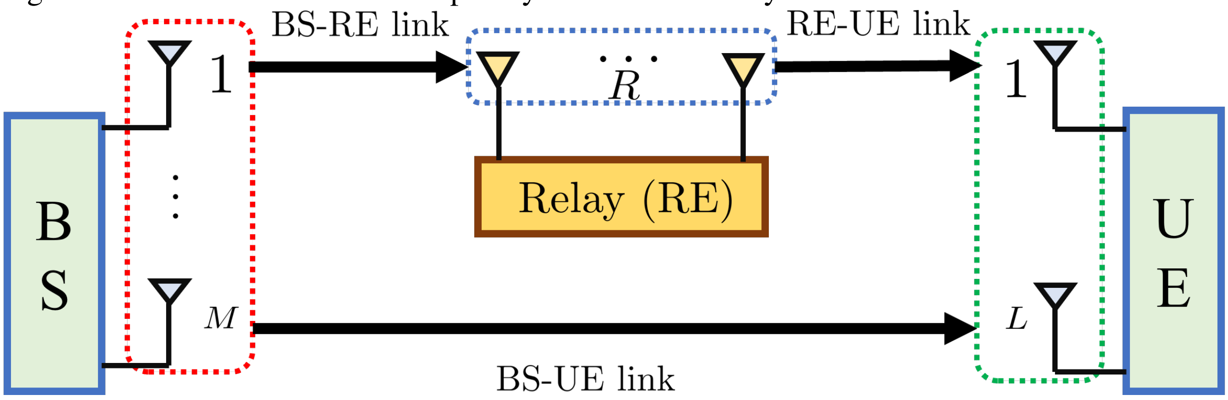

3.9.4 MmWave communication systems

Tensor decompositions were also exploited more recently in the context of mmWave communications, assuming hybrid analog-digital architectures. The work (Zilli; Zhu, 2021) proposes a novel two-stage joint hybrid precoder and combiner design for maximizing the average achievable sum rate of frequency-selective millimeter-wave massive MIMO-OFDM systems, where the analog precoder and combiner are designed as a constrained Tucker2 tensor decomposition problem that seeks to maximize the effective baseband gains over every subcarrier while suppressing inter-user and intra-user interferences. The authors of (Zhang *et al.*, 2022) addressed the challenge of channel state information acquisition in wideband millimeter-wave massive MIMO systems in high-mobility scenarios with Doppler shifts. Exploiting the channel sparsity, the frequency-domain received signal is modeled as a third-order PARAFAC tensor model that is exploited to estimate the channel.

The work (Araújo *et al.*, 2019b) combines tensor decompositions and compressive sensing to formulate a sparse channel estimation method for massive MIMO-OFDM systems. It introduced a tensor-based minimum mean square error (MMSE) channel estimator and a tensor-compressive sensing (tensor-CS), estimator that exploits the three-dimensional sparse nature of frequency-selective massive MIMO channels. Therein, a sparse Tucker3 tensor representation is utilized to derive a tensor-CS algorithm that offers a good tradeoff between computational complexity and performance. Adopting a similar approach, the paper (Du *et al.*, 2021) developed a tensor-based joint channel parameter estimation and symbol detection scheme for mmWave massive MIMO communication systems. This scheme utilizes a nested parallel factor (PARAFAC) model, considering time-varying mmWave massive MIMO channels. The proposed method leverages a fourth-order tensor structure to achieve accurate channel state information (CSI) without resorting to pilot-assisted estimation.

3.10 Intelligent reflecting surfaces

The brief historical review presented so far on the use of tensor decompositions in wireless communications showed that tensors have been present at every moment in the evolution of technological generations, at least since the 2000s. As mentioned in the introductory chapter of this thesis, research efforts on the evolution of current technologies towards 6G are ongoing. In this context, IRS is one of the promising technologies to be adopted in future wireless communication systems. Tensors was recently exploited to solve different problems arising in IRS-assisted communications, including channel estimation, active/passive beamforming design, and feedback control signaling. In Figure 23, we highlight these main problems/topics where tensor modeling was applied in IRS-assisted wireless communication systems.

Figura 23 – Illustration of different fronts that tensor modeling can be introduced into IRS technology.

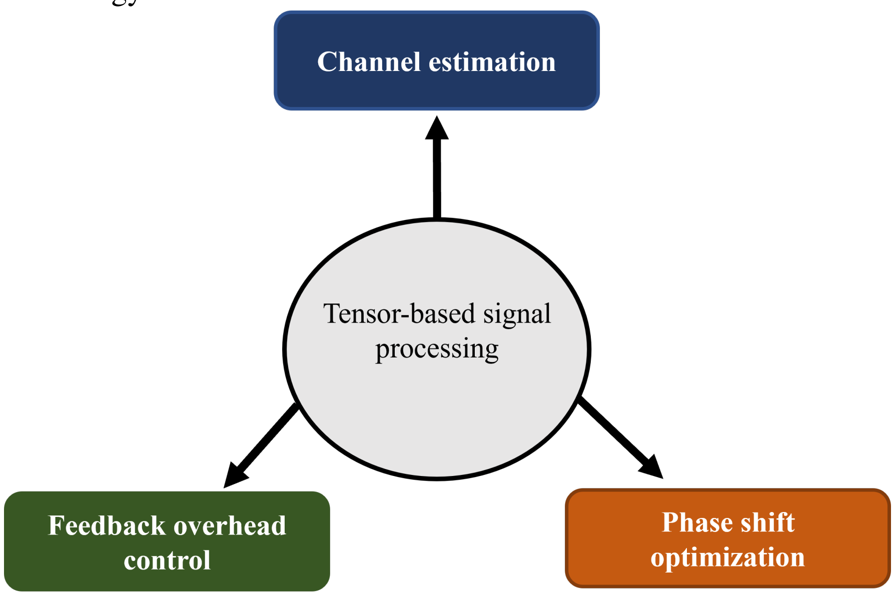

Phase shift optimization: The work (Ribeiro *et al.*, 2023) proposed innovative methods for beamforming in intelligent reflecting surface (IRS)-assisted MIMO systems. It introduced a low-complexity approach to optimize joint active and passive beamforming by exploiting the geometrical structure of propagation channels. The proposed solutions, leveraging the Kronecker product structure of channel matrices, were shown to significantly reduce the computational complexity of the beamforming design while maintaining spectral efficiency. The key contributions include two closed-form methods based on second-order and higher-order singular value decomposition (SVD)-based algorithms.

Feedback overhead control: The work (Sokal *et al.*, 2023) presented an interesting method to manage the control overhead in intelligent reconfigurable surfaces (IRS). This approach involves representing the (tensorized version of the) IRS phase shift vector as a low-rank tensor model, significantly reducing feedback requirements between the base station and the IRS controller. The paper formulated both a PARAFAC- and a Tucker-based model for the IRS phase shift tensor and discussed the tradeoffs of these models to reduce/control the feedback overhead with minimal spectral efficiency loss, particularly for line-of-sight dominant scenarios.

Channel estimation: It is known that the promised gains of IRS depend on the accuracy of channel state information. In this sense, recent studies, including those of this thesis, proposed solutions to the channel estimation problem in IRS-assisted communications based on tensor modeling approaches. In the recent work (Benício *et al.*, 2023), the authors introduced a novel tensor-based approach that significantly enhances the performance of IRS-assisted MIMO systems. The work presents a two-stage framework for channel estimation and data tracking in IRS-assisted MIMO systems. The first stage combines a constrained ALS-PARAFAC algorithm with the Khatri-Rao and Kronecker factorization methods to estimate the static channel parameters. The second stage estimates block-varying channel fading coefficients and the transmitted symbols using a Tucker-based tracking algorithm.

The recent work (Gomes *et al.*, 2023) developed channel estimation schemes for IRS-MIMO systems considering hardware imperfections affecting the IRS phase shifts. The key contributions are two sets of tensor-based algorithms that rely on the PARAFAC decomposition. These include an iterative alternating least squares (ALS)-based algorithm for long-term imperfection models, where IRS imperfections are static within the channel coherence time, and another set for short-term imperfection models, where IRS amplitude and phase imperfections are dynamic. The work (Zheng *et al.*, 2022) offered an approach to IRS-assisted mmWave systems for channel estimation through a tensor-based framework. It targets downlink channel estimation for IRS-aided mmWave OFDM systems exploiting channel sparsity using a low-rank third-order tensor modeling. In particular, therein the authors formulate a structured CPD-based method for estimating the channel parameters.

The above discussion corroborates the widespread use of tensor modeling to provide solutions to IRS-assisted communication systems. It is worth noting that conventional matrix-based methods offer many solutions to channel/data estimation problems. However, leveraging the powerful uniqueness properties of tensor decompositions, the use of tensor-based methods can be exploited to solve these problems under more relaxed, or less restrictive, parameter settings and assumptions, compared to matrix-based methods (Lathauwer, 1997; Cichocki *et al.*, 2015). In addition, tensor-based methods efficiently exploit the multiple signal diversity for performance improvement (Sidiropoulos *et al.*, 2017). However, there are situations where traditional matrix-based solutions are insufficient. Specifically, when the problem involves estimating factor matrices in a fully blind manner, such as in chapter 4 where the IRS phase shift matrix is unknown at the receiver due to hardware impairments. In this challenging scenario, conventional matrix-based signal processing cannot be used to estimate the involved channels and the phase shift matrix at the same time due to the lack of uniqueness. In the rest of this thesis, we concentrate on the use of tensor modeling for IRS-assisted MIMO systems by presenting the contributions developed in this work, namely, methods and algorithms for channel estimation as well as joint channel and symbol estimation in IRS-assisted wireless MIMO systems.

3.11 Summary

This chapter provides a concise overview of tensor algebra and tensor decompositions. We explain the main definitions and properties, focusing on the matrix representations of tensors through the unfolding and the n-mode product concepts. These tools are quite useful for representing practical problems as tensors. We also discuss various special matrix products, including Kronecker, Khatri-Rao, and Hadamard products. Additionally, we introduce the Tucker and Kruskal operators, which are useful for representing the n-mode unfolding of tensors with order higher than 3. Then, we describe the PARAFAC and PARATUCK decompositions and their associated alternating least squares algorithms in detail. This chapter also provides a historical perspective on the use of the tensor decompositions applied to wireless communications. We highlight applications in different wireless systems and popular problems over the years, showing that tensor modeling has been present in the different phases of the evolution of wireless communications.

4 PILOT-ASSISTED CHANNEL ESTIMATION FOR SINGLE USER IRS-ASSISTED MIMO SYSTEM

4.1 Introduction

In a typical wireless propagation environment, the transmitted signals suffer attenuation and scattering caused by absorption and reflection, diffraction, and refraction phenomena. In general, multipath propagation is known as one of the main limiting factors to the performance of a wireless communication system (Singal, 2010). Indeed, the randomness of the physical radio environment turns the wireless propagation uncontrollable.

As discussed in Chapter 2, intelligent reflecting surface is an emergent and promising technology for future wireless communications that consists of a 2D array with a large number of passive or semi-passive elements capable of to control the electromagnetic properties of the RF waves so that the reflected signals add coherently at the intended receiver or destructively to reduce the co-channel interference. Each element can act independently and can be reconfigured in a software-defined manner utilizing an external controller. The IRS does not require dedicated radio-frequency chains and is usually wirelessly powered by an external RF-based source, as opposed to amplify-and-forward or decode-and-forward relays, which require dedicated power sources (Huang *et al.*, 2019). In the literature, IRS is being considered in several application scenarios, such as to provide coverage to users located in a dead zone and to suppress co-channel interference when the user is at the edge of the cell (Wu; Zhang, 2020b; Wu; Zhang, 2020a), and to improve the physical layer security (Song *et al.*, 2020; Dong; Wang, 2020; Wang; Swindlehurst, 2023). Besides, the IRS can be employed for simultaneous wireless information and power transfer in an IoT network (Wu; Zhang, 2020b). Regarding wireless communication systems, recently, (Ying *et al.*, 2020) established a connection between IRS technology and a millimetre-wave (mmWave) hybrid MIMO system. In this case, the authors consider a hybrid MIMO-OFDM assisted by IRS working in the mmWave band.

4.2 Some related works and motivation

Recent works have discussed the potentials and challenges of IRS-assisted wireless communications (see, e.g., (Basar *et al.*, 2019), (Gong *et al.*, 2020) and references therein). Among the several open issues, we highlight the acquisition of channel state information. One challenge is related to the assumption that the IRS usually consists of passive elements, which means that the estimation of the cascaded channel should be performed at the receiver based on pilots sent by the transmitter *via* the IRS. At this point, the pattern of phase shifts used by the IRS during the training phase plays an important role. In addition, the large number of IRS elements imposes an extra challenge to address the channel estimation problem. Two approaches have been proposed in the literature. The first one assumes a semi-passive structure, where the IRS has a few active elements connected to receive radio-frequency chains. In this case, the availability of some baseband processing at the IRS facilitates the CSI acquisition. An example of this approach is discussed in (Taha *et al.*, 2019), where the involved channels are estimated through compressive sensing. The second approach, which is the one adopted in this work, assumes a fully passive structure, where the IRS operates by reflecting the impinging waves according to some phase-shift pattern. This is a more challenging scenario, where the estimation of the cascaded (transmitter-IRS-receiver) should be done at the receiver based on pilots sent by the transmitter and reflected by the IRS.

A few works have addressed the channel estimation problem and provided different solutions to the passive IRS case (Swindlehurst *et al.*, 2022; Zhou *et al.*, 2022; Peng *et al.*, 2022). In (Jensen; Carvalho, 2020), a minimum variance unbiased estimator is proposed, and an optimal design of the IRS phase shift matrix is found. The authors of (He; Yuan, 2020) propose a two-stage algorithm by exploiting sparse representations of low-rank multipath channels. In (Ning *et al.*, 2020), links between massive MIMO and IRS are discussed in the context of Terahertz communications, and a cooperative channel estimation *via* beam training is presented. In (Cui; Yin, 2019), IRS is proposed as a solution to mitigate the blockage problem in mmWave communications, and a channel estimation approach is presented. The work (Chen *et al.*, 2019) proposes an uplink channel estimation protocol for an IRS aided multi-user MIMO system applying compressing sensing (CS) methods. In (Mirza; Ali, 2021), an IRS-aided MIMO system is considered and channel estimation is carried out in a two-stage approach, while the IRS-assisted link is estimated using an approximate message-passing method. Considering an IRS-assisted internet of things scenario, (Xia; Shi, 2020) formulates a joint active detection and channel estimation based on sparse matrix factorization, matrix completion, and multiple measurement vector problems.

The authors of (Hu *et al.*, 2021) propose a channel estimation framework where the BS-IRS, IRS-UT, and BS-UT channels are estimated in a two-timescale approach, while in (You *et al.*, 2020b) a practical transmission protocol is proposed to accomplish channel estimation and passive beamforming. In (Mishra; Johansson,), channel estimation is carried out by resorting to an on-off strategy that sequentially activates the IRS elements one by one. The work (Wei *et al.*,) proposes a parallel factor model to solve the channel estimation problem in a multi-user multiple-input single-output (MISO) setting. In general, most of the existing works on IRS-assisted communications consider the multiple input single output case, where the receiver station is equipped with a single antenna.

4.3 This chapter

In this chapter, we establish an existing connection between IRS-assisted MIMO communications and tensor modeling. By assuming a structured time-domain pattern of pilots and IRS phase shifts, we show that the received signal follows a parallel factor (PARAFAC) tensor model. By exploiting the PARAFAC signal structure in two different ways, we propose two simple and effective algorithms to estimate the cascaded MIMO channel via decoupling the transmitter-IRS and IRS-receiver MIMO channels, respectively. The first algorithm is a closed-form solution based on the Khatri-Rao factorization (KRF) of the combined BS-IRS and IRS-UT channels, while the second one consists of an iterative bilinear alternating least squares algorithm. While the first algorithm is a closed-form algebraic and less complex solution, the second one can operate under less restrictive conditions on the system parameters.

The common feature of the two algorithms is that the estimation of the cascaded channel is achieved via decoupling the estimation of the two involved channel matrices, which provides a performance enhancement compared to the direct estimation of the cascaded channel via conventional least squares. By focusing on pilot-assisted channel estimation schemes, this work presents a comprehensive formulation of tensor-based IRS-assisted channel estimation methods, while bringing a discussion on the uniqueness conditions for the channel estimation problem considering the proposed receivers, from which useful design recommendations on the training parameters are derived. We discuss how to deal with a non-ideal setup where the IRS phase shifts are not perfectly known at the receiver and provide a solution to handle this problem. In addition, we also present generalizations of the proposed approach to multi-user scenarios.

The contributions of this chapter are summarized as follows.

- Resorting to tensor modeling, we connect the channel estimation problem for IRS-assisted MIMO systems to that of fitting PARAFAC model to a third-order tensor;
- We derive two simple pilot-assisted channel estimation algorithms (namely, KRF and

BALS) that exploit the algebraic structure of the PARAFAC model of the received signals in two different ways;

– We provide system design recommendations for the proposed KRF and BALS receivers that ensure the uniqueness of the channel estimation problem;
– We discuss how to handle perturbations/fluctuations on the IRS phase shifts through a joint channel and IRS matrix estimation at the receiver;
– Generalizations of the proposed tensor signal model to multi-user scenarios are provided, which include the multi-UT and the multi-BS cases.

4.4 System Model

We consider a MIMO communication system assisted by an IRS. Both the transmitter and the receiver are equipped with multiple antennas. Although the terminology adopted in our work assumes a downlink communication, where the transmitter is the base station and the receiver is the user terminal, our signal model also applies to the uplink case by just inverting the roles of the transmitter and the receiver. The BS and UT are equipped with arrays of M and L antennas, respectively. The IRS is composed of N elements, or unit cells, capable of individually adjusting their reflection coefficients (i.e., phase shifts). The system model is illustrated in Figure 24. In a time-slotted transmission, we assume that the IRS adjusts its phase shifts as a function of the time $t = 1, \ldots, T$. We also assume a block-fading channel, which means that the BS-IRS and IRS-UT channels are constant during T time slots. The received signal is given as (He; Yuan, 2020)

$$\mathbf{y}[t] = \mathbf{G}(\mathbf{s}[t] \odot \mathbf{H}\mathbf{x}[t]) + \mathbf{b}[t], \quad 1 \leq t \leq T, \tag{4.1}$$

or, alternatively,

$$\mathbf{y}[t] = \mathbf{G}\mathrm{diag}(\mathbf{s}[t])\mathbf{H}\mathbf{x}[t] + \mathbf{b}[t], \tag{4.2}$$

where $\mathbf{x}[t] \in \mathbb{C}^{M\times 1}$ is the vector containing the transmitted pilot signals at time t, $\mathbf{s}[t] = \left[s_{1,t}e^{j\phi_1}, \ldots, s_{N,t}e^{j\phi_N}\right]^{\mathrm{T}} \in \mathbb{C}^{N\times 1}$ is the vector that models the phase shifts and activation pattern of the IRS, where $\phi_n \in (0, 2\pi]$, and $s_{n,t} \in \{0, 1\}$ controls the on-off state of the corresponding element at time t. The matrices $\mathbf{H} \in \mathbb{C}^{N\times M}$ and $\mathbf{G} \in \mathbb{C}^{L\times N}$ denote the BS-IRS and IRS-UT MIMO channels, respectively, while $\mathbf{b}[t] \in \mathbb{C}^{L\times 1}$ is the additive white Gaussian noise (AWGN) vector.

Figura 24 – IRS-assisted MIMO system.

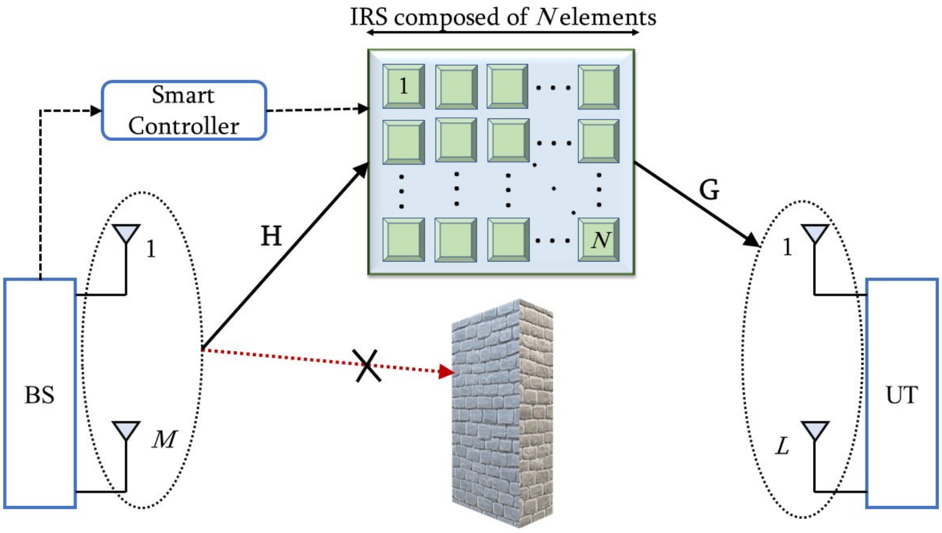

Figura 25 – Structured pilot pattern in the time domain.

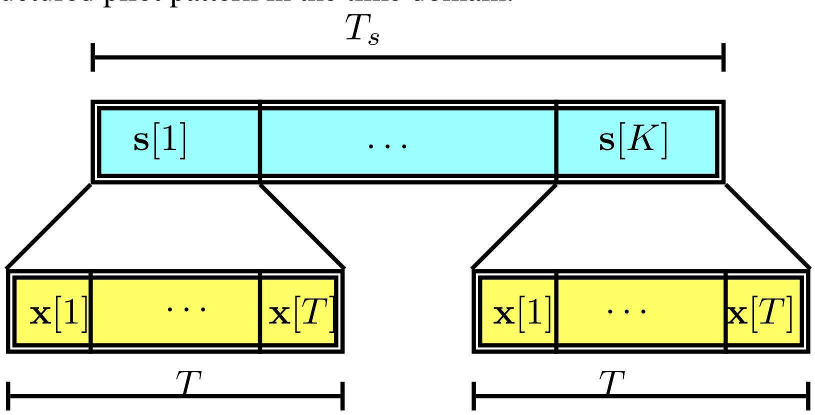

The channel training time T_s is divided into K blocks, where each block has T time slots so that $T_s = KT$. Let us define $\mathbf{y}[k,t] \doteq y[(k-1)T+t]$ as the received signal at the tth time slot of the kth block, $t = 1,\ldots,T$, $k = 1,\ldots,K$. Likewise, denote $\mathbf{x}[k,t]$ and $\mathbf{s}[k,t]$ as the pilot signal and phase shift vectors associated with the tth time slot of the kth block. We propose the following structured time-domain protocol: i) the IRS phase shift vector is constant during the T time slots of the kth block and varies from block to block; ii) the pilot signals $\{\mathbf{x}[1],\ldots,\mathbf{x}[T]\}$ are repeated over the K blocks. Mathematically, this means that

$$\mathbf{s}[k,t] = \mathbf{s}[k], \text{ for } 1 \leq t \leq T, \tag{4.3}$$

$$\mathbf{x}[k,t] = \mathbf{x}[t], \text{ for } 1 \leq k \leq K. \tag{4.4}$$

An illustration of this time-domain protocol is shown in Figure 25. Under these assumptions, the received signal model (4.2) can be written as

$$\mathbf{y}[k,t] = \mathbf{G}\text{diag}(\mathbf{s}[k])\mathbf{H}\mathbf{x}[t] + \mathbf{b}[k,t]. \tag{4.5}$$

Collecting the received signals during T time slots for the kth block in $\mathbf{Y}[k] = [\mathbf{y}[k,1]\ldots\mathbf{y}[k,T]] \in \mathbb{C}^{L\times T}$ leads to

$$\mathbf{Y}[k] = \mathbf{G}\mathrm{diag}(\mathbf{s}[k])\mathbf{H}\mathbf{X}^{\mathrm{T}} + \mathbf{B}[k], \tag{4.6}$$

where $\mathbf{X} \doteq [\mathbf{x}[1],\ldots,\mathbf{x}[T]]^{\mathrm{T}} \in \mathbb{C}^{T\times M}$, and $\mathbf{B} \doteq [\mathbf{b}[1],\ldots,\mathbf{b}[T]]^{\mathrm{T}} \in \mathbb{C}^{L\times T}$.

4.4.1 Cascaded Least squares method for cascaded channel estimation

A baseline method consists of estimating a combined version of the communication channels $\mathbf{G}$ and $\mathbf{H}$ using the least squares (LS) approach. To derive the LS estimator, we apply property (6) to (4.6) to obtain

$$\begin{aligned}\mathbf{y}[k] &= \big((\mathbf{X}\mathbf{H}^{\mathrm{T}})\diamond\mathbf{G}\big)\mathbf{s}[k]\\ &= \big(\mathbf{X}\otimes\mathbf{I}_L\big)\big(\mathbf{H}^{\mathrm{T}}\diamond\mathbf{G}\big)\mathbf{s}[k] + \mathbf{b}[k],\end{aligned} \tag{4.7}$$

where $\mathbf{y}[k] \doteq \mathrm{vec}(\mathbf{Y}[k]) \in \mathbb{C}^{LT}$, $\mathbf{b}[k] \doteq \mathrm{vec}(\mathbf{B}[k]) \in \mathbb{C}^{LT}$, and we have used property (4). Defining $\tilde{\mathbf{Y}} \doteq [\mathbf{y}[1]\ldots\mathbf{y}[K]] \in \mathbb{C}^{LT\times K}$, and $\tilde{\mathbf{X}} \doteq (\mathbf{X}\otimes\mathbf{I}_L) \in \mathbb{C}^{TL\times ML}$, we have

$$\tilde{\mathbf{Y}} = \tilde{\mathbf{X}}\big(\mathbf{H}^{\mathrm{T}}\diamond\mathbf{G}\big)\mathbf{S}^{\mathrm{T}} + \mathbf{B}, \tag{4.8}$$

where $\mathbf{S} \doteq [\mathbf{s}[1],\ldots,\mathbf{s}[K]]^{\mathrm{T}} \in \mathbb{C}^{K\times N}$, $\mathbf{B} \in \mathbb{C}^{LT\times K}$ is the noise matrix constructed in the same way as $\mathbf{Y}$. Finally, defining $\mathbf{y} \doteq \mathrm{vec}(\tilde{\mathbf{Y}}) \in \mathbb{C}^{LTK}$, and applying property (6) to (4.8), we get

$$\mathbf{y} = (\mathbf{S}\otimes\tilde{\mathbf{X}})\mathrm{vec}\big(\mathbf{H}^{\mathrm{T}}\diamond\mathbf{G}\big) + \mathbf{b}, \tag{4.9}$$

or, compactly,

$$\mathbf{y} = \mathbf{U}\theta + \mathbf{b}, \tag{4.10}$$

where $\mathbf{U} \doteq \mathbf{S}\otimes\tilde{\mathbf{X}} \in \mathbb{C}^{KTL\times NML}$ and $\theta \doteq \mathrm{vec}\left(\mathbf{H}^{\mathrm{T}}\diamond\mathbf{G}\right) \in \mathbb{C}^{MLN}$ is the *composite channel parameter* combining the BS-IRS and IRS-UT channels. The LS estimate of this composite channel minimizes the problem

$$\hat{\theta} = \underset{\theta}{\arg\min}\ \|\mathbf{y}-\mathbf{U}\theta\|^2, \tag{4.11}$$

the solution of which is known to be $\theta = \mathbf{U}^{\dagger}\mathbf{y}$. The computation of this solution can indeed be simplified to $\theta = (\mathbf{S}^{\dagger}\otimes\tilde{\mathbf{X}}^{\dagger})\mathbf{y}$, due to the Kronecker structure of $\mathbf{U}$.

It should be noted that the conventional LS problem ignores the Katri-Rao structure of the composite channel that is present in the linearized parameter vector θ. Indeed, the signal model (4.6), or equivalently, (4.8) has a tensor structure, and can be recast as a PARAFAC tensor model. As we show in Section 4.5, adopting this tensor modeling allows us to enhance the channel estimation accuracy (compared to conventional LS methods). This is achieved by decoupling the estimates of $\mathbf{H}$ and $\mathbf{G}$, rather them estimating $\theta = \text{vec}\left(\mathbf{H}^{\text{T}} \diamond \mathbf{G}\right)$ as a whole. Moreover, useful system design recommendations can be derived from the proposed modeling approach.

4.4.2 Tensor signal modeling

To simplify the exposition of the signal model, we remove the noise term from the following developments. The noise term is taken into account later. We can rewrite the signal part of the equation (4.6) as

$$\overline{\mathbf{Y}}[k] = \mathbf{G}\mathbf{D}_k(\mathbf{S})\mathbf{Z}^{\text{T}}, \quad \mathbf{Z} \doteq \mathbf{X}\mathbf{H}^{\text{T}} \in \mathbb{C}^{T\times N}, \tag{4.12}$$

where $\mathbf{D}_k(\mathbf{S}) \doteq \text{diag}(\mathbf{s}[k])$ denotes a diagonal matrix holding the kth row of the IRS phase shift matrix $\mathbf{S}$ on its main diagonal. The matrix $\overline{\mathbf{Y}}[k]$ can be viewed as the kth frontal matrix slice of a three-way tensor $\overline{\mathscr{Y}} \in \mathbb{C}^{L\times T\times K}$ that follows a PARAFAC decomposition, also known as canonical polyadic decomposition (CPD) (Harshman, 1970; Kolda; Bader, 2009; Comon *et al.*, 2009; Almeida *et al.*, 2016; Sidiropoulos *et al.*, 2017)). Figure 26 bring a friendly visualization how our system model fits a third-order tensor. Each (ℓ,t,k)th entry of the noiseless received

Figura 26 – Three way tensor

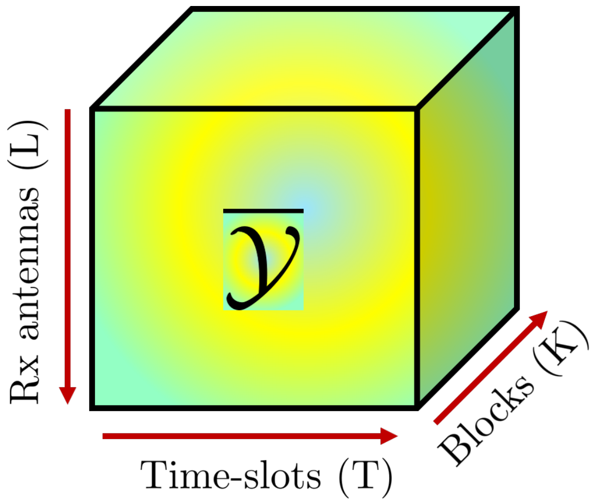

signal tensor $\overline{\mathscr{Y}}$ can be written as:

$$\bar{y}_{\ell,t,k} = \sum_{n=1}^{N} g_{\ell,n} z_{t,n} s_{k,n}, \tag{4.13}$$

where $g_{\ell,n} \doteq [\mathbf{G}]_{\ell,n}$, $z_{t,n} \doteq [\mathbf{Z}]_{t,n}$, and $s_{k,n} \doteq [\mathbf{S}]_{k,n}$. A shorthand notation for the PARAFAC decomposition (4.13) is denoted as $\overline{\mathscr{Y}} = [[\mathbf{G}, \mathbf{Z}, \mathbf{S}]]$. Using the n-mode product notation, the PARAFAC decomposition of the noiseless received signal tensor $\overline{\mathscr{Y}}$ can be represented as

$$\overline{\mathscr{Y}} \quad = \quad \mathscr{I}_{3,N} \times_1 \mathbf{G} \times_2 \mathbf{Z} \times_3 \mathbf{S}. \tag{4.14}$$

Exploiting the trilinearity of the PARAFAC decomposition, we can "unfold" received signal tensor $\overline{\mathscr{Y}}$ into the following three matrix forms (Harshman, 1970; Kolda; Bader, 2009):

$$\overline{\mathbf{Y}}_1 = \mathbf{G}(\mathbf{S} \diamond \mathbf{Z})^{\mathrm{T}} \in \mathbb{C}^{L \times TK}, \tag{4.15}$$

$$\overline{\mathbf{Y}}_2 = \mathbf{Z}(\mathbf{S} \diamond \mathbf{G})^{\mathrm{T}} \in \mathbb{C}^{T \times LK}, \tag{4.16}$$

$$\overline{\mathbf{Y}}_3 = \mathbf{S}(\mathbf{Z} \diamond \mathbf{G})^{\mathrm{T}} \in \mathbb{C}^{K \times LT}, \tag{4.17}$$

where $\overline{\mathbf{Y}}_1 \doteq [\overline{\mathbf{Y}}[1], \ldots, \overline{\mathbf{Y}}[K]]$, $\overline{\mathbf{Y}}_2 \doteq [\overline{\mathbf{Y}}^{\mathrm{T}}[1], \ldots, \overline{\mathbf{Y}}^{\mathrm{T}}[K]]$, and $\overline{\mathbf{Y}}_3 \doteq [\mathrm{vec}(\overline{\mathbf{Y}}[1]), \ldots, \mathrm{vec}(\overline{\mathbf{Y}}[K])]^{\mathrm{T}}$. In the following, the algebraic structure of the PARAFAC model (4.13) is exploited to formulate two different channel estimation methods. The PARAFAC model is powerful due to its essential factor identification uniqueness property, which has its roots in the concept of Kruskal rank (k-rank). Details can be found in (Kruskal, 1977; Stegeman; Sidiropoulos, 2007). comparing equations (3.19) and (4.12), the following correspondence can be established

$$(\mathbf{A}, \mathbf{B}, \mathbf{C}) \leftrightarrow (\mathbf{G}, \mathbf{S}, \mathbf{Z}). \tag{4.18}$$

Figure 27 is a pictorial representation of the (noiseless) received signal as a PARAFAC decom-

Figura 27 – PARAFAC model for the received signal.

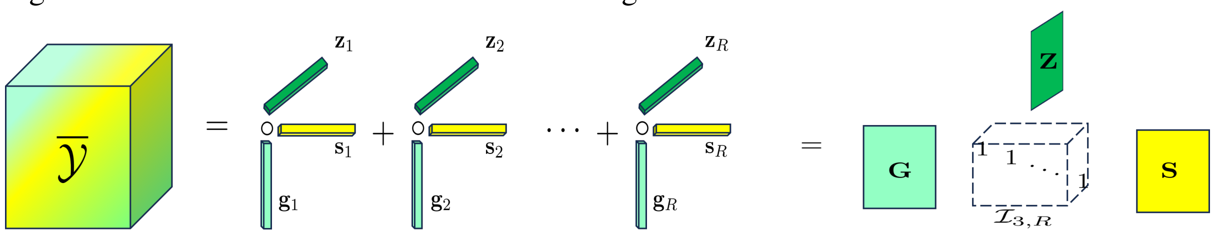

position.

4.5 Channel Estimation Methods From Tensor Signal Modeling

Our goal is to estimate the channel matrices **H** (BS-IRS) and **G** (IRS-UT) from the received signal tensor given in (4.13). Let us define $\mathscr{Y} \doteq \overline{\mathscr{Y}} + \mathscr{B}$ as the noise-corrupted received signal tensor, where $\mathscr{B} \in \mathbb{C}^{L\times T\times K}$ is the additive noise tensor. Likewise, $\mathbf{Y}_i \doteq \overline{\mathbf{Y}}_i + \mathbf{B}_i$, $i = 1,2,3$, are the noisy versions of the 1-mode, 2-mode and 3-mode matrix unfoldings (4.15)-(4.17) of the received signal tensor, and $\mathbf{B}_{i=1,2,3}$ the corresponding matrix unfoldings of the noise tensor.

The pilot signal matrix $\mathbf{X}$ and the IRS phase shifts matrix $\mathbf{S}$ can be designed as semi-unitary matrices satisfying $\mathbf{X}^{\mathrm{H}}\mathbf{X} = T\mathbf{I}_M$ and $\mathbf{S}^{\mathrm{H}}\mathbf{S} = K\mathbf{I}_N$, respectively. A good choice is to design both $\mathbf{X}$ and $\mathbf{S}$ as truncated discrete Fourier transform (DFT) matrices. The optimal design of the IRS matrix $\mathbf{S}$ is discussed in (Jensen; Carvalho, 2020) for the MISO case (i.e., for single-antenna users).

4.5.1 Closed formed Khatri-Rao Factorization based channel estimation

First, note that we can rewrite the noise-corrupted matrix unfolding (4.17) as:

$$\begin{aligned}\mathbf{Y}_3 &= \mathbf{S}(\mathbf{Z}\diamond\mathbf{G})^{\mathrm{T}} + \mathbf{B}_3 \\ &= \mathbf{S}\big(\mathbf{H}^{\mathrm{T}}\diamond\mathbf{G}\big)^{\mathrm{T}}(\mathbf{X}\otimes\mathbf{I}_L)^{\mathrm{T}} + \mathbf{B}_3,\end{aligned} \tag{4.19}$$

where we have applied the property $(\mathbf{A}\otimes\mathbf{B})(\mathbf{C}\diamond\mathbf{D}) = (\mathbf{AC})\diamond(\mathbf{BD})$ to the term $(\mathbf{Z}\diamond\mathbf{G}) = ((\mathbf{X}\mathbf{H}^{\mathrm{T}})\diamond\mathbf{G})$. A bilinear time-domain filtering is applied at the receiver by exploiting the knowledge of the IRS matrix and the pilot signal matrix, as follows

$$\Omega \doteq (\mathbf{X}^{\dagger}\otimes\mathbf{I}_L)\mathbf{Y}_3^{\mathrm{T}}(\mathbf{S}^{\mathrm{T}})^{\dagger} = \mathbf{H}^{\mathrm{T}}\diamond\mathbf{G} + \widetilde{\mathbf{B}}_3, \tag{4.20}$$

where $\widetilde{\mathbf{B}}_3 = (\mathbf{X}^{\dagger}\otimes\mathbf{I}_L)\mathbf{B}_3^{\mathrm{T}}(\mathbf{S}^{\mathrm{T}})^{\dagger}$ is the filtered noise term. Note that $\Omega \in \mathbb{C}^{ML\times N}$ is a noisy version of the (Khatri-Rao structured) *virtual MIMO channel* that models the IRS-assisted MIMO transmission. Due to the semi-unitary structure of $\mathbf{S}$ and $\mathbf{X}$, the correlation properties of the additive noise are not affected by the bilinear filtering step.

From (4.20), we propose to estimate $\mathbf{H}$ and $\mathbf{G}$ by solving the following Khatri-Rao least squares approximation problem

$$\min_{\mathbf{H},\mathbf{G}} \left\|\Omega - \mathbf{H}^{\mathrm{T}}\diamond\mathbf{G}\right\|_F^2. \tag{4.21}$$

An efficient solution to this problem is given by the Khatri-Rao factorization (KRF) algorithm (Kibangou; Favier,),(Roemer; Haardt, 2010). Note that the problem (4.21) can be interpreted as finding estimates of $\mathbf{H}$ and $\mathbf{G}$ that minimize a set of rank-1 matrix approximations, i.e.,

$$(\hat{\mathbf{H}},\hat{\mathbf{G}}) = \underset{\{\mathbf{h}_n\},\{\mathbf{g}_n\}}{\arg\min} \sum_{n=1}^{N} \left\|\widetilde{\Omega}_n - \mathbf{g}_n\mathbf{h}_n^{\mathrm{T}}\right\|_F^2, \tag{4.22}$$

Algoritmo 3: Khatri-Rao factorization (KRF)

Procedure
output : $\hat{\mathbf{H}}$ and $\hat{\mathbf{G}}$

begin
  Bilinear filtering of $\mathbf{Y}_3$:
  $\Omega^{\mathrm{T}} \longleftarrow \mathbf{S}^{\mathrm{H}}\mathbf{Y}_3(\mathbf{X}^* \otimes \mathbf{I}_L)$
  for $n = 1, \ldots, N$ **do**
    $\widetilde{\Omega}_n \longleftarrow \mathrm{unvec}_{L\times M}(\omega_n)$
    $(\mathbf{u}_1, \sigma_1, \mathbf{v}_1) \longleftarrow \text{t-SVD}(\widetilde{\Omega}_n)$
    $\hat{\mathbf{h}}_n \longleftarrow \sqrt{\sigma_1}\mathbf{v}_1^*$
    $\hat{\mathbf{g}}_n \longleftarrow \sqrt{\sigma_1}\mathbf{u}_1$
    end
  end
  Reconstruct $\hat{\mathbf{H}}$ *and* $\hat{\mathbf{G}}$:
  $\hat{\mathbf{H}} \longleftarrow \left[\hat{\mathbf{h}}_1, \ldots, \hat{\mathbf{h}}_N\right]^{\mathrm{T}}$
  $\hat{\mathbf{G}} \longleftarrow [\hat{\mathbf{g}}_1, \ldots, \hat{\mathbf{g}}_N]$
  end
end

where $\widetilde{\Omega}_n \doteq \mathrm{unvec}_{L\times M}(\omega_n) \in \mathbf{C}^{L\times M}$, while $\mathbf{g}_n \in \mathbf{C}^{L\times 1}$ and $\mathbf{h}_n^{\mathrm{T}} \in \mathbf{C}^{1\times M}$ are the nth column of $\mathbf{G}$ and nth row of $\mathbf{H}$, respectively. The estimates of $\mathbf{g}_n$ and $\mathbf{h}_n$ in (4.22) can be obtained from the dominant left and right singular vectors of $\widetilde{\Omega}_n$, respectively, for $1 \leq n \leq N$. Hence, our channel estimation problem translates into solving N rank-1 matrix approximation subproblems, for which several efficient solutions exist in the literature (Golub; Loan, 2013). A summary of the KRF algorithm is given in Algorithm 1, where t-SVD denotes a truncated SVD (t-SVD denotes also tensor SVD in the tensor literature) that returns the dominant singular vector and its associated singular value. Once $\hat{\mathbf{H}}$ and $\hat{\mathbf{G}}$ are found from problem (4.22), we can build the composite channel.

4.5.2 Iterative solution: BALS channel estimation

From the noisy versions of the matrix unfoldings (4.15) and (4.16), we can derive an iterative solution based on a bilinear alternating least squares (BALS) algorithm. This algorithm is a simplified version of the well-known trilinear ALS algorithm for estimating the factor matrices of a PARAFAC model (Bro, 1998). In our case, since $\mathbf{S}$ is known at the receiver, it consists of estimating the matrices $\mathbf{G}$ and $\mathbf{H}$ in an alternating way by iteratively optimizing the

Algoritmo 4: Bilinear alternating least squares (BALS)

Procedure
input : $i = 0$; *Initialize* $\hat{\mathbf{H}}_{(i=0)}$
output : $\hat{\mathbf{H}}$, $\hat{\mathbf{G}}$

begin
  $i = i + 1$;
  while $\|e(i) - e(i-1)\| \geq \delta$ **do**
    1: *Find a least squares estimate of* $\mathbf{G}$:
    $$\hat{\mathbf{G}}_{(i)} = \mathbf{Y}_1 \left[\left(\mathbf{S} \diamond \left(\mathbf{X}\hat{\mathbf{H}}^{\mathrm{T}}_{(i-1)} \right) \right)^{\mathrm{T}} \right]^{\dagger}$$
    2: *Find a least squares estimate of* $\mathbf{H}$:
    $$\hat{\mathbf{H}}^{\mathrm{T}}_{(i)} = \mathbf{X}^{\dagger}\mathbf{Y}_2 \left[\left(\mathbf{S} \diamond \hat{\mathbf{G}}_{(i)} \right)^{\mathrm{T}} \right]^{\dagger}$$
    3: *Repeat steps* 1 to 2 *until convergence.*
    end
  end
  end
end

following two cost functions:

$$\hat{\mathbf{G}} = \arg\min_{\mathbf{G}} \left\| \mathbf{Y}_1 - \mathbf{G} \left(\mathbf{S} \diamond \left(\mathbf{X}\mathbf{H}^{\mathrm{T}} \right) \right)^{\mathrm{T}} \right\|_F^2, \tag{4.23}$$

$$\hat{\mathbf{H}} = \arg\min_{\mathbf{H}} \left\| \mathbf{Y}_2 - \left(\mathbf{X}\mathbf{H}^{\mathrm{T}} \right) \left(\mathbf{S} \diamond \mathbf{G} \right)^{\mathrm{T}} \right\|_F^2, \tag{4.24}$$

the solutions of which are respectively given by

$$\hat{\mathbf{G}} = \mathbf{Y}_1 \left[\left(\mathbf{S} \diamond \left(\mathbf{X}\mathbf{H}^{\mathrm{T}} \right) \right)^{\mathrm{T}} \right]^{\dagger}, \tag{4.25}$$

$$\hat{\mathbf{H}}^{\mathrm{T}} = \mathbf{X}^{\dagger}\mathbf{Y}_2 \left[\left(\mathbf{S} \diamond \mathbf{G} \right)^{\mathrm{T}} \right]^{\dagger}. \tag{4.26}$$

The convergence is declared when $\|e_{(i)} - e_{(i-1)}\| \leq \delta$, where $e_{(i)} = \|\mathscr{Y} - \hat{\mathscr{Y}}_{(i)}\|_F^2$ denotes the reconstruction error computed at the ith iteration, δ is a threshold, and $\hat{\mathscr{Y}}_{(i)} = [\hat{\mathbf{G}}_{(i)}, \mathbf{X}\hat{\mathbf{H}}^{\mathrm{T}}_{(i)}, \hat{\mathbf{S}}]$ is the reconstructed PARAFAC model (c.f. (4.6), (4.13)) obtained from the estimated channel matrices $\hat{\mathbf{G}}_{(i)}$ and $\hat{\mathbf{H}}_{(i)}$ at the end of the ith iteration. In this work, we adopt $\delta = 10^{-5}$. Despite the iterative nature of the BALS algorithm, only a few iterations are necessary for convergence (usually less than 10 iterations) thanks to the knowledge of the IRS matrix $\mathbf{S}$ that remains fixed during the iterations.

If $\mathbf{X}$ and $\mathbf{S}$ are column-orthogonal (which requires $K \geq N$ and $T \geq M$), the right pseudo-inverses in (4.25) and (4.26) can be replaced by matrix products. This leads to a lower complexity implementation of the BALS algorithm with simplified estimation steps, as shown in Appendix B.

4.5.3 Computational complexity

The computational complexity is in general dominated by the (truncated) SVD steps involved in Algorithm 1 (KRF) to compute rank-1 matrix approximations, as well as in Algorithm 2 (BALS) to calculate the LS estimates of the channel matrices. First, recall that computing the SVD of a matrix $P \times Q$ has a complexity order of $\mathscr{O}(PQ\min(P,Q))$ while computing the inner product of two matrices of dimensions $P \times F$ and $F \times Q$ has complexity $\mathscr{O}(PQF)$. The complexity of KRF is that of computing N rank-1 approximation routines from the matrix $\widetilde{\Omega}_n$, $n = 1,\ldots,N$, which can be efficiently implemented through the well-known power method (Golub; Loan, 2013). From these results, we find that the KRF algorithm has a complexity of order $\mathscr{O}(MLN)$ owing to the N rank-1 matrix approximations. As for the iterative BALS receiver, as discussed in Section 4.5.2, the computational cost associated with steps 1 and 2 is that of computing two right pseudo-inverses per iteration, which is equivalent to $\mathscr{O}(NKT[2N+L])$ and $\mathscr{O}(MT[2M+LK]+N^2[LK+M]+MNLK)$, respectively. Note, however, that this computational cost is greatly reduced when $\mathbf{S}$ and $\mathbf{X}$ have orthogonal columns (which require $K \geq N$ and $T \geq M$, respectively). According to the steps derived in Appendix B, the cost per iteration is that of computing the matrix products in steps 1 and 2 of Algorithm 10, which corresponds to $\mathscr{O}(LN[TK+N])$ and $\mathscr{O}(M[LKT+LKN+N^2])$, respectively.

4.5.4 Dealing with IRS perturbations and blockages (non-ideal IRS)

In outdoor scenarios, due to the exposure of the IRS to weather and atmospheric conditions, its elements may be subject to unknown blockages, as well as time-dependent fluctuations on their phase and amplitude responses (Li *et al.*, 2020). Such unknown perturbations have a random nature and may be caused by water droplets, snowflakes, and dry and damp sand particles, among others. In this case, the IRS matrix $\mathbf{S}$ deviates from its desired structure, and the assumption of a perfect knowledge of all the phase shifts at the receiver may not hold. Otherwise stated, the receiver cannot benefit from the full knowledge of the IRS phase shifts to estimate the cascade channel, i.e., it should be able to operate in a *semi-blind* way. Adopting our tensor modeling approach, it is possible to deal with this issue by resorting to a trilinear alternating least squares (TALS) algorithm that jointly estimates $\mathbf{G}$, $\mathbf{H}$, and $\mathbf{S}$ by fully exploiting the trilinear structure of the received signal tensor in (4.13)-(4.14). The TALS algorithm is an extension of the BALS one by adding in Algorithm 2 a third estimation step (see algorithm 5)

$$\hat{\mathbf{S}}_{(i)} = \mathbf{Y}_3\left[\left(\left(\mathbf{X}\hat{\mathbf{H}}_{(i)}^{\mathrm{T}}\right) \diamond \hat{\mathbf{G}}_{(i)}\right)^{\mathrm{T}}\right]^{\dagger}$$

that includes the update/refinement of the IRS matrix within the loop. The TALS arises as a good alternative to deal with IRS phase shift perturbations. Since the channel matrices are now estimated blindly, i.e., without the knowledge of the IRS matrix $\mathbf{S}$, more iterations are required to achieve convergence. Moreover, the complexity is also increased due to the additional LS estimation step at each iteration. TALS is a well-known algorithm for fitting a PARAFAC model (Bro, 1998; Kolda; Bader, 2009; Comon *et al.*, 2009). In such a blind approach, we can resort to Kruskal's uniqueness conditions for the PARAFAC model (Kruskal, 1977) to obtain useful system design recommendations. A simplified condition can be obtained when the channel matrices have full rank.[1] In this case, $\min(L,N)+\min(M,N)+\min(K,N) \geq 2N+2$ guarantees the uniqueness of $\mathbf{G}$, $\mathbf{H}$ and $\mathbf{S}$ (see (Stegeman; Sidiropoulos, 2007; Sidiropoulos *et al.*, 2017) for a deeper uniqueness discussion in the general case). It is known that TALS may suffer from slow convergence due to its sensitivity to initialization. However, several enhancements may be used to improve its performance (see (Comon *et al.*, 2009) and references therein).

4.6 Design recommendations

The KRF method (Algorithm 1) has a bilinear filtering step as shown in (4.20) requiring that the IRS phase shift matrix $\mathbf{S}$ and the pilot symbol matrix $\mathbf{X}$ have full column-rank, which implies the following conditions

$$K \geq N \quad \text{and} \quad T \geq M. \tag{4.27}$$

As mentioned earlier, a good choice is to design $\mathbf{X}$ and $\mathbf{S}$ as semi-unitary (or column-orthogonal) matrices, for two reasons. First, because the semi-unitary design replaces matrix inversions in (4.20) by simple matrix products, simplifying the receiver processing. Second, because the correlation properties of the filtered noise term in (4.20) are preserved.

The BALS method (Algorithm 2) requires that the two Khatri-Rao product terms $\mathbf{M}_1 = \mathbf{S} \diamond \left(\mathbf{X}\mathbf{H}^{\mathrm{T}}\right) \in \mathbb{C}^{KT\times N}$ and $\mathbf{M}_2 = \mathbf{S} \diamond \mathbf{G} \in \mathbb{C}^{KL\times N}$ have full column-rank, so that (4.25) and (4.26) (resp. steps 1 and 2 of Algorithm 2) admit unique solutions. This means that the

[1] The condition $\min(L,N)+\min(M,N)+\min(K,N) \geq 2N+2$ usually implies more restrictive choices on the system parameters L, M, and K, compared to the conditions discussed in Section V, which are valid when considering the perfect knowledge of the IRS matrix.

Algoritmo 5: Trilinear alternating least squares (TALS)

Procedure

input : $i = 0$; *Initialize* $\hat{\mathbf{H}}_{(i=0)}$ *and* $\hat{\mathbf{S}}_{(i=0)}$

output : $\hat{\mathbf{H}}$, $\hat{\mathbf{G}}$

begin

  $i = i + 1$;

  while $\|e(i) - e(i-1)\| \geq \delta$ **do**

    1: *Find a least squares estimate of* $\mathbf{G}$:

$$\hat{\mathbf{G}}_{(i)} = \mathbf{Y}_1 \left[\left(\hat{\mathbf{S}}_{(i-1)} \diamond \left(\mathbf{X}\hat{\mathbf{H}}^{\mathrm{T}}_{(i-1)} \right)^{\mathrm{T}} \right) \right]^{\dagger}$$

    2: *Find a least squares estimate of* $\mathbf{H}$:

$$\hat{\mathbf{H}}^{\mathrm{T}}_{(i)} = \mathbf{X}^{\dagger}\mathbf{Y}_2 \left[\left(\hat{\mathbf{S}}_{(i-1)} \diamond \hat{\mathbf{G}}_{(i)} \right)^{\mathrm{T}} \right]^{\dagger}$$

    3: *Find a least squares estimate of* $\mathbf{S}$:

$$\hat{\mathbf{S}}_{(i)} = \mathbf{Y}_3 \left[\left(\left(\mathbf{X}\hat{\mathbf{H}}^{\mathrm{T}}_{(i)} \right) \diamond \hat{\mathbf{G}}_{(i)} \right)^{\mathrm{T}} \right]^{\dagger}$$

    4: *Repeat steps* 1 to 3 *until convergence.*

   end

  end

  end

end

---

conditions $KT \geq N$ and $KL \geq N$ must be satisfied. Combining these two inequalities implies $\min(KT, KL) \geq N$, or, equivalently, $K\min(T, L) \geq N$. In addition, the condition $T \geq M$ in (4.24) is required, since $\mathbf{X}$ must have full column-rank to be left-invertible. Hence, the following conditions are necessary

$$K\min(T, L) \geq N \quad \text{and} \quad T \geq M \tag{4.28}$$

Comparing the conditions (4.27) and (4.28), we can note that BALS has a less restrictive requirement on the minimum number K of time blocks for the channel training compared to KRF method. Note that, in the special case $L = 1$ (MISO or SISO system), the inequalities (4.27) and (4.28) are identical, i.e., BALS and KRF are subject to the same training requirements. The advantage of BALS over KRF appears in the MIMO case since BALS can operate under $K < N$, while KRF requires $K \geq N^2$. On the other hand, KRF usually has a lower computational complexity than BALS, as shown later in the discussion of our numerical results.

Note that condition (4.28) is necessary but does not guarantee the uniqueness of the BALS estimates. Sufficient conditions can be derived by studying the rank properties of

---

[2] Note that if $K = 1$, KRF reduces to the conventional LS estimator. However, in this case, we cannot resolve/decouple the estimation of both channel matrices, and the performance gain obtained with such a decoupling *via* solving the problem (4.21) is lost.

$\mathbf{M}_1 = \mathbf{S} \diamond \left(\mathbf{X}\mathbf{H}^{\mathrm{T}}\right) \in \mathbb{C}^{KT \times N}$ and $\mathbf{M}_2 = \mathbf{S} \diamond \mathbf{G} \in \mathbb{C}^{KL \times N}$. To this end, let us invoke the following result.

Lemma 1 (Rank of the Khatri-Rao product (Sidiropoulos; Bro, 2000; Stegeman; Sidiropoulos, 2007)): For $\mathbf{A} \in \mathbb{C}^{I \times N}$ and $\mathbf{B} \in \mathbb{C}^{J \times N}$, if $\text{rank}(\mathbf{A}) \geq 1$ and $\text{rank}(\mathbf{B}) \geq 1$, then $\text{rank}(\mathbf{A} \diamond \mathbf{B}) \geq \min\left(\text{rank}(\mathbf{A}) + \text{rank}(\mathbf{B}) - 1, N\right)$. A concise proof of this lemma can be found in (Stegeman; Sidiropoulos, 2007; Lathauwer, 2008). This result means that the Khatri-Rao product of $\mathbf{A}$ and $\mathbf{B}$ have full column-rank if $\text{rank}(\mathbf{A}) + \text{rank}(\mathbf{B}) \geq N + 1$.

The application of Lemma 1 to the Khatri-Rao structured matrices $\mathbf{M}_1 = \mathbf{S} \diamond \mathbf{X}\mathbf{H}^{\mathrm{T}}$ and $\mathbf{M}_2 = \mathbf{S} \diamond \mathbf{G}$ leads to the following conditions that guarantee the uniqueness of the channel estimates via solving the problems (4.23) and (4.24)

$$\text{rank}(\mathbf{S}) + \text{rank}(\mathbf{X}\mathbf{H}^{\mathrm{T}}) \geq N + 1 \tag{4.29}$$

$$\text{rank}(\mathbf{S}) + \text{rank}(\mathbf{G}) \geq N + 1 \tag{4.30}$$

Let us consider that our channel training design parameters, namely, the IRS phase shift matrix $\mathbf{S}$ and the pilot symbols matrix $\mathbf{X}$ are designed to have full rank. The above conditions yield useful corollaries for the system design when BALS is used. In the following, we discuss these corollaries.

4.6.1 The BS-IRS and IRS-UT channel matrices have full rank

Assuming that both channel matrices $\mathbf{H}$ and $\mathbf{G}$ have full rank (e.g. i.i.d. Rayleigh fading), conditions (4.29)-(4.30) can be rewritten as

$$\min(K, N) + \min(M, N) \geq N + 1 \tag{4.31}$$

$$\min(K, N) + \min(L, N) \geq N + 1. \tag{4.32}$$

We may distinguish two cases, as follows.

- $N \geq T \geq M$ and $N \geq L$: In this scenario, the BS and the UT have small to moderate antenna array sizes, whose number of antennas are smaller than the number of IRS elements. In this case, conditions (4.29)-(4.30) reduce to

$$M + \min(K, N) \geq N + 1 \tag{4.33}$$

$$L + \min(K, N) \geq N + 1 \tag{4.34}$$

– $T \geq M \geq N$: In this scenario, the BS is assumed to be equipped with a large antenna array, which has as many antennas as the number of IRS elements (massive MIMO setup). Since condition (4.29) is always satisfied regardless of the value of K, the uniqueness of the channel estimates only depends on (4.30), which translates to

$$\min(K,N) + \min(L,N) \geq N+1 \tag{4.35}$$

The conditions (4.33) and (4.34) establish a tradeoff between the time dimension (number K of IRS training blocks) and the two spatial dimensions (number M and L of transmit and receive antennas, respectively) from a channel recovery viewpoint. For instance, if $K < N$, these conditions imply $M+K \geq N+1$ and $L+K \geq N+1$, which is equivalent to $\min(M+K, L+K) \geq N+1$. Hence, reducing the number of transmit (or receive) antennas should be compensated by an increase in the number of time blocks to ensure the uniqueness of the channel estimates via the BALS algorithm.

4.6.2 The BS-IRS and IRS-UT channel matrices are rank-deficient

In millimeter-wave MIMO systems, the large number of transmit/receive antennas combined with scattering-poor propagation may result in low-rank channel matrices $\mathbf{H}$ and $\mathbf{G}$. Let us assume that the signal propagating between the BS and IRS experiences R_1 clusters, while the signal propagating between the IRS and the UT experiences R_2 clusters. Moreover, assume that each cluster contributes with one ray that has a complex amplitude and an associated angle of arrival/departure. We can represent the BS-IRS and IRS-UT channels as follows (Heath *et al.*, 2016)

$$\mathbf{H} = \mathbf{A}_{\text{IRS}} \text{diag}(\beta) \mathbf{A}_{\text{BS}}^{\text{H}}, \tag{4.36}$$

$$\mathbf{G} = \mathbf{B}_{\text{UT}} \text{diag}(\gamma) \mathbf{B}_{\text{IRS}}^{\text{H}}, \tag{4.37}$$

where $\mathbf{A}_{\text{BS}} \in \mathbb{C}^{M \times R_1}$, $\mathbf{A}_{\text{IRS}} \in \mathbb{C}^{N \times R_1}$, $\mathbf{B}_{\text{UT}} \in \mathbb{C}^{L \times R_2}$ and $\mathbf{B}_{\text{IRS}} \in \mathbb{C}^{N \times R_2}$ are the array response matrices, and the vectors β and γ hold the complex amplitude coefficients of the BS-IRS and IRS-UT channels, respectively. More specifically, we have $\text{rank}(\mathbf{H}) = R_1$ and $\text{rank}(\mathbf{G}) = R_2$, where it is assumed that $R_1 \leq \min(M,N)$ and $R_2 \leq \min(L,N)$ (rank-deficient case).

First, note that the conditions (4.27) required by the KRF algorithm to solve the decoupled channel estimation problem are not affected by the rank deficiency of the channel matrices. However, this is not the case for BALS, since the uniqueness of the LS estimates of $\mathbf{G}$ and $\mathbf{H}$ depend on the rank of these matrices, as shown in conditions (4.29) and (4.30). Considering BALS, we can draw useful corollaries as follows.

- $T \geq M$: Conditions (4.29) and (4.30) reduce to

$$\min(K,N) + R_1 \geq N+1 \tag{4.38}$$

$$\min(K,N) + R_2 \geq N+1 \tag{4.39}$$

  It is worth discussing the following cases. If $K \geq N$, we conclude that these conditions are always satisfied, irrespective of the ranks of the channel matrices. If $K < N$, these conditions reduce to $K + R_1 \geq N+1$ and $K + R_2 \geq N+1$, yielding a useful design recommendation for the number K of blocks that guarantee the uniqueness of the channel estimates in the rank-deficient case.

- $K \geq N$: In this case, conditions (4.29) and (4.30) are always satisfied, irrespective of the rank of $\mathbf{G}$ and $\mathbf{H}$.

Discussion: It is worth noting that the proposed channel estimation methods still work for $K = 1$. However, in this setup only the cascaded channel $\mathbf{C} = \mathbf{G}\text{diag}(\mathbf{s})\mathbf{H}$ can be estimated. The performance enhancements that come from the decoupling of the estimates of $\mathbf{H}$ and $\mathbf{G}$ (via KRF or BALS) cannot be obtained. Otherwise stated, leveraging extra training time diversity by increasing the number K of IRS phase shift patterns allows us to extract additional gains in comparison to the traditional LS estimator, as shown in our numerical results. However, such gains come at the expense of an increase in training resources. Therefore, here, we see a trade-off between training overhead and performance.

In addition, it is clear from conditions (4.29)-(4.30), or equivalently, from conditions (4.31) and (4.32), that BALS can operate under more flexible choices for K than KRF, since the latter always requires $K \geq N$. Note that, for $M \geq N$ and $L \geq N$, these conditions are satisfied even for small values of K. In practice, this means that BALS may operate with a much lower training overhead than KRF and the traditional LS methods. However, our experience shows that for a large number of IRS elements, working with small values of K results in a slower convergence speed of BALS due to the limited time diversity. Therefore, a trade-off between training overhead and complexity arises when BALS is considered.

Note also that, in terms of the required training time resources, BALS becomes equivalent to KRF in the single transmit antenna case ($M = 1$) and/or in the single receive antenna case ($L = 1$). Otherwise stated, for MISO and/or SIMO IRS-assisted systems, BALS and KRF have the same requirement $K \geq N$. Thus, we can say that BALS is advantageous over KRF in terms of training overhead when considering the MIMO case. Likewise, performance gains of KRF and BALS over the baseline LS method also arise in the MIMO setup, where spatial degrees of freedom at the transmitter and the receiver are efficiently exploited to obtain more accurate channel estimates. Finally, one can note that the channel estimates $\hat{\mathbf{G}}$ and $\hat{\mathbf{H}}$ are affected by scaling factors[3] satisfying $\hat{\mathbf{H}} = \Delta_H \mathbf{H}$ and $\hat{\mathbf{G}} = \mathbf{G}\Delta_G$, where $\Delta_H \Delta_G = \mathbf{I}_N$. These scaling ambiguities are irrelevant in our context since they compensate each other when building the estimate of the cascade BS-IRS-UT channel.

4.7 Generalizations to multi-user scenarios

Although we have focused on the single BS and single UT scenario, the proposed approach, as well as the derived results, can be easily generalized and adapted to IRS-assisted multiple-access/multi-user MIMO systems. Let us take the uplink case as an example. The downlink case follows the same model by just inverting the roles of BS and UT and assuming the channel reciprocity. We can distinguish two scenarios, which are discussed as follows.

4.7.1 Multiple users communicate with a single BS via the IRS

Let us consider U UTs communicating with a single BS via the IRS. The direct link between the UTs and the BS is assumed to be too weak or unavailable. Assuming for simplicity that all the users have the same number L of transmit antennas, we can adapt equation (4.12) such that the contribution of the uth user to the received signal at the BS is given as

$$\overline{\mathbf{Y}}_u[k] = \mathbf{H}^{\mathrm{T}} \mathbf{D}_k(\mathbf{S}) \mathbf{G}_u^{\mathrm{T}} \mathbf{X}_u^{\mathrm{T}} \tag{4.40}$$

where $\mathbf{X}_u \in \mathbb{C}^{T \times L}$ and $\mathbf{G}_u \in \mathbb{C}^{L \times N}$ are respectively the uth user pilot matrix and uplink channel matrix. Note that the IRS-BS channel $\mathbf{H}$ is common to all the users. The total signal received from the U users at the kth time block, in the noiseless case, can then be expressed as

$$\begin{aligned} \overline{\mathbf{Y}}[k] &= \mathbf{H}^{\mathrm{T}} \mathbf{D}_k(\mathbf{S}) \left(\mathbf{X}_1 \mathbf{G}_1\right)^{\mathrm{T}} + \cdots + \mathbf{H}^{\mathrm{T}} \mathbf{D}_k(\mathbf{S}) \left(\mathbf{X}_U \mathbf{G}_U\right)^{\mathrm{T}} \\ &= \mathbf{H}^{\mathrm{T}} \mathbf{D}_k(\mathbf{S}) \left[\sum_{u=1}^{U} \left(\mathbf{X}_u \mathbf{G}_u\right)^{\mathrm{T}}\right]. \end{aligned} \tag{4.41}$$

[3] The permutation ambiguity inherent to blind estimation is not present due to the knowledge of the IRS phase shift matrix $\mathbf{S}$ at the receiver.

Defining $\overline{\mathbf{X}} \doteq [\mathbf{X}_1,\ldots,\mathbf{X}_U] \in \mathbb{C}^{T\times UL}$, and $\overline{\mathbf{G}} \doteq [\mathbf{G}_1^{\mathrm{T}},\ldots,\mathbf{G}_U^{\mathrm{T}}]^{\mathrm{T}} \in \mathbb{C}^{UL\times N}$, equation (4.41) translates to[4]

$$\mathbf{Y}[k] = \mathbf{H}^{\mathrm{T}}\mathbf{D}_k(\mathbf{S})\overline{\mathbf{Z}}^{\mathrm{T}} \quad \overline{\mathbf{Z}} \doteq \overline{\mathbf{X}\mathbf{G}} \in \mathbb{C}^{T\times N}. \tag{4.42}$$

Comparing (4.42) with (4.12), we can see that the multi-user signal model has the same tensor structure as the single-user one, the essential difference being on the definition of the factor matrix $\overline{\mathbf{Z}}$ which is now given by inner product of block matrices composed of U blocks (each having L columns as in the single-user scenario). Otherwise stated (4.42) corresponds to a PARAFAC model of $\overline{\mathscr{Y}} \in \mathbb{C}^{M\times T\times K}$ with factor matrices $(\mathbf{H}^{\mathrm{T}},\overline{\mathbf{X}\mathbf{G}},\mathbf{S})$, and unfoldings 1-mode and 2-mode given as $\overline{\mathbf{Y}}_1 = \mathbf{H}^{\mathrm{T}}\left(\mathbf{S}\diamond\left(\overline{\mathbf{X}\mathbf{G}}\right)\right)^{\mathrm{T}}$ and $\overline{\mathbf{Y}}_2 = \overline{\mathbf{X}\mathbf{G}}(\mathbf{S}\diamond\mathbf{H}^{\mathrm{T}})^{\mathrm{T}}$, respectively. Since the structure of the tensor model is not changed, both KRF and BALS algorithms can be directly applied to the multi-user model (4.42) under more restrictive choices for T, due to the fact the full rankness of $\mathbf{X}$ now requires $T \geq UL$. In this case, assuming that the channel matrices have full rank, the application of Lemma 1 leads to

$$\min(K,N)+\min(UL,N) \geq N+1 \tag{4.43}$$

$$\min(K,N)+\min(M,N) \geq N+1. \tag{4.44}$$

These conditions are analogous to (4.31)-(4.32), by exchanging the roles of M and L, while adding the factor U.

4.7.2 Multiple users communicate with multiple BSs via the IRS

We consider that P BSs receive the signals transmitted by the U users via the IRS. Without loss of generality, the BSs are assumed to be equipped with the same number M of antennas. The model (4.42) is only slightly modified by adding a dependency of the received signal on the index p of the receiving BS, i.e.,

$$\overline{\mathbf{Y}}_p[k] = \mathbf{H}_p^{\mathrm{T}}\mathbf{D}_k(\mathbf{S})\overline{\mathbf{Z}}^{\mathrm{T}}, \quad \overline{\mathbf{Z}} \doteq \overline{\mathbf{X}\mathbf{G}}. \tag{4.45}$$

In particular, in a cooperative setting where the P BSs communicate (e.g. via a common backhauling structure), we can derive an equivalent augmented signal model as follows

$$\overline{\overline{\mathbf{Y}}}[k] = \begin{bmatrix} \overline{\mathbf{Y}}_1[k] \\ \vdots \\ \overline{\mathbf{Y}}_P[k] \end{bmatrix} = \begin{bmatrix} \mathbf{H}_1^{\mathrm{T}} \\ \vdots \\ \mathbf{H}_P^{\mathrm{T}} \end{bmatrix} \mathbf{D}_k(\mathbf{S})\overline{\mathbf{Z}}^{\mathrm{T}} = \overline{\mathbf{H}}^{\mathrm{T}}\mathbf{D}_k(\mathbf{S})\overline{\mathbf{Z}}^{\mathrm{T}}, \tag{4.46}$$

[4] Note that the positions of $\mathbf{H}$ and $\mathbf{G}$ in are swapped in (4.42) compared to (4.12) in addition to transposition, since channel reciprocity is assumed for the UT-IRS and IRS-BS links.

where $\overline{\mathbf{H}} \doteq [\mathbf{H}_1, \ldots, \mathbf{H}_P]^{\mathrm{T}} \in \mathbb{C}^{PM \times N}$ is the composite channel combining the IRS links to the P BSs. The received signal (4.46) corresponds to a PARAFAC model of $\overline{\overline{\mathscr{Y}}} \in \mathbb{C}^{PM \times T \times K}$ with factor matrices $(\overline{\mathbf{H}}, \overline{\mathbf{XG}}, \mathbf{S})$. Note that, differently from the single-user single-BS model (4.12) and the multi-user single-BS model (4.42), in the multi-user multi-BS model (4.46) the dimensionality of the first mode of the received signal tensor has been increased by a factor P due to the assumption of cooperating BSs. In this scenario, condition (4.43) remains the same, while condition (4.44) slightly changes to $\min(K,N) + \min(PM,N) \geq N+1$. As a final remark, in terms of receiver processing, it is clear that both KRF and BALS have increased computational complexity in the discussed multi-user scenarios, due to the increased dimensionality of the channel matrices $\overline{\mathbf{G}}$ and $\overline{\mathbf{H}}$.

In the next section, we discuss the performance of two algorithms - KRF and BALS. The results show the advantages and disadvantages of both methods, including the associated complexities and the restrictions on the choice of the system parameters imposed by each solution. To get a quick overview of the key differences between KRF and BALS, please refer to Table 1.

Tabela 1 – Comparison between the KRF and BALS algorithms

	Solution	Complexity	Parameter choices	Pilot overhead
KRF	Closed-Form	Low	Restrictive	Higher
BALS	Iterative	Moderate/High	Flexible	Lower

4.8 Performance Evaluation

In this section, several numerical results are presented to evaluate the performance of the proposed channel estimation methods, while comparing them to competing approaches. We also evaluate the CRB as a reference for comparisons. The channel estimation accuracy is evaluated in terms of the normalized mean square error (NMSE) given by

$$\mathrm{NMSE}(\hat{\mathbf{H}}) = \frac{1}{R}\sum_{r=1}^{R} \frac{\|\mathbf{H}^{(r)} - \hat{\mathbf{H}}^{(r)}\|_F^2}{\|\mathbf{H}^{(r)}\|_F^2}, \tag{4.47}$$

where $\hat{\mathbf{H}}^{(r)}$ is the BS-IRS channel estimated at the rth run, and R denotes the number of Monte Carlo runs. The same definition applies to the estimated IRS-UT channel. The SNR (in dB) is defined as

$$\mathrm{SNR} = 10\log_{10}(\|[\mathscr{Y}]\|_F^2 / \|[\mathscr{B}]\|_F^2), \tag{4.48}$$

Figura 28 – NMSE of the estimated channels $\hat{\mathbf{H}}$ and $\hat{\mathbf{G}}$.

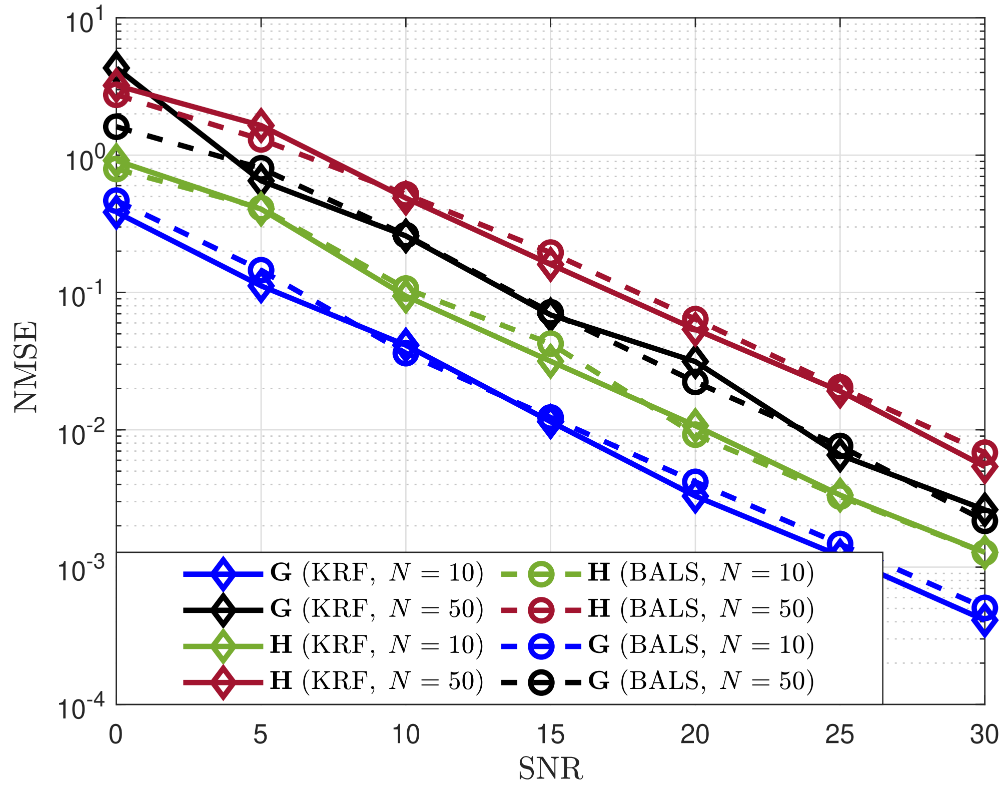

where $\overline{\mathscr{Y}}$ is the noiseless received signal tensor generated according to (4.13), and $\mathscr{B}$ is the additive noise tensor.

We assume that the entries of the BS-IRS and IRS-UT channel matrices $\mathbf{H}$ and $\mathbf{G}$ are independent and identically distributed zero-mean circularly-symmetric complex Gaussian random variables. The Figures 28, 30 and 31, represent an average from $R = 5000$ run Monte Carlo runs for the fixed system parameters $\{T = 4, L = 2, K = 50, M = 3\}$ and $N \in \{50, 100\}$.

Figure 28 depicts the NMSE vs. SNR curves for the KRF and the BALS algorithms. We can see that both algorithms provide satisfactory performances. The performance degrades as the number of IRS elements is increased, which is an expected result since the number of channel coefficients in $\mathbf{G}$ and $\mathbf{H}$ to be estimated also increases with N. In Figure 29, the NMSE of the composite parameter vector θ is shown. The parameters used to get this figure was $K = 100$, $M = 3$, $T = 4$, $L = 20$, $N \in \{10, 50, 100\}$ and 1000 Monte Carlo runs. The results are in line with those of the previous figure, where we observe a performance degradation as N is increased, which confirms our expectations. An approach to overcome such a performance degradation is to partition the IRS into groups and activate/deactivate each group sequentially in the time domain so that at each time, the sub-channels associated with a given group are estimated (You

Figura 29 – NMSE for the equivalent channel $\hat{\theta}$.

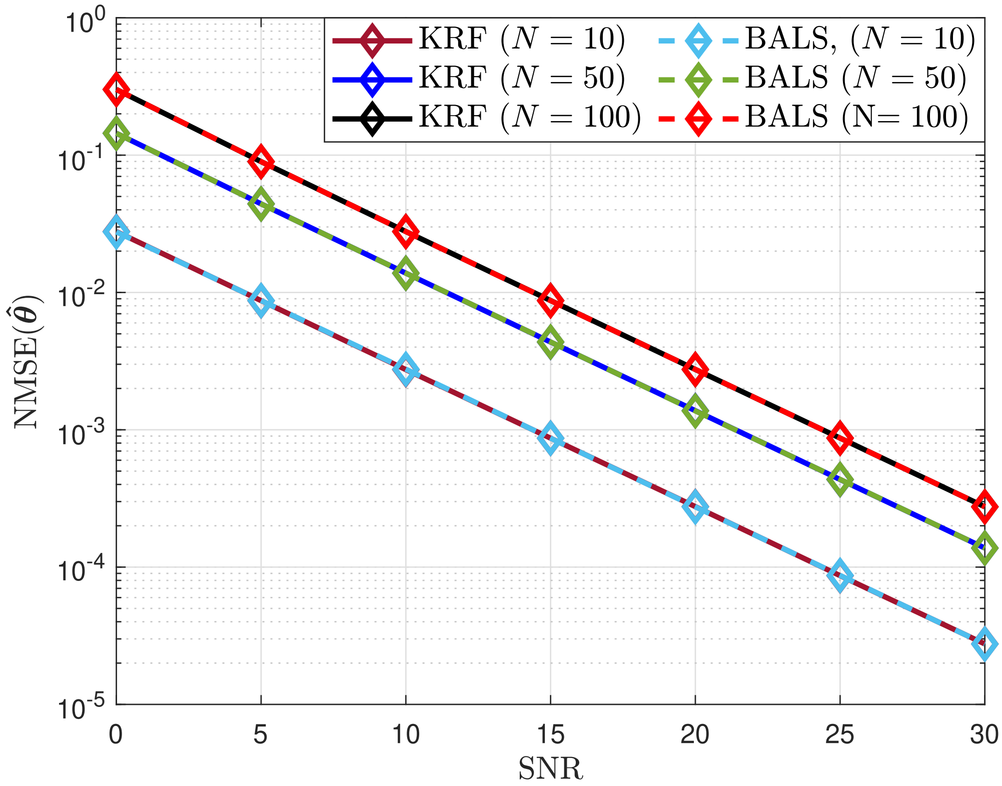

et al., 2020b; You *et al.*, 2020a; Yang *et al.*, 2020). This approach, however, would increase the total training time by a factor corresponding to the number of groups.

The following experiments compare the average runtime of KRF and BALS. The results are depicted in Figure 30 and corroborate the higher complexity of BALS compared to KRF. Note that the runtime of BALS grows faster than that of KRF with the increase in the number N of IRS elements. On the other hand, as we pointed out earlier (comparison between (4.27) and (4.28)), BALS can operate under less restrictive choices (smaller values) for K in comparison to KRF. Hence, there is a tradeoff between complexity and operating conditions for the two proposed channel estimation methods.

In Figure 31, we evaluate the required number of iterations of the BALS algorithm to achieve convergence according to the criterion discussed in Section 4.5.2. We can note that the required number of iterations grows with N, as expected. The difference in the convergence speed for different values of N is more pronounced in the low SNR range. For high SNRs, the convergence becomes less sensitive to N.

In Figure 32, we consider the uplink multi-BS scenario, which follows the signal model (4.46). We assume $P = 2$, $M = 1$, and $U = 1$. We compare the KRF receiver with a

Figura 30 – Average runtime of KRF and BALS algorithms.

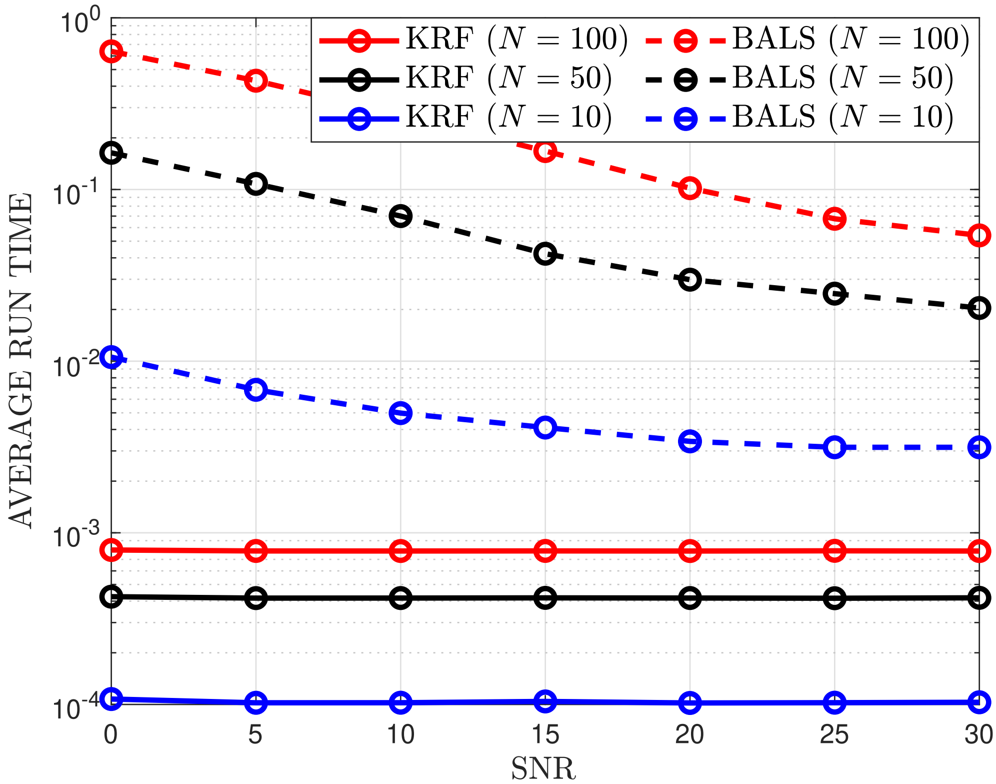

Figura 31 – Number of iterations to convergence of the BALS algorithm.

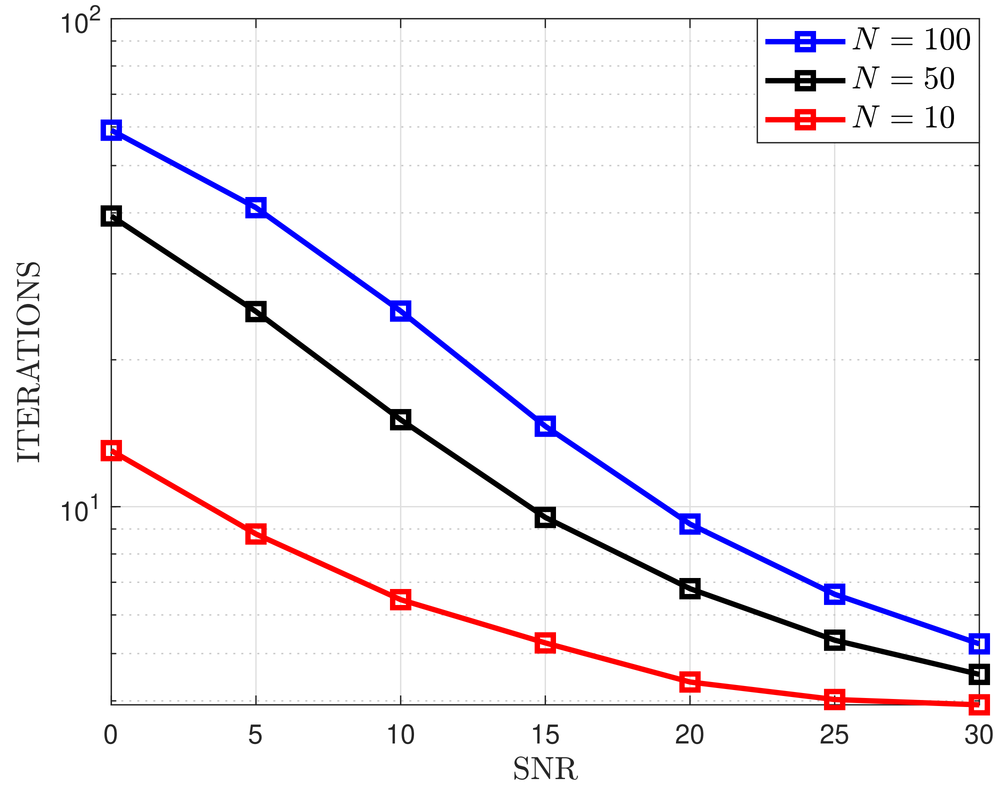

Figura 32 – NMSE of the estimated cascaded channel via the method of (Wang *et al.*, 2020b).

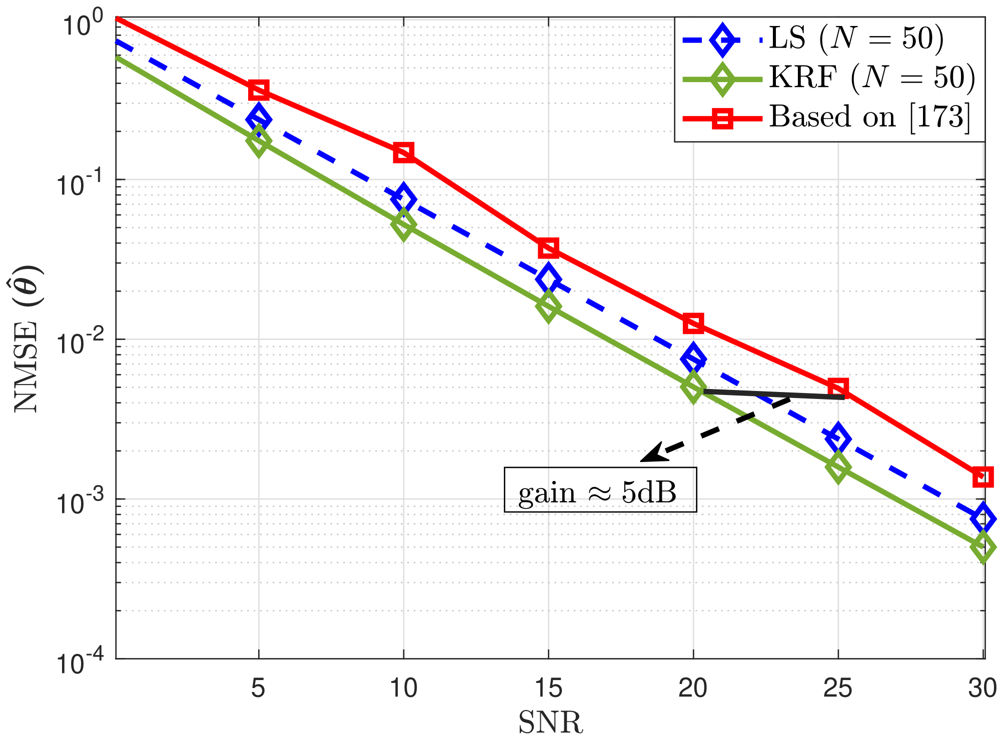

competing channel estimation method proposed recently in (Wang *et al.*, 2020b), which considers the single-antenna multi-user reception scenario[5]. Therein, the channel estimation requires three sequential stages, i.e., three time windows. In the first stage, the direct channel is estimated. In the second one, the equivalent channel between the first user and the BS is estimated. Finally, in the third stage, the channel associated with the remaining users is estimated. Similar to our model, in (Wang *et al.*, 2020b) the equivalent channel is obtained by stacking the contributions of the U users, i.e., $\mathbf{G} \diamond \mathbf{H} = \left[(\mathbf{H}\mathrm{diag}(\mathbf{g}_1))^{\mathrm{T}}, \ldots, (\mathbf{H}\mathrm{diag}(\mathbf{g}_U))^{\mathrm{T}} \right]^{\mathrm{T}}$. We can see that KRF outperforms the competing method, providing an SNR gain of nearly 5dB. Indeed, KRF jointly estimates all the involved channels in a single training stage, while in (Wang *et al.*, 2020b) the channel estimation is carried out in a sequential way, which can induce error propagation. This is a key difference that explains the performance gap in Figure 32.

In Figure 33, we compare the results of the proposed KRF method with the conventional LS method. In this experiment, we consider $K = N = 50$, $T = M = 20$, $L = 8$, and 1000 Monte Carlo runs. The CRB derived in Appendix A (equations (A.16)- (A.17)) is also plotted

[5] In (Wang *et al.*, 2020b) the authors assume multiple receiving single-antenna UTs and a single multi-antenna BS in the downlink, while our model (4.46) assumes multiple receiving BSs and a single multi-antenna UT in the uplink. Due to the channel reciprocity assumption, the signal model of (Wang *et al.*, 2020b) is equivalent to our signal model (4.46). For a fair comparison, we assume $P = 2$ UTs for the channel estimation method of (Wang *et al.*, 2020b). In this case, the dimensions of the channel matrices are the same for both methods.

Figura 33 – Normalized CRB for the equivalent Khatri-Rao channel $\boldsymbol{\theta}$.

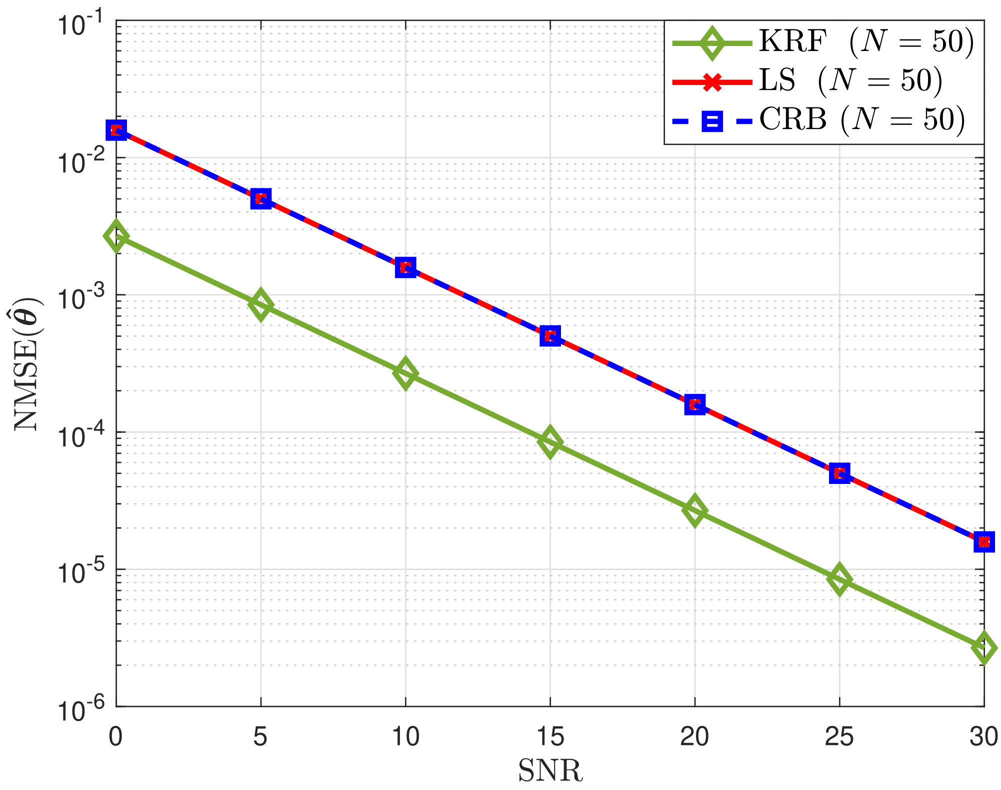

Figura 34 – Noise rejection gain

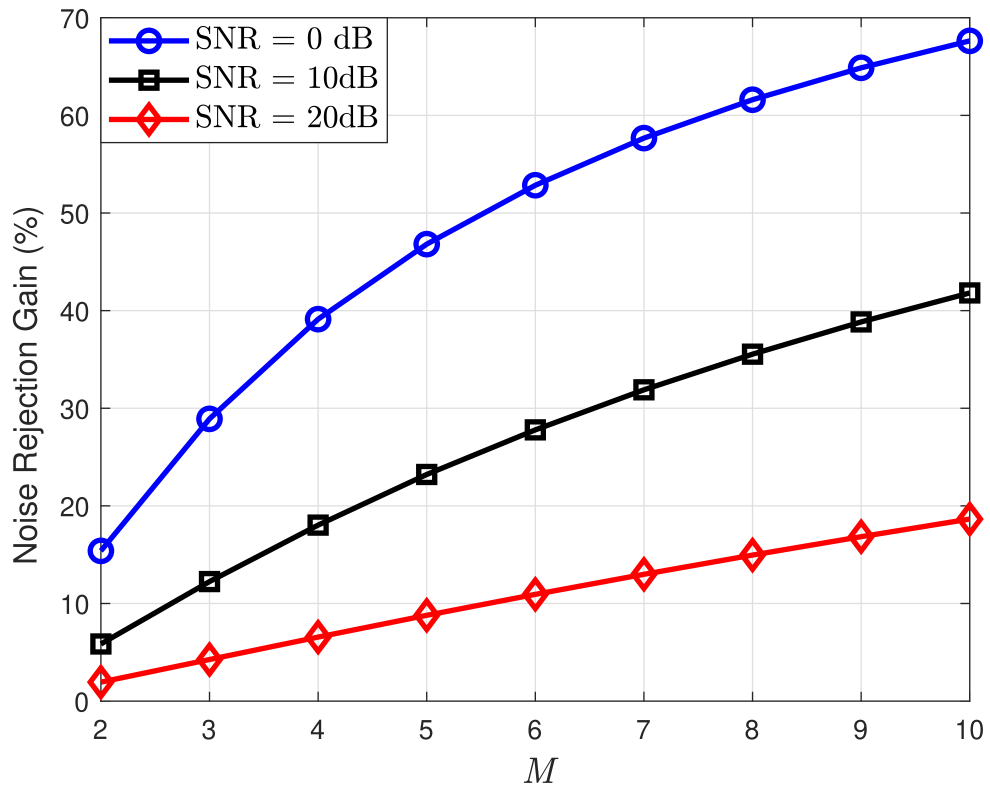

here as a reference for comparison. Recall that the CRB considers the equivalent linear model obtained from the vectorized version of the received signal model given in (4.10), which we repeat here for convenience

$$\mathbf{y} = \mathrm{vec}\left(\mathscr{Y}\right) = \mathbf{U}\theta + \mathbf{b},$$

where $\mathbf{U} = \mathbf{S} \otimes \tilde{\mathbf{X}}$ and $\theta = \mathrm{vec}\left(\mathbf{H}^{\mathrm{T}} \diamond \mathbf{G}\right) \in \mathbb{C}^{MNL}$ is the parameter vector consisting of a vectorized version of the (Khatri-Rao structured) channel matrix combining the IRS-UT and the BS-IRS channel matrices. The conventional LS method plotted in the figure estimates this vectorized channel parameter as $\hat{\theta} = \mathbf{U}^{\dagger}\mathbf{y}$, which ignores the Khatri-Rao structure that is lost in the vectorization of the signal model. In contrast, the proposed KRF method exploits the Khatri-Rao channel structure and builds $\hat{\theta}$ from the decoupled estimates $\hat{\mathbf{H}}$ and $\hat{\mathbf{G}}$ obtained according to Algorithm 3. We can see that the LS solution attains the CRB. Furthermore, an interesting result can be noted. The proposed KRF algorithm outperforms the LS solution. The gain in terms of SNR is around 7dB. This result is explained by the fact that KRF effectively exploits the Khatri-Rao structure that is present in the equivalent channel model. Note that the KRF method solves the problem by reshaping the $ML \times N$ Khatri-Rao channel in the form of N IRS subchannels of dimension $M \times L$. Since $\widetilde{\Omega}_n$ can be approximated as a rank one matrix, the best estimates of $\mathbf{g}_n$ and $\mathbf{h}_n$ can be found from the dominant left and right singular vectors of $\widetilde{\Omega}_n$, respectively, i.e. $\hat{\mathbf{h}}_n = \sqrt{\sigma_1}\mathbf{v}_1^*$ and $\hat{\mathbf{g}}_n = \sqrt{\sigma_1}\mathbf{u}_1$ as shown in Algorithm 3. This means that each rank one approximation applied to $\widetilde{\Omega}_n$ involves discarding $\min(M,L) - 1$ singular values associated with its noise subspace. We can then compute a noise rejection measure associated with the estimation of $\mathbf{g}_n$ and $\mathbf{h}_n$ as

$$R_n = \sum_{r=2}^{\min(M,L)} \sigma_n(r), \quad n = 1,\ldots,N, \tag{4.49}$$

where $\sigma_n(r)$ denotes the r-th singular value of the matrix $\widetilde{\Omega}_n$, $r = 1,\ldots,\min(M,L)$. The noise rejection gain associated with the decoupled estimation of $\mathbf{G}$ and $\mathbf{H}$ is then given by

$$\mathrm{NR} = \sum_{n=1}^{N} \frac{R_n}{||\widetilde{\Omega}_n||_F}. \tag{4.50}$$

The equation (4.50) provides the sum-ratio of the energy of the noise subspace and the energy of the whole space of the set of matrices $\widetilde{\Omega}_n$, yielding a relative measure of how much estimation noise is rejected when the decoupled estimates of $\mathbf{G}$ and $\mathbf{H}$ are extracted from $\hat{\theta}$ by leveraging its intrinsic Khatri-Rao structure. Naturally, when M and L increase (which is the case, for instance,

Figura 35 – NMSE of the $\hat{\theta}$ assuming that $\hat{\mathbf{H}}$ and $\hat{\mathbf{G}}$ are rank-deficient.

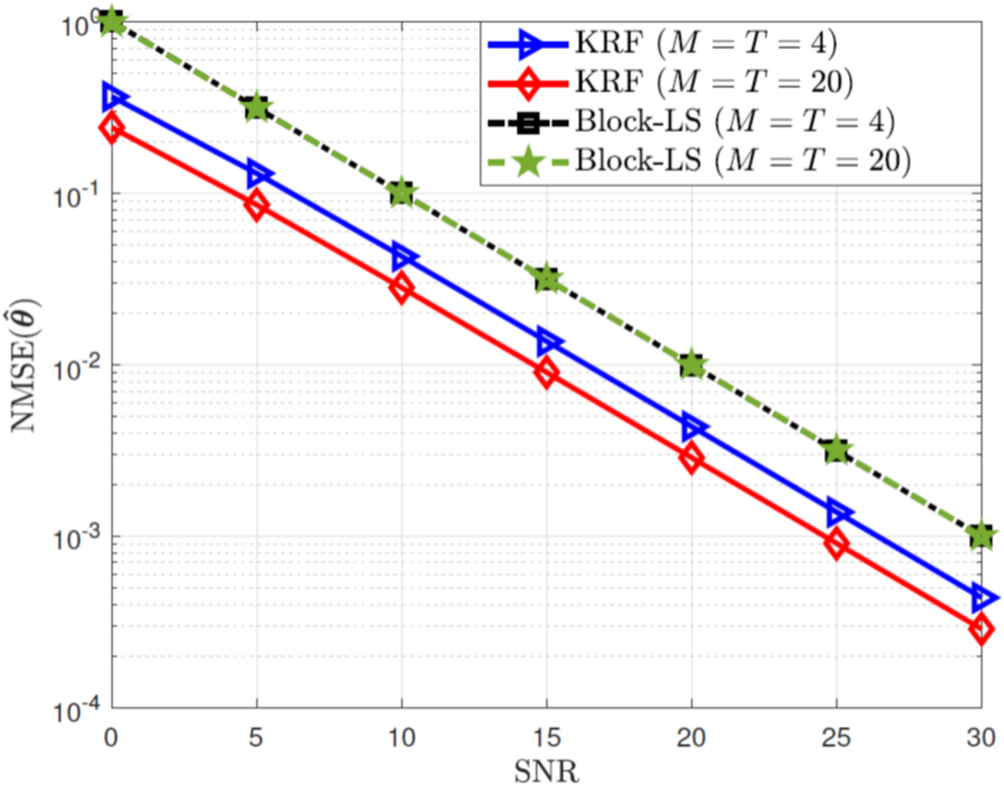

when assuming massive antenna arrays at the BS and UT), the larger is the spreading of the noise across the noise subspace and, consequently, higher levels of noise rejection is achieved, in particular in low SNR values, as shown in Figure 34. This is a distinctive feature of the KRF method that is not exploited by the conventional LS channel estimator.

In Figure 35, we assume that the channel matrices $\mathbf{H}$ and $\mathbf{G}$ are rank-deficient. In this experiment, the channel matrices are generated according to the model given in (4.36)-(4.37). We assume uniform linear arrays at the BS and UT. The IRS has a uniform rectangular array structure. The angles of arrival (AoAs) and angles of departure (AoDs) are randomly generated according to a uniform distribution. At each Monte Carlo run, the azimuth and elevation angles are drawn within the intervals $[-\pi/2, \pi/2]$ and $[0, \pi/2]$, respectively. We consider a single path scenario, where $R_1 = R_2 = 1$, and assume $K = N = 64$, $L = 4$ and $T = M \in \{4, 20\}$. As a reference for comparison, we also plot the NMSE of the LS-based channel estimation method proposed in (Deepak *et al.*, 2021). Therein, the time-domain pilot protocol is the same as the one considered in this work, which consists of dividing the total training time into K blocks across which the phase shift pattern of the IRS is varied. In (Deepak *et al.*, 2021), a two-stage scheme is proposed. In the first stage, the cascaded channel $\mathbf{C}_k = \mathbf{G}\mathbf{D}_k(\mathbf{S})\mathbf{H}$ associated with every time block k is individually estimated via an LS method. We refer to this approach as a "block-LS" method. The second stage extracts the AoA and AoD parameters by combining the K cascaded channel matrices. Since our method does not estimate the angular parameters of the channel matrices, we compare the proposed KRF method with the first stage of the block-LS method of (Deepak *et al.*, 2021), which also provides the unstructured estimate of the channel matrices $\mathbf{H}$ and $\mathbf{G}$. We can see that KRF outperforms block-LS in the two considered system setups. Note that the performance of the block-LS method is not affected when the number M of transmit antennas (assuming $T = M$) is increased. This is in contrast to the KRF method that provides more accurate channel estimates for larger antenna arrays. In particular, the SNR gain of KRF over block-LS is nearly 3.5 dB for $M = T = 4$, and increases to 5.5dB for $M = T = 20$. Indeed, higher values of M and/or L imply higher levels of noise rejection provided by the KRF method *via* exploiting the Khatri-Rao structure of the cascaded channel. These gains come at the expense of an increased computational complexity, as well as an increase in the length of the pilot sequences. Note that the channel ranks R_1 and R_2 do not need to be known by our channel estimation methods. Nevertheless, a performance enhancement could be obtained by exploiting the knowledge of these ranks (see, e.g. methods like (Cheng *et al.*, 2020)) or, alternatively, utilizing compressed sensing methods that capitalize on sparse representations of the channel matrices $\mathbf{H}$ and $\mathbf{G}$. This is an interesting topic for future research.

In Figure 36, we assume that the IRS is affected by amplitude and phase perturbations, as well as unknown blockages, due to hardware and/or environmental-induced impairments. In this scenario, the receiver has an imperfect knowledge of the IRS phase shift matrix. The estimation/refinement of these phase shifts is carried out using the TALS algorithm, which extends BALS by including an additional LS estimation step associated with the update of $\mathbf{S}$ within the loop, as discussed in Section III-D. To model these impairments, we assume $s_{k,n} = \left(a_{k,n} f_{k,n}\right) \bar{s}_{k,n}$, where $\bar{s}_{k,n}$ is the originally designed phase shift (i.e., (k,n)th element of a DFT matrix), $a_{k,n} \in \{0,1\}$ models the presence or not of a blockage at the nth element and kth block, $f_{k,n} \sim CN(0,\gamma)$ models the hardware impairments (Badiu; Coon, 2020; Liu *et al.*, 2020), and γ denotes the variance of these perturbations. In the TALS algorithm, the initialization of $\hat{\mathbf{S}}$ is chosen as a DFT matrix, following its original design. This initialization always provides better results than a random one. Our simulations assume $T = M = 50$, $K = 100$, $L = 4$, $\gamma = 0.01$, 20% blocked IRS elements, and i.i.d. channel matrices. Although a performance degradation is observed in comparison with the perfectly-known IRS phase shifts case, we can see that the

Figura 36 – TALS performance under IRS amplitude/phase perturbations.

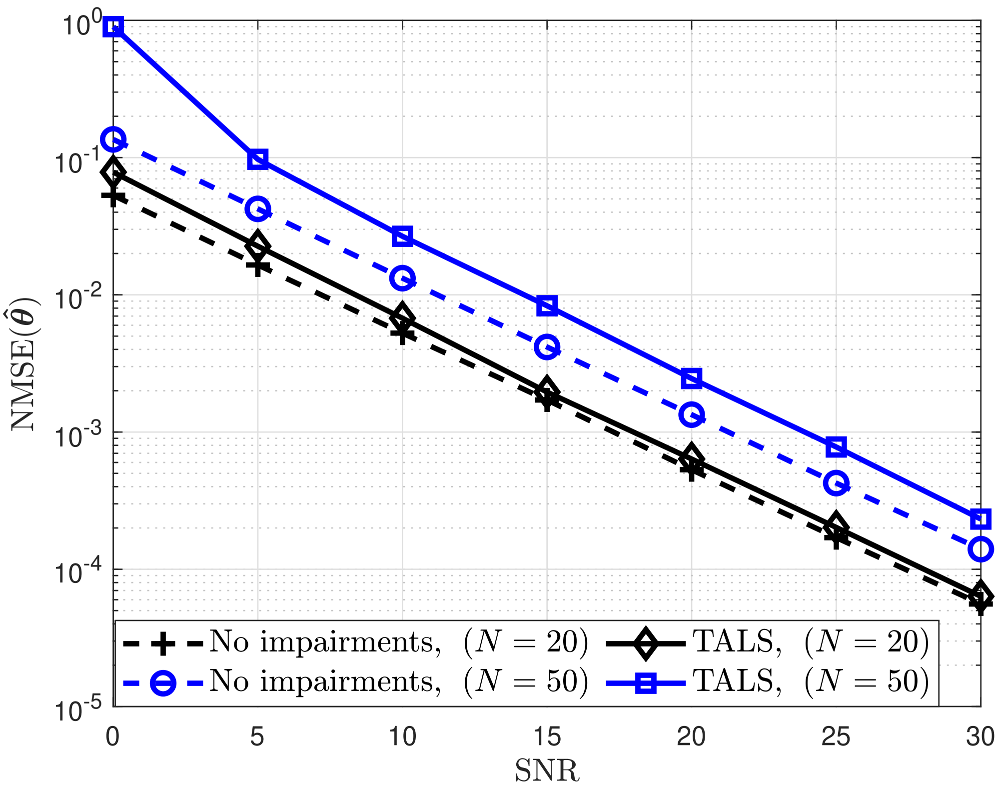

TALS algorithm can handle this more challenging scenario. In particular, the NMSE gap to the ideal case increases as more elements are used in the IRS. Indeed, in the imperfect IRS scenario, the total number of parameters to be estimated by the TALS algorithm is $(K+M+L)N$, in contrast to $(M+L)N$ in the perfectly-known IRS case, implying an addition of KN unknown factors.

4.9 Summary

In this chapter, we have proposed novel pilot-assisted receiver designs for IRS-assisted MIMO communication systems via a tensor modeling approach. The proposed KRF and BALS receivers effectively exploit the tensor structure that is present in the received signal. Both solutions yield decoupled estimates of the BS-IRS and IRS-UT channels at the receiver for a passive IRS. In addition, the proposed tensor modeling approach allows us to deal with a non-ideal setup where the IRS phase shifts are not perfectly known at the receiver due to phase perturbations/fluctuations. In terms of performance, our numerical results have demonstrated the superior performance of KRF and BALS compared to the conventional LS estimator, which ignores the Khatri-Rao structure of the combined channel matrix. Despite its merits, the proposed algorithms may require a significant training overhead that scales linearly with the number of IRS panels. For large IRS panels, a possible solution to this problem is to adopt an IRS element grouping strategy, where a region of neighboring reflecting elements is associated with a single phase shift. Consequently, the "effective" number of channel coefficients to be estimated is reduced. Such a design allows for reducing the training overhead at the expense of some performance degradation.

5 SEMI-BLIND JOINT CHANNEL AND SYMBOL ESTIMATION FOR IRS-ASSISTED MIMO SYSTEM

5.1 Introduction

Acquiring CSI is an important issue since the accuracy of the channel estimate has a direct impact on the gains obtained by IRS-assisted communications. The difficulty is in part due to the passive nature of the surface and the high number of reconfigurable elements. Recent works have proposed channel estimation (CE) methods to IRS-assisted communications. These works can be classified according to the IRS architecture, IRS system setup, and signal processing methodology (Zheng *et al.*, 2022), as follows.

IRS architecture: when the IRS is fully passive, it does not have signal processing capabilities and cannot send/process pilot sequences, as it was pointed out in (Ma *et al.*,). For semi-passive IRSsd, some IRS elements are linked with a few RF chains to facilitate the CE, as discussed in (Hu *et al.*, 2022).[1]

IRS system setup: As far as the system setup is concerned, we can distinguish single and multiuser systems. Additionally, the communication links may be assisted by a single or multiple IRS. As an example, the authors in (Guan *et al.*,) and (Guan *et al.*, 2021) consider a multiuser system, and the CE solution is based on an anchoring scheme, where two nodes are positioned near the IRS to aid the BS. Also, the works (Mirza; Ali, 2021; Hu *et al.*, 2021; Mishra; Johansson,) propose CE strategies consisting of multi-stage or multi-time scale estimation procedures. A double IRS-assisted system is considered in (Zheng *et al.*, 2021a), in which CE and passive beamforming design are investigated.

Signal processing method: Recently, several mechanisms based on deep learning and compressed sensing to acquire CSI have been proposed (Jin *et al.*, 2021; Wang *et al.*, 2020a). The conventional LS CE is assumed in (Jensen; Carvalho, 2020), where a minimum variance unbiased estimator is proposed. In (Deepak *et al.*, 2021), channel training is divided into I blocks. Each block provides a partial channel estimate in the LS sense so that the total channel matrix is estimated once all blocks are processed. The work (Zegrar *et al.*,) proposes a matrix factorization-based method for channel estimation using the eigenvalue decomposition (EVD). The works (Wei *et al.*, 2021) and (Wei *et al.*,) exploit tensor modeling to solve the CE task in

[1] Note that a fully passive architecture is more challenging since the estimation of the cascaded channel, TX-IRS-Rx, or the individual channels Tx-IRS and IRS-Rx channels must be carried out at the ends nodes of the system.

IRS-assisted downlink multi-user systems.

5.2 Related works

The use of tensor methods has been investigated in several previous works in the context of point-to-point (Dou *et al.*, 2020; Khamidullina *et al.*, ; Araújo *et al.*, 2019a; Qian *et al.*, 2019) and cooperative (relay-assisted) MIMO systems (Du *et al.*, 2020b; Rui *et al.*, ; Zniyed *et al.*, 2019). The success of tensor-based methods comes from the powerful uniqueness properties of tensor decompositions compared to matrix-based ones. Moreover, in wireless communications, tensor-based algorithms efficiently exploit the multi-dimensional nature of the received signals in the time, space, and frequency domains. This multi-dimensional characterization of the received signals leads to more flexible transceiver designs than those offered by conventional matrix-based solutions. Recently, a few works have proposed semi-blind solutions for channel estimation in IRS-assisted communications (Alwakeel; Elzanaty, 2022; Huang *et al.*, 2022; Wei *et al.*, 2022). The works (Alwakeel; Elzanaty, 2022) and (Huang *et al.*, 2022) are concerned with the estimation of the cascaded channel only while considering a multi-user SIMO setup. Moreover, (Huang *et al.*, 2022) and (Wei *et al.*, 2022) do not consider the direct links whereas in our work we include the direct link in our two-stage semi-blind receiver, showing that it can be useful to refine the estimation of the data symbol matrix as well as that of the direct channel matrix.

5.3 This chapter

Assuming a fully passive surface architecture and introducing a simple space-time coding[2] scheme at the transmitter, we recast the received signal as a PARATUCK tensor model, which can be seen as a hybrid of PARAFAC and Tucker models (Oliveira *et al.*, 2019; Almeida *et al.*, 2009; Harshman; Lundy, 1996; Bro, 1998). Exploiting the algebraic structure of the PARATUCK tensor model, namely, the different matrix unfoldings of the received signal tensor, a semi-blind receiver based on a TALS estimation scheme is proposed. Our receiver design iteratively estimates the two involved (IRS-BS and UT-IRS) communication channels and the symbol matrix. Moreover, by resorting to the identifiability results of the PARATUCK tensor model, we derive useful system design recommendations that ensure the joint semi-blind recovery of the involved channel and the symbol matrices. In particular, we propose a joint design of

[2] In this work, we use the terminology “coding” to avoid any misunderstanding with the usual concept of precoding, where the channel knowledge is used at the transmitter before the data transmission stage.

the coding matrix and the IRS reflection matrix to optimize the receiver performance. We also present an extension of the proposed receiver algorithm to a scenario, in which the direct link is available. In this scenario, an initial estimation of the transmitted symbol matrix obtained from the direct link is used as a warm start to enhance the semi-blind joint channel and symbol estimation *via* the IRS-assisted link. Finally, we provide expressions for the expected CRB for the proposed semi-blind receiver.

In the following, we summarize the main contributions of this work.

- We present a novel tensor-based semi-blind receiver algorithm for IRS-assisted MIMO systems. The proposed algorithm iteratively estimates the two involved channel matrices as well as the symbol matrix using a TALS algorithm, which exploits a PARATUCK tensor model for the received signals.
- We derive conditions for the joint channel and symbol identifiability, and discuss the design of the coding matrix and the IRS phase shift matrix. A joint design is proposed to improve the receiver performance.
- We extend the proposed semi-blind receiver to a scenario, in which the direct link between transmitter and receiver is available. In this case, the receiver processing has two stages. In the first one, an initial semi-blind estimate of the data symbols obtained *via* the direct link is used as a warm start to a second stage where joint channel and symbol estimation is carried out *via* the IRS-assisted link.
- We show that the proposed semi-blind receiver efficiently exploits the direct link to refine the channel and symbol estimates iteratively. In particular, we discuss the impact of an imperfect IRS absorption (residual reflection) on the performance of the proposed receiver.

Estimating the individual channels is important since, for optimizing the IRS phase shifts, the precoder, and the combiner jointly in a MIMO scenario, the knowledge of the individual channel matrices $\mathbf{H}$ and $\mathbf{G}$ is required (see, e.g., (Qian *et al.*, 2021; Zappone *et al.*, 2021; Zhao *et al.*, 2022)). On the other hand, in the SISO and MISO cases, the knowledge of the cascaded channel is enough (see, e.g, (Subhash *et al.*, 2022), (An *et al.*, 2022)). Moreover, as shown in Chapter 4, estimating the individual channels followed by reconstructing the cascaded channel yields a significant gain in terms of estimation accuracy, compared with the baseline LS method used in most channel estimation schemes. This performance gain comes from the noise rejection achieved by the channel decoupling process.

5.4 System Model

Let us consider a MIMO communication system assisted by an IRS, where the BS and UT have arrays of M and L antennas, respectively, while the IRS is composed of N elements, which can be individually adjusted/configured to generate phase shifts. We assume a quasi-static flat-fading channel, where the coherence time T_C is large enough to span the total transmission duration, as illustrated in Fig. 37, [3] where the channel estimation time window T_E is split into K blocks, and each block has T symbol periods each, with $T_E = KT \ll T_C$. We focus on the uplink scenario, where a multi-antenna UT encodes L independent data streams that are received at the BS with the assistance of an IRS, and possibly reach the BS directly (if the direct link is available).[4] In the general case (when the direct link is available), the discrete-time baseband

Figura 37 – Transmission time structure.

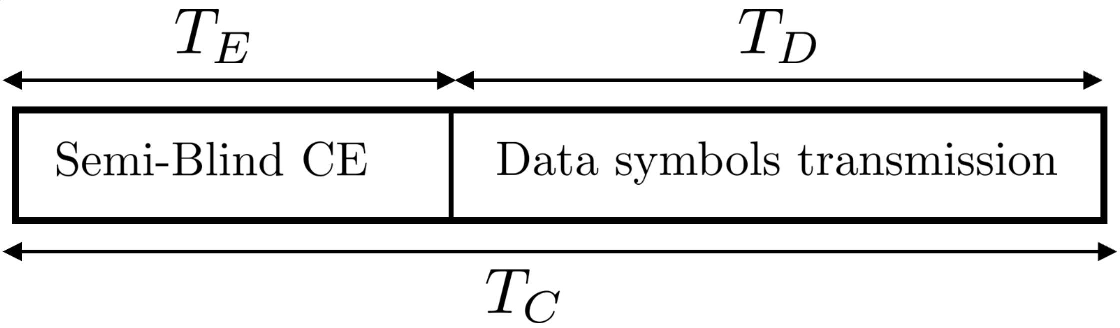

received signal vector during the tth symbol period of the kth block is given by

$$\mathbf{y}[k,t] = \underbrace{\mathbf{H}^{(\mathrm{D})}\mathbf{x}[k,t]}_{\text{Direct link}} + \underbrace{\mathbf{H}\mathrm{diag}(\mathbf{s}[k,t])\mathbf{G}\mathbf{x}[k,t]}_{\text{IRS-assisted link}} + \mathbf{b}[k,t]\,, \tag{5.1}$$

where $\mathbf{H}^{(\mathrm{D})} \in \mathbb{C}^{M\times L}$ is the direct channel matrix between the UT and the BS, whereas $\mathbf{H} \in \mathbb{C}^{M\times N}$ and $\mathbf{G} \in \mathbb{C}^{N\times L}$ denotes the IRS-BS and UT-IRS channel matrices, respectively. The UT employs a space-time encoding scheme that "diagonally" encodes the input symbols such that $\mathbf{x}[k,t] = \mathrm{diag}(\mathbf{w}[k,t])\mathbf{x}[t] \in \mathbb{C}^{L\times 1}$ contains the encoded symbol vector, $\mathbf{x}[t]$, transmitted during the tth symbol period of the kth block. The vector $\mathbf{s}[k,t] \in \mathbb{C}^{N\times 1}$ collects the IRS phase shifts, and $\mathbf{b}[k,t] \in \mathbb{C}^{M\times 1}$ is the corresponding additive white Gaussian noise vector. We assume that the phase shift vector $\mathbf{s} \in \mathbb{C}^{N\times 1}$ and the coding vector $\mathbf{w} \in \mathbb{C}^{L\times 1}$ are constant during the T time slots

[3] Our semi-blind solution acts only within the channel estimation window, i.e., during the time window T_E. The optimization of the IRS phase shifts as well as the precoder and combiner, followed by optimized data transmission in the time window T_D are out of the scope of this work.

[4] Although the uplink case is assumed here, the signal model and the algorithms proposed in this work are equally applicable to the downlink case by inverting the roles of the transmitter and the receiver.

Figura 38 – Uplink IRS-assisted MIMO system diagram.

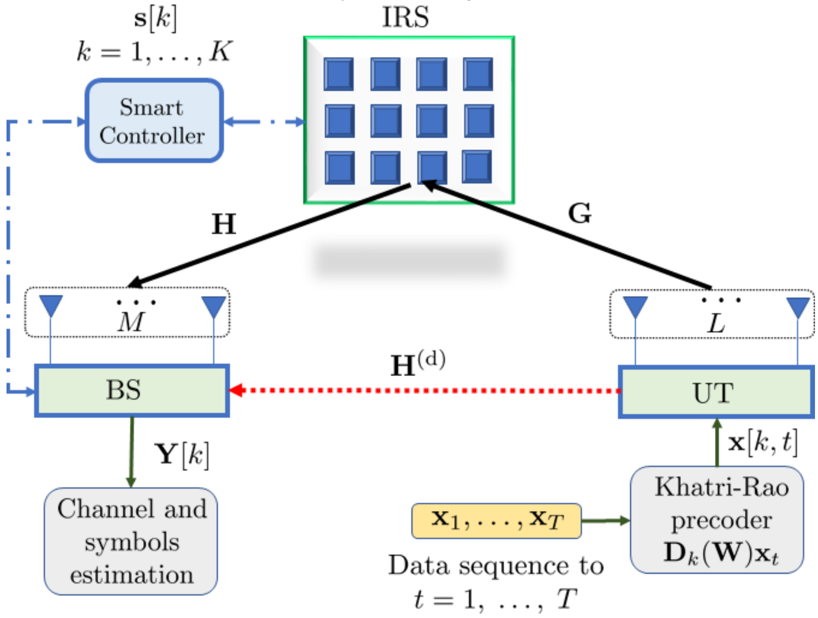

Figura 39 – Time protocol when the direct BS-UT link is not available.

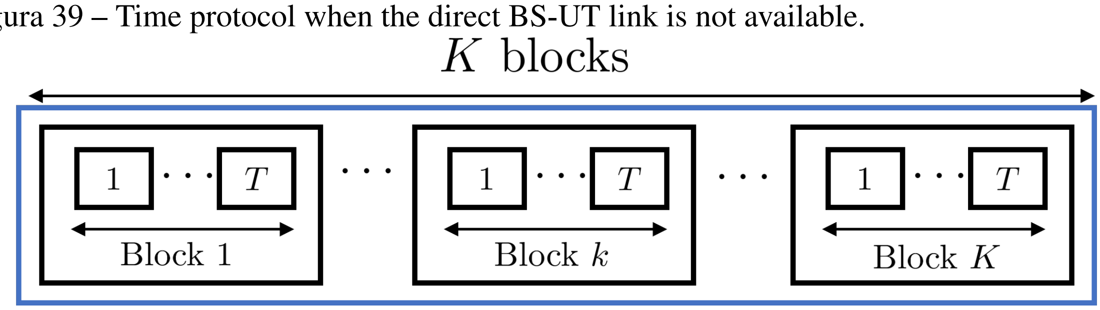

of the kth block and vary from block to block, which means that $\mathbf{s}[k,t] = \mathbf{s}[k]$ and $\mathbf{w}[k,t] = \mathbf{w}[k]$, for $1 \leq t \leq T$.

With these assumptions, collecting the received signals during the T time slots of each block yields

$$\mathbf{Y}[k] = \mathbf{H}^{(\mathrm{D})} D_k(\mathbf{W})\mathbf{X}^{\mathrm{T}} + \mathbf{H} D_k(\mathbf{S}) \mathbf{G} D_k(\mathbf{W})\mathbf{X}^{\mathrm{T}} + \mathbf{B}[k]\,, \tag{5.2}$$

where $\mathbf{Y}[k] \doteq [\mathbf{y}[k,1], \ldots, \mathbf{y}[k,T]] \in \mathbb{C}^{M\times T}$ collects the received signal vectors during the $t = 1, \ldots, T$ time slots of the kth block. In this chapter, we consider two possible scenarios. In the first one, the direct link is assumed to be weak, or unavailable. In the second one, both the IRS-assisted link and the direct link are exploited as illustrated in Fig. 38.

Regarding the channel model, no particular assumption is made in this chapter. We can assume that the channel matrices follow an i.i.d Rayleigh fading model or, alternatively, are described by a geometrical model with a few specular paths. For instance, we can assume that the UT-IRS and IRS-BS links are subject to low scattering propagation, such that $\mathbf{H} = \mathbf{A}_{\mathrm{IRS}}\mathrm{diag}(\beta)\mathbf{A}_{\mathrm{BS}}^{\mathrm{H}}$, and $\mathbf{G} = \mathbf{B}_{\mathrm{UT}}\mathrm{diag}(\gamma)\mathbf{B}_{\mathrm{IRS}}^{\mathrm{H}}$, where $\mathbf{A}_{\mathrm{BS}} \in \mathbb{C}^{M\times R_1}$, $\mathbf{A}_{\mathrm{IRS}} \in \mathbb{C}^{N\times R_1}$, $\mathbf{B}_{\mathrm{UT}} \in \mathbb{C}^{L\times R_2}$

and $\mathbf{B}_{\text{IRS}} \in \mathbb{C}^{N \times R_2}$ are the array response matrices, and the vectors β and γ hold the complex amplitude coefficients of the IRS-BS and UT-IRS channels, respectively, while R_1 and R_2 denote the number of clusters between IRS-BS and UT-IRS, respectively (Heath *et al.*, 2016).

5.5 Semi-blind receiver without the direct link

Considering the first scenario, when the direct link is weak or unavailable, the received signal in (5.2) reduces to

$$\mathbf{Y}[k] = \mathbf{H}D_k(\mathbf{S})\mathbf{G}D_k(\mathbf{W})\mathbf{X}^{\text{T}} + \mathbf{B}[k], \tag{5.3}$$

where $\mathbf{S} \doteq [\mathbf{s}[1], \ldots, \mathbf{s}[K]]^{\text{T}} \in \mathbb{C}^{K \times N}$, $\mathbf{W} \doteq [\mathbf{w}[1], \ldots, \mathbf{w}[K]]^{\text{T}} \in \mathbb{C}^{K \times L}$ are the phase shift matrix and coding matrix, respectively, and $\mathbf{X} \doteq [\mathbf{x}[1], \ldots, \mathbf{x}[T]]^{\text{T}} \in \mathbb{C}^{T \times L}$ is the transmitted symbol matrix. Note that the useful (signal) part of the received signal during the kth block can be identified as the kth matrix slice of a *received signal tensor* $\mathcal{Y} \in \mathbb{C}^{M \times T \times K}$ that satisfies a PARATUCK decomposition (Almeida *et al.*, 2009; Harshman; Lundy, 1996), where the scalar form of the noiseless received signal tensor $\overline{\mathcal{Y}}$ can be expressed as

$$\bar{y}_{m,t,k} = \sum_{n=1}^{N} \sum_{l=1}^{L} g_{n,l} x_{t,l} h_{m,n} s_{k,n} w_{k,l}. \tag{5.4}$$

Note that the interaction matrices of the PARATUCK model correspond to the matrices $\mathbf{S}$ and $\mathbf{W}$ that collect, respectively, the phase shifts (introduced by the IRS) and the coding coefficients (applied at the transmitter), which are fixed and known at the receiver. To summarize, comparing equations (3.31) and (5.3), the following correspondence can be established

$$\left(\mathbf{A}, \mathbf{B}, \mathbf{R}, \mathbf{C}^{\mathbf{A}}, \mathbf{C}^{\mathbf{B}}\right) \leftrightarrow \left(\mathbf{H}, \mathbf{X}, \mathbf{G}, \mathbf{S}, \mathbf{W}\right). \tag{5.5}$$

Figure 40 illustrates the representation of the (noiseless) received signal as a PARATUCK2 decomposition.

Figura 40 – PARATUCK2 model for the received signal

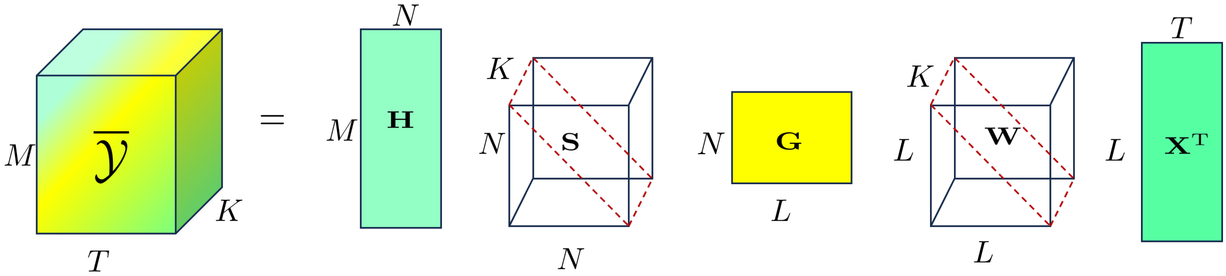

The algebraic properties of this PARATUCK tensor signal model are exploited to formulate our semi-blind receiver for joint channel and symbol estimation. A more complete scenario, in which the direct link is available, as indicated in (5.2), is discussed later.

Remark 4 *The IRS-assisted channel is usually represented in an equivalent form in which the channels* $\mathbf{G}$ *and* $\mathbf{H}$ *are linked by a Khatri-Rao product. This link can be seen by defining the channel parameter vector* $\theta = vec(\mathbf{G}^T \diamond \mathbf{H})$. *In general,* θ *can be directly estimated in the LS sense from the received signal or constructed once the individual estimates of* $\mathbf{G}$ *and* $\mathbf{H}$ *are obtained. In this chapter, we adopt the second approach.*

Our goal is to jointly estimate all the UT-IRS channel $\mathbf{G} \in \mathbb{C}^{N \times L}$, the IRS-BS channel $\mathbf{H} \in \mathbb{C}^{M \times N}$, and the symbol matrix $\mathbf{X} \in \mathbb{C}^{T \times L}$ by exploiting the tensor structure of the received signal model (5.3). We start by stating the following optimization problem:

$$\min_{\mathbf{H},\mathbf{G},\mathbf{X}} \sum_{k=1}^{K} \left\| \mathbf{Y}[k] - \mathbf{H} D_k(\mathbf{S}) \mathbf{G} D_k(\mathbf{W}) \mathbf{X}^{\mathrm{T}} \right\|_F^2. \tag{5.6}$$

This problem is highly nonlinear since it involves multiple products of the unknown variables, represented by the matrices $\mathbf{H}, \mathbf{G}$, and $\mathbf{X}$. However, we take a simpler route to solve the above problem by capitalizing on the multi-linear nature of the received signal and exploiting the PARATUCK tensor model structure (Almeida *et al.*, 2009; Harshman; Lundy, 1996). By operating on each one of the three different matrix unfoldings of this tensor model, we derive the key equations for conditionally minimizing the cost function (5.6) for each unknown matrix in the least squares (LS) sense, while assuming that the remaining quantities are fixed. To simplify the presentation, we temporarily omit the noise term during the development of the main steps.

5.5.1 Estimation of the IRS-BS channel

Let us first consider the estimation of the IRS-BS channel matrix. Starting from the frontal slice representation in (5.3), and stacking column-wise the K matrix slices $\{\mathbf{Y}[k]\}$, $k = 1, \ldots, K$, we get

$$\mathbf{Y}_1 \doteq \left[\mathbf{Y}[1], \ldots, \mathbf{Y}[K]\right] = \mathbf{H}\mathbf{F}^{\mathrm{T}} + \mathbf{B}_1 \ \in \mathbb{C}^{M \times TK}, \tag{5.7}$$

which corresponds to the 1-mode unfolding of the received signal tensor in (5.4), where

$$\mathbf{F} \doteq \begin{bmatrix} \mathbf{X} D_1(\mathbf{W}) \mathbf{G}^{\mathrm{T}} D_1(\mathbf{S}) \\ \vdots \\ \mathbf{X} D_K(\mathbf{W}) \mathbf{G}^{\mathrm{T}} D_K(\mathbf{S}) \end{bmatrix} \ \in \ \mathbb{C}^{TK \times N}, \tag{5.8}$$

and $\mathbf{B}_1$ is the corresponding 1-mode unfolding of the additive noise tensor. The estimation of $\mathbf{H}$ can be obtained by solving the following LS problem

$$\hat{\mathbf{H}} = \arg\min_{\mathbf{H}} \left\| \mathbf{Y}_1 - \mathbf{H}\mathbf{F}^{\mathrm{T}} \right\|_F^2, \tag{5.9}$$

the solution of which is given by

$$\hat{\mathbf{H}} = \mathbf{Y}_1 \left(\mathbf{F}^{\mathrm{T}}\right)^{\dagger}. \tag{5.10}$$

5.5.2 UT-IRS channel estimation

To derive the update equation for the estimation of the UT-IRS channel matrix $\mathbf{G}$, let us apply the vec(.) operator to (5.3), which gives

$$\begin{aligned} \mathrm{vec}\left(\mathbf{Y}[k]\right) &= (\mathbf{X} \otimes \mathbf{H})\mathrm{vec}\left(D_k(\mathbf{S})\mathbf{G}D_k(\mathbf{W})\right) \\ &= (\mathbf{X} \otimes \mathbf{H})\left(D_k(\mathbf{W}) \otimes D_k(\mathbf{S})\right)\mathrm{vec}(\mathbf{G}) + \mathrm{vec}\left(\mathbf{B}[k]\right), \end{aligned} \tag{5.11}$$

where we have applied property (6) twice. Now, applying property (7) to (5.11) yields

$$\mathrm{vec}\left(\mathbf{Y}[k]\right) = (\mathbf{X} \otimes \mathbf{H})\mathrm{diag}(\mathrm{vec}(\mathbf{G}))\left(\mathbf{W}_{k.}^{\mathrm{T}} \otimes \mathbf{S}_{k.}^{\mathrm{T}}\right) + \mathrm{vec}\left(\mathbf{B}[k]\right), \tag{5.12}$$

where we have used the fact that $(D_k(\mathbf{W}) \otimes D_k(\mathbf{S}))$ is actually $\mathrm{diag}\left(\mathbf{W}_{k.}^{\mathrm{T}} \otimes \mathbf{S}_{k.}^{\mathrm{T}}\right)$. By stacking column-wise $\mathrm{vec}\left(\mathbf{Y}[1]\right), \ldots, \mathrm{vec}\left(\mathbf{Y}[K]\right)$, and using (5.12), we can obtain the 3-mode unfolding of the received signal tensor as follows

$$\begin{aligned} \mathbf{Y}_3 &\doteq \left[\mathrm{vec}\left(\mathbf{Y}[1]\right), \ldots, \mathrm{vec}\left(\mathbf{Y}[K]\right)\right] \\ &= (\mathbf{X} \otimes \mathbf{H})\mathrm{diag}(\mathrm{vec}(\mathbf{G}))\Psi + \mathbf{B}_3, \in \mathbb{C}^{TM \times K} \end{aligned} \tag{5.13}$$

where

$$\begin{aligned} \Psi &\doteq \left[\mathbf{W}_{1.}^{\mathrm{T}} \otimes \mathbf{S}_{1.}^{\mathrm{T}}, \ldots, \mathbf{W}_{K.}^{\mathrm{T}} \otimes \mathbf{S}_{K.}^{\mathrm{T}}\right] \\ &= \mathbf{W}^{\mathrm{T}} \diamond \mathbf{S}^{\mathrm{T}} \in \mathbb{C}^{LN \times K}. \end{aligned} \tag{5.14}$$

Finally, vectorizing (5.13) and applying property (6) yields

$$\mathrm{vec}\left(\mathbf{Y}_3\right) = \left[\Psi^{\mathrm{T}} \diamond (\mathbf{X} \otimes \mathbf{H})\right]\mathrm{vec}(\mathbf{G}) + \mathrm{vec}\left(\mathbf{B}_3\right). \tag{5.15}$$

Thus, an estimate of $\mathbf{G}$ in the LS sense can be obtained by solving the following problem

$$\hat{\mathbf{G}} = \arg\min_{\mathbf{G}} \left\| \mathrm{vec}\left(\mathbf{Y}_3\right) - \left[\Psi^{\mathrm{T}} \diamond (\mathbf{X} \otimes \mathbf{H})\right]^{\dagger}\mathrm{vec}(\mathbf{G}) \right\|_F^2, \tag{5.16}$$

the solution of which is given by

$$\hat{\mathbf{G}} = \mathrm{unvec}_{N \times L}\Big(\left[\Psi^{\mathrm{T}} \diamond (\mathbf{X} \otimes \mathbf{H})\right]^{\dagger}\mathrm{vec}(\mathbf{Y}_3)\Big). \tag{5.17}$$

Remark 5 *Step 2 of Algorithm 1, which is concerned with the estimation of the UT-IRS channel matrix, can be simplified by assuming that Ψ defined in (5.14) is an $LN \times K$ semi-unitary matrix satisfying $\Psi^* \Psi^T = K\mathbf{I}_{LN}$ (this choice is discussed in Appendix A.1). In this case, it can be shown that the LS estimation step (5.17) simplifies to*

$$vec(\mathbf{G}) = (1/K) \cdot \Sigma_{\mathbf{Q}}^{-1} (\Psi^T \diamond \mathbf{Q})^H vec(\mathbf{Y}_3), \tag{5.18}$$

where $\mathbf{Q} \doteq [\mathbf{q}_1, \ldots, \mathbf{q}_{LN}] = \mathbf{X} \otimes \mathbf{H} \in \mathbb{C}^{TM \times LN}$, and

$$\Sigma_{\mathbf{Q}} \doteq \begin{bmatrix} \|\mathbf{q}_1\|^2 & & \\ & \ddots & \\ & & \|\mathbf{q}_{LN}\|^2 \end{bmatrix}. \tag{5.19}$$

In addition to the complexity reduction, our numerical experiments have shown that the semi-unitary design for Ψ also improves the convergence speed of Algorithm 1. On the other hand, this condition requires $K \geq LN$. It is worth noting, however, that although advantageous from a performance/complexity viewpoint, the semi-unitary condition is not necessary.

5.5.3 Symbol estimation

The final step of our semi-blind receiver estimates the transmitted symbol matrix. To this end, we start from (5.3), and stack column-wise the matrix slices $\mathbf{Y}[1], \ldots, \mathbf{Y}[K]$, to get

$$\mathbf{Y}_2 \doteq \left[\mathbf{Y}[1]^{\mathrm{T}}, \ldots, \mathbf{Y}[K]^{\mathrm{T}}\right] = \mathbf{X}\mathbf{E}^{\mathrm{T}} \in \mathbb{C}^{T \times MK}, \tag{5.20}$$

which corresponds to the 2-mode unfolding of the received signal tensor in (5.4), where

$$\mathbf{E} \doteq \begin{bmatrix} \mathbf{H}D_1(\mathbf{S})\mathbf{G}D_1(\mathbf{W}) \\ \vdots \\ \mathbf{H}D_K(\mathbf{S})\mathbf{G}D_K(\mathbf{W}) \end{bmatrix} \in \mathbb{C}^{MK \times L}. \tag{5.21}$$

Adding the noise term, we have $\mathbf{Y}_2 = \mathbf{X}\mathbf{E}^{\mathrm{T}} + \mathbf{B}_2$. The LS estimate of $\mathbf{X}$ is then obtained by solving

$$\hat{\mathbf{X}} = \arg\min_{\mathbf{X}} \left\|\mathbf{Y}_2 - \mathbf{X}\mathbf{E}^{\mathrm{T}}\right\|_F^2, \tag{5.22}$$

the solution of which is given by

$$\hat{\mathbf{X}} = \mathbf{Y}_2 \left(\mathbf{E}^{\mathrm{T}}\right)^{\dagger}. \tag{5.23}$$

Algoritmo 6: TALS

Procedure

input : $i = 0$; Initialize $\hat{\mathbf{G}}_{(i=0)}$ *and* $\hat{\mathbf{X}}_{(i=0)}$

output : $\hat{\mathbf{H}}$, $\hat{\mathbf{G}}$ and $\hat{\mathbf{X}}$

begin

$i = 1$;

while $\|e(i) - e(i-1)\| \geq \delta$ **do**

1. Using $\hat{\mathbf{G}}_{(i-1)}$ and $\hat{\mathbf{X}}_{(i-1)}$, compute $\hat{\mathbf{F}}_{(i-1)}$ from (5.8) and find a least squares estimate of $\mathbf{H}$: $\hat{\mathbf{H}}_{(i)} = \mathbf{Y}_1 \left(\hat{\mathbf{F}}^{\mathrm{T}}_{(i-1)}\right)^{\dagger}$
2. Using $\hat{\mathbf{H}}_{(i)}$ and $\hat{\mathbf{X}}_{(i-1)}$, find a least squares estimate of $\mathbf{G}$: $\mathrm{vec}(\hat{\mathbf{G}}_{(i)}) = \left[\Psi^{\mathrm{T}} \diamond (\hat{\mathbf{X}}_{(i-1)} \otimes \hat{\mathbf{H}}_{(i)})\right]^{\dagger} \mathrm{vec}(\mathbf{Y}_3)$
3. Using $\hat{\mathbf{G}}_{(i)}$ and $\hat{\mathbf{H}}_{(i)}$, compute $\hat{\mathbf{E}}_{(i)}$ from (5.21) and find a least squares estimate of $\mathbf{X}$: $\hat{\mathbf{X}}_{(i)} = \mathbf{Y}_2 \left(\hat{\mathbf{E}}^{\mathrm{T}}_{(i)}\right)^{\dagger}$

4: $i \leftarrow i + 1$

5: Repeat steps 1 to 4 until convergence.

end

end

end

end

The proposed semi-blind receiver makes use of (5.10), (5.18) and (5.23) to obtain the estimates of channel matrices $\mathbf{G}$ and $\mathbf{H}$, and the symbol $\mathbf{X}$ via a trilinear alternating least squares based estimation scheme, herein referred to as TALS receiver. More specifically, the algorithm consists of a three-step estimation procedure that estimates one matrix at each step, while fixing the other two matrices to their values obtained at the previous estimation steps. Note that the proposed TALS receiver is a semi-blind method since no training sequences are required. The receiver algorithm is summarized in Algorithm 6.

The stopping criterion relies on the normalized squared error measure computed at the end of the ith iteration, given by $\varepsilon_{(i)} = \sum_{k=1}^{K} \|\mathbf{Y}[k] - \hat{\mathbf{Y}}[k]_{(i)}\|_F^2 / \|\mathbf{Y}[k]\|_F^2$, where $\hat{\mathbf{Y}}[k]_{(i)} = \hat{\mathbf{H}}_{(i)} D_k(\mathbf{S}) \hat{\mathbf{G}}_{(i)} D_k(\mathbf{W}) \hat{\mathbf{X}}^{\mathrm{T}}_{(i)}$. The convergence is declared when the difference between the reconstruction errors of two successive iterations falls below a threshold, i.e., $|\varepsilon_{(i)} - \varepsilon_{(i-1)}| \leq \delta$. In this work, we assume $\delta = 10^{-5}$. The convergence criterion of TALS is based on the difference between the reconstruction errors computed in two successive iterations. The complexity of the TALS receiver is dominated by the matrix inverses in steps 1 and 3, which have complexity orders $\mathscr{O}(TKN^2)$ and $\mathscr{O}(LKM^2)$, respectively (Oliveira *et al.*, 2019). Considering the complexity of step 2, which only involves matrix products, the total complexity by iteration of the TALS receiver is given by $\mathscr{O}(TKN^2[1+M^2L]+KLM[NT+M])$.

5.5.4 Identifiability

The joint recovery of $\mathbf{H}$, $\mathbf{G}$, and $\mathbf{X}$ requires that the three LS problems in (5.9), (5.16), and (5.22), have unique solutions, respectively. More specifically, the uniqueness of $\mathbf{H}$ requires that $\mathbf{F}$ defined in (5.8) have full column-rank, which implies $TK \geq N$, while the uniqueness of $\mathbf{G}$ requires that $\left[\Psi^{\mathrm{T}} \diamond (\mathbf{X} \otimes \mathbf{H})\right]$ have full column-rank, implying $TKM \geq LN$. Likewise, the uniqueness of $\mathbf{X}$ requires that $\mathbf{E}$ defined in (5.21) be of full column-rank, which implies $MK \geq L$. Note that the number K of transmitted blocks is the common parameter in these three conditions, which must be simultaneously satisfied. In summary, the following conditions must simultaneously be satisfied the joint uniqueness of $\mathbf{H}$, $\mathbf{G}$, and $\mathbf{X}$:

$$TK \geq N, \quad TKM \geq LN, \quad MK \geq L. \tag{5.24}$$

These conditions establish useful trade-offs involving the time diversities (parameters K and T) and spatial diversities (parameters N, M, L) for the joint recovery of the channel and symbol matrices. More specifically, reducing the number of blocks K and/or the number of symbol periods T can be compensated by a corresponding increase in the number of BS antennas M. As a special case, if the number of BS antennas exceeds the number of UT antennas ($M \geq L$), satisfying these conditions reduces to $TK \geq N$.

Under the conditions stated above, the estimates of $\mathbf{G}$, $\mathbf{H}$, and $\mathbf{X}$ delivered by Algorithm 6 are affected by scaling ambiguities that compensate each other, as follows

$$\hat{\mathbf{H}}\Delta_H = \mathbf{H}, \quad \hat{\mathbf{X}}\Delta_X = \mathbf{X}, \quad \Delta_H^{-1}\hat{\mathbf{G}}\Delta_X^{-1} = \mathbf{G}, \tag{5.25}$$

where Δ_G, Δ_H, and Δ_X are diagonal matrices. These scaling ambiguities can be handled by assuming that the first row of the symbol matrix $\mathbf{X}_{1.} \in \mathbb{C}^{1\times L}$ contains identification symbols that are known at the receiver. Note that the columns of $\mathbf{X} \in \mathbb{C}^{T\times L}$ correspond to the L data streams that are spatially multiplexed at the transmitter. Hence, the knowledge of the first row of $\mathbf{X} \in \mathbb{C}^{T\times L}$ means that the first symbol of each data stream is a known pilot. Therefore, the knowledge of L pilots allows us to eliminate the scaling ambiguity by normalization[5]. A simple

[5] Due to the knowledge of the first row of the data matrix, we use the term “semi-blind” to refer to the proposed

Figura 41 – Time protocol when the assisted link via IRS link is activated.

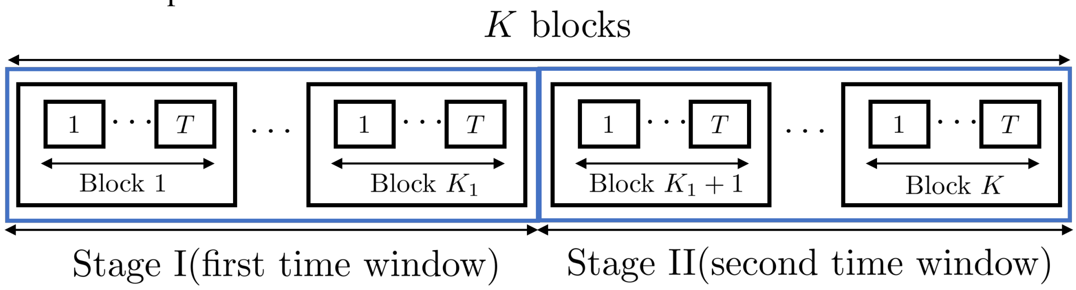

choice is to assume that $\mathbf{X}_{1.} = [1, 1, \ldots, 1]$ so that Δ_X can be determined from the first row of the estimated symbol matrix $\hat{\mathbf{X}}$ after convergence of Algorithm 6 and canceled out by normalization.

Remark 6 *The identifiability conditions (32) show that the minimum value of K can be small if the block length T is large enough. More specifically, a reduction of K can be compensated by an increase of T. Indeed, there is a trade-off between performance and overhead established by our solution. Our experience shows that our solution still works with small values of K that are close to the lower bound established by (32), with a sacrifice on the channel estimation accuracy, especially when the number of IRS elements is large. On the other hand, by increasing K, we obtain finer channel estimates at the expense of increased overhead. In summary, our solution offers the system designer some freedom to trade channel estimation quality for overhead and vice-versa, while still benefiting from a smaller data decoding delay offered by our proposed semi-blind method. To deal with this practical challenge, we can alternatively resort to recent strategies proposed in the literature, which consist of grouping the IRS elements (Yang et al., 2020; Wei et al., 2021; Zheng et al., 2022). However, practical implementation challenges associated with IRS elements grouping must be better investigated since this strategy may cause performance degradation. Nonetheless, this method has drawn attention recently, and some optimal grouping strategies have been investigated, for example in (Kundu et al., 2022; Mao et al., 2022). In particular, (Li et al., 2023) indicates that the grouping of the correlated IRS elements can reach better performance in comparison with the uncorrelated IRS elements scenario.*

5.6 Direct link aided Semi-Blind Receiver

In this section, we present an enhanced version of the semi-blind receiver derived in the previous Section that exploits the direct link between UT and BS, whenever it is available.

receiver. Strictly speaking, a fully-blind solution would not require any knowledge about the data. In our case, the first row of **X** contains known pilots that are embedded into the data blocks to eliminate the scaling ambiguities on the transmitted data streams before demodulation.

The idea is to dedicate part of the transmission time resources to the direct link so that an initial estimate of the transmitted symbols and direct channel can be obtained. The initial symbol estimates are exploited as a “warm start” of the TALS algorithm for estimating the UT-IRS and IRS-BS channels while refining the estimates of the symbols and the direct channel. To this end, we slightly modify the transmission protocol by splitting the total transmission time of K blocks into two-time windows of duration $T_1 = K_1 T$ and $T_2 = K_2 T$ symbol periods, respectively, where $K = K_1 + K_2$ is the total number of time blocks, and $T_c = T_1 + T_2$ the total transmission duration. The time protocol is depicted in Figure 41. During the first time window, the UE transmits data using a coding matrix $\mathbf{W}_1 \in \mathbb{C}^{K_1 \times L}$, while in the second time window, it uses the coding matrix $\mathbf{W}_2 \in \mathbb{C}^{K_2 \times L}$ and the phase shift matrix $\mathbf{S} \in \mathbb{C}^{K_2 \times N}$. A short discussion on the design of $\mathbf{W}_2$ and $\mathbf{S}$ is provided in Appendix A.1.

The receiver processing has two stages. In the first one, joint estimation of the direct channel and the transmitted symbols is carried out during the first time window by exploiting the PARAFAC tensor model of the received signals. The second stage makes use of the estimated symbols in the first time window as an initialization of the TALS algorithm that jointly estimates the involved channel matrices while refining the symbol estimates during its iterative process. As shown later in our numerical experiments, the initialization of the IRS-assisted link using the direct link estimates yields an enhanced TALS algorithm with accelerated convergence and improved estimation accuracy. Therefore, in stage one the IRS is “off", following the approach of (Guan *et al.*, 2021), so that the received signal at BS is given as

$$\mathbf{Y}^{(\mathrm{D})}[k_1] = \mathbf{H}^{(\mathrm{D})} D_{k_1}(\mathbf{W}_1)\mathbf{X}^{\mathrm{T}} + \mathbf{B}[k_1], \tag{5.26}$$

for $k_1 = 1, \ldots, K_1$, where $\mathbf{W}_1 \in \mathbb{C}^{K_1 \times L}$ is the coding matrix used during the first time window of K_1 blocks. The signal part of (5.26) can be viewed as the k_1th frontal matrix slice of a three-way tensor $\overline{\mathscr{Y}}^{(\mathrm{D})} \in \mathbb{C}^{M \times T \times K_1}$ that follows a PARAFAC decomposition with factor matrices $\mathbf{H}^{(\mathrm{D})}, \mathbf{X}, \mathbf{W}_1$. By analogy with (3.19), the following correspondences can be deduced:

$$\left(\mathbf{A}, \mathbf{B}, \mathbf{C}\right) \leftrightarrow \left(\mathbf{H}^{(\mathrm{D})}, \mathbf{X}, \mathbf{W}_1\right). \tag{5.27}$$

From the uniqueness property of the PARAFAC model (Kruskal, 1977; Stegeman; Sidiropoulos, 2007), one can obtain a useful condition for guaranteed direct channel and symbol recovery in the general case where all the factor matrices are unknown. In our context, however, since the coding matrix $\mathbf{W}_1$ is assumed to be known at the receiver (BS), simplified conditions can be obtained. Since $\mathbf{W}_1$ has full column-rank (which requires $K_1 \geq L$), $M \geq 2$ receive antennas and $T \geq 2$ time slots are enough for the joint recovery of $\mathbf{H}^{(\mathrm{D})}$ and $\mathbf{X}$. This problem can be efficiently solved utilizing the Khatri-Rao Factorization algorithm in Chapter 4, as detailed next.

5.6.1 Stage I: Joint direct channel and symbol estimation

Starting from (5.26), and defining

$$\mathbf{Y}^{(\mathrm{D})} \doteq \left[\mathrm{vec}(\mathbf{Y}^{(\mathrm{D})}[1]), \ldots, \mathrm{vec}(\mathbf{Y}^{(\mathrm{D})}[K_1])\right] \in \mathbb{C}^{MT \times K_1}, \tag{5.28}$$

that collects the signals received during the first K_1 time blocks, we have

$$\mathbf{Y}^{(\mathrm{D})} = (\mathbf{X} \diamond \mathbf{H}^{(\mathrm{D})})\mathbf{W}_1^{\mathrm{T}} + \mathbf{B}, \tag{5.29}$$

where we have used property (6), and $\mathbf{B} = [\mathrm{vec}(\mathbf{B}[1]), \ldots, \mathrm{vec}(\mathbf{B}[K_1])] \in \mathbb{C}^{MT \times K_1}$ is the corresponding noise matrix. Defining

$$\mathbf{Z} \doteq (1/K_1)\mathbf{Y}^{(\mathrm{D})}\mathbf{W}_1^{*} = \mathbf{X} \diamond \mathbf{H}^{(\mathrm{D})} + (1/K_1)\mathbf{B}\mathbf{W}_1^{*}, \tag{5.30}$$

an estimate of $\mathbf{X}$ and $\mathbf{H}^{(\mathrm{D})}$ can be found using the Khatri-Rao Factorization algorithm that solves the following problem (Kibangou; Favier, ; Roemer; Haardt, 2010)

$$\min_{\mathbf{X}, \mathbf{H}^{(\mathrm{D})}} \left\| \mathbf{Z} - \mathbf{X} \diamond \mathbf{H}^{(\mathrm{D})} \right\|_F^2, \tag{5.31}$$

which is equivalent to solving L rank-one matrix approximation subproblems, and can be stated as

$$(\hat{\mathbf{X}}, \hat{\mathbf{H}}^{(\mathrm{D})}) = \underset{\{\mathbf{x}_l\}, \{\mathbf{h}_l^{(\mathrm{D})}\}}{\arg\min} \sum_{l=1}^{L} \left\| \widetilde{\mathbf{Z}}_l - \mathbf{h}_l^{(\mathrm{D})} \mathbf{x}_l^{\mathrm{T}} \right\|_F^2, \tag{5.32}$$

where $\widetilde{\mathbf{Z}}_l \doteq \mathrm{unvec}_{M \times T}(\mathbf{z}_l) \in \mathbf{C}^{M \times T}$, and $\mathbf{z}_l \in \mathbb{C}^{MT \times 1}$ denotes the lth column of $\mathbf{Z}$, while $\mathbf{h}_l^{(\mathrm{D})} \in \mathbf{C}^{M \times 1}$ and $\mathbf{x}_l^{\mathrm{T}} \in \mathbf{C}^{1 \times T}$ are the lth column of $\mathbf{H}^{(\mathrm{D})}$ and lth row of $\mathbf{X}$, respectively. Due to space limitations, we have suppressed the details of the KRF algorithm. A pseudo-code of this algorithm can be found in Chapter 4.

Remark 7 *As an alternative to the KRF algorithm, one can also resort to the bilinear alternating least squares (BALS) algorithm that jointly estimates the direct channel matrix and the symbol matrix in an alternating way. In this work, we advocate using the KRF algorithm since it provides similar performance to BALS while being a closed-form solution that affords an efficient implementation since the N involved rank-one matrix approximations can be optimized if executed in parallel processing hardware.*

5.6.2 Stage II: IRS-assisted channel estimation and symbol refinement

After stage I, the IRS is turned "on" during the second transmission time window that spans K_2 blocks. In this case, the total received signal is given by the sum of the direct link and IRS-assisted contributions, and is given by

$$\begin{aligned}\mathbf{Y}[k_2] &= \mathbf{H}^{(\mathrm{D})}D_{k_2}(\mathbf{W}_2)\mathbf{X}^{\mathrm{T}} \\ &+ \mathbf{H}D_{k_2}(\mathbf{S})\mathbf{G}D_{k_2}(\mathbf{W}_2)\mathbf{X}^{\mathrm{T}} + \mathbf{B}[k_2].\end{aligned} \tag{5.33}$$

From the estimated symbol and direct channel matrices $\hat{\mathbf{X}}$ and $\hat{\mathbf{H}}^{(\mathrm{D})}$ delivered by the KRF algorithm in stage I (c.f. problem (5.32)), the interference from the direct link can be removed (or minimized) by subtracting an estimate of its contribution from the total received signal in stage II, yielding

$$\mathbf{Q}[k_2] = \mathbf{Y}[k_2] - \hat{\mathbf{H}}^{(\mathrm{D})}D_{k_2}(\mathbf{W}_2)\hat{\mathbf{X}}^{\mathrm{T}}. \tag{5.34}$$

From (5.33), we can write (5.34) as

$$\mathbf{Q}[k_2] = \mathbf{H}D_{k_2}(\mathbf{S})\mathbf{G}D_{k_2}(\mathbf{W}_2)\mathbf{X}^{\mathrm{T}} + \overline{\mathbf{B}}[k_2], \tag{5.35}$$

where $\overline{\mathbf{B}}[k_2] = \mathbf{B}[k_2] + \mathbf{E_H}D_{k_2}(\mathbf{W}_2)\mathbf{E}_{\mathbf{X}}^{\mathrm{T}}$ is the effective noise, while $\mathbf{E_H} \doteq \mathbf{H}^{(\mathrm{D})} - \hat{\mathbf{H}}^{(\mathrm{D})}$ and $\mathbf{E_X} \doteq \mathbf{X} - \hat{\mathbf{X}}$ are error matrices associated with the estimates of the direct channel and symbol matrix in stage I. It is clear that the energy of the overall additive noise term in (5.34) depend on the energy of these error terms, which in turn depends on the quality of the direct link compared with the IRS-assisted link.

Note that the signal part of (5.35) corresponds to a PARATUCK decomposition of $\mathcal{Q} \in \mathbb{C}^{M\times T\times K_2}$, which is analogous to the (5.3), where the third mode has dimension K_2 (instead of K). Hence, estimates of the IRS-assisted channel matrices $\mathbf{G}$ and $\mathbf{H}$, as well as refined estimates of the symbol matrix $\mathbf{X}$ can be obtained from $\mathcal{Q}$ by following the procedure discussed in Section IV.A-IV.C. This leads to a second semi-blind receiver, referred to as E-TALS, summarized in Algorithm 7.

In addition, from the refined symbol estimates, an enhanced estimate of the direct channel matrix $\mathbf{H}^{(\mathrm{D})}$ can also be obtained at the end of stage II, i.e., at the convergence of the algorithm. More specifically, suppose that the E-TALS algorithm has converged at the ith iteration, and let $\mathbf{X}_{(i)}$ be the refined estimate of the symbol matrix obtained at this iteration.

Substituting $\hat{\mathbf{X}}_{(i)}$ into (5.26), a refined estimate of the direct channel can be obtained by solving the following problem

$$\min_{\mathbf{H}^{(\mathrm{D})}} \sum_{k_1=1}^{K_1} \left\| \mathbf{Y}^{(\mathrm{D})}[k_1] - \mathbf{H}^{(\mathrm{D})} D_{k_1}(\mathbf{W}_1) \hat{\mathbf{X}}_{(i)}^{\mathrm{T}} \right\|_F^2, \tag{5.36}$$

the solution of which is given by

$$\hat{\mathbf{H}}^{(\mathrm{D})} = \left[\mathbf{Y}^{(\mathrm{D})}[1], \ldots, \mathbf{Y}^{(\mathrm{D})}[K_1]\right] \left[(\mathbf{W}_1 \diamond \hat{\mathbf{X}}_{(i)})^{\mathrm{T}}\right]^{\dagger}. \tag{5.37}$$

In summary, when the direct link is available, the proposed E-TALS receiver not only improves the convergence speed of stage II by using previous symbol estimates as a "warm start", but also allows for continuous improvement in the accuracy of these symbol estimates *via* the IRS-assisted link, while enhancing the estimate of the involved channel matrices, including the direct channel matrix. As shown from our numerical experiments, the availability of the direct link makes E-TALS (Algorithm 2) advantageous compared to TALS without the availability of the direct link (Algorithm 1). Note that the identifiability condition for the TALS algorithm also applies to E-TALS algorithm 7 with an additional restriction, which consists in satisfying $K_1 \geq L$ in stage I.

Algoritmo 7: Enhanced TALS (E-TALS)

Procedure
output : $\hat{\mathbf{H}}$, $\hat{\mathbf{G}}$, $\hat{\mathbf{X}}$, and $\hat{\mathbf{H}}^{(\mathrm{D})}$

begin

■ **Stage I: Joint direct channel and symbol estimation**

1. *From* $\{\mathbf{Y}^{(D)}[1], \ldots, \mathbf{Y}^{(D)}[K_1]\}$*, compute* $\hat{\mathbf{H}}^{(D)}$ *and* $\hat{\mathbf{X}}$ *from the KRF algorithm*

■ **Stage II: IRS-assisted channel estimation and symbol refinement**

input : i = 0; *initialize* $\hat{\mathbf{X}}_{(i=0)} = \hat{\mathbf{X}}$,

2. $i \leftarrow i+1$
3. From $\{\mathbf{Q}[1], \ldots, \mathbf{Q}[K_2]\}$, *do*:
   (a) Compute $\hat{\mathbf{H}}_{(i)}$ and $\hat{\mathbf{G}}_{(i)}$ *from steps 1 and 2 of Algorithm 6, respectively.*
   (b) Compute a refined symbol estimate $\hat{\mathbf{X}}_{(i)}$ *from step 3 of Algorithm 6.*
4. Repeat steps 2 and 3 until convergence.
5: From the refined estimate $\hat{\mathbf{X}}_{(i)}$, compute a final estimate of the direct link channel:
$\hat{\mathbf{H}}^{(\mathrm{D})} = \left[\mathbf{Y}^{(\mathrm{D})}[1], \ldots, \mathbf{Y}^{(\mathrm{D})}[K_1]\right] \left[(\mathbf{W}_1 \diamond \hat{\mathbf{X}}_{(i)})^{\mathrm{T}}\right]^{\dagger}$.

end

5.7 Performance Evaluation

We evaluate the performance of the proposed semi-blind receivers. The CE accuracy is evaluated in terms of the normalized mean square error (NMSE) given by

$$\text{NMSE}(\hat{\Pi}) = \frac{1}{R}\sum_{r=1}^{R} \frac{\|\Pi^{(r)} - \hat{\Pi}^{(r)}\|_F^2}{\|\Pi^{(r)}\|_F^2}, \tag{5.38}$$

where $\Pi = \mathbf{H}, \mathbf{G}$ and $\hat{\Pi}^{(r)}$ denotes the estimation of the channels at the rth run, and R denotes the number of Monte-Carlo runs. The same definition applies to the estimated UT-IRS channel. We also evaluate the symbol error rate (SER) performance as a function of the signal-to-noise ratio (SNR) defined as $\text{SNR} = 10\log_{10}(\|\overline{\mathscr{Y}}\|_F^2/\|\mathscr{B}\|_F^2)$, where $\overline{\mathscr{Y}}$ is the noiseless received signal tensor generated according (5.4), and $\mathscr{B}$ is the additive noise tensor. All the results represent an average from at least $R = 3000$ Monte Carlo runs. Each run corresponds to an independent realization of the channel matrices, transmitted symbols, and noise term. Regarding the channel model, we consider the Rayleigh fading case (i.e. the entries of channel matrices are independent and identically distributed zero-mean circularly-symmetric complex Gaussian random variables) as well as the geometrical channel model with a few specular paths, as described in Section II. We assume uniform linear arrays at the BS and UT, while the IRS panel has a uniform rectangular array structure. The transmitted symbols follow a 16-PSK constellation. When considering the direct link, we define α as the effective SNR gap (in dB) between the direct link and the IRS-assisted link. Otherwise stated, the average received signal power for the direct link is α dB smaller than that of the IRS-assisted link. In Figures 42-44, we assume that the direct link is blocked and focus on the TALS receiver (Algorithm 1), while in the remaining figures, the direct link is available and both TALS and E-TALS are considered. In the following numerical results, we study the NMSE performance associated with the vectorized equivalent channel θ reconstructed from the estimated individual channels, as mentioned in Remark 4 of Section 5.5.

5.7.1 TALS performance: NMSE, CRB, and SER

In Figure 42, we evaluate the NMSE performance of the semi-blind TALS receiver while comparing it with competing CE methods. We consider as references for comparisons the Block-LS[6] CE method of (Deepak *et al.*, 2021) and the pilot-assisted PARAFAC-BALS method proposed in Chapter 4. Both methods are direct competitors since they operate on the

[6] The competing CE method of (Deepak *et al.*, 2021) has two stages. In the first one, the cascaded channel $\mathbf{C}_k = \mathbf{G}D_k(\mathbf{S})\mathbf{H}$ associated with each time block k is individually estimated via an LS method, while in the

same system model as the proposed semi-blind receiver. The second is based on an iterative estimation of the UT-IRS and IRS-BS channel matrices using a BALS algorithm. However, the main difference is in the fact that these methods require the transmission of pilot sequences, while the proposed receiver jointly estimates the channel and the transmitted symbols semi-blindly. In this experiment, we assume $M = 5$ antennas at the BS, $L = 2$ antennas at the UT, and an IRS composed of $N = 64$ reflecting elements. The total transmission time consists of $K = 128$ blocks of $T = 5$ time slots each. The channel matrices associated with the IRS-BS and UT-IRS are generated according to a geometrical channel model, assuming a single path scenario (line of sight case). The path directions are randomly generated according to a uniform distribution. At each Monte Carlo run, the azimuth and elevation angles are drawn within the intervals $[-\pi/2, \pi/2]$ and $[0, \pi/2]$, respectively.

As it can be seen from the figure, the TALS receiver offers a more accurate overall channel estimate than Block-LS and PAFAFAC-BALS. In particular, the Block-LS method has an SNR gap of approximately 5dB compared to TALS. Indeed, the TALS receiver fully exploits the trilinear structure of the received signal, and its improved performance comes from the data-aided nature of the receiver, where the symbol estimates are used to further improve the channel estimates during the iterative process. On the other hand, we should point out that the TALS receiver is more complex than PARFAFAC-BALS and Block-LS due to the additional symbol estimation step at every iteration.

In Figure 43, we compare the NMSE performance of the individual channel matrices $\mathbf{H}$ and $\mathbf{G}$ with their corresponding CRB references (more details given in Appendix B). Note that the NMSE curves decrease linearly with the SNR, presenting a constant gap concerning their CRB references regardless of the SNR value. In particular, note that the estimate of $\mathbf{G}$ is closer to its CRB than is the estimate of $\mathbf{H}$. Figure 44 depicts the SER for some values of N and $T = 2$. The other parameters follow the same setup as in Figures 42 and 43. Note that the SER performance degrades with an increasing N. This result is comprehensive since more IRS elements imply more channel coefficients to be estimated while the training time window is fixed.

---

second stage, the path angles are extracted from the unstructured channel estimates. Since our semi-blind receiver is not concerned with the extraction of the angular parameters of the channel matrices (which can be done using existing methods), we compare the proposed TALS method with the first stage of the Block-LS method of (Deepak *et al.*, 2021).

Figura 42 – NMSE performance of TALS in comparison with competing methods.

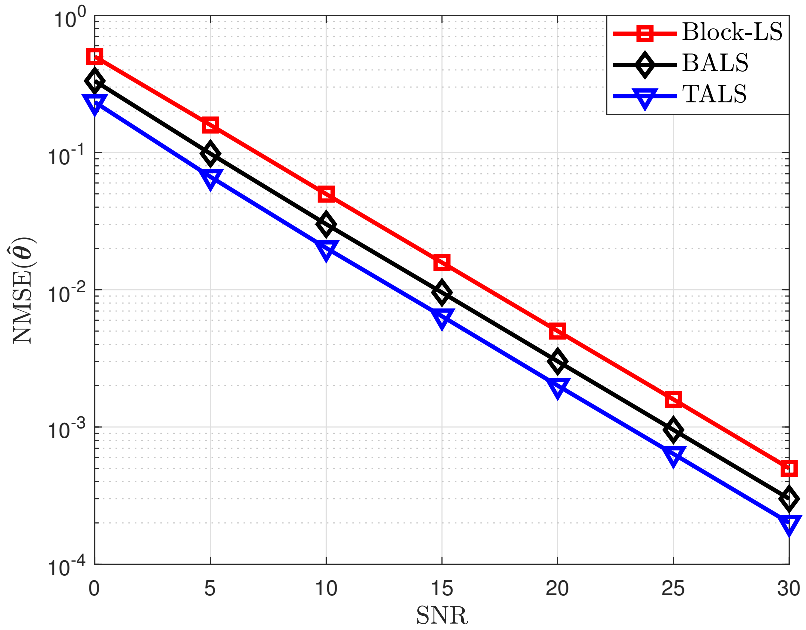

Figura 43 – Comparison with the CRB.

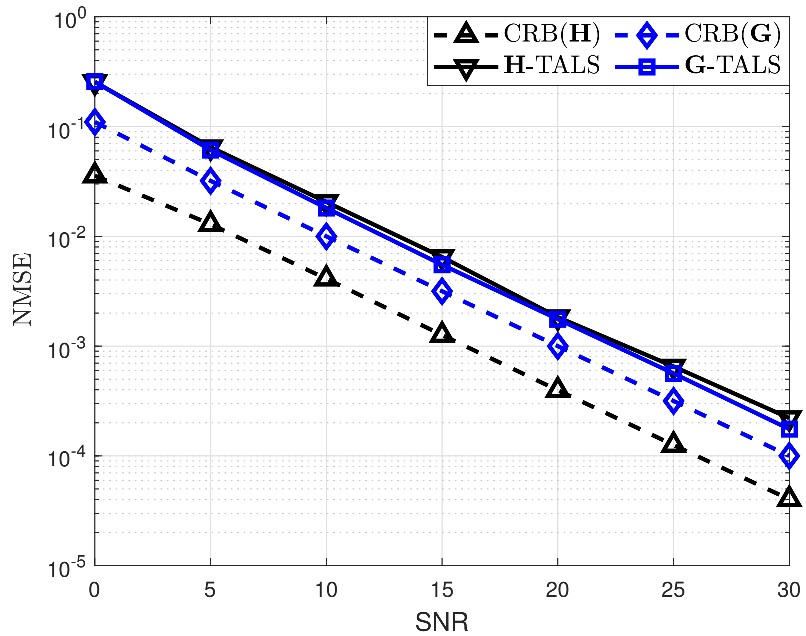

5.7.2 E-TALS performance: NMSE, complexity, and SER

According to classical studies involving IRS-assisted wireless communications (e.g. (Bjornson *et al.*, 2022) and references therein), the most significant gains of the IRS are achieved when the direct link is weak or unavailable. To investigate the impact of the influence of the direct link in the channel estimation performance, we define the parameter α representing the relationship between the received signal power in the BS via the direct link and the received

Figura 44 – SER performance of the TALS algorithm.

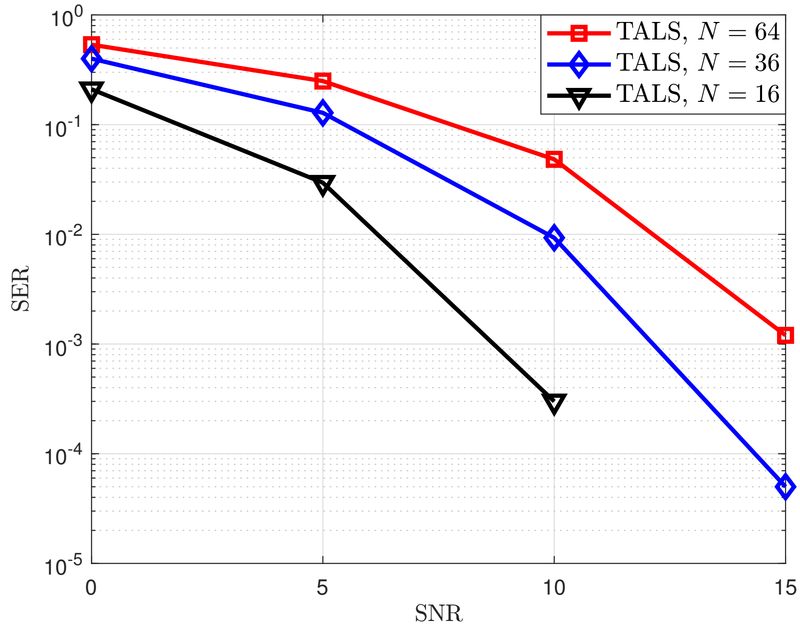

Figura 45 – NMSE performance of E-TALS for different values of α, and the impact of symbol refinements.

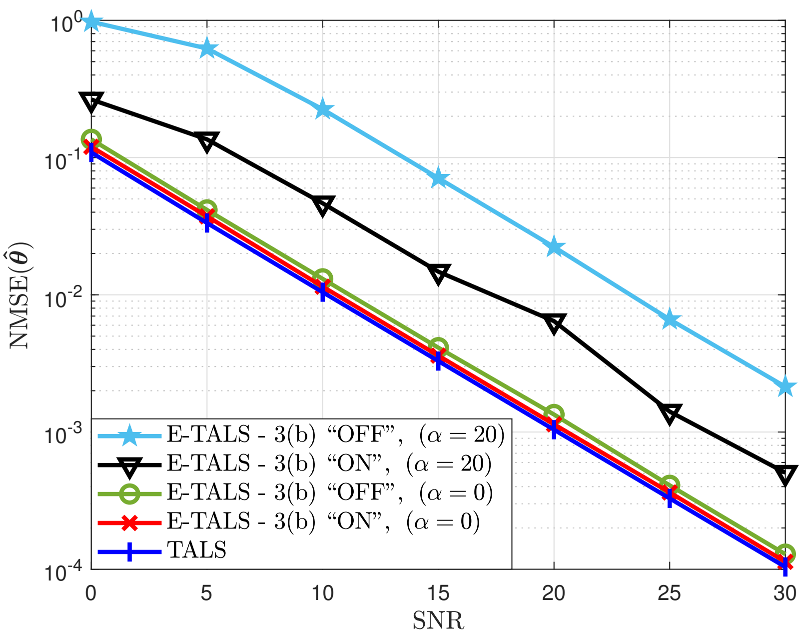

signal power via the IRS link. More specifically, let $\alpha = 10^{(PL_{DL}-PL_{IRS})/10}$, where PL_{DL} and PL_{IRS} are the path losses associated with the direct and IRS links, respectively. This means that α (in dB) is given by $\alpha(\text{dB}) = PL_{DL} - PL_{IRS}$. For instance, $\alpha(\text{dB}) = 10$ means that the path loss of the direct link is 10dB higher than that of the IRS-assisted link.

In Figures 45, we present how the refinement step in algorithm E-TALS affects the CE performance. Assuming the parameter set $\{N, M, L, T, K_1, K_2\} = \{70, 10, 2, 5, 10, 140\}$, we

Figura 46 – Convergence (number of iterations) as a function of the SNR.

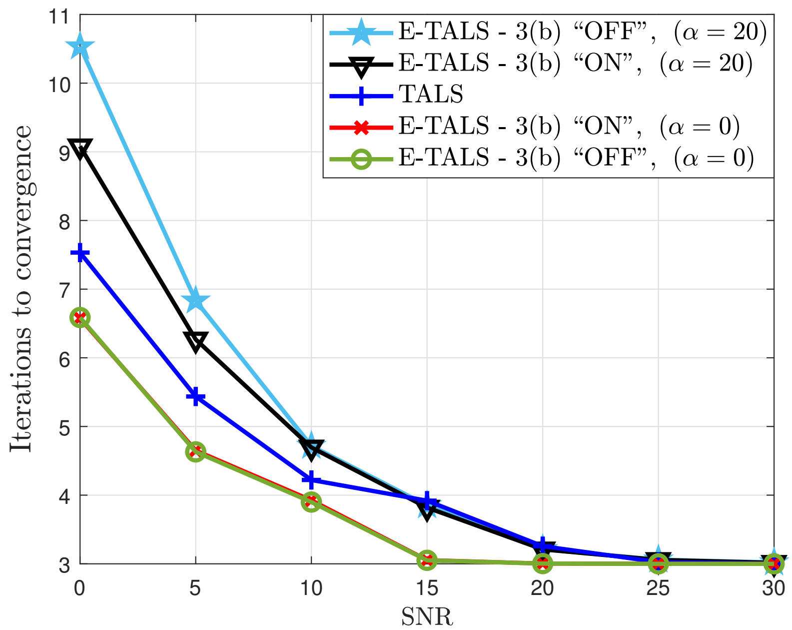

Figura 47 – SER performance of E-TALS algorithm for different values of N.

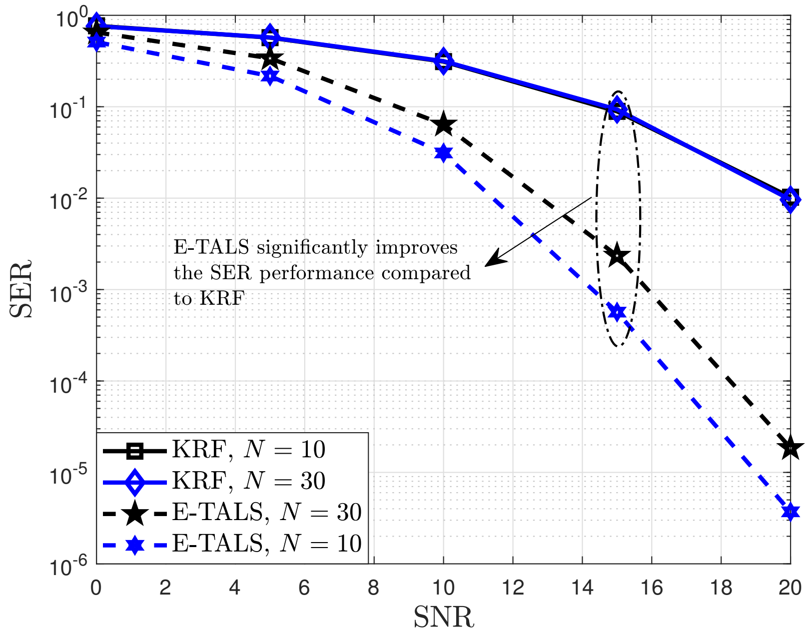

consider two cases: (1) the direct and the IRS-assisted links have the same power ($\alpha = 0$), and (2) the direct link is 20dB weaker than the IRS- assisted link ($\alpha = 20$). Let us first consider the case 1. In this case, the result depicted in 45 shows that E-TALS and TALS present a very close NMSE performance, indicating that the impact of the refinement of the symbol estimates in the performance is negligible. Although a performance gain is not obtained, as shown in Figure 46, the E-TALS algorithm needs fewer iterations to converge in comparison to TALS.

Figura 48 – NMSE of the $\mathbf{H}^{(\mathrm{D})}$ for E-TALS.

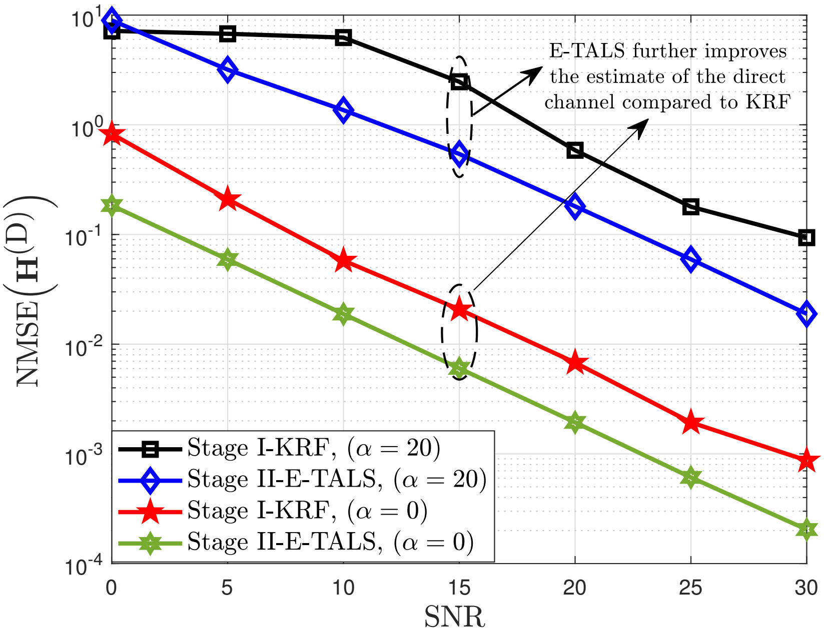

Figure 47 depicts the SER performance of E-TALS, assuming $M = L = 3$, $T = 10$, and $\alpha = 0$dB. The number of time blocks is set to $K = 27$, where $K_1 = 3$ blocks are allocated to stage I (channel estimation) and $K_2 = 24$ blocks to stage II (data decoding). We see that the SER associated with the refined symbol estimates provided by stage II is significantly lower than that delivered by stage I (KRF), corroborating the enhancement provided by the iterative joint channel and symbol estimation in stage II of E-TALS. In Figure 48, we highlight the benefit of the symbol refinements provided by stage II of E-TALS to further improve the estimate of the direct channel $\mathbf{H}^{(\mathrm{D})}$ delivered by stage I. The system parameters are $N = 50$, $M = 10$, $L = 3$, $T = 10$ and $K = 37$, with $K_1 = 13$ and $K_2 = 34$. Recall that step 5 of the E-TALS algorithm makes use of the refined symbol estimates$\hat{\mathbf{X}}$ to obtain a final LS estimate of the direct channel as $\hat{\mathbf{H}}^{(\mathrm{D})} = \left[\mathbf{Y}^{(\mathrm{D})}[1], \ldots, \mathbf{Y}^{(\mathrm{D})}[K_1]\right]\left[(\mathbf{W}_1 \diamond \hat{\mathbf{X}}_{(i)})^{\mathrm{T}}\right]^{\dagger}$. We can see that stage II of E-TALS indeed provides an enhanced estimate of the direct channel compared to stage I, for both $\alpha = 0$ and $\alpha = 20$. This result confirms that the refinement of the symbol estimates obtained via the IRS-assisted link is also beneficial to further improve the accuracy of the estimate of the direct channel while providing estimates of the IRS-assisted channels.

In Figure 50, we show the SER performance of the proposed semi-blind receiver operating with and without an IRS. In this experiment, we consider that both direct and IRS-assisted links have the same power to have a meaningful comparison with a point-to-point MIMO case without the IRS. Two conclusions can be drawn from this experiment. First, we

Figura 49 – Orthogonal *versus* non-orthogonal designs for ■.

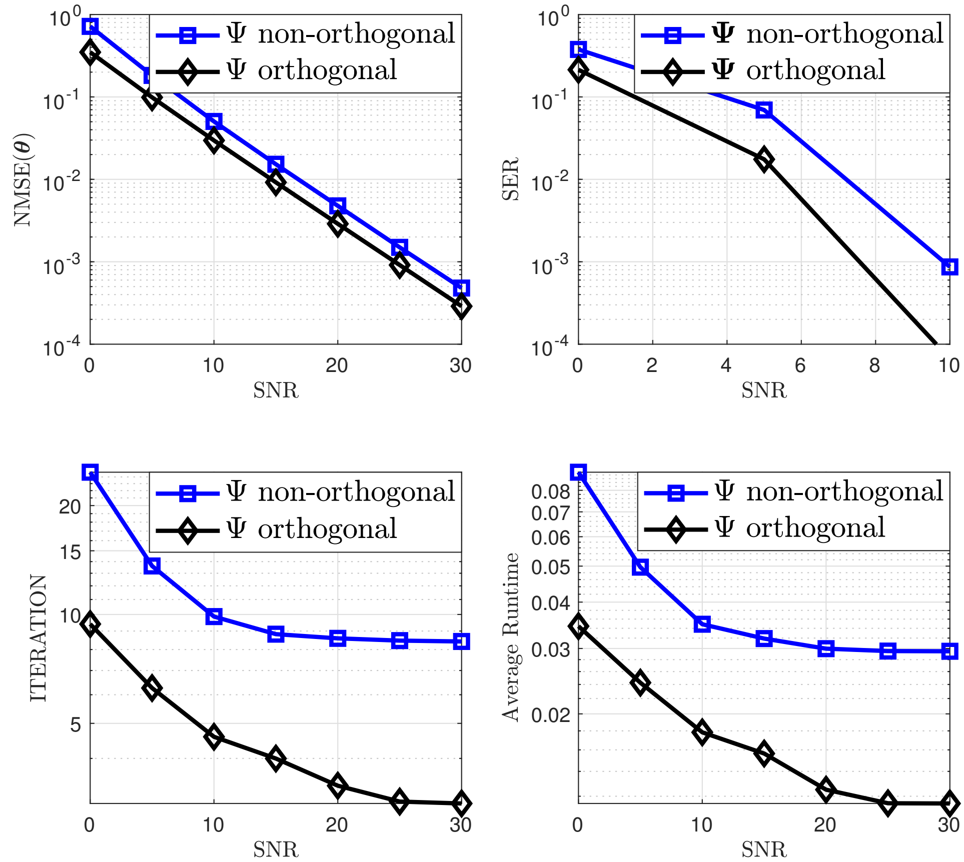

can see the SER performance of the special case of our semi-blind receiver without the IRS (red curve) is close to that when the IRS-assisted link is present and exploited. Secondly, by comparing the black and the black curves, we show the importance of stage II of the E-TALS that effectively yields refined symbol estimates (blue curve), compared to the SER obtained after stage I. This result corroborates the effectiveness of the proposed semi-blind receiver while showing its validity even without the presence of the IRS (for instance when a failure of the IRS happens). In Figure 49, we evaluate the impact of the design of Ψ on the performance of the proposed semi-blind receiver. As can be seen from these results, the proposed joint orthogonal design enhances the channel and symbol estimation performances. Moreover, the orthogonal design reduces the overall computational cost of the semi-blind receiver, since fewer iterations are required for convergence.

Figura 50 – SER with and without the IRS.

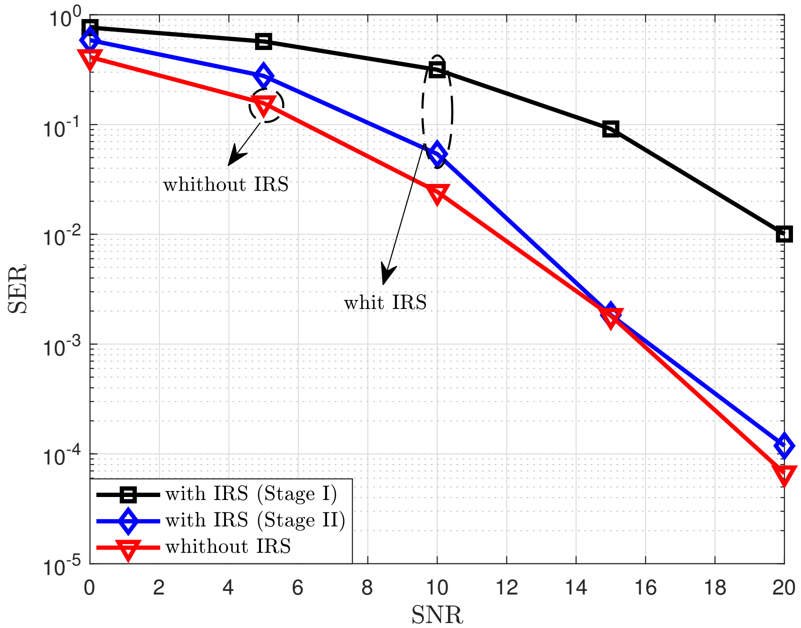

5.7.3 *Impact of imperfect IRS absorption*

In the previous result, we consider a perfect IRS absorption of the incident signal at the IRS when it is set to OFF. This means that the estimation of the UT-IRS and IRS-BS channel and the data symbol matrix carried out in stage II of Algorithm 2 suffer only the effect of the estimation error of the BS-UT channel. It is worth mentioning that this assumption is adopted in most of the works in the IRS literature when the direct link is considered. However, by working with a non-ideal and more practical assumption, (Mishra; Johansson,) considers an imperfect absorption when the IRS is turned OFF, which means that a residual signal reflection at the IRS reaches the BS even when it is assumed to be OFF. In this chapter, we evaluate the impact of such a non-ideal behavior on the performance of the proposed semi-blind receiver. Considering imperfect absorption and path loss component modeling as in (Nadeem *et al.*, 2020), the received signal at the BS when the IRS is OFF can be rewritten as

$$\begin{aligned}\mathbf{Y}^{\mathrm{D}} &= \sqrt{PL_1}\mathbf{H}_{\mathrm{D}}D_{k1}(\mathbf{W}_1)\mathbf{X}^{\mathrm{T}}+ \\ &\underbrace{+\sqrt{PL_2}\mathbf{H}\xi D_{k1}(\mathbf{S})\mathbf{G}D_{k1}(\mathbf{W}_1)\mathbf{X}^{\mathrm{T}}}_{\text{Residual IRS interferent signal when IRS is OFF.}} \qquad ,0<\xi<1\end{aligned} \tag{5.39}$$

where ξ (residual factor) denotes the fraction of the IRS signal that arrives at the BS when it is turned off, PL_1 is the path loss component associated with the direct link (BS-UT), and PL_2 is the combined path loss of the cascaded UT-IRS-BS link.

Figura 51 – Network nodes position.

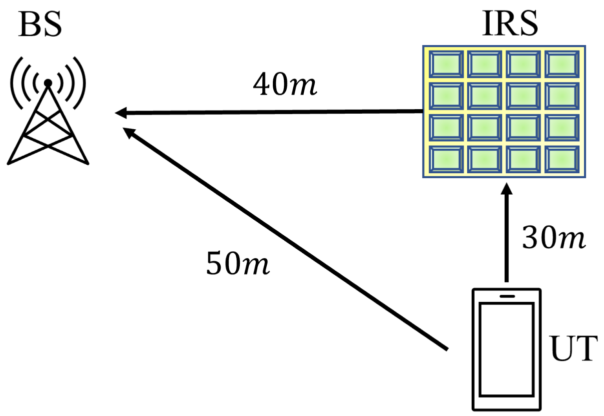

Figura 52 – NMSE of the equivalent channel θ considering residual IRS reflection affecting stage I.

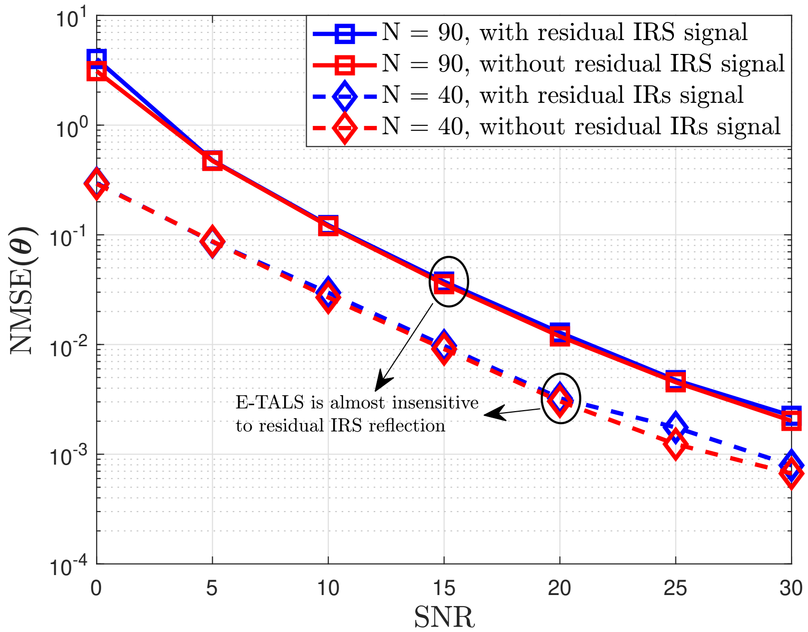

Note that the residual IRS reflection due to imperfect absorption highlighted in (5.39) can potentially degrade the receiver performance, in particular in stage I of Algorithm 2. In Figures 53 and 52, we evaluate the impact of such a non-ideality in our semi-blind receiver. For this experiment, we consider that the IRS, the UT, and the BS are positioned as illustrated in Figure 51. The fixed parameters are $K = 55$, with $K_1 = 5$ and $K_2 = 50$, $T = L = 5$, $M = 50$ and $\xi = 10^{-2}$. Figure 52 depicts the NMSE performance for $N = 40$ and $N = 90$. In this interesting result, we can see that the E-TALS algorithm is almost insensitive to residual IRS reflection in both cases. When looking at the symbol estimation performance in Figure 53, we can see that stage I of E-TALS (which is represented by the KRF algorithm) significantly suffers from residual IRS reflection, especially in the high SNR region, resulting in degraded symbol

Figura 53 – NMSE of the estimated symbol matrix $\mathbf{X}$ considering residual IRS reflection in stage I.

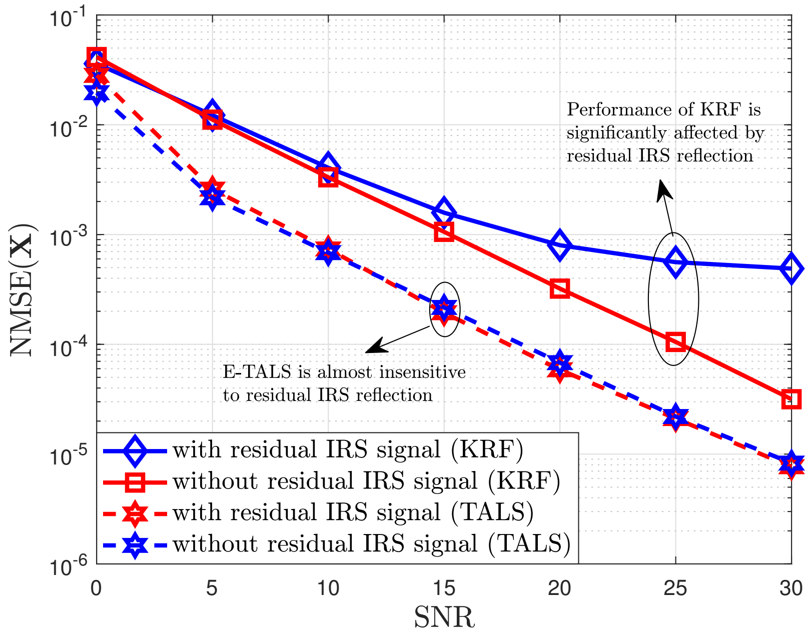

Figura 54 – Behaviour of the NMSE performance by compensating the reduction of K with an increase of M and/or T.

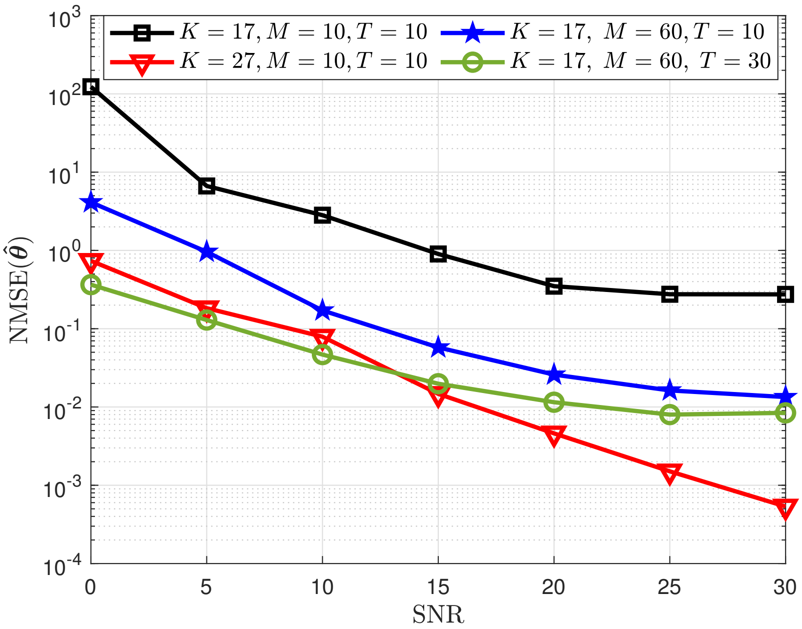

estimates. In contrast, the complete E-TALS receiver that includes stage II does not suffer from residual reflection. Indeed, the iterative nature of stage II allows refining the channel and symbol estimates in the presence of such a residual interference. Note that in the results of Figures 53 and 52, we consider $K = 55$ with $K_1 = 5$ blocks dedicated to stage I and $K_2 = 50$ to stage II. If we look at the worst-case scenario, where $N = 90$, the channel estimation time window spans

$T_E = TK = 275$ symbols. However, the number of channel coefficients to be estimated in this scenario is $(MN+M+T)L = (50\times 90+50+5)\times 5 = 22.775$, which is much bigger compared to the number of training symbols.

In Figure 54, we illustrate the existing trade-off between the number of blocks K, the size of each block T, and the number of receive antennas M. We assume $N = 30$, $L = 5$, $M = 10$ and choose different values of K. We can see that the NMSE performance degrades when fewer blocks are used. This is expected since channel estimation time is reduced by a factor of K. However, in our proposed method the effects of the reduction in K can be compensated by increasing the data block length or the number of receive antennas. Figure 54 shows how to mitigate the degradation caused by the reduction of K, by increasing T and/or M. Note that for $M = 60$ and $T = 30$, using $K = 17$ yields slightly better performance in the low SNR region in comparison with $K = 27$. To summarize, a reduction in K can be compensated by increasing the data block length and/or by using more receive antennas.

5.8 Summary

In this chapter, we have proposed a novel tensor-based semi-blind receiver design for IRS-assisted MIMO communication systems exploiting a PARATUCK tensor modeling for the received signals. The proposed semi-blind receiver performing a joint estimation of the IRS-BS channel, UT-IRS channel, and the transmitted symbols in an iterative way utilizing a TALS (Algorithm 6) when the direct link is unavailable or negligible or utilizing E-TALS (Algorithm 7) if the direct link is available. We have studied the design of the coding matrix and IRS phase shift matrix, and a joint design has been proposed that optimizes the receiver performance while simplifying the CRB derivations. In terms of performance, our results also indicate that the TALS receiver yields an improved CE accuracy than “block-LS"and BALS algorithms while offering a joint channel and symbol recovery, thus being a good solution for IRS-assisted MIMO systems, especially when pilot resources are limited or not available. The proposed semi-blind receiver effectively exploits the direct link, if available, to further refine the estimate of the direct channel and the transmitted symbols in an iterative process. In addition, the E-TALS proved to be robust enough to deal with imperfect IRS absorption during the direct link channel estimation stage. Analytical expressions for the CRB have been derived for the proposed semi-blind receiver.

6 SEMI-BLIND RECEIVER FOR IRS-ASSISTED UPLINK MULTIUSER MIMO SYSTEM

6.1 Introduction

As mentioned in the previous chapters, intelligent reflecting surface is a promising technology that may offer high spectral efficiency while improving the energy efficiency/reliability and reducing the end-to-end latency and cost (Guo *et al.*, 2022). In this context, we have also highlighted that the acquisition of CSI is an important and challenging task since its accuracy has a significant impact on the optimization of the IRS phase shifts and the final system performance.

Recent works have proposed different solutions to tackle the CE problem in IRS-assisted communications in single-user single-antenna/multi-antenna systems (see, for example, Chapter 4)). In (Chen *et al.*, 2021a), the authors assume a semi-active IRS structure. This assumption undermines the low-cost structure of the IRS since RF chains are used. Considering a multi-user (MU) scenario, (Zheng *et al.*, 2020) and (Wang *et al.*, 2020c) exploit IRS element grouping and spatial correlation to control the pilot overhead. In both (Zheng *et al.*, 2020) and (Wang *et al.*, 2020c), the authors assume a quasi-static block fading channel model for all the involved links, which leads to a degradation in the performance of CE when some mobility of the UT is considered. In particular, (Wang *et al.*, 2020c) exploits the correlation among the UT-IRS-BS channels of different users. Note that all these methods are pilot-assisted schemes.

6.2 This chapter

Blind and semi-blind receivers can perform CE and data detection without employing pilot sequences. In contrast to the previous chapter and to the works cited above, this chapter formulates a semi-blind receiver that solves the problem of joint channel and symbol estimation in an IRS-assisted wireless network without the need for a dedicated training stage. We address a realistic scenario, in which the channels between the UT and the IRS undergo shorter-term variations compared to the channel between the BS and the IRS. Considering an uplink MU-MIMO setup, we show that the signals reflected by the IRS and received at the BS follow a generalized PARATUCK tensor model. By exploiting the algebraic structure of this tensor model, we derive a semi-blind receiver algorithm that allows the BS to jointly estimate the uplink multiple UT-IRS channels, the common IRS-BS channel, and the data symbols transmitted by all UTs, in a closed-form way by solving simple rank-one matrix approximation problems.

The proposed two-stage closed-form semi-blind receiver consists of a sequential combination of the KRF and KF schemes and is referred to as KAKF in the sequel. We compare our proposed semi-blind method with a recently proposed PARAFAC-based receiver (Wei *et al.*,) and with the KRF receiver in Chapter 4, which are two pilot-assisted methods. The first is an iterative solution that solves two LS problems to estimate the involved channel matrices, while the second is a closed-form scheme based on rank-one matrix approximations. In terms of performance, the numerical results corroborate the improved CE accuracy, superior SER performance, and lower computational complexity offered by the proposed semi-blind receiver.

6.3 System Model

Figura 55 – IRS-assisted MU-MIMO communication system.

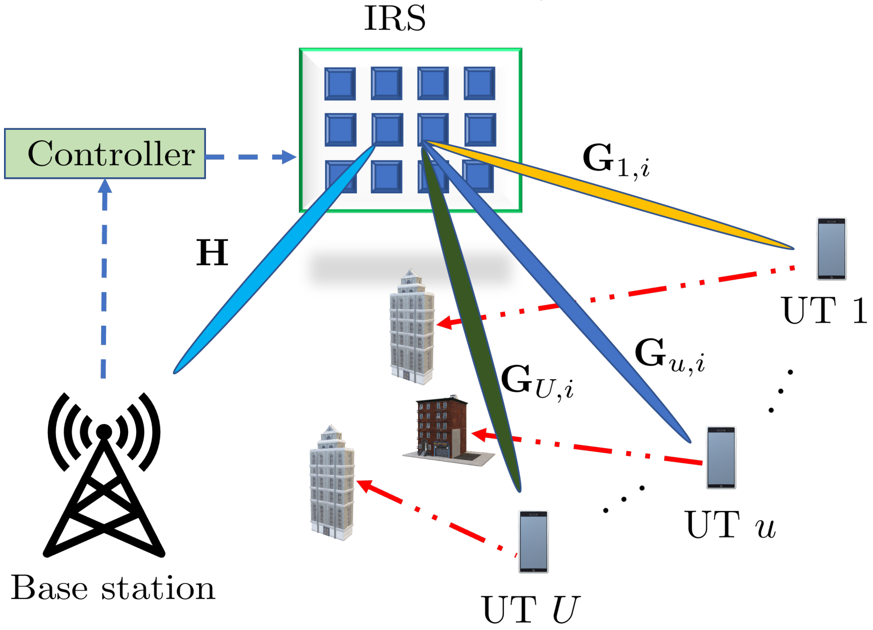

Consider the uplink communication in an IRS-assisted MU-MIMO system, as illustrated in Figure 55, in which the BS is equipped with M antennas, the IRS is composed of N passive scattering elements, while each of the U UTs has L antennas[1]. We assume that the BS and the IRS are deployed at fixed heights, e.g., on the roof of a building, compared to the moving UTs. In this sense, we assume that the transmitted data is organized into I data frames. Each frame is composed of KT symbol periods, where K denotes the number of blocks contained in each frame and T is the number of time slots in each block. This transmission

[1] We assume that the users have the same number of antennas for simplicity of exposition. However, the proposed solution can be straightforwardly adapted to users with different numbers of antennas.

structure is illustrated in Figure 56. To capture a certain level of UT mobility, we assume that

Figura 56 – Transmission structure.

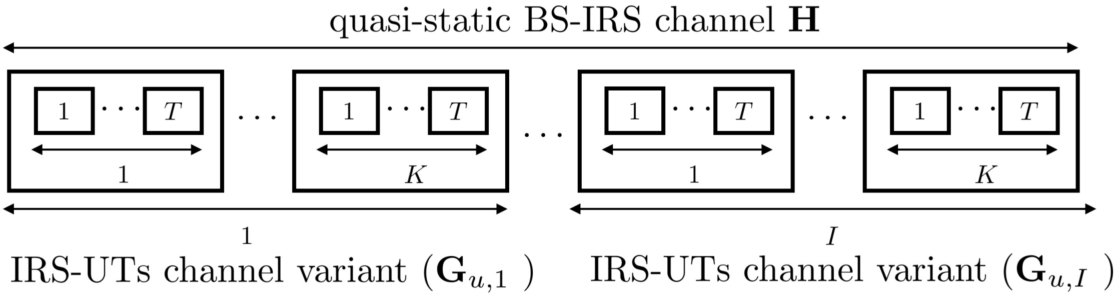

the UT-IRS channels stay constant during a frame, but vary in different frames independently. On the other hand, the IRS-BS channel follows a quasi-static model (Hu *et al.*, 2021), and is assumed to remain constant during the transmission time. This is a reasonable assumption since the BS and the IRS are assumed to be deployed at fixed positions. We also assume that the direct communication links between the UTs and the BS are weak or not available. Each UT sends L data symbol vector that are *diagonally* coded as $\mathbf{z}_u[k,t] = \text{diag}(\mathbf{w}_u[k])\mathbf{x}_u[t] \in \mathbb{C}^{L\times 1}$, where $\mathbf{x}_u[t] \in \mathbb{C}^{L\times 1}$ is the symbol vector transmitted by the uth UT at the tth time slot, $t = 1,\ldots,T$, whose entries are drawn from any finite-alphabet constellation. The vector $\mathbf{w}_u[k] \in \mathbb{C}^{L\times 1}$ denotes the coding vector associated with the uth UT at the kth block. The quasi-static IRS-BS channel matrix is denoted by $\mathbf{H} \in \mathbb{C}^{M\times N}$, while the time-varying channel matrix between the IRS and the uth UT at frame i is denoted as $\mathbf{G}_{u,i} \in \mathbb{C}^{N\times L}$. Therefore, the received signal at the BS coming from the uth UT via IRS is given by

$$\mathbf{y}_u[k,i,t] = \mathbf{H}\text{diag}(\mathbf{s}[k])\mathbf{G}_{u,i}\mathbf{z}_u[k,t] + \mathbf{v}[k,i,t] \in \mathbb{C}^{M\times 1}, \tag{6.1}$$

where $\mathbf{s}[k] \in \mathbb{C}^{N\times 1}$ collects the phase shifts $s_n[k] = e^{j\phi_n[k]}$ applied by the IRS during the kth block, and $\mathbf{v}[k,i,t] \in \mathbb{C}^{M\times 1}$ denotes the additive white Gaussian noise (AWGN) term. Note that the IRS phase shifts configuration and the coding vectors are known by the BS and remain constant during the T time slots within the kth block, but vary between different blocks.

At the BS, the received signal is represented as the superposition of the signals coming from the U UTs. Therefore, the total received signal can be expressed as

$$\begin{aligned} \mathbf{y}[k,i,t] &= \sum_{u=1}^{U} \mathbf{H}\text{diag}(\mathbf{s}[k])\mathbf{G}_{u,i}\text{diag}(\mathbf{w}_u[k])\mathbf{x}_u[t] + \mathbf{v}[k,i,t] \\ &= \mathbf{H}\text{diag}(\mathbf{s}[k])\Big(\sum_{u=1}^{U} \mathbf{G}_{u,i}\text{diag}(\mathbf{w}_u[k])\mathbf{x}_u[t]\Big) + \mathbf{v}[k,i,t], \end{aligned} \tag{6.2}$$

or, more compactly,

$$\mathbf{y}[k,i,t] = \mathbf{H}\text{diag}(\mathbf{s}[k])\mathbf{G}_i\text{diag}(\mathbf{w}[k])\mathbf{x}[t] + \mathbf{v}[k,i,t], \tag{6.3}$$

where $\mathbf{G}_i = [\mathbf{G}_{1,i},\ldots,\mathbf{G}_{U,i}] \in \mathbb{C}^{N\times UL}$ represents the augmented MU uplink channel matrix at frame i. Also, $\mathbf{x}[t] = \left[\mathbf{x}_1^{\mathrm{T}}[t],\ldots,\mathbf{x}_U^{\mathrm{T}}[t]\right]^{\mathrm{T}} \in \mathbb{C}^{UL\times 1}$ collects the transmitted data symbol vectors from all UTs, and $\mathbf{w}[k] = \left[\mathbf{w}_1^{\mathrm{T}}[k]\ \ldots\ \mathbf{w}_U^{\mathrm{T}}[k]\right]^{\mathrm{T}} \in \mathbb{C}^{UL\times 1}$ collects the U coding vectors used by the UTs in block k. Defining $\mathbf{Y}[k,i] \doteq [\mathbf{y}[k,i,1],\ldots,\mathbf{y}[k,i,T]] \in \mathbb{C}^{M\times T}$ that collects the received signal vectors during the $t = 1,\ldots,T$ time slots, we obtain

$$\mathbf{Y}[k,i] = \mathbf{H}D_k(\mathbf{S})\mathbf{G}_iD_k(\mathbf{W})\mathbf{X}^{\mathrm{T}} + \mathbf{V}[k,i], \tag{6.4}$$

where $\mathbf{S} \in \mathbb{C}^{K\times N}$ is the phase shifts matrix, $\mathbf{W} = [\mathbf{w}[1]\ldots\mathbf{w}[K]]^{\mathrm{T}} \in \mathbb{C}^{K\times UL}$ and $\mathbf{X} = [\mathbf{x}[1]\ldots\mathbf{x}[T]]^{\mathrm{T}} \in \mathbb{C}^{T\times UL}$. By comparing equations (3.33) and (6.4), the following correspondence can be established

$$\left(\mathbf{A},\mathbf{B},\mathbf{C}^{\mathbf{A}},\mathbf{C}^{\mathbf{B}},\mathscr{R}\right) \leftrightarrow \left(\mathbf{H},\mathbf{X},\mathbf{S},\mathbf{W},\mathscr{G}\right). \tag{6.5}$$

The useful part of the received signal in (6.4) can be identified as a generalized fourth-order PARATUCK decomposition of a tensor $\mathscr{Y} \in \mathbb{C}^{M\times T\times K\times I}$ written in terms of its (k,i)th matrix slices, where the frame i and block k dimensions are fixed. Our goal is to jointly estimate in a semi-blind way, i.e., without resorting to a dedicated training stage, the IRS-BS channel $\mathbf{H}$, the UTs-IRS channels that yield $\mathbf{G}_i$ and the transmitted data symbols $\mathbf{X}$ from the received signal tensor in (6.4). To this end, we formulate the detailed processing stages of the proposed closed-form semi-blind receiver in the following.

6.4 Proposed Semi-Blind KAKF Receiver

The vectorized form of the received signal in (6.4) as

$$\begin{aligned}\mathbf{y}_{k,i} &= (\mathbf{X}\otimes\mathbf{H})\,\text{vec}(D_k(\mathbf{S})\mathbf{G}_iD_k(\mathbf{W})) \\ &= (\mathbf{X}\otimes\mathbf{H})\,(D_k(\mathbf{W})\otimes D_k(\mathbf{S}))\,\mathbf{g}_i\end{aligned} \in \mathbb{C}^{TM\times 1}, \tag{6.6}$$

where $\mathbf{g}_i \doteq \text{vec}(\mathbf{G}_i) \in \mathbb{C}^{NLU}$, and we have used the Kronecker product property $\text{vec}(\mathbf{ABC}) = \left(\mathbf{C}^{\mathrm{T}}\otimes\mathbf{A}\right)\text{vec}(\mathbf{B})$. Defining $\mathbf{y}_k \doteq [\mathbf{y}_{k,1},\ldots,\mathbf{y}_{k,I}]$ that collects the I received signals for the kth block, we can rewrite (6.6) as

$$\mathbf{Y}_k = \mathbf{Q}\,(D_k(\mathbf{W})\otimes D_k(\mathbf{S}))\,\mathbf{G}^{\mathrm{T}},\ k = 1,\ldots,K, \tag{6.7}$$

where $\mathbf{G} = [\mathbf{g}_1, \ldots, \mathbf{g}_I]^{\mathrm{T}} \in \mathbb{C}^{I \times P}$ and $\mathbf{Q} = \mathbf{X} \otimes \mathbf{H} \in \mathbb{C}^{TM \times P}$, with $P = NLU$. Resorting again to the property of the Kronecker product, we rewrite (6.7) more compactly as

$$\mathbf{y}_k = (\mathbf{G} \diamond \mathbf{Q}) \, (\mathbf{W}_{k.} \otimes \mathbf{S}_{k.})^{\mathrm{T}} \in \mathbb{C}^{ITM \times 1}. \tag{6.8}$$

Finally, by collecting the received signals $\mathbf{y}_k$, $k = 1, \ldots, K$, over the K blocks, we have

$$\mathbf{Y} \doteq [\mathbf{y}_1, \ldots, \mathbf{y}_K] = (\mathbf{G} \diamond \mathbf{Q}) \, \Psi \in \mathbb{C}^{ITM \times K}, \tag{6.9}$$

where $\Psi = \mathbf{W}^{\mathrm{T}} \diamond \mathbf{S}^{\mathrm{T}} = \left[\mathbf{W}_{1.}^{\mathrm{T}} \otimes \mathbf{S}_{1.}^{\mathrm{T}} \ldots \mathbf{W}_{K.}^{\mathrm{T}} \otimes \mathbf{S}_{K.}^{\mathrm{T}} \right] \in \mathbb{C}^{P \times K}$. From (6.9), we observe that the LS estimate of the Khatri-Rao product $\mathbf{G} \diamond \mathbf{Q}$ can be obtained. To avoid the pseudo inverse calculation, we assume that Ψ is constructed based on a Discrete Fourier Transform factorization design[2] as in (Sokal *et al.*, 2020), such that $(1/K) \, \Psi \Psi^{\mathrm{H}} = \mathbf{I}_P$. Note, however, that the orthogonality of Ψ is not a requirement of our semi-blind receiver. Using $\mathbf{G} \diamond \mathbf{Q}$ estimated from $\mathbf{Y}$, the individual estimates of $\mathbf{G}$ (i.e., UTs-IRS channels) and $\mathbf{Q} = \mathbf{X} \otimes \mathbf{H}$ can be obtained using the KRF approach, which consists of solving a set of rank-one matrix approximation problems. Sequentially, from $\mathbf{Q}$, which is estimated via KRF in the previous stage, the individual estimates of $\mathbf{H}$ and $\mathbf{X}$ can be obtained using the KF, which consists of solving a single rank-one matrix approximation problem. The KAKF receiver accomplishes joint channel and symbol estimation in closed form from two stages as detailed in the following.

6.4.1 Khatri-Rao Factorization (KRF) Stage

Considering the noisy version of (6.9), and exploiting the knowledge of the phase shifts and coding matrices $\mathbf{S}$ and $\mathbf{W}$, respectively (and thus Ψ), the BS firstly applies linear filtering with Ψ^{H}, yielding

$$\mathbf{Z} \doteq (1/K) \mathbf{Y} \Psi^{\mathrm{H}} = \mathbf{G} \diamond \mathbf{Q} + \overline{\mathbf{N}} \in \mathbb{C}^{ITM \times P}, \tag{6.10}$$

where $\overline{\mathbf{N}} = \mathbf{N} \Psi^{\mathrm{H}}$ represents the equivalent filtered noise term. From (6.10), the individual estimates of $\hat{\mathbf{G}}$ and $\hat{\mathbf{Q}}$ can be obtained from their noisy Khatri-Rao product by solving

$$\left(\hat{\mathbf{G}}, \hat{\mathbf{Q}} \right) = \min_{\{\mathbf{G}, \mathbf{Q}\}} \left\| \mathbf{Z} - \mathbf{G} \diamond \mathbf{Q} \right\|_{\mathrm{F}}^2. \tag{6.11}$$

Defining μ_p as the pth column of $\mathbf{Z}$, we have $\mu_p \doteq (\mathbf{g}_p \otimes \mathbf{q}_p) + \mathbf{n}_p$, where $\mathbf{n}_p$ is the corresponding column of the noise matrix in (6.10), and $\mathbf{g}_p \in \mathbb{C}^{I \times 1}$ and $\mathbf{q}_p \in \mathbb{C}^{TM \times 1}$ corresponds to the pth

[2] The design of the phase shifts $\mathbf{S}$ and the coding $\mathbf{W}$ matrices is a relevant point, especially in the optimization context. However, the optimization study on these matrices is out of the scope of this work. Further, the structure of $\mathbf{S}$ and $\mathbf{W}$ impacts the design of the matrix Ψ regarding complexity aspects.

Algoritmo 8: Khatri-Rao Factorization (KRF) Stage

Procedure
input : $\mathbf{Z}$
output : $\hat{\mathbf{G}}$ and $\hat{\mathbf{Q}}$

begin
  for $p = 1, \ldots, P$ **do**
    $\overline{\mathbf{Z}}_p \longleftarrow \text{unvec}_{TM \times I}(\mu_p)$
    $(\mathbf{u}_1, \sigma_1, \mathbf{v}_1) \longleftarrow \text{truncated-SVD}(\overline{\mathbf{Z}}_p)$
    $\hat{\mathbf{g}}_p \longleftarrow \sqrt{\sigma_1}\mathbf{v}_1^*$, where σ_1 is the dominant singular value
    $\hat{\mathbf{q}}_p \longleftarrow \sqrt{\sigma_1}\mathbf{u}_1$
    end
  end
  Reconstruct $\hat{\mathbf{Q}}$ *and* $\hat{\mathbf{G}}$:
  $\hat{\mathbf{Q}} \longleftarrow [\hat{\mathbf{q}}_1, \ldots, \hat{\mathbf{q}}_P]; \quad \hat{\mathbf{G}} \longleftarrow [\hat{\mathbf{g}}_1, \ldots, \hat{\mathbf{g}}_P]$
  Remove the scaling ambiguities of $\hat{\mathbf{Q}}$ *and* $\hat{\mathbf{G}}$.
  end
end

column of the matrices $\mathbf{G}$ and $\mathbf{Q}$, respectively. Using the property $\mathbf{g}_p \otimes \mathbf{q}_p = \text{vec}(\mathbf{q}_p \mathbf{g}_p^{\text{T}})$, Problem (6.11) can be equivalently recast as

$$\big(\hat{\mathbf{G}}, \hat{\mathbf{Q}}\big) = \underset{\{\mathbf{q}_p, \mathbf{g}_p\}}{\arg\min} \sum_{p=1}^{P} \|\tilde{\mathbf{Z}}_p - \mathbf{q}_p \mathbf{g}_p^{\text{T}}\|_{\text{F}}^2, \tag{6.12}$$

where $\tilde{\mathbf{Z}}_p = \text{unvec}_{TM \times I}(\mu_p)$. Note that $\widetilde{\mathbf{Z}}_p$ can be approximated as a rank-one matrix given by the outer product of $\mathbf{q}_p$ and $\mathbf{g}_p$. The solution of (6.12) is given by the best rank-one approximation obtained from the dominant left and right singular vectors of $\widetilde{\mathbf{Z}}_p$ (Eckart; Young, 1936). Therefore, the KRF stage of the proposed receiver thus consists of solving P independent rank one-approximation problems, as summarized in **Algorithm 8**.

6.4.2 Kronecker Factorization Stage

Recall that the estimate of $\hat{\mathbf{Q}}$ is delivered from the KRF stage in Section 6.4.1. From (6.6) and (6.7), we have that $\hat{\mathbf{Q}}$ can be approximated as the Kronecker product of the transmitted data matrix and IRS-BS channel matrix, i.e.

$$\hat{\mathbf{Q}} \approx \mathbf{X} \otimes \mathbf{H} \in \mathbb{C}^{TM \times P}. \tag{6.13}$$

According to the Kronecker product definition, $\hat{\mathbf{Q}}$ is the following block matrix

$$\hat{\mathbf{Q}} = \begin{bmatrix} \hat{\mathbf{Q}}_{1,1} & \ldots & \hat{\mathbf{Q}}_{1,UL} \\ \vdots & \ldots & \vdots \\ \hat{\mathbf{Q}}_{T,1} & \ldots & \hat{\mathbf{Q}}_{T,UL} \end{bmatrix} \in \mathbb{C}^{TM \times P}, \tag{6.14}$$

Algoritmo 9: Kronecker Factorization Stage

Procedure
input : $\hat{\mathbf{Q}}$
output : $\hat{\mathbf{X}}$ and $\hat{\mathbf{H}}$

begin

1. Construct the matrix $\widetilde{\mathbf{Q}}$ from $\hat{\mathbf{Q}}$
2. $(\mathbf{u}_1, \sigma_1, \mathbf{v}_1) \longleftarrow$ truncated-SVD$(\widetilde{\mathbf{Q}})$
   $\hat{\mathbf{x}} \longleftarrow \sqrt{\sigma_1}\mathbf{u}_1; \quad \hat{\mathbf{h}} \longleftarrow \sqrt{\sigma_1}\mathbf{v}_1^*$
3. Reconstruct $\hat{\mathbf{X}}$ and $\hat{\mathbf{H}}$ by reshaping $\hat{\mathbf{x}}$ and $\hat{\mathbf{h}}$
4. Remove the scaling ambiguities of $\hat{\mathbf{X}}$ and $\hat{\mathbf{H}}$

end

end

where each sub-matrix corresponds to a scaled version of $\mathbf{H}$, i.e.,

$$\hat{\mathbf{Q}}_{t,j} = x_{t,j}\mathbf{H}, \tag{6.15}$$

for $t = 1, \ldots, T$ and $j = 1, \ldots, UL$. Therefore, the individual estimates for $\hat{\mathbf{X}}$ and $\hat{\mathbf{H}}$ can be obtained from $\hat{\mathbf{Q}}$ by solving

$$(\hat{\mathbf{X}}, \hat{\mathbf{H}}) = \min_{\mathbf{X},\mathbf{H}} \left\| \hat{\mathbf{Q}} - \mathbf{X} \otimes \mathbf{H} \right\|_{\mathrm{F}}^2. \tag{6.16}$$

The matrix $\hat{\mathbf{Q}}$ can be properly rearranged by stacking the vectorized form of the blocks $\hat{\mathbf{Q}}_{t,j}$ in (6.15), as in (Pitsianis, 1997), so that a rank-one matrix $\widetilde{\mathbf{Q}}$ is constructed, as follows

$$\begin{aligned} \widetilde{\mathbf{Q}} &= \begin{bmatrix} \hat{x}_{1,1}\mathrm{vec}(\hat{\mathbf{H}})^{\mathrm{T}} \\ \vdots \\ \hat{x}_{T,UL}\mathrm{vec}(\hat{\mathbf{H}})^{\mathrm{T}} \end{bmatrix} = \begin{bmatrix} \hat{x}_{1,1} \\ \vdots \\ \hat{x}_{T,UL} \end{bmatrix} \mathrm{vec}(\hat{\mathbf{H}})^{\mathrm{T}} \\ &= \mathrm{vec}(\hat{\mathbf{X}})\mathrm{vec}(\hat{\mathbf{H}})^{\mathrm{T}} \in \mathbb{C}^{(TUL)\times(NM)}. \end{aligned} \tag{6.17}$$

Therefore, the problem in (6.16) becomes equivalent to solving the following rank-one matrix approximation problem

$$(\hat{\mathbf{X}}, \hat{\mathbf{H}}) = \min_{\mathbf{X},\mathbf{H}} \left\| \widetilde{\mathbf{Q}} - \hat{\mathbf{x}}\hat{\mathbf{h}}^{\mathrm{T}} \right\|_{\mathrm{F}}^2, \tag{6.18}$$

where $\hat{\mathbf{x}} = \mathrm{vec}(\hat{\mathbf{X}})$ and $\hat{\mathbf{h}} = \mathrm{vec}(\hat{\mathbf{H}})$. The best estimates to $\hat{\mathbf{x}}$ and $\hat{\mathbf{h}}$ (and consequently to $\hat{\mathbf{X}}$ and $\hat{\mathbf{H}}$) are obtained by truncating the SVD of $\widetilde{\mathbf{Q}}$ to its rank-one approximation. Therefore, the KF stage of the proposed receiver is solved from a single rank-one matrix approximation step, as shown in **Algorithm 9**.

6.4.3 Identifiability Analysis and Computational Complexity

The necessary condition on the identifiability of the proposed KAKF receiver is linked to the linear filtering step in (6.10). It requires that the designed matrix Ψ be full row-rank, implying that $K \geq P$. This condition establishes a lower bound on the number of transmission blocks necessary for the proposed receiver to jointly estimate the channels and data symbols of all the users. This indicates that the required number of transmission blocks scales with L, N, and U at least linearly, as $P = NLU$. Note that the computational complexity in both stages (Algorithms 1 and 2) of the proposed KAKF receiver is dominated by the truncated SVD. This truncated SVD can be efficiently obtained from partial QR factorization schemes (Halko *et al.*, 2011). The total complexity of KAKF receiver is given by $\mathcal{O}(PTM) + P\mathcal{O}(TMI)$, since the KF stage involves a single rank-1 approximation step, while the KRF one has P rank-1 approximation steps. It is worth noting that in the KRF stage the P factors of the Khatri-Rao product can be estimated independently. Hence, the processing delay can be controlled by executing the P estimation steps in parallel processors at the BS. The pilot-assisted method (Wei *et al.*,), used as a benchmark, is an iterative solution where the computational complexity is dominated by the pseudo-inverse calculation such that the total complexity is $I_{\max}\mathcal{O}(2N^3 + 4N^2K(L+M) - NK(L+M))$.

6.4.4 Scaling Ambiguities

Once the rank-one approximations are computed via truncated SVD, the estimates provided by the KRF and KF stages are unique up to scaling ambiguities. From the KRF stage, the following estimates are obtained $\hat{\mathbf{G}} = \mathbf{G}\Delta_{\mathbf{G}}$ and $\hat{\mathbf{Q}} = \mathbf{Q}\Delta_{\mathbf{Q}}$, where $\Delta_{\mathbf{G}}$ and $\Delta_{\mathbf{Q}}$ are diagonal matrices that contain the column scaling ambiguities such that $\Delta_{\mathbf{G}}\Delta_{\mathbf{Q}} = \mathbf{I}_P$. To remove these scaling ambiguities, the BS needs to know one row of $\mathbf{G}$ or $\mathbf{Q}$. Such a scaling can be handled by assuming that the first row of $\mathbf{Q}$ is known. This is equivalent to assuming that the BS knows the first row of $\mathbf{X}$ and the first row of the BS-IRS channel $\mathbf{H}$. In practice, the BS can estimate the first row of $\mathbf{H}$ based on a simple scheme proposed in (Hu *et al.*, 2021), where the IRS reflects pilots sent by the BS.

6.5 Simulation Results

In this section, the performance of the proposed two-stage KAKF semi-blind receiver is evaluated in terms of the normalized mean square error (NMSE) of the estimated channels, average SER, and average runtime metrics. Particularly, the NMSE of the BS-IRS CE is defined as $\text{NMSE}(\hat{\Omega}) = (1/R)\sum_{r=1}^{R} \|\Omega_{(r)} - \hat{\Omega}_{(r)}\|_F^2 / \|\Omega_{(r)}\|_F^2$, where $\Omega = \mathbf{H}$ or $\mathbf{G}$, and $\hat{\Omega}_{(r)}$ represents the estimation of the channel at the rth Monte Carlo run. The results are averaged over $R = 10^4$ independent Monte Carlo runs. We assume that the involved channels follow geometric models such that $\mathbf{H} = \mathbf{A}_{\text{IRS}}\text{diag}(\beta)\mathbf{A}_{\text{BS}}^{\text{H}}$ and $\mathbf{G} = \mathbf{B}_{\text{UT}}\text{diag}(\gamma)\mathbf{B}_{\text{IRS}}^{\text{H}}$ (for each UT), in which the number of dominant paths in the IRS-BS and UTs-IRS links are denoted by L_h and L_g[3], respectively, while β and γ denote the channel gain vectors. The departure and arrival angles are randomly and uniformly distributed between 0 and 2π, while the path gains follow a complex Gaussian distribution with zero mean and unitary variance. The transmitted data symbols are chosen from a 16-PSK alphabet, and each UT has a transmission rate of $\rho = [(T-1)+T_D]\log_2(M)L / T_c$ for a given coherence time T_c and data transmission time T_D.

Figure 57 depicts the NMSE performance of the proposed semi-blind KAKF receiver as a function of the signal-to-noise ratio (SNR). As a performance benchmark, we also depict the results of the BALS method proposed in (Wei *et al.*,), as well as the results of the closed-form KRF solution proposed in Chapter 4, which are pilot-assisted methods. Although the competitive methods do not consider UTs-IRS time-varying channels, we adapt them to the time-varying case to ensure a fair comparison. In this experiment, we assume $N = 36$, $M = 4$, $U \in \{5,7\}$, each UT equipped with 2 antennas ($L = 2$). Besides, we consider $L_h = 1$ and $L_g = 1$. Further, the BS captures $I = 5$ UTs-IRS channel variations and $\{T,K\} = \{2,720\}$. As it can be observed, our proposed semi-blind KAKF receiver significantly outperforms the BALS method in the accuracy of the estimation of the UTs-IRS channel $\mathbf{G}$. As for the IRS-BS channel $\mathbf{H}$, the BALS method outperforms the proposed receiver in the low SNR regime for $U = 5$. However, in the medium-to-high SNR regime, the two receivers show similar performances. Besides, the BALS estimator, which requires pilot sequences, has a very modest gain for $U = 7$. This is an expected result since the IRS-BS channel $\mathbf{H}$ is estimated in the second KF stage when using the KAKF receiver. Therefore, it is affected by the error propagation originating from the first KRF stage. This explains its worse performance in estimating $\mathbf{H}$ in the low SNR regime compared to BALS, in which each channel matrix is estimated in an alternating way, thus avoiding error propagation. Note that the KRF performance is similar to the BALS performance. However, considering the end-to-end channel, our proposed scheme offers a remarkable improvement in the CE accuracy. For an SNR equal to 20 dB, while KAKF and BALS have similar NMSE performances for

[3] For simplicity, in the simulations, we assume that each UT contributes with the same number L_g of dominant paths.

the estimation of $\mathbf{H}$, the proposed scheme offers an order of magnitude improvement in the estimation of $\mathbf{G}$ (see Figure 57).

Figura 57 – Channels NMSE versus SNR.

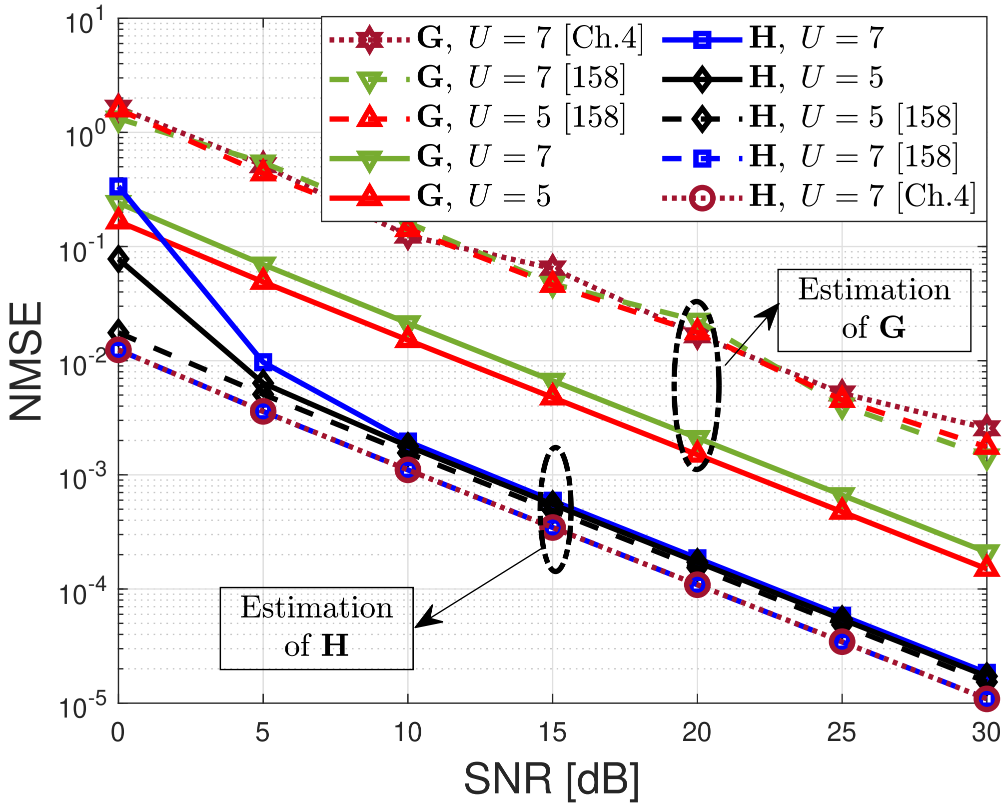

To evaluate the computational complexity of the proposed semi-blind KAKF receiver, we consider the same parameters as in Figure 57 and plot in Figure 58 the average runtime as a function of the SNR. Since the KAKF receiver has a closed-form solution, it offers a considerable complexity reduction compared to the iterative BALS receiver (Wei *et al.*,). On the other hand, the KRF method is a bit faster than our proposed method, since the KAKF receiver involves an additional processing step to estimate the symbol matrix. Furthermore, the computational complexity of KAKF does not depend on the SNR, unlike BALS, where the number of iterations for convergence increases for lower SNR values. This is an interesting result since the CE performance and the computational complexity depend on the number of parameters to be estimated, which scales with the number of UTs. In particular, the estimate of $\mathbf{H}$ is more accurate than that of $\mathbf{G}$ since the latter has more coefficients to be estimated. However, even in this situation, KAKF has a much lower runtime compared to the method of (Wei *et al.*,) and, thus, an improved end-to-end latency, for the same data block length.

The SER performance is illustrated in Figure 59 considering different numbers of

Figura 58 – Average runtime versus SNR.

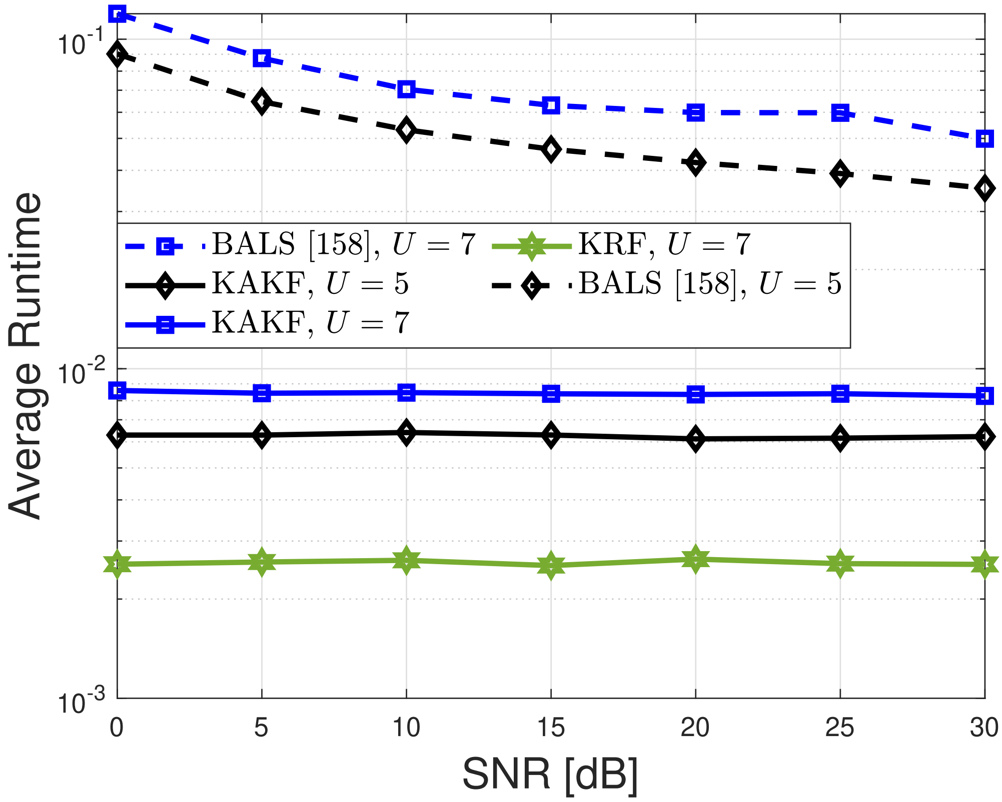

users $U \in \{4, 10\}$, different numbers of antennas $M \in \{4, 16\}$, and different numbers of IRS elements $N \in \{16, 36\}$. Besides, $K = NLU$ and $T = 4$. The other parameters are the same as in Figure 57. This result shows that the SER decreases as a function of the number of IRS elements. This is an interesting result since no optimization process is carried out, which may further improve the system performance[4]. Fixing $N = 16$, the effect of the number of antennas at the BS and the number of users is shown. By increasing M and keeping $U = 4$, the SER improves due to a spatial diversity gain. Changing the roles, i.e., keeping $M = 4$ and increasing U, the SER degrades as U increases. This is intuitive since the number of channel components to be estimated increases as more users are active in the system.

6.6 Summary

In this chapter, a two-stage closed-form semi-blind receiver for joint channel and symbol estimation in IRS-assisted MU-MIMO systems based on a generalized PARATUCK tensor modeling was proposed. We have seen that the KAKF receiver yields more accurate

[4] In practice, in the BALS and KRF methods, optimizing the beamforming weights for data transmission takes place before data transmission. However, this optimization step is out of the scope of the present work.

Figura 59 – SER *versus* SNR.

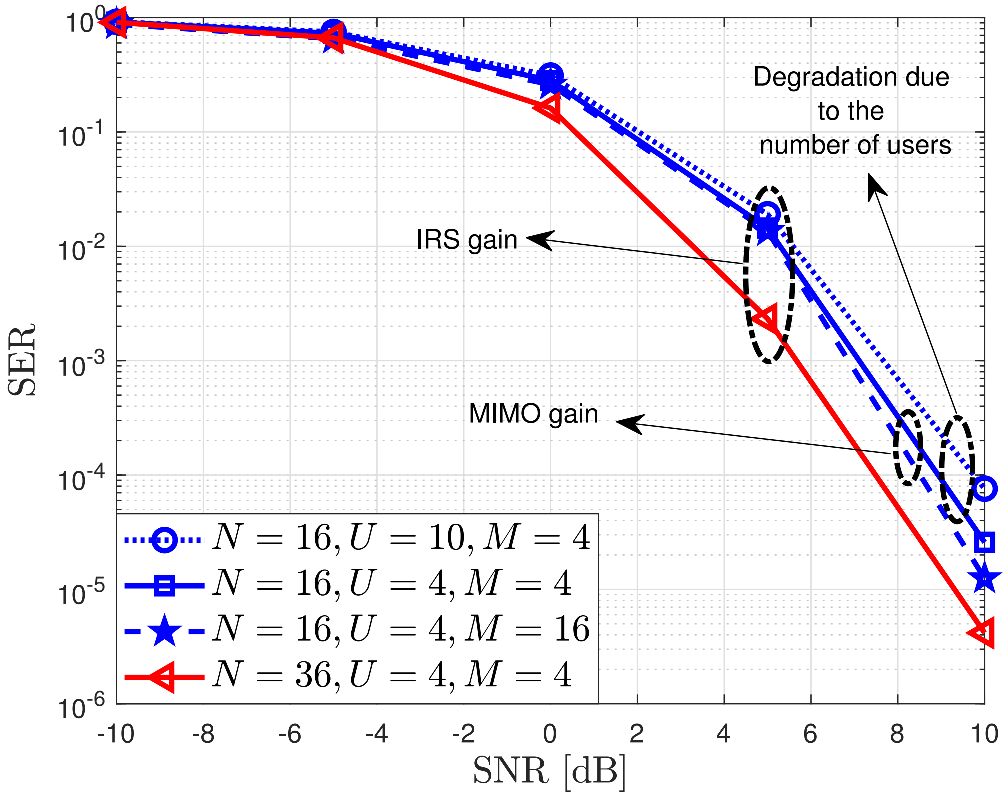

channel estimates while handling time-varying channels with low computational complexity. One limitation of the proposed receiver is the error propagation between the two estimation processing stages since symbol estimation and channel estimation are accomplished by solving problems (6.11) and (6.16) sequentially. Such a limitation may degrade the channel estimation performance in the low SNR regime. Moreover, the required number of transmission blocks may be too high for large systems with many antennas, IRS elements, and/or users. A possible solution to overcome this limitation is to resort to iterative estimation approaches exploiting the PARATUCK-(2,4) received signal model in (6.4). For instance, it is possible to recast it as a structured PARAFAC model and solve the joint channel and symbol estimation iteratively using a BALS estimation procedure similar to the one discussed in Chapter 4 for the pilot-assisted case.

7 CONCLUSIONS AND PERSPECTIVES

7.1 Conclusions

This thesis addressed intelligent reflecting surface-assisted wireless MIMO communications from the perspective of channel estimation using a tensor modeling approach. We have shown how the cascaded channel estimation problem can be solved by recasting the received signals as tensors. Resorting to PARAFAC and PARATUCK tensor decomposition algorithms, different algorithms for estimating the involved communication channels in pilot-assisted and semi-blind cases have been derived. More specifically, we can mention the following contributions:

In Chapter 4, we have proposed novel pilot-assisted receiver designs for IRS-assisted MIMO communication systems via a tensor modeling approach. The proposed KRF and BALS receivers effectively exploit the tensor structure in the received signal. Both solutions yield decoupled estimates of the BS-IRS and IRS-UT channels at the receiver for a passive IRS. The closed-form KRF method has a lower complexity but a more restrictive requirement on the training parameter K. In contrast, although more computationally complex, the iterative BALS method can operate under more flexible choices for this parameter with a lower training overhead. Our design recommendations provide useful conditions on the system parameters that guarantee the uniqueness of the channel estimates. Our numerical results have demonstrated the superior performance of KRF and BALS compared to the conventional LS estimator, which ignores the Khatri-Rao structure of the combined channel matrix. In addition, the proposed tensor modeling approach allows us to deal with a nonideal setup where the IRS phase shifts are not perfectly known at the receiver due to phase perturbations/fluctuations. In this more complex setup, leveraging the trilinear structure of the received signal using a TALS algorithm provides a joint estimation of the channel matrices and the IRS phase shift matrix. The proposed solutions also provide better results than recently proposed competing methods. Generalizations of our tensor modeling approach to multi-user scenarios have also been discussed, and analytical expressions for the CRB have been derived (see appendix A).

In Chapter 5, we have proposed a novel tensor-based semi-blind receiver design for IRS-assisted MIMO communication systems exploiting a PARATUCK tensor modeling for the received signals. The proposed semi-blind receiver is a data-aided channel estimator that performs a joint estimation of the IRS-BS channel, UT-IRS channel, and the transmitted symbols in an iterative way through a TALS (algorithm 6) when the direct link is unavailable or negligible or employing E-TALS (algorithm 7) if the direct link is available. We have studied the design of the coding matrix and IRS phase shift matrix, and a joint design has been proposed that optimizes the receiver performance while simplifying the CRB derivations (see appendices B and C). The results indicated that the TALS receiver yields an improved CE accuracy than “block-LS"and BALS algorithms while offering a joint channel and symbol recovery, thus being a good solution for IRS-assisted MIMO systems, especially when pilot resources are limited or not available. The proposed semi-blind receiver effectively exploited the direct link to refine the direct channel estimate and the transmitted symbols in an iterative process. In addition, the E-TALS proved robust to deal with imperfect IRS absorption during the direct link channel estimation stage.

Finally, in Chapter 6, we proposed a two-stage closed-form semi-blind receiver for joint channel and symbol estimation in IRS-assistedMU-MIMO systems based on a generalized PARATUCK tensor modeling. The so-called KAKF receiver provided joint estimates of the UTs-IRS and IRS-BS channels and the transmitted symbols with low computational complexity. Compared to its pilot-assisted competitor, KAKF yields more accurate channel estimates while handling time-varying channels.

Tabela 2 – Comparison of the proposed algorithms

Algorithm	Solution	Scenario	System parameter choices	Pilot-assisted method	Semi-blind method
KRF	Closed Form	Single user	Restrictive	✓	
BALS	Iterative	Single user	Flexible	✓	
TALS	Iterative	Single user	Flexible		✓
E-TALS	Iterative	Single user	Flexible/ restrictive		✓
KAKF	Closed Form	Multi user	restrictive		✓

We conclude this discussion by providing in Table 2 a summary of the main aspects related to the algorithms developed in this thesis. First, the two closed-form solutions, namely, KRF (for the pilot-assisted case) and KAKF (for the semi-blind case) are attractive due to their implementation simplicity since both involve computing a set of rank-one matrix approximation problems for which very efficient solutions exist. Moreover, they cope well with a parallel processing architecture, once the associated rank-one approximation steps can all be executed in parallel. However, as indicated in the table, both solutions are more restrictive in terms of system parameter choices such as the number of antennas at the BS and/or UE, and require a larger training overhead than the iterative algorithms BALS (for the pilot-assisted case) and TALS/E-TALS (for the semi-blind case). The latter ones, despite these advantages, are more complex due to their iterative nature, requiring the computation of matrix inverses at each iteration. Nevertheless, they become more powerful than the closed-form ones in certain (nonideal) cases such as the one where the IRS phase shift matrix is not perfectly known at the receiver due to unknown hardware impairments, as discussed in Chapter 4 when pilot-assisted estimation is considered. In this case, a TALS algorithm can be used to jointly estimate the involved channel matrices and the IRS phase shift matrix. This scenario is particularly interesting from a practical viewpoint.

7.2 Perspectives

As perspectives from this thesis work, we may highlight the following points.

- The investigation of new IRS architectures such as hybrid IRS, STAR-IRS, and non-diagonal IRS, also named beyond diagonal IRS (BD-IRS) is a point that deserves further study and may lead to new solutions. Such a study is important since it brings new features and implications in terms of solutions presented up to now for IRS-assisted wireless communications. For example, in the BD-IRS scenario, the channel estimation methods presented throughout this thesis are not directly applicable, since the PARAFAC and PARATUCK tensor models derived in Chapters 4, 5, and 6 assume that the structure of the phase shift matrix is diagonal. Assuming a non-diagonal design for the phase shift matrix, these models must be generalized, which may lead to new channel estimation algorithms. Moreover, more complex tensor models may imply a higher channel estimation complexity, requiring low-complexity optimization methods and/or a reformulation of the problem that involves shorter pilot sequences and manageable training overheads.
- The study of the new tensor-based algorithms for IRS-assisted joint communication and sensing is also interesting. In this context, tensor-based approaches can also be exploited for joint multidimensional target parameter estimation/tracking combined with channel/data estimation. The development of semi-blind methods would be welcome to minimize the training overhead and data decoding delay. In addition, considering passive IRS structures,

the choice of the sensing and communication protocol involving the IRS operation is also relevant and directly affects the formulation of the tensor models characterizing the received signals. Hence, new tensor-based receivers may arise in this promising research direction.

– The investigation of the near-field case may also be the subject of further work. The assumption of extremely large antenna arrays combined with terahertz communications has been studied recently. In this scenario, due to the extremely large array aperture and bandwidth, near-field wideband channel models should be adopted, which necessarily change the multilinear algebraic structure of the tensor models discussed in this thesis, which would perhaps require the development of new tensor models. Since the associated tensor modeling and signal processing will likely be more complex, the study of strategies to simplify channel estimation, target sensing/tracking, and data detection would be welcome.

REFERENCES

ABEYWICKRAMA, S.; ZHANG, R.; WU, Q.; YUEN, C. Intelligent reflecting surface: Practical phase shift model and beamforming optimization. **IEEE Transactions on Communications**, v. 68, n. 9, p. 5849–5863, 2020.

ALMEIDA, A. L.; FAVIER, G.; MOTA, J. C. Space–time spreading–multiplexing for MIMO wireless communication systems using the PARATUCK-2 tensor model. **Signal Processing**, v. 89, n. 11, p. 2103–2116, 11 2009.

ALMEIDA, A. L. de; FAVIER, G. Unified tensor model for space-frequency spreading-multiplexing (SFSM) MIMO communication systems. **EURASIP J. Adv. Signal Process**, v. 38, 2013.

ALMEIDA, A. L. de; FAVIER, G.; MOTA, J. C. Space–time spreading MIMO-CDMA downlink systems using constrained tensor modeling. **Signal Processing**, v. 88, n. 10, p. 2403–2416, 2008.

ALMEIDA, A. L. de; FAVIER, G.; MOTA, J. C. M. Parafac-based unified tensor modeling for wireless communication systems with application to blind multiuser equalization. **Signal Processing**, v. 87, n. 2, p. 337–351, 2007. Tensor Signal Processing.

ALMEIDA, A. L. F. de. **Tensor Modeling and Signal Processing for wireless communication Systems**. Tese (Doutorado) — Universidade de Nice-Sophia Antipolis, 11 2007.

ALMEIDA, A. L. F. de; FAVIER, G.; COSTA, J. P. C. L. da; MOTA, J. C. M. Overview of tensor decompositions with applications to communications. In: COELHO, R.; NASCIMENTO, V.; QUEIROZ, R. de; ROMANO, J.; CAVALCANTE, C. (Ed.). **Signals and Images: Advances and Results in Speech, Estimation, Compression, Recognition, Filtering, and Processing**. [S.l.]: CRC-Press, 2016. p. 325–356.

ALMEIDA, A. L. F. de; FAVIER, G.; MOTA, J. C. M. A constrained factor decomposition with application to MIMO antenna systems. **IEEE Transactions on Signal Processing**, v. 56, n. 6, p. 2429–2442, 2008.

ALMEIDA, A. L. F. de; FAVIER, G.; MOTA, J. C. M. Constrained tensor modeling approach to blind multiple-antenna CDMA schemes. **IEEE Transactions on Signal Processing**, v. 56, n. 6, p. 2417–2428, 2008.

ALMEIDA, A. L. F. de; FAVIER, G.; MOTA, J. C. M.; LACERDA, R. L. de. Estimation of frequency-selective block-fading MIMO channels using parafac modeling and alternating least squares. In: **2006 Fortieth Asilomar Conference on Signals, Systems and Computers**. [S.l.: s.n.], 2006. p. 1630–1634.

ALMEIDA, A. L. F. de; FAVIER, G.; XIMENES, L. R. Space-time-frequency (STF) MIMO communication systems with blind receiver based on a generalized paratuck2 model. **IEEE Transactions on Signal Processing**, v. 61, n. 8, p. 1895–1909, 2013.

ALWAKEEL, A. S.; ELZANATY, A. Semi-blind channel estimation for intelligent reflecting surfaces in massive MIMO systems. **IEEE Access**, v. 10, p. 127783–127797, 11 2022.

AN, J.; XU, C.; WANG, L.; LIU, Y.; GAN, L.; HANZO, L. Joint training of the superimposed direct and reflected links in reconfigurable intelligent surface assisted multiuser communications. **IEEE Transactions on Green Communications and Networking**, v. 6, n. 2, p. 739–754, 2022.

ARAÚJO, D. C. de; ALMEIDA, A. L. F. de; COSTA, J. P. C. L.; SOUSA, R. T. Tensor-based channel estimation for massive MIMO-OFDM systems. **IEEE Access**, v. 7, p. 42133–42147, 3 2019.

ARAÚJO, D. C. de; ALMEIDA, A. L. F. de; COSTA, J. P. C. L. D.; SOUSA, R. T. de. Tensor-based channel estimation for massive MIMO-OFDM systems. **IEEE Access**, v. 7, p. 42133–42147, 2019.

ARAÚJO, G. T. de; ALMEIDA, A. L. F. de. Closed-form channel estimation for MIMO space–time coded systems using a fourth-order tensor-based receiver. **Circuits Syst Signal Process**, v. 37, n. 3, p. 1343–1357, 2017.

BADIU, M.; COON, J. P. Communication through a large reflecting surface with phase errors. **IEEE Wireless Commun. Letters**, v. 9, n. 2, p. 184–188, 2020.

BANAFAA, M.; SHAYEA, I.; DIN, J.; Hadri Azmi, M.; ALASHBI, A.; Ibrahim Daradkeh, Y.; ALHAMMADI, A. 6G mobile communication technology: Requirements, targets, applications, challenges, advantages, and opportunities. **Alexandria Engineering Journal**, v. 64, p. 245–274, 2023. ISSN 1110-0168. Disponível em: https://www.sciencedirect.com/science/article/pii/S111001682200549X.

BASAR, E.; RENZO, M. D.; ROSNY, J. D.; DEBBAH, M.; ALOUINI, M.-S.; ZHANG, R. Wireless communications through reconfigurable intelligent surfaces. **IEEE Access**, v. 7, p. 116753–116773, 2019.

BENÍCIO, K. B. A.; ALMEIDA, A. L. F. de; SOKAL, B.; FAZAL-E-ASIM; MAKKI, B.; FODOR, G. Tensor-based channel estimation and data-aided tracking in irs-assisted MIMO systems. **IEEE Wireless Communications Letters**, p. 1–1, 2023.

BJORNSON, E.; WYMEERSCH, H.; MATTHIESEN, B.; POPOVSKI, P.; SANGUINETTI, L.; CARVALHO, E. de. Reconfigurable intelligent surfaces: A signal processing perspective with wireless applications. **IEEE Signal Proces. Mag.**, v. 39, n. 2, p. 135–158, 2 2022.

BRO, R. **Multi- Way Analysis In The Food Industry: Models, Algorithms & Applications**. Tese (Doutorado) — University of Amsterdam, 11 1998.

CAROLL, J. D.; CHANG, J. J. Analysis of individual differences in multidimensional scaling via n-way generalization of Eckart–Young decomposition. **Psychometrika**, v. 35, p. 283–319, 1970.

CAVALCANTE, V.; ALMEIDA, A. L. F. de; HAARDT, M. Joint channel estimation for three-hop MIMO relaying systems. **IEEE Signal Processing Letters**, v. 22, n. 12, p. 2430–2434, 2015.

CHEN, H.; AHMAD, F.; VOROBYOV, S.; PORIKLI, F. Tensor decompositions in wireless communications and MIMO radar. **IEEE Journal of Selected Topics in Signal Processing**, v. 15, n. 3, p. 438–453, 2021.

CHEN, H.; YANG, H. H.; TAO, Q.; ZHONG, C. Coverage analysis of cell-edge users in reconfigurable intelligent surface-assisted cellular networks. In: **2022 14th International Conference on Wireless Communications and Signal Processing (WCSP)**. [S.l.: s.n.], 2022. p. 759–763.

CHEN, J.; LIANG, Y.-C.; CHENG, H. V.; YU, W. **Channel Estimation for Reconfigurable Intelligent Surface Aided Multi-User MIMO Systems**. 2019.

CHEN, L.; YUAN, X.; ZHANG, Y.-J. A. Coverage analysis of intelligent reflecting surface assisted cellular networks. In: **2022 IEEE/CIC International Conference on Communications in China (ICCC)**. [S.l.: s.n.], 2022. p. 1014–1019.

CHEN, X.; SHI, J.; YANG, Z.; WU, L. Low-complexity channel estimation for intelligent reflecting surface-enhanced massive MIMO. **IEEE Wireless Commun. Lett.**, v. 10, n. 5, p. 996–1000, 5 2021.

CHEN, Z.; NING, B.; HAN, C.; TIAN, Z.; LI, S. Intelligent reflecting surface assisted terahertz communications toward 6G. **IEEE Wireless Communications**, v. 28, n. 6, p. 110–117, 2021.

CHENG, L.; TONG, X.; WANG, S.; WU, Y.; POOR, H. V. Learning nonnegative factors from tensor data: Probabilistic modeling and inference algorithm. **IEEE Trans. Signal. Process.**, v. 68, p. 1792–1806, 2020.

CICHOCKI, A.; MANDIC, D.; LATHAUWER, L. D.; ZHOU, G.; ZHAO, Q.; CAIAFA, C.; PHAN, H. A. Tensor decompositions for signal processing applications: From two-way to multiway component analysis. **IEEE Signal Processing Magazine**, v. 32, n. 2, p. 145–163, 2015.

COMON, P.; LUCIANI, X.; ALMEIDA, A. L. F. de. Tensor decompositions, alternating least squares and other tales. **Journal of Chemometrics**, v. 23, n. 7-8, p. 393–405, 2009. ISSN 08869383.

COSTA, N.; HAYKIN, S. A novel wideband MIMO channel model and experimental validation. **IEEE Transactions on Antennas and Propagation**, v. 56, n. 2, p. 550–562, 2008.

CUI, Y.; YIN, H. **An Efficient CSI Acquisition Method for Intelligent Reflecting Surface-assisted mmWave Networks**. 2019.

DEEPAK, B.; SANKAR, R. S. P.; CHEPURI, S. P. **Channel Estimation for RIS-assisted Millimeter-wave MIMO Systems**. 2021. ArXiv:2011.00900v2 [eess.SP].

DGR/RIS-001. **Reconfigurable Intelligent Surfaces (RIS); Use Cases, Deployment Scenarios and Requirements**.

DGR/RIS-003. **Reconfigurable Intelligent Surfaces (RIS); Communication Models, Channel Models, Channel Estimation and Evaluation Methodology**.

DOCOMO, I. N. **5G Evolution and 6G**. 2022. White Paper.

DONG, L.; WANG, H.-M. Secure MIMO transmission via intelligent reflecting surface. **IEEE Wireless Commun. Letters**, v. 9, n. 6, p. 787–790, 2020.

DOU, Z.; LI, C.; GAO, X.; QI, L. Tensor communication waveform design with semi-blind receiver in the MIMO system. **IEEE Trans. Veh. Technol.**, v. 69, n. 2, p. 1727–1740, 2 2020.

DU, J.; HAN, M.; CHEN, Y.; JIN, L.; GAO, F. Tensor-based joint channel estimation and symbol detection for time-varying mmwave massive MIMO systems. **IEEE Transactions on Signal Processing**, v. 69, p. 6251–6266, 2021.

DU, J.; HAN, M.; JIN, L.; HUA, Y.; LI, X. Semi-blind receivers for multi-user massive MIMO relay systems based on block tucker2-parafac tensor model. **IEEE Access**, v. 8, p. 32170–32186, 2020.

DU, J.; HAN, M.; JIN, L.; HUA, Y.; LI, X. Semi-blind receivers for multi-user massive MIMO relay systems based on block Tucker2-PARAFAC tensor model. **IEEE Access**, v. 8, p. 32170–32186, 2 2020.

DU, J.; YE, S.; JIN, L.; LI, X.; NGO, H. Q.; DOBRE, O. A. Tensor-based joint channel estimation for multi-way massive MIMO hybrid relay systems. **IEEE Transactions on Vehicular Technology**, v. 71, n. 9, p. 9571–9585, 2022.

E-ASIM, F.; ALMEIDA, A. L. F. de; HAARDT, M.; CAVALCANTE, C. C.; NOSSEK, J. A. Rank-one detector for kronecker-structured constant modulus constellations. **IEEE Signal Processing Letters**, v. 27, p. 1420–1424, 2020.

ECKART, C.; YOUNG, G. The approximation of one matrix by another of lower rank. **Psychometrika**, v. 1, n. 3, p. 211–218, 9 1936.

FAVIER, G.; ALMEIDA, A. L. F. de. Overview of constrained PARAFAC models. **EURASIP Journal on Advances in Signal Processing**, v. 2014, n. 142, 9 2014.

FAVIER, G.; ALMEIDA, A. L. F. de. Tensor space-time-frequency coding with semi-blind receivers for MIMO wireless communication systems. **IEEE Trans. Signal Process.**, v. 62, n. 22, p. 5987–6002, 11 2014.

FAVIER, G.; BOUILLOC, T.; ALMEIDA, A. L. de. Blind constrained block-tucker2 receiver for multiuser SIMO NL-CDMA communication systems. **Signal Processing**, v. 92, n. 7, p. 1624–1636, 2012. ISSN 0165-1684. Disponível em: https://www.sciencedirect.com/science/article/pii/S0165168411004610.

FAVIER, G.; COSTA, M. N.; ALMEIDA, A. L. de; ROMANO, J. M. T. Tensor space–time (TST) coding for MIMO wireless communication systems. **Signal Processing**, v. 92, n. 4, p. 1079–1092, 2012. ISSN 0165-1684. Disponível em: https://www.sciencedirect.com/science/article/pii/S0165168411003835.

FAVIER, G.; FERNANDES, C. A. R.; ALMEIDA, A. L. de. Nested tucker tensor decomposition with application to MIMO relay systems using tensor space–time coding (tstc). **Signal Processing**, v. 128, p. 318–331, 2016. ISSN 0165-1684. Disponível em: https://www.sciencedirect.com/science/article/pii/S0165168416300482.

FAZAL-E-ASIM; ALMEIDA, A. L. F. de; ANTREICH, F.; HAARDT, M.; CAVALCANTE, C. C. Kronecker product-based space-time block codes. **IEEE Wireless Communications Letters**, v. 11, n. 2, p. 386–390, 2022.

FAZAL-E-ASIM; ALMEIDA, A. L. F. de; HAARDT, M.; CAVALCANTE, C. C.; NOSSEK, J. A. Multi-linear encoding and decoding for MIMO systems. In: **2020 IEEE 11th Sensor Array and Multichannel Signal Processing Workshop (SAM)**. [S.l.: s.n.], 2020. p. 1–5.

FERNANDES, C. A. R.; ALMEIDA, A. L. F. de; COSTA, D. B. da. Unified tensor modeling for blind receivers in multiuser uplink cooperative systems. **IEEE Signal Processing Letters**, v. 19, n. 5, p. 247–250, 2012.

FREITAS, W.; FAVIER, G.; ALMEIDA, A. L. F. de. Generalized khatri-rao and kronecker space-time coding for MIMO relay systems with closed-form semi-blind receivers. **Signal Processing**, v. 151, p. 19–31, 2018. ISSN 0165-1684. Disponível em: https://www.sciencedirect.com/science/article/pii/S0165168418301324.

GHAZALIAN, R.; CHEN, H.; ALEXANDROPOULOS, G. C.; SECO-GRANADOS, G.; WYMEERSCH, H.; JäNTTI, R. Joint user localization and location calibration of a hybrid reconfigurable intelligent surface. **IEEE Transactions on Vehicular Technology**, p. 1–6, 2023.

GOLUB, G. H.; LOAN, C. F. van. **Matrix Computations**. Fourth. [S.l.]: John Hopkins University Press, 2013.

GOMES, P. R.; ALMEIDA, A. L. de; COSTA, J. P. C. da; SOUSA, R. T. de. A nested-parafac based approach for target localization in bistatic MIMO radar systems. **Digital Signal Processing**, v. 89, p. 40–48, 2019. ISSN 1051-2004. Disponível em: https://www.sciencedirect.com/science/article/pii/S1051200418301118.

GOMES, P. R.; COSTA, J. P. C.; ALMEIDA, A. L. de; SOUSA, R. T. de. Tensor-based multiple denoising via successive spatial smoothing, low-rank approximation and reconstruction for r-d sensor array processing. **Digital Signal Processing**, v. 89, p. 1–7, 2019. ISSN 1051-2004. Disponível em: https://www.sciencedirect.com/science/article/pii/S1051200418302847.

GOMES, P. R. B.; ARAÚJO, G. T. de; SOKAL, B.; ALMEIDA, A. L. F. d. de; MAKKI, B.; FODOR, G. Channel estimation in ris-assisted MIMO systems operating under imperfections. **IEEE Transactions on Vehicular Technology**, v. 72, n. 11, p. 14200–14213, 2023.

GONG, S.; LU, X.; HOANG, D. T.; NIYATO, D.; SHU, L.; KIM, D. I.; LIANG, Y. C. Toward smart wireless communications via intelligent reflecting surfaces: A contemporary survey. **IEEE Commun. Surveys Tuts.**, v. 22, n. 4, p. 2283–2314, 6 2020.

GRADONI, G.; RENZO, M. D. End-to-end mutual coupling aware communication model for reconfigurable intelligent surfaces: An electromagnetic-compliant approach based on mutual impedances. **IEEE Wireless Communications Letters**, v. 10, n. 5, p. 938–942, 2021.

GUAN, X.; WU, Q.; ZHANG, R. Anchor-assisted intelligent reflecting surface channel estimation for multiuser communications. In: **proc. GLOBECOM "2020"**. [S.l.: s.n.]. p. 1–6.

GUAN, X.; WU, Q.; ZHANG, R. Anchor-assisted channel estimation for intelligent reflecting surface aided multiuser communication. **IEEE Trans. Wireless Commun.**, p. 1–1, 11 2021.

GUO, H.; MAKKI, B.; ÅSTRöM, M.; ALOUINI, M.-S.; SVENSSON, T. **Dynamic Blockage Pre-Avoidance using Reconfigurable Intelligent Surfaces**. 2022. ArXiv:2201.06659v1 [cs.IT].

HALKO, N.; MARTINSSON, P. G.; TROPP, J. A. Finding structure with randomness: Probabilistic algorithms for constructing approximate matrix decompositions. **SIAM Review**, v. 53, n. 2, p. 217–288, 2011.

HAN, K.; NEHORAI, A. Nested vector-sensor array processing via tensor modeling. **IEEE Transactions on Signal Processing**, v. 62, n. 10, p. 2542–2553, 2014.

HAN, X.; ZHAO, X.; ALMEIDA, A. L. F. de; FREITAS, W. d. C.; BAI, W. Enhanced tensor-based joint channel and symbol estimation in dual-hop MIMO relaying systems. **IEEE Communications Letters**, v. 25, n. 5, p. 1655–1659, 2021.

HAN, X.; ZHOU, Y.; ALMEIDA, A. L. de; FREITAS, W. da C. Semiblind unials receiver for a two-way MIMO relaying system based on the paratuck2 model. **Digital Signal Processing**, v. 110, p. 102916, 2021. ISSN 1051-2004. Disponível em: https://www.sciencedirect.com/science/article/pii/S105120042030261X.

HARSHMAN, R.; LUNDY, M. Uniqueness proof for a family of models sharing features of tucker's three-mode factor analysis and parafac/candecomp. **Psychometrika**, v. 61, n. 1, p. 133–154, 1996.

HARSHMAN, R. A. Foundations of the PARAFAC procedure: Models and conditions for an "explanatory" multi-modal factor analysis. **UCLA Working Papers in Phonetics**, v. 16, p. 1–84, 12 1970.

HASSOUNA, S.; JAMSHED, M. A.; RAINS, J.; KAZIM, J. u. R.; REHMAN, M. U.; ABUALHAYJA, M.; MOHJAZI, L.; CUI, T. J.; IMRAN, M. A.; ABBASI, Q. H. A survey on reconfigurable intelligent surfaces: Wireless communication perspective. **IET Communications**, v. 17, n. 5, p. 497–537, 2023.

HE, Z.-Q.; YUAN, X. Cascaded channel estimation for large intelligent metasurface assisted massive MIMO. **IEEE Wireless Commun. Lett.**, v. 9, n. 2, p. 210–214, 2020.

HEATH, R. W.; GONZáLEZ-PRELCIC, N.; RANGAN, S.; ROH, W.; SAYEED, A. M. An overview of signal processing techniques for millimeter wave MIMO systems. **IEEE J. Sel. Topics Signal Process.**, v. 10, n. 3, p. 436–453, 2016.

HITCHCOCK, F. L. The expression of a tensor or a polyadic as a sum of products. **Journal of Mathematical Physics**, v. 6, n. 1, p. 164–189, 4 1927.

HU, C.; DAI, L.; HAN, S.; WANG, X. Two-timescale channel estimation for reconfigurable intelligent surface aided wireless communications. **IEEE Trans. Commun.**, v. 69, n. 11, p. 7736–7747, 11 2021.

HU, X.; ZHANG, R.; ZHONG, C. Semi-passive elements assisted channel estimation for intelligent reflecting surface-aided communications. **IEEE Transactions on Wireless Communications**, v. 21, n. 2, p. 1132–1142, 2 2022.

HUA, M.; WU, Q.; HE, C.; MA, S.; CHEN, W. Joint active and passive beamforming design for irs-aided radar-communication. **IEEE Transactions on Wireless Communications**, v. 22, n. 4, p. 2278–2294, 2023.

HUANG, C.; XU, J.; ZHANG, W.; XU, W.; NG, D. W. K. Semi-blind channel estimation for RIS-assisted MISO systems using expectation maximization. **IEEE Trans.s Veh. Tech.**, v. 71, n. 9, p. 10173–10178, 9 2022.

HUANG, C.; ZAPPONE, A.; ALEXANDROPOULOS, G. C.; DEBBAH, M.; YUEN, C. Reconfigurable intelligent surfaces for energy efficiency in wireless communication. **IEEE Trans. Wireless Commun.**, v. 18, n. 8, p. 4157–4170, 8 2019.

INC., M. **6G vision whitepaper**. 2022. White Paper.

JENSEN, T. L.; CARVALHO, E. D. An optimal channel estimation scheme for intelligent reflecting surfaces based on a minimum variance unbiased estimator. In: **proc. ICASSP "2020"**. Barcelona, Spain: [s.n.], 2020. p. 5000–5004.

JIANG, W.; LUO, F.-L. Intelligent reflecting surface-aided communications for 6G. In: ____. **6G Key Technologies: A Comprehensive Guide**. [S.l.: s.n.], 2023. p. 295–362.

JIN, Y.; ZHANG, J.; ZHANG, X.; XIAO, H.; AI, B.; NG, D. W. K. Channel estimation for semi-passive reconfigurable intelligent surfaces with enhanced deep residual networks. **IEEE Trans. Veh. Technol.**, v. 70, n. 10, p. 11083–11088, 10 2021.

KANG, Z.; YOU, C.; ZHANG, R. **Active-IRS-Aided Wireless Communication: Fundamentals, Designs and Open Issues**. 2023.

KHAMIDULLINA, L.; ALMEIDA, A. L. F. de; HAARDT, M. Multilinear generalized singular value decomposition (ml-gsvd) with application to coordinated beamforming in multi-user MIMO systems. In: **proc. ICASSP “2020"**. Barcelona, Spain: [s.n.]. p. 4587–4591.

KHAMIDULLINA, L.; PODKURKOV, I.; HAARDT, M. Conditional and unconditional cramér-rao bounds for near-field localization in bistatic MIMO radar systems. **IEEE Transactions on Signal Processing**, v. 69, p. 3220–3234, 2021.

KHOSHAFA, M. H.; NGATCHED, T. M. N.; AHMED, M. H.; NDJIONGUE, A. R. Active reconfigurable intelligent surfaces-aided wireless communication system. **IEEE Communications Letters**, v. 25, n. 11, p. 3699–3703, 2021.

KIBANGOU, A. Y.; FAVIER, G. Non-iterative solution for PARAFAC with a toeplitz matrix factor. In: **Proc. EUSIPCO “2009"**. [S.l.: s.n.]. p. 691–695.

KOFIDIS, E.; CHATZICHRISTOS, C.; ALMEIDA, A. L. F. de. Joint channel estimation / data detection in MIMO-FBMC/OQAM systems — a tensor-based approach. In: **2017 25th European Signal Processing Conference (EUSIPCO)**. [S.l.: s.n.], 2017. p. 420–424.

KOLDA, T. G. **Multilinear Operators for Higher-order Decompositions**. [S.l.], 2006. Disponível em: http://www.osti.gov/scitech/biblio/923081.

KOLDA, T. G.; BADER, B. W. Tensor decompositions and applications. **SIAM REVIEW**, v. 51, n. 3, p. 455–500, 8 2009.

KRUSKAL, J. B. Three-way arrays: rank and uniqueness of trilinear decompositions, with application to arithmetic complexity and statistics. **Linear Algebra and its Applications**, v. 18, n. 2, p. 95–138, 1977. ISSN 0024-3795. Disponível em: https://www.sciencedirect.com/science/article/pii/0024379577900696.

KUNDU, N. K.; LI, Z.; RAO, J.; SHEN, S.; MCKAY, M. R.; MURCH, R. Optimal grouping strategy for reconfigurable intelligent surface assisted wireless communications. **IEEE Wireless Commun. Lett.**, v. 11, n. 5, p. 1082–1086, 5 2022.

LATHAUWER, L. D. Signal processing based on multilinear algebra. In: . [s.n.], 1997. Disponível em: https://api.semanticscholar.org/CorpusID:115852714.

LATHAUWER, L. D. Decompositions of a higher-order tensor in block terms—part I: Lemmas for partitioned matrices. **SIAM Journal on Matrix Analysis and Applications**, v. 30, n. 3, p. 1022–1032, 2008.

LATHAUWER, L. D.; CASTAING, J. Tensor-based techniques for the blind separation of DS–CDMA signals. **Signal Processing**, v. 87, n. 2, p. 322–336, 2007. Tensor Signal Processing.

LATHAUWER, L. D.; MOOR, B. D. From matrix to tensor : Multilinear algebra and signal processing. In: . [s.n.], 1996. Disponível em: https://api.semanticscholar.org/CorpusID:125104227.

LI, B.; ZHANG, Z.; HU, Z.; CHEN, Y. Joint array diagnosis and channel estimation for RIS-aided mmWave MIMO system. **IEEE Access**, v. 8, p. 193992–194006, 2020.

LI, H.; SHEN, S.; CLERCKX, B. Beyond diagonal reconfigurable intelligent surfaces: From transmitting and reflecting modes to single-, group-, and fully-connected architectures. **IEEE Transactions on Wireless Communications**, v. 22, n. 4, p. 2311–2324, 2023.

LI, Q.; EL-HAJJAR, M.; HEMADEH, I.; SHOJAEIFARD, A.; MOURAD, A. A. M.; CLERCKX, B.; HANZO, L. Reconfigurable intelligent surfaces relying on non-diagonal phase shift matrices. **IEEE Transactions on Vehicular Technology**, v. 71, n. 6, p. 6367–6383, 2022.

LI, S.; SUN, Z.; ZHANG, X.; CHEN, W.; XU, D. Joint doa and frequency estimation for linear array with compressed sensing parafac framework. **Journal of Circuits, Systems and Computers**, v. 26, n. 09, p. 1750136, 2017.

LI, Z.; KUNDU, N. K.; RAO, J.; SHEN, S.; MCKAY, M. R.; MURCH, R. Performance analysis of RIS-assisted communications with element grouping and spatial correlation. **IEEE Wireless Commun. Let.**, p. 1–1, 2023.

LIANG, R.; FAN, J.; LIU, H.; GE, Y.; ZHANG, J. Dual-hop hybrid irs-aided outdoor-to-indoor mmwave communications. **IEEE Communications Letters**, v. 26, n. 12, p. 2979–2983, 2022.

LIN, Y.; JIN, S.; MATTHAIOU, M.; YOU, X. Tensor-based algebraic channel estimation for hybrid irs-assisted MIMO-OFDM. **IEEE Transactions on Wireless Communications**, v. 20, n. 6, p. 3770–3784, 2021.

LIU, K.; COSTA, J. P. C. L. da; SO, H. C.; ALMEIDA, A. L. F. de. Semi-blind receivers for joint symbol and channel estimation in space-time-frequency MIMO-OFDM systems. **IEEE Transactions on Signal Processing**, v. 61, n. 21, p. 5444–5457, 2013.

LIU, K.; ZHANG, Z.; DAI, L.; XU, S.; YANG, F. Active reconfigurable intelligent surface: Fully-connected r sub-connected? **IEEE Communications Letters**, v. 26, n. 1, p. 167–171, 2022.

LIU, Y.; LIU, E.; WANG, R. Energy efficiency analysis of intelligent reflecting surface system with hardware impairments. In: **2020 IEEE Global Communications Conference**. [S.l.: s.n.], 2020. p. 1–6.

LIU, Y.; MU, X.; XU, J.; SCHOBER, R.; HAO, Y.; POOR, H. V.; HANZO, L. Star: Simultaneous transmission and reflection for 360° coverage by intelligent surfaces. **IEEE Wireless Communications**, v. 28, n. 6, p. 102–109, 2021.

LIU, Y.; XU, J.; WANG, Z.; MU, X.; ZHANG, J.; ZHANG, P. **Simultaneously Transmitting And Reflecting (STAR) RIS for 6G: Fundamentals, Recent Advances, and Future Directions**. 2023.

LOAN, C. F. The ubiquitous kronecker product. **Journal of Computational and Applied Mathematics**, v. 123, n. 1, p. 85–100, 2000. ISSN 0377-0427. Numerical Analysis 2000. Vol. III: Linear Algebra. Disponível em: https://www.sciencedirect.com/science/article/pii/S0377042700003939.

LONG, W.; CHEN, R.; MORETTI, M.; ZHANG, W.; LI, J. A promising technology for 6G wireless networks: Intelligent reflecting surface. **Journal of Communications and Information Networks**, v. 6, n. 1, p. 1–16, 2021.

LYU, W.; XIU, Y.; YANG, S.; YUEN, C.; ZHANG, Z. Energy-efficient cell-free network assisted by hybrid riss. **IEEE Wireless Communications Letters**, v. 12, n. 4, p. 718–722, 2023.

M.2370-0, R. I.-R. **IMT Traffic estimates for the years 2020 to 2030**. [S.l.], 2015.

MA, X.; CHEN, Z.; CHI, Y.; CHEN, W.; DU, L.; LI, Z. Channel estimation for intelligent reflecting surface enabled terahertz MIMO systems. In: **proc. ICC workshops “2020"**. [S.l.: s.n.]. p. 1–6.

MAO, Z.; WANG, W.; XIA, Q.; ZHONG, C.; PAN, X.; YE, Z. Element-grouping intelligent reflecting surface: Electromagnetic-compliant model and geometry-based optimization. **IEEE Trans. Wireless Commun.**, v. 21, n. 7, p. 5362–5376, 7 2022.

MIRZA, J.; ALI, B. Channel estimation method and phase shift design for reconfigurable intelligent surface assisted MIMO networks. **IEEE Trans.s on Cognitive Commun. and Networking**, v. 7, n. 2, p. 441–451, 6 2021.

MISHRA, D.; JOHANSSON, H. Channel estimation and low-complexity beamforming design for passive intelligent surface assisted MISO wireless energy transfer. In: **proc. ICASSP “2019"**. Brighton, UK: [s.n.]. p. 4659–4663.

MU, X.; LIU, Y.; GUO, L.; LIN, J.; SCHOBER, R. Simultaneously transmitting and reflecting (star) ris aided wireless communications. **IEEE Transactions on Wireless Communications**, v. 21, n. 5, p. 3083–3098, 2022.

NADEEM, Q.-U.-A.; KAMMOUN, A.; CHAABAN, A.; DEBBAH, M.; ALOUINI, M.-S. Asymptotic max-min SINR analysis of reconfigurable intelligent surface assisted MISO systems. **IEEE Trans. Wireless Commun.**, v. 19, n. 12, p. 7748–7764, 12 2020.

NEMATI, M.; MAHAM, B.; POKHREL, S. R.; CHOI, J. Modeling ris empowered outdoor-to-indoor communication in mmwave cellular networks. **IEEE Transactions on Communications**, v. 69, n. 11, p. 7837–7850, 2021.

NING, B.; CHEN, Z.; CHEN, W.; DU, Y. Channel estimation and transmission for intelligent reflecting surface assisted THz communications. In: **ICC 2020 - 2020 IEEE International Conference on Communications (ICC)**. [S.l.: s.n.], 2020. p. 1–7.

NION, D.; SIDIROPOULOS, N. D. Tensor algebra and multidimensional harmonic retrieval in signal processing for MIMO radar. **IEEE Transactions on Signal Processing**, v. 58, n. 11, p. 5693–5705, 2010.

OLIVEIRA, P. M. R. de; FERNANDES, C. A. R.; FAVIER, G.; BOYER, R. PARATUCK semi-blind receivers for relaying multi-hop MIMO systems. **Digital Signal Processing**, v. 92, p. 127 – 138, 9 2019.

PALMUCCI, S.; GUERRA, A.; ABRARDO, A.; DARDARI, D. Two-timescale joint precoding design and ris optimization for user tracking in near-field MIMO systems. **IEEE Transactions on Signal Processing**, p. 1–16, 2023.

PENG, Z.; ZHOU, G.; PAN, C.; REN, H.; SWINDLEHURST, A. L.; POPOVSKI, P.; WU, G. Channel estimation for ris-aided multi-user mmwave systems with uniform planar arrays. **IEEE Transactions on Communications**, v. 70, n. 12, p. 8105–8122, 2022.

PEROVIĆ, N. S.; TRAN, L.-N.; RENZO, M. D.; FLANAGAN, M. F. Achievable rate optimization for MIMO systems with reconfigurable intelligent surfaces. **IEEE Transactions on Wireless Communications**, v. 20, n. 6, p. 3865–3882, 2021.

PINHO, P. H. U. de; COURAS, M. d. F. K. B.; FAVIER, G.; ALMEIDA, A. L. F. de; COSTA, J. P. J. Semi-blind receivers for two-hop MIMO relay systems with a combined TSTF-MSMKron coding. **Sensors**, v. 23, n. 13, 2023.

PITSIANIS, N. P. **The Kronecker Product in Approximation and Fast Transform Generation**. Tese (Doutorado), USA, 1 1997.

PODKURKOV, I.; SEIDL, G.; KHAMIDULLINA, L.; NADEEV, A.; HAARDT, M. Tensor-based near-field localization using massive antenna arrays. **IEEE Transactions on Signal Processing**, v. 69, p. 5830–5845, 2021.

PODKURKOV, I.; ZHANG, J.; NADEEV, A. F.; HAARDT, M. Efficient multidimensional wideband parameter estimation for OFDM based joint radar and communication systems. **IEEE Access**, v. 7, p. 112792–112808, 2019.

QIAN, C.; FU, X.; SIDIROPOULOS, N. D. Algebraic channel estimation algorithms for FDD massive MIMO systems. **IEEE J. Sel. Topics Signal Process.**, v. 13, n. 5, p. 961–973, 9 2019.

QIAN, X.; RENZO, M. D. Mutual coupling and unit cell aware optimization for reconfigurable intelligent surfaces. **IEEE Wireless Communications Letters**, v. 10, n. 6, p. 1183–1187, 2021.

QIAN, X.; RENZO, M. D.; LIU, J.; KAMMOUN, A.; ALOUINI, M.-S. Beamforming through reconfigurable intelligent surfaces in single-user MIMO systems: SNR distribution and scaling laws in the presence of channel fading and phase noise. **IEEE Wireless Commun. Lett.**, v. 10, n. 1, p. 77–81, 1 2021.

RAIMONDI, F. E. D.; FARIAS, R. C.; MICHEL, O. J.; COMON, P. Wideband multiple diversity tensor array processing. **IEEE Transactions on Signal Processing**, v. 65, n. 20, p. 5334–5346, 2017.

RANA, B.; CHO, S.-S.; HONG, I.-P. Review paper on hardware of reconfigurable intelligent surfaces. **IEEE Access**, v. 11, p. 29614–29634, 2023.

RASILAINEN, K.; PHAN, T. D.; BERG, M.; PäRSSINEN, A.; SOH, P. J. Hardware aspects of sub-thz antennas and reconfigurable intelligent surfaces for 6G communications. **IEEE Journal on Selected Areas in Communications**, v. 41, n. 8, p. 2530–2546, 2023.

RENZO, M. D.; ZAPPONE, A.; DEBBAH, M.; ALOUINI, M.-S.; YUEN, C.; ROSNY, J. de; TRETYAKOV, S. Smart radio environments empowered by reconfigurable intelligent surfaces: How it works, state of research, and the road ahead. **IEEE Journal on Selected Areas in Communications**, v. 38, n. 11, p. 2450–2525, 2020.

RIBEIRO, L. N.; ALMEIDA, A. L. F. de; MOTA, J. C. M. Tensor beamforming for multilinear translation invariant arrays. In: **2016 IEEE International Conference on Acoustics, Speech and Signal Processing (ICASSP)**. [S.l.: s.n.], 2016. p. 2966–2970.

RIBEIRO, Y. S.; ALMEIDA, A. L. F. de; FAZAL-E-ASIM; MAKKI, B.; FODOR, G. Low-complexity joint active and passive beamforming design for irs-assisted MIMO. **IEEE Wireless Communications Letters**, p. 1–1, 2023.

ROEMER, F.; BECKER, H.; HAARDT, M. Analytical performance assessment for multi-dimensional tensor-esprit-type parameter estimation algorithms. In: **2010 IEEE International Conference on Acoustics, Speech and Signal Processing**. [S.l.: s.n.], 2010. p. 2598–2601.

ROEMER, F.; HAARDT, M. Tensor-based channel estimation and iterative refinements for two-way relaying with multiple antennas and spatial reuse. **IEEE Trans. Signal Process.**, v. 58, n. 11, p. 5720–5735, 11 2010.

RUI, W.; GUO-SHENG, R.; SONG, Z. Channel estimation of MIMO relay system using cascaded tucker model. In: **proc. ICISPC "2019"**. Singapore: [s.n.]. p. 1–5.

SALMI, J.; RICHTER, A.; KOIVUNEN, V. Sequential unfolding svd for tensors with applications in array signal processing. **IEEE Transactions on Signal Processing**, v. 57, n. 12, p. 4719–4733, 2009.

SANKAR, R. P.; CHEPURI, S. P. Beamforming in hybrid ris assisted integrated sensing and communication systems. In: **2022 30th European Signal Processing Conference (EUSIPCO)**. [S.l.: s.n.], 2022. p. 1082–1086.

SAVKIN, A. V.; HUANG, C.; NI, W. On-demand deployment of aerial base stations for coverage enhancement in reconfigurable intelligent surface-assisted cellular networks on uneven terrains. **IEEE Communications Letters**, v. 27, n. 2, p. 666–670, 2023.

SEJAN, M. A. S.; RAHMAN, M. H.; SHIN, B.-S.; OH, J.-H.; YOU, Y.-H.; SONG, H.-K. Machine learning for intelligent-reflecting-surface-based wireless communication towards 6G: A review. **Sensors**, v. 22, n. 14, 2022.

SEMAAN, E.; TEJEDOR, E.; KOCHHAR, R. K.; MAGNUSSON, S.; PARKVALL, S. **6G spectrum - enabling the future mobile life beyond 2030**. 2023. White Paper.

SIDIROPOULOS, N.; BUDAMPATI, R. Khatri-rao space-time codes. **IEEE Transactions on Signal Processing**, v. 50, n. 10, p. 2396–2407, 2002.

SIDIROPOULOS, N.; DIMIC, G. Blind multiuser detection in W-CDMA systems with large delay spread. **IEEE Signal Processing Letters**, v. 8, n. 3, p. 87–89, 2001.

SIDIROPOULOS, N.; GIANNAKIS, G.; BRO, R. Blind parafac receivers for DS-CDMA systems. **IEEE Transactions on Signal Processing**, v. 48, n. 3, p. 810–823, 2000.

SIDIROPOULOS, N. D.; BRO, R. On the uniqueness of multilinear decomposition of n-way arrays. **Journal of Chemometrics**, v. 14, n. 3, p. 229–239, 2000.

SIDIROPOULOS, N. D.; LATHAUWER, L. D.; FU, X.; HUANG, K.; PAPALEXAKIS, E. E.; FALOUTSOS, C. Tensor decomposition for signal processing and machine learning. **IEEE Transactions on Signal Processing**, v. 65, n. 13, p. 3551–3582, 2017.

SINGAL, T. L. **Wireless Communications**. [S.l.]: Tata McGraw Hill Education Private Limited, 2010.

SOKAL, B.; ALMEIDA, A. L. de; HAARDT, M. Semi-blind receivers for MIMO multi-relaying systems via rank-one tensor approximations. **Signal Processing**, v. 166, 1 2020.

SOKAL, B.; GOMES, P. R. B.; ALMEIDA, A. L. F. d. de; HAARDT, M. Tensor-based receiver for joint channel, data, and phase-noise estimation in MIMO-OFDM systems. **IEEE Journal of Selected Topics in Signal Processing**, v. 15, n. 3, p. 803–815, 2021.

SOKAL, B.; GOMES, P. R. B.; ALMEIDA, A. L. F. de; MAKKI, B.; FODOR, G. Reducing the control overhead of intelligent reconfigurable surfaces via a tensor-based low-rank factorization approach. **IEEE Transactions on Wireless Communications**, v. 22, n. 10, p. 6578–6593, 2023.

SONG, Y.; KHANDAKER, M. R. A.; TARIQ, F.; WONG, K.-K. **Truly Intelligent Reflecting Surface-Aided Secure Communication Using Deep Learning**. 2020.

STEGEMAN, A.; SIDIROPOULOS, N. D. On kruskal's uniqueness condition for the CANDECOMP/PARAFAC decomposition. **Linear Algebra and its Applications**, v. 420, n. 2, p. 540 – 552, 1 2007. ISSN 0024-3795.

STOICA, P.; MOSES, R. **Spectral Analysis of Signals**. [S.l.]: Prentice Hall, Inc, 2005.

SUBHASH, A.; KAMMOUN, A.; ELZANATY, A.; KALYANI, S.; AL-BADARNEH, Y. H.; ALOUINI, M.-S. **Max-Min Data Rate Optimization for RIS-aided Uplink Communications with Green Constraints**. 2022. ArXiv:2208.00182v1 [cs.IT].

SUR, S. N.; BERA, R. Intelligent reflecting surface assisted MIMO communication system: A review. **Physical Communication**, v. 47, p. 101386, 2021. ISSN 1874-4907.

SUR, S. N.; KANDAR, D.; IMOIZE, A. L.; BERA, R. An overview of intelligent reflecting surface assisted uav communication systems. In: ____. **Unmanned Aerial Vehicle Cellular Communications**. Cham: Springer International Publishing, 2023. p. 67–94.

SWINDLEHURST, A. L.; ZHOU, G.; LIU, R.; PAN, C.; LI, M. Channel estimation with reconfigurable intelligent surfaces—a general framework. **Proceedings of the IEEE**, v. 110, n. 9, p. 1312–1338, 2022.

SøRENSEN, M.; LATHAUWER, L. D. Coupled tensor decompositions for applications in array signal processing. In: **2013 5th IEEE International Workshop on Computational Advances in Multi-Sensor Adaptive Processing (CAMSAP)**. [S.l.: s.n.], 2013. p. 228–231.

TAHA, A.; ALRABEIAH, M.; ALKHATEEB, A. **Enabling Large Intelligent Surfaces with Compressive Sensing and Deep Learning**. 2019.

TUCKER, L. R. The extension of factor analysis to three-dimensional matrices. **Contributions to mathematical psychology**, p. 109–127, 1964.

TUCKER, L. R. Some mathematical notes on three-mode factor analysis. **Psychometrika**, v. 31, n. 3, p. 279–311, 9 1966.

WANG, C.-X.; YOU, X.; GAO, X.; ZHU, X.; LI, Z.; ZHANG, C.; WANG, H.; HUANG, Y.; CHEN, Y.; HAAS, H.; THOMPSON, J. S.; LARSSON, E. G.; RENZO, M. D.; TONG, W.; ZHU, P.; SHEN, X.; POOR, H. V.; HANZO, L. On the road to 6G: Visions, requirements, key technologies, and testbeds. **IEEE Communications Surveys & Tutorials**, v. 25, n. 2, p. 905–974, 2023.

WANG, F.; LI, H.; FANG, J. Joint active and passive beamforming for irs-assisted radar. **IEEE Signal Processing Letters**, v. 29, p. 349–353, 2022.

WANG, F.; SWINDLEHURST, A. L. Applications of absorptive reconfigurable intelligent surfaces in interference mitigation and physical layer security. **IEEE Transactions on Wireless Communications**, p. 1–1, 2023.

WANG, P.; FANG, J.; DUAN, H.; LI, H. Compressed channel estimation for intelligent reflecting surface-assisted millimeter wave systems. **IEEE Signal Process. Lett.**, v. 27, p. 905–909, 5 2020.

WANG, Z.; LIU, L.; CUI, S. Channel estimation for intelligent reflecting surface assisted multiuser communications. In: **2020 IEEE Wireless Communications and Networking Conference (WCNC)**. Seoul, Korea (South): [s.n.], 2020. p. 1–6.

WANG, Z.; LIU, L.; CUI, S. Channel estimation for intelligent reflecting surface assisted multiuser communications: Framework, algorithms, and analysis. **IEEE Trans. Wireless Commun.**, v. 19, n. 10, p. 6607–6620, 10 2020.

WEI, L.; HUANG, C.; ALEXANDROPOULOS, G. C.; YUEN, C. Parallel factor decomposition channel estimation in RIS-assisted multi-user MISO communication. In: **proc. SAM "2020"**. Hangzhou, China: [s.n.].

WEI, L.; HUANG, C.; ALEXANDROPOULOS, G. C.; YUEN, C.; ZHANG, Z.; DEBBAH, M. Channel estimation for RIS-empowered multi-user MISO wireless communications. **IEEE Trans.Commun.**, v. 69, n. 6, p. 4144–4157, 6 2021.

WEI, L.; HUANG, C.; GUO, Q.; YANG, Z.; ZHANG, Z.; ALEXANDROPOULOS, G. C.; DEBBAH, M.; YUEN, C. Joint channel estimation and signal recovery for RIS-empowered multiuser communications. **IEEE Trans. Commun.**, v. 70, n. 7, p. 4640–4655, 7 2022.

WEICHSELBERGER, W. On the decomposition of the MIMO channel correlation tensor. In: **ITG Workshop on Smart Antennas (IEEE Cat. No.04EX802)**. [S.l.: s.n.], 2004. p. 268–273.

WEIS, M.; GALDO, G. D.; HAARDT, M. A correlation tensor-based model for time variant frequency selective MIMO channels. In: **Proceedings of International ITG/IEEE Workshop on Smart Antennas (WSA'07)**. [S.l.: s.n.], 2007.

WONG, K.-K.; NEW, W. K.; HAO, X.; TONG, K.-F.; CHAE, C.-B. Fluid antenna system—part i: Preliminaries. **IEEE Communications Letters**, v. 27, n. 8, p. 1919–1923, 2023.

WU, Q.; ZHANG, R. Intelligent reflecting surface enhanced wireless network via joint active and passive beamforming. **IEEE Transactions on Wireless Communications**, v. 18, n. 11, p. 5394–5409, 2019.

WU, Q.; ZHANG, R. Beamforming optimization for wireless network aided by intelligent reflecting surface with discrete phase shifts. **IEEE Trans. on Communications**, v. 68, n. 3, p. 1838–1851, 2020.

WU, Q.; ZHANG, R. Towards smart and reconfigurable environment: Intelligent reflecting surface aided wireless network. **IEEE Communications Magazine**, v. 58, n. 1, p. 106–112, 2020.

WU, Q.; ZHANG, S.; ZHENG, B.; YOU, C.; ZHANG, R. Intelligent reflecting surface-aided wireless communications: A tutorial. **IEEE Trans. Commun.**, v. 69, n. 5, p. 3313–3351, 5 2021.

XIA, S.; SHI, Y. Intelligent reflecting surface for massive device connectivity: Joint activity detection and channel estimation. In: **ICASSP 2020 - 2020 IEEE International Conference on Acoustics, Speech and Signal Processing (ICASSP)**. [S.l.: s.n.], 2020. p. 5175–5179.

XIMENES, L. R.; FAVIER, G.; ALMEIDA, A. L. F. de. Semi-blind receivers for non-regenerative cooperative MIMO communications based on nested parafac modeling. **IEEE Transactions on Signal Processing**, v. 63, n. 18, p. 4985–4998, 2015.

XIMENES, L. R.; FAVIER, G.; ALMEIDA, A. L. F. de; SILVA, Y. C. B. Parafac-paratuck semi-blind receivers for two-hop cooperative MIMO relay systems. **IEEE Transactions on Signal Processing**, v. 62, n. 14, p. 3604–3615, 2014.

XING, Z.; WANG, R.; YUAN, X. Joint active and passive beamforming design for reconfigurable intelligent surface enabled integrated sensing and communication. **IEEE Transactions on Communications**, v. 71, n. 4, p. 2457–2474, 2023.

YANG, Y.; ZHENG, B.; ZHANG, S.; ZHANG, R. Intelligent reflecting surface meets OFDM: Protocol design and rate maximization. **IEEE Trans. Commun.**, v. 68, n. 7, p. 4522–4535, 7 2020.

YIGIT, Z.; BASAR, E.; WEN, M.; ALTUNBAS, I. Hybrid reflection modulation. **IEEE Transactions on Wireless Communications**, v. 22, n. 6, p. 4106–4116, 2023.

YING, K.; GAO, Z.; LYU, S.; WU, Y.; WANG, H.; ALOUINI, M. GMD-based hybrid beamforming for large reconfigurable intelligent surface assisted millimeter-wave massive MIMO. **IEEE Access**, v. 8, p. 19530–19539, 2020.

YOU, C.; ZHENG, B.; ZHANG, R. Channel estimation and passive beamforming for intelligent reflecting surface: Discrete phase shift and progressive refinement. **IEEE Journal on Selected Areas in Communications**, v. 38, n. 11, p. 2604–2620, 2020.

YOU, C.; ZHENG, B.; ZHANG, R. Intelligent reflecting surface with discrete phase shifts: Channel estimation and passive beamforming. In: **ICC 2020 - 2020 IEEE International Conference on Communications (ICC)**. [S.l.: s.n.], 2020. p. 1–6.

ZAPPONE, A.; RENZO, M. D.; SHAMS, F.; QIAN, X.; DEBBAH, M. Overhead-aware design of reconfigurable intelligent surfaces in smart radio environments. **IEEE Transactions on Wireless Communications**, v. 20, n. 1, p. 126–141, 2021.

ZEGRAR, S. E.; AFEEF, L.; ARSLAN, H. Reconfigurable intelligent surface (RIS): Eigenvalue decomposition-based separate channel estimation. In: **Proc. PIMRC "2021**. [S.l.: s.n.].

ZHANG, H.; SHLEZINGER, N.; ALEXANDROPOULOS, G. C.; SHULTZMAN, A.; ALAMZADEH, I.; IMANI, M. F.; ELDAR, Y. C. Channel estimation with hybrid reconfigurable intelligent metasurfaces. **IEEE Transactions on Communications**, v. 71, n. 4, p. 2441–2456, 2023.

ZHANG, R.; CHENG, L.; WANG, S.; LOU, Y.; WU, W.; NG, D. W. K. Tensor decomposition-based channel estimation for hybrid mmwave massive MIMO in high-mobility scenarios. **IEEE Transactions on Communications**, v. 70, n. 9, p. 6325–6340, 2022.

ZHANG, S.; ZHANG, R. Capacity characterization for intelligent reflecting surface aided MIMO communication. **IEEE Journal on Selected Areas in Communications**, v. 38, n. 8, p. 1823–1838, 2020.

ZHANG, T.; MAO, S. Joint beamforming design in reconfigurable intelligent surface-assisted rate splitting networks. **IEEE Transactions on Wireless Communications**, p. 1–1, 2023.

ZHANG, X.; ZHANG, H. Hybrid reconfigurable intelligent surfaces-assisted near-field localization. **IEEE Communications Letters**, v. 27, n. 1, p. 135–139, 2023.

ZHANG, Z.; DAI, L.; CHEN, X.; LIU, C.; YANG, F.; SCHOBER, R.; POOR, H. V. Active ris vs. passive ris: Which will prevail in 6G? **IEEE Transactions on Communications**, v. 71, n. 3, p. 1707–1725, 2023.

ZHAO, F.; HAO, W.; YOU, X.; WANG, Y.; CHU, Z.; XIAO, P. Joint beamforming optimization for irs-aided thz communication with time delays. **IEEE Wireless Communications Letters**, p. 1–1, 2023.

ZHAO, X.; XU, K.; MA, S.; GONG, S.; YANG, G.; XING, C. Joint transceiver optimization for irs-aided MIMO communications. **IEEE Trans. Commun.**, v. 70, n. 5, p. 3467–3482, 5 2022.

ZHENG, B.; YOU, C.; MEI, W.; ZHANG, R. A survey on channel estimation and practical passive beamforming design for intelligent reflecting surface aided wireless communications. **IEEE Commun. Surveys Tuts.**, v. 24, n. 2, p. 1035–1071, 2 2022.

ZHENG, B.; YOU, C.; ZHANG, R. Intelligent reflecting surface assisted multi-user OFDMA: Channel estimation and training design. **IEEE Trans. Wireless Commun.**, v. 19, n. 12, p. 8315–8329, 12 2020.

ZHENG, B.; YOU, C.; ZHANG, R. Efficient channel estimation for double-IRS aided multi-user MIMO system. **IEEE Trans. Commun.**, v. 69, n. 6, p. 3818–3832, 6 2021.

ZHENG, H.; SHI, Z.; ZHOU, C.; HAARDT, M.; CHEN, J. Coupled coarray tensor cpd for doa estimation with coprime l-shaped array. **IEEE Signal Processing Letters**, v. 28, p. 1545–1549, 2021.

ZHENG, H.; ZHOU, C.; SHI, Z.; GU, Y.; ZHANG, Y. D. Coarray tensor direction-of-arrival estimation. **IEEE Transactions on Signal Processing**, v. 71, p. 1128–1142, 2023.

ZHENG, X.; WANG, P.; FANG, J.; LI, H. Compressed channel estimation for irs-assisted millimeter wave OFDM systems: A low-rank tensor decomposition-based approach. **IEEE Wireless Communications Letters**, v. 11, n. 6, p. 1258–1262, 2022.

ZHOU, G.; PAN, C.; REN, H.; POPOVSKI, P.; SWINDLEHURST, A. L. Channel estimation for ris-aided multiuser millimeter-wave systems. **IEEE Transactions on Signal Processing**, v. 70, p. 1478–1492, 2022.

ZHU, Y.; MAO, B.; KATO, N. Intelligent reflecting surface in 6G vehicular communications: A survey. **IEEE Open Journal of Vehicular Technology**, v. 3, p. 266–277, 2022.

ZILLI, G. M.; ZHU, W.-P. Constrained tensor decomposition-based hybrid beamforming for mmwave massive MIMO-OFDM communication systems. **IEEE Transactions on Vehicular Technology**, v. 70, n. 6, p. 5775–5788, 2021.

ZNIYED, Y.; BOYER, R.; ALMEIDA, A. L. F. de; FAVIER, G. Tensor-train modeling for MIMO-OFDM tensor coding-and-forwarding relay systems. In: **proc. EUSIPCO “2019"**. [S.l.: s.n.], 2019. p. 1–5.

APÊNDICE A – APPENDIX – A: EXPECTED CRAMÉR RAO LOWER BOUND FOR THE PILOT ASSISTED METHOD

In the following, we derive the closed-form CRB expressions for the channel estimation problem proposed in this work. The CRB provides the lower bound on the variance of achieved by an unbiased estimator. If $\hat{\theta}$ is an unbiased estimate of θ, the NMSE measurements is lower bounded by the CRB such as,

$$\mathbb{E}\|\theta-\hat{\theta}\|^2 \geq Tr\{\text{CRB}((\theta))\}, \tag{A.1}$$

where CRB(θ) is given as the inverse of the Fisher Information Matrix (FIM), denoted by $\mathbf{F}(\theta)$, such as

$$\text{CRB}(\theta) \geq \mathbf{F}(\theta)^{-1}. \tag{A.2}$$

An extension for complex-valued parameters is derived in (Oliveira *et al.*, 2019) by working on the structured parameter vector $\theta_c = [\overline{\theta}^{\text{T}}\ \widetilde{\theta}^{\text{T}}]^{\text{T}}$, where $\overline{\theta} = Re(\theta)$, and $\widetilde{\theta} = Im(\theta)$. Thereby, with a nuisance parameter γ, the CRB for complex-valued random parameters is given as

$$\mathbb{E}\|\theta_c-\hat{\theta}_c\|^2 \geq \mathbb{E}_{\overline{\theta},\widetilde{\theta},\gamma}\left\{Tr\{\text{CRB}((\overline{\theta}))\}+Tr\{\text{CRB}((\widetilde{\theta}))\}\right\}. \tag{A.3}$$

For an observation vector that follows a complex circular Gaussian distribution, $\mathbf{y} \sim CN(\mu,\mathbf{R})$, a useful way used to obtain the FIM is to use the Slepian-Bangs (SB) formula (Stoica; Moses, 2005):

$$\begin{aligned}
[\mathbf{F}(\theta)]_{i,j} &= 2Re\left\{\left(\frac{\partial\mu}{\partial[\theta]_i}\right)^H \mathbf{R}^{-1}\left(\frac{\partial\mu}{\partial[\theta]_j}\right)\right\} && \text{(A.4)}\\
&+ Tr\left\{\left(\frac{\partial\mathbf{R}}{\partial[\theta]_i}\right)\mathbf{R}^{-1}\left(\frac{\partial\mathbf{R}}{\partial[\theta]_j}\right)\mathbf{R}^{-1}\right\}. && \text{(A.5)}
\end{aligned}$$

Let us recall (4.17):

$$\begin{aligned}
[\mathscr{Y}]_{(3)} = &\ \mathbf{S}\left[(\mathbf{X}\otimes\mathbf{I}_L)\left(\mathbf{H}^{\text{T}}\diamond\mathbf{G}\right)\right]^{\text{T}}\\
= &\ \mathbf{S}(\mathbf{H}^{\text{T}}\diamond\mathbf{G})^{\text{T}}(\mathbf{X}\otimes\mathbf{I}_L)^{\text{T}},
\end{aligned} \tag{A.6}$$

or, equivalently,

$$[\mathscr{Y}]_{(3)}^{\text{T}} = (\mathbf{X}\otimes\mathbf{I}_L)\left(\mathbf{H}^{\text{T}}\diamond\mathbf{G}\right)\mathbf{S}^{\text{T}}. \tag{A.7}$$

Considering the vectorized version of the 3-mode unfolding $[\mathscr{Y}]_{(3)}^{\mathrm{T}}$, the following linear model with respect to the parameters of interest is obtained according to

$$\mathbf{y} = \operatorname{vec}\left([\mathscr{Y}]_{(3)}^{\mathrm{T}}\right) = \mathbf{U}\theta, \tag{A.8}$$

where $\mathbf{U} = (\mathbf{S} \otimes \mathbf{X} \otimes \mathbf{I}_L)$, and

$$\theta = \operatorname{vec}\left(\mathbf{H}^{\mathrm{T}} \diamond \mathbf{G}\right) \in \mathbb{C}^{MNL} \tag{A.9}$$

denotes the vectorized version of the Khatri-Rao structured channel. From the observation vector $\mathbf{y}$ given by (A.8), the statistics of the noisy observation is given by

$$\mathbf{y} \sim CN(\mu_1, \mathbf{R}_1), \tag{A.10}$$

where,

$$\mu_1 = \mathbf{U}\theta, \tag{A.11}$$

$$\mathbf{R}_1 = \sigma^2\mathbf{I}. \tag{A.12}$$

As $\mathbf{R}_1$ parameter-invariant, the second term of the SB formula vanishes, hence the $(2MNL) \times (2MNL)$ FIM, obtained after the calculation from (A.4), is given by

$$\mathbf{F}(\theta_c) = \frac{2}{\sigma^2}\begin{bmatrix} Re\{\mathbf{U}^{\mathbf{H}}\mathbf{U}\} & -Im\{\mathbf{U}^{\mathbf{H}}\mathbf{U}\} \\ Im\{\mathbf{U}^{\mathbf{H}}\mathbf{U}\}^{\mathrm{T}} & Re\{\mathbf{U}^{\mathbf{H}}\mathbf{U}\} \end{bmatrix}. \tag{A.13}$$

Considering the trace and the inverse of a 2×2 block matrix, we obtain

$$Tr\{\mathrm{CRB}(\overline{\theta})\} = \frac{\sigma^2}{2} Tr\left\{\left(\overline{\mathbf{M}} + \widetilde{\mathbf{M}}\overline{\mathbf{M}}^{-1}\widetilde{\mathbf{M}}\right)^{-1}\right\}, \tag{A.14}$$

$$\begin{aligned} Tr\{\mathrm{CRB}(\widetilde{\theta})\} = \frac{\sigma^2}{2} Tr\Big\{&\overline{\mathbf{M}}^{-1} - \overline{\mathbf{M}}^{-1}\widetilde{\mathbf{M}}\big(\overline{\mathbf{M}} + \\ &+\widetilde{\mathbf{M}}\overline{\mathbf{M}}^{-1}\widetilde{\mathbf{M}}\big)^{-1}\widetilde{\mathbf{M}}\overline{\mathbf{M}}^{-1}\Big\}, \end{aligned} \tag{A.15}$$

where $\overline{\mathbf{M}} = Re\left\{\mathbf{U}^H\mathbf{U}\right\}$ and $\widetilde{\mathbf{M}} = Im\{\mathbf{U}^{\mathbf{H}}\mathbf{U}\}$.

Let us recall that $\mathbf{U} = (\mathbf{S} \otimes \mathbf{X} \otimes \mathbf{I}_L)$, $\mathbf{X}^{\mathrm{H}}\mathbf{X} = T\mathbf{I}_M$, and $\mathbf{S}^{\mathrm{H}}\mathbf{S} = K\mathbf{I}_N$. Hence, $\mathbf{U}^{\mathbf{H}}\mathbf{U} = KT\mathbf{I}_{MNL}$. This implies that $\widetilde{\mathbf{M}} = \mathbf{0}$. The two above expressions can be simplified as

$$\mathrm{CRB}(\overline{\theta}) = \frac{\sigma^2}{2KT}\mathbf{I}_{MNL}, \tag{A.16}$$

$$\mathrm{CRB}(\widetilde{\theta}) = \frac{\sigma^2}{2KT}\mathbf{I}_{MNL}. \tag{A.17}$$

Therefore, using definition (A.3):

$$\mathbb{E}\|\theta_c - \hat{\theta}_c\|^2 \geq \frac{\sigma^2}{KT} MNL. \tag{A.18}$$

It is important to note that there is no need to derive the mathematical expectation in the right-hand side of (A.3) over the parameters of interest and of nuisance due to the simple expression of the CRB.

A.1 Simplified version of BALS

Under the column-orthogonality assumption for $\mathbf{X}$ and $\mathbf{S}$, the right pseudo-inverses in (4.25) and (4.26) can be replaced by lower complexity matrix products, leading to a faster implementation of the BALS algorithm. Defining $\mathbf{M}_1 \doteq \mathbf{S} \diamond \mathbf{X}\hat{\mathbf{H}}^{\mathrm{T}}$ and $\mathbf{M}_2 \doteq \mathbf{S} \diamond \mathbf{G}$, and using property (5), we have

$$\begin{aligned} \mathbf{M}_1^{\mathrm{H}}\mathbf{M}_1 &= (\mathbf{S}^{\mathrm{H}}\mathbf{S}) \odot (\mathbf{H}\mathbf{X}^{\mathrm{H}}\mathbf{X}\mathbf{H}^{\mathrm{H}}) \\ &= KT \begin{bmatrix} \|\mathbf{h}_1\|^2 & & \\ & \ddots & \\ & & \|\mathbf{h}_N\|^2 \end{bmatrix} \doteq KT\Sigma_{\mathbf{H}} \end{aligned} \tag{A.19}$$

and

$$\begin{aligned} \mathbf{M}_2^{\mathrm{H}}\mathbf{M}_2 &= (\mathbf{S}^{\mathrm{H}}\mathbf{S}) \odot (\mathbf{G}^{\mathrm{H}}\mathbf{G}) \\ &= K \begin{bmatrix} \|\mathbf{g}_1\|^2 & & \\ & \ddots & \\ & & \|\mathbf{g}_N\|^2 \end{bmatrix} \doteq K\Sigma_{\mathbf{G}}, \end{aligned} \tag{A.20}$$

which implies that

$$\hat{\mathbf{G}} = (1/KT) \cdot \mathbf{Y}_1\mathbf{M}_1^{*}\Sigma_{\mathbf{H}}^{-1} \quad \text{and} \quad \hat{\mathbf{H}}^{\mathrm{T}} = (1/KT) \cdot \mathbf{X}^{\mathrm{H}}\mathbf{Y}_2\mathbf{M}_2^{*}\Sigma_{\mathbf{G}}^{-1}. \tag{A.21}$$

Due to the diagonal structure of $\Sigma_{\mathbf{H}}$ and $\Sigma_{\mathbf{G}}$, these expressions provide lower complexity implementations of (4.25) and (4.26), respectively, by replacing matrix inversions by simpler matrix products. In particular, each update of $\hat{\mathbf{G}}$ and $\hat{\mathbf{H}}$ can be viewed as a set of N independent processes (one for each IRS element) that can be carried out in parallel. The BALS is summarized in Algorithm 10.

Algoritmo 10: Simplified BALS

Procedure

input : $i = 0$; *Initialize* $\hat{\mathbf{H}}_{(i=0)}$

output : $\hat{\mathbf{H}}$, $\hat{\mathbf{G}}$

begin

$i = i + 1$;

while $\|e(i) - e(i-1)\| \geq \delta$ **do**

1: *Compute* $\hat{\mathbf{M}}_{1_{(i)}} = \mathbf{S} \diamond (\mathbf{X}\hat{\mathbf{H}}_{(i-1)})$
and find a least squares estimate of $\mathbf{G}$*:*

$$\hat{\mathbf{G}}_{(i)} = \frac{1}{KT}\mathbf{Y}_1\hat{\mathbf{M}}^*_{1_{(i)}}\hat{\Sigma}^{-1}_{\mathbf{H}_{(i-1)}}$$

2: *Compute* $\hat{\mathbf{M}}_{2_{(i)}} = \mathbf{S} \diamond (\mathbf{X}\hat{\mathbf{G}}_{(i)})$
and find a least squares estimate of $\mathbf{H}$*:*

$$\hat{\mathbf{H}}^{\mathrm{T}}_{(i)} = \frac{1}{KT}\mathbf{X}^{\mathrm{H}}\mathbf{Y}_2\hat{\mathbf{M}}^*_{2_{(i)}}\hat{\Sigma}^{-1}_{\mathbf{G}_{(i)}}$$

3: *Repeat steps* 1 to 2 *until convergence.*

end

end

end

end

APÊNDICE B – APPENDIX – B: DESIGN OF W AND S AND ITS IMPLICATIONS

In this appendix, we discussed the design of the coding matrix $\mathbf{W}$ and the IRS phase shift matrix $\mathbf{S}$ from their Khatri-Rao product combination $\Psi = \mathbf{W} \diamond \mathbf{S} \in \mathbb{C}^{LN \times K}$. Assuming that Ψ is a Vandermonde matrix constructed by truncating a $K \times K$ DFT matrix to its first LN rows, with $LN \leq K$, $\mathbf{W}$ and $\mathbf{S}$ given by (B.5) and (B.6) can be obtained from an exact Khatri-Rao factorization of Ψ. Let us consider that $\Psi \in \mathbb{C}^{LN \times K}$, with $LN \leq K$, is a Vandermonde matrix constructed by truncating a $K \times K$ matrix to its first LN rows. Defining $\psi_k \doteq e^{-j2\pi(k-1)/K}$, $k = 1, \ldots, K$, as the generators of Ψ yields

$$\Psi = \begin{bmatrix} 1 & 1 & \ldots & 1 \\ \psi_1 & \psi_2 & \ldots & \psi_K \\ \vdots & \vdots & \ldots & \vdots \\ \psi_1^{(LN-1)} & \psi_2^{(LN-1)} & \ldots & \psi_K^{(LN-1)} \end{bmatrix}. \tag{B.1}$$

Since the kth column of Ψ is a Vandermonde vector, it can be factorized as Kronecker product of two Vandermonde vectors with generators ψ_k^N and ψ^k, respectively, as follows

$$\begin{bmatrix} 1 \\ \vdots \\ \psi_k^{(LN-1)} \end{bmatrix} = \begin{bmatrix} 1 \\ \vdots \\ \psi_k^{N(L-1)} \end{bmatrix} \otimes \begin{bmatrix} 1 \\ \vdots \\ \psi_k^{(N-1)} \end{bmatrix}. \tag{B.2}$$

Defining $\mathbf{W}_{k.} \doteq \left[1, \psi_k^N, \ldots, \psi_k^{N(L-1)}\right] \in \mathbb{C}^{1 \times L}$ and $\mathbf{S}_{k.} \doteq \left[1, \psi_k, \ldots, \psi_k^{(N-1)}\right] \in \mathbb{C}^{1 \times N}$, we have

$$\Psi_{.k} = \mathbf{W}_{k.}^{\mathrm{T}} \otimes \mathbf{S}_{k.}^{\mathrm{T}}, \quad k = 1, \ldots, K, \tag{B.3}$$

or, equivalently,

$$\begin{aligned} \Psi &= [\Psi_{.1}, \ldots, \Psi_{.K}] \\ &= [\mathbf{W}_{1.}^{\mathrm{T}} \otimes \mathbf{S}_{1.}^{\mathrm{T}}, \ldots, \mathbf{W}_{K.}^{\mathrm{T}} \otimes \mathbf{S}_{K.}^{\mathrm{T}}] \\ &= \mathbf{W}^{\mathrm{T}} \diamond \mathbf{S}^{\mathrm{T}} \in \mathbb{C}^{LN \times K}, \end{aligned} \tag{B.4}$$

where

$$\mathbf{W} = \begin{bmatrix} \mathbf{W}_{1.} \\ \vdots \\ \mathbf{W}_{K.} \end{bmatrix} = \begin{bmatrix} 1 & \psi_1^N & \ldots & \psi_1^{N(L-1)} \\ \vdots & \vdots & \ddots & \vdots \\ 1 & \psi_K^N & \ldots & \psi_K^{N(L-1)} \end{bmatrix} \in \mathbb{C}^{K \times L}, \tag{B.5}$$

and

$$\mathbf{S} = \begin{bmatrix} \mathbf{S}_{1\cdot} \\ \vdots \\ \mathbf{S}_{K\cdot} \end{bmatrix} = \begin{bmatrix} 1 & \psi_1 & \dots & \psi_1^{(N-1)} \\ \vdots & \vdots & \ddots & \vdots \\ 1 & \psi_K & \dots & \psi_K^{(N-1)} \end{bmatrix} \in \mathbb{C}^{K\times N}. \tag{B.6}$$

In order to show that the assumption $\Psi^*\Psi^{\mathrm{T}} = K\mathbf{I}_{LN}$ implies the equivalence between (5.17) and (5.18), recall the LS estimation step for $\mathbf{G}$ given by (5.17), which involves computing the left pseudo-inverse of matrix $\mathbf{C} = \left[\Psi^{\mathrm{T}} \diamond (\mathbf{X}\otimes\mathbf{H})\right]$. Taking the Khatri-Rao structure of $\mathbf{C}$ into account, and using property (5), we have

$$\begin{aligned} \mathbf{C}^{\dagger} &= (\mathbf{C}^{\mathrm{H}}\mathbf{C})^{-1}\mathbf{C}^{\mathrm{H}} \\ &= \left((\Psi^*\Psi^{\mathrm{T}}) \odot \left((\mathbf{X}^{\mathrm{H}}\mathbf{X}) \otimes (\mathbf{H}^{\mathrm{H}}\mathbf{H})\right)\right)^{-1} (\Psi \diamond (\mathbf{X}\otimes\mathbf{H}))^{\mathrm{H}} \\ &= \left(K\mathbf{I}_{LN} \odot \left((\mathbf{X}^{\mathrm{H}}\mathbf{X}) \otimes (\mathbf{H}^{\mathrm{H}}\mathbf{H})\right)\right)^{-1} (\Psi \diamond (\mathbf{X}\otimes\mathbf{H}))^{\mathrm{H}}. \end{aligned} \tag{B.7}$$

Defining $\mathbf{Q} = \mathbf{X}\otimes\mathbf{H} \in \mathbb{C}^{TM\times LN}$, and using the property $(\mathbf{A}\otimes\mathbf{B})(\mathbf{C}\otimes\mathbf{D}) = (\mathbf{AC}\otimes\mathbf{BD})$, equation (B.7) can be rewritten as

$$\mathbf{C}^{\dagger} = (1/K)\left(\mathbf{I}_{LN} \odot (\mathbf{Q}^{\mathrm{H}}\mathbf{Q})\right)^{-1} (\Psi \diamond \mathbf{Q})^{\mathrm{H}}. \tag{B.8}$$

Since the Hadamard product in (B.8) will null out the non-diagonal terms of the Gramian $\mathbf{Q}^{\mathrm{H}}\mathbf{Q}$, this equation can be simplified to

$$\mathbf{C}^{\dagger} = (1/K)\Sigma_{\mathbf{Q}}^{-1}(\Psi \diamond \mathbf{Q})^{\mathrm{H}}, \tag{B.9}$$

where $\Sigma_{\mathbf{Q}}$ is given in (5.19).

APÊNDICE C – APPENDIX – C: EXPECTED CRAMÉR RAO LOWER BOUND FOR THE SEMI-BLIND METHOD

The CRB is the lowest estimation accuracy that an unbiased estimator can reach. If $\hat{\theta}$ is an unbiased estimate of θ, the MSE measurements is lower bounded by the CRB such as,

$$\mathbb{E}\|\theta - \hat{\theta}\|^2 \geq Tr\{\text{CRB}(\theta))\}, \tag{C.1}$$

where $\text{CRB}(\theta)$ is given as the inverse of the Fisher Information Matrix (FIM), denoted by $\mathbf{F}(\theta)$, such as $\text{CRB}(\theta) = \mathbf{F}(\theta)^{-1}$. An extension for complex-valued parameters can be as in (Oliveira *et al.*, 2019), making by structured parameters vector $\theta_c = [\overline{\theta}^{\text{T}}\ \widetilde{\theta}^{\text{T}}]^{\text{T}}$, where $\overline{\theta} = Re(\theta)$, and $\widetilde{\theta} = Im(\theta)$. Thereby, with a nuisance parameter γ the expected CRB for complex-valued random parameters is given as

$$\mathbb{E}\|\theta_c - \hat{\theta}_c\|^2 \geq \mathbb{E}_{\overline{\theta},\widetilde{\theta},\gamma}\left\{Tr\{\text{CRB}(\overline{\theta})\} + Tr\{\text{CRB}(\widetilde{\theta})\}\right\}. \tag{C.2}$$

For an observation vector that follows a complex circular Gaussian distribution, $\mathbf{y} \sim CN(\mu, \mathbf{R})$, a useful formula, used to obtain the FIM, is the Slepian-Bangs (SB) Formula (Stoica; Moses, 2005):

$$[\mathbf{F}(\theta)]_{i,j} = 2Re\left\{\left(\frac{\partial \mu}{\partial [\theta_c]_i}\right)^{\text{H}} \mathbf{R}^{-1} \left(\frac{\partial \mu}{\partial [\theta_c]_j}\right)\right\} \tag{C.3}$$

$$+ \; Tr\left\{\left(\frac{\partial \mathbf{R}}{\partial [\theta_c]_i}\right) \mathbf{R}^{-1} \left(\frac{\partial \mathbf{R}}{\partial [\theta_c]_j}\right) \mathbf{R}^{-1}\right\}. \tag{C.4}$$

such that,

$$\mathbf{F}(\theta_c) = 2\begin{bmatrix} \overline{\mathbf{M}} & -\widetilde{\mathbf{M}} \\ \widetilde{\mathbf{M}} & \overline{\mathbf{M}} \end{bmatrix}, \tag{C.5}$$

and by deriving analytically $\mathbf{F}(\theta_c)^{-1}$ using the Schur complement method and considering the trace operator we obtain

$$Tr\{\text{CRB}(\overline{\theta})\} = \frac{1}{2} Tr\left\{\left(\overline{\mathbf{M}} + \widetilde{\mathbf{M}}\overline{\mathbf{M}}^{-1}\widetilde{\mathbf{M}}\right)^{-1}\right\}, \tag{C.6}$$

$$Tr\{\text{CRB}(\widetilde{\theta})\} = \frac{1}{2} Tr\left\{\overline{\mathbf{M}}^{-1} - \overline{\mathbf{M}}^{-1}\widetilde{\mathbf{M}}\big(\overline{\mathbf{M}} + \right.$$
$$\left. + \widetilde{\mathbf{M}}\overline{\mathbf{M}}^{-1}\widetilde{\mathbf{M}}\big)^{-1} \widetilde{\mathbf{M}}\overline{\mathbf{M}}^{-1}\right\}. \tag{C.7}$$

The matrices $\overline{\mathbf{M}}$ and $\widetilde{\mathbf{M}}$ are defined in posterior subsections according to parameters of observation.

The CRB derivations for the proposed semi-blind receiver are split into two parts. In the first part, we derive the CRB for the IRS-BS channel $\mathbf{H}$, whereas in the second part the CRB for the UT-IRS channel $\mathbf{G}$ is derived.

C.0.1 CRB for the UT-IRS channel

Here, the UT-IRS channel $\mathbf{G}$ is viewed as an unknown nuisance, and the CRB is derived for the IRS-BS channel $\mathbf{H}$. Let

$$\theta_c = [\overline{\mathbf{g}}^{\mathrm{T}} \ \widetilde{\mathbf{g}}^{\mathrm{T}}]^{\mathrm{T}}, \quad \mathbf{g} = \mathrm{vec}(\mathbf{G}) \tag{C.8}$$

$$\gamma = [\overline{\mathbf{h}}^{\mathrm{T}} \ \widetilde{\mathbf{h}}^{\mathrm{T}} \ \mathrm{vec}(\mathbf{X})^{\mathrm{T}}]^{\mathrm{T}}, \tag{C.9}$$

where,

$$\mu_2 = \mathbf{C}\mathbf{g} \quad \text{and} \quad \mathbf{R}_2 = \sigma^2 \mathbf{I}_{TKM}. \tag{C.10}$$

The CRB for $\mathbf{G}$ is given by summing (C.6) and (C.7) where $\overline{\mathbf{M}} = Re\{\mathbf{C}^{\mathrm{H}}\mathbf{R}^{-1}\mathbf{C}\}$ and $\widetilde{\mathbf{M}} = Im\{\mathbf{C}^{\mathrm{H}}\mathbf{R}^{-1}\mathbf{C}\}$, where $\mathbf{C}^{\mathrm{H}}\mathbf{R}^{-1}\mathbf{C}$ can be expanded as follows

$$\begin{aligned}
\mathbf{C}^{\mathrm{H}}\mathbf{R}^{-1}\mathbf{C} &= (1/\sigma^2)\left(\Psi^{\mathrm{T}} \diamond (\mathbf{X} \otimes \mathbf{H})\right)^{\mathrm{H}} \left(\Psi^{\mathrm{T}} \diamond (\mathbf{X} \otimes \mathbf{H})\right) \\
&= (1/\sigma^2)\left((\Psi^{*}\Psi^{\mathrm{T}}) \odot (\mathbf{X} \otimes \mathbf{H})^{\mathrm{H}} (\mathbf{X} \otimes \mathbf{H})\right) \\
&= (1/\sigma^2)\left((\Psi^{*}\Psi^{\mathrm{T}}) \odot \left((\mathbf{X}^{\mathrm{H}}\mathbf{X}) \otimes (\mathbf{H}^{\mathrm{H}}\mathbf{H})\right)\right).
\end{aligned} \tag{C.11}$$

Under the assumption that Ψ is a semi-unitary matrix satisfying $\Psi^{*}\Psi^{\mathrm{T}} = K\mathbf{I}_{LN}$ (see our discussion in Appendix A.1), we have

$$\mathbf{C}^{\mathrm{H}}\mathbf{R}^{-1}\mathbf{C} = (K/\sigma^2)\left(\mathbf{I}_{LN} \odot \left((\mathbf{X}^{\mathrm{H}}\mathbf{X}) \otimes (\mathbf{H}^{\mathrm{H}}\mathbf{H})\right)\right). \tag{C.12}$$

Note that according to (C.12), $\mathbf{C}^{\mathrm{H}}\mathbf{R}^{-1}\mathbf{C}$ is a real-valued diagonal matrix, which implies $\widetilde{\mathbf{M}} = \mathbf{0}$. As a consequence (C.5) is a block diagonal matrix, meaning that the real and imaginary parts are decoupled. Plugging (C.12) into (C.6) and (C.7), the CRB for $\mathbf{G}$ is obtained.

C.0.2 CRB for the IRS-BS channel

Here, the IRS-BS channel $\mathbf{H}$ is treated as an unknown nuisance, and the CRB is derived for the UT-IRS channel $\mathbf{G}$. Thus

$$\theta_c = [\overline{\mathbf{h}}^{\mathrm{T}} \ \widetilde{\mathbf{h}}^{\mathrm{T}}]^{\mathrm{T}}, \quad \mathbf{h} = \mathrm{vec}(\mathbf{H}) \quad \text{and} \quad \gamma = [\overline{\mathbf{g}}^{\mathrm{T}} \ \widetilde{\mathbf{g}}^{\mathrm{T}} \ \mathrm{vec}(\mathbf{X})^{\mathrm{T}}]^{\mathrm{T}}. \tag{C.13}$$

Applying the vec$(\cdot)$ operator to (5.7), we obtain the following noisy observation vector

$$\mathbf{y}_1 = (\mathbf{F} \otimes \mathbf{I}_M)\,\mathbf{h} = \mathbf{P}\mathbf{h}, \tag{C.14}$$

where, $\mathbf{y}_1 = \mathrm{vec}(\mathbf{Y}_1)$ and $\mathbf{y}_1 \sim CN\,(\mu_3, \mathbf{R}_3)$, and

$$\mu_3 = \mathbf{P}\mathbf{h} \quad \text{and} \quad \mathbf{R}_3 = \sigma^2\mathbf{I}. \tag{C.15}$$

We have $\overline{\mathbf{M}} = Re\{\mathbf{P}^{\mathrm{H}}\mathbf{R}_2^{-1}\mathbf{P}\}$ and $\widetilde{\mathbf{M}} = Im\{\mathbf{P}^{\mathrm{H}}\mathbf{R}_2^{-1}\mathbf{P}\}$. Then,

$$\begin{aligned} \mathbf{P}^{\mathrm{H}}\mathbf{R}_2^{-1}\mathbf{P} &= (1/\sigma^2)\,(\mathbf{F} \otimes \mathbf{I}_M)^{\mathrm{H}}\,(\mathbf{F} \otimes \mathbf{I}_M) \\ &= (1/\sigma^2)\left((\mathbf{F}^{\mathrm{H}}\mathbf{F}) \otimes \mathbf{I}_M\right)^{\mathrm{H}}. \end{aligned} \tag{C.16}$$

Finally, from the Slepian-Bangs formula, the CRB for $\mathbf{H}$ is obtained by summing (C.6) and (C.7).

APÊNDICE D – APPENDIX – D: CASCADED JOINT CHANNEL AND SYMBOL ESTIMATION

The solution proposed in this thesis yields joint estimates of the individual channel matrices as well as the data symbol matrix. In the following, we show that our semi-blind method can be slightly modified to provide an estimate of the cascaded channel instead. Since some IRS optimization schemes rely on the cascaded channel (see., e.g. (Subhash *et al.*, 2022)), our solution is also applicable in this context, i.e., it can deliver a joint estimate of the cascaded channel and the data symbol matrix.

Defining $\mathbf{S} \in \mathbb{C}^{N \times N}$ as the diagonal IRS phase shift matrix (which is now fixed across the K blocks), and assuming that the direct link is not available, the received signal can be written as

$$\mathbf{y}[k,t] = \mathbf{HSG}D_k(\mathbf{W})\mathbf{x}[t] \in \mathbb{C}^{M \times 1}, \tag{D.1}$$

Defining the cascaded channel $\mathbf{H}_{EQ} = \mathbf{HSG} \in \mathbb{C}^{M \times L}$ and collecting the received signal during T time slots, we have $\mathbf{Y}[k] = \mathbf{H}_{EQ}D_k(\mathbf{W})\mathbf{X}^{\mathrm{T}} \in \mathbb{C}^{M \times T}$, which corresponds to the frontal slice of the following PARAFAC tensor model

$$\mathscr{Y} = \mathscr{I}_{3,L} \times_1 \mathbf{H}_{EQ} \times_2 \mathbf{X} \times_3 \mathbf{W} \ \in \mathbb{C}^{L \times T \times K} \tag{D.2}$$

The 3-mode unfolding of tensor $\mathscr{Y}$ can be expressed as

$$\mathbf{Y}_3 = \mathbf{W}\left(\mathbf{X} \diamond \mathbf{H}_{EQ}\right)^{\mathrm{T}}. \tag{D.3}$$

After left-filtering with the known coding matrix, we get $\mathbf{Z} = \mathbf{W}^{\dagger}\mathbf{Y}_3 = (\mathbf{X} \diamond \mathbf{H}_{EQ})^{\mathrm{T}}$. This step requires that $\mathbf{W} \in \mathbb{C}^{K \times L}$ be full column-rank to be right-invertible, which implies having $K \geq L$. A joint estimate of the cascaded channel $\mathbf{H}_{EQ}$ and the data symbol matrix $\mathbf{X}$ can be obtained by solving $\underset{\mathbf{X},\mathbf{H}_{EQ}}{\min} \|\mathbf{Z}^{\mathrm{T}} - \mathbf{X} \diamond \mathbf{H}_{EQ}\|_F^2$ via the least squares Khatri-Rao factorization algorithm. Therefore, the proposed semi-blind solution can also be modified to estimate the cascaded channel instead of providing decoupled estimates of the individual channels.